ALMA MATER STUDIORUM
UNIVERSITÀ DI BOLOGNA

DOTTORATO DI RICERCA IN

MECCANICA E SCIENZE AVANZATE DELL'INGEGNERIA

Ciclo 38

Settore Concorsuale: 09/A3 - PROGETTAZIONE INDUSTRIALE, COSTRUZIONI MECCANICHE E METALLURGIA

Settore Scientifico Disciplinare: ING-IND/15 - DISEGNO E METODI DELL'INGEGNERIA INDUSTRIALE

ADVANCED SURGICAL SIMULATION PROCESSES IN THE CORRECTION OF FUNCTIONAL DEFECTS AND MUSCULOSKELETAL DISORDERS IN PAEDIATRIC AGE

Presentata da: Grazia Chiara Menozzi

Coordinatore Dottorato

Lorenzo Donati

Supervisore

Leonardo Frizziero

Co-supervisore

Gian Maria Santi

Giovanni Trisolino

Esame finale anno 2026

ABSTRACT

This thesis was developed through a collaboration between the Department of Industrial Engineering of the University of Bologna and the Paediatric Orthopedics and Traumatology Unit of the Rizzoli Orthopaedic Institute in Bologna, to integrate CAD and 3D printing technologies into a hospital-based point-of-care (POC) model for Virtual Surgical Planning (VSP) and in-house production of personalized surgical instruments using scalable and cost-effective technologies.

The work focused on optimizing the VSP workflow for paediatric musculoskeletal deformities and bone tumours by combining structured deformity analysis, virtual simulation, and FDM 3D printing of Patient-Specific (PSI) and Graft-Specific (GSI) instruments in HTPLA. A standardized deformity analysis protocol was defined to formalize the planning process from geometric assessment to surgical simulation.

The manufacturing phase was systematically investigated to improve dimensional accuracy and process stability. Printing optimization demonstrated that low fan speed combined with a 45° infill pattern minimized 3D deformation, with a standard deviation of 0.47 mm in 3D distance maps. A regression-based compensation model was developed to adjust fixation-hole diameters, according to the manufacturing process, ensuring reliable transfer from digital planning to physical surgical guides.

The consolidated workflow was applied to 144 procedures in 114 patients, including 22 oncological cases. Angular correction was achieved in 91 procedures (mean 26.3°, range 3–151°), while bone grafts or massive allografts were used in 58 procedures, 22 of which were shaped using GSIs. Sterilizable PSIs were employed in 93 procedures, with a total of 199 guides produced (mean 2 per procedure). Complication rates were comparable to traditional surgery. Operative time was the only independent predictor of complications, while PSI-related technical issues were infrequent (6%) and mainly related to suboptimal imaging quality.

Finally, an international research experience expanded the approach toward soft-tissue–aware and functional VSP models, outlining future developments toward prognostic applications in paediatric orthopaedics.

INDEX

LIST OF FIGURES

LIST OF TABLES

GLOSSARY OF ABBREVIATIONS

3

3DFI: three-dimensional fatty infiltration; 114
3DML: three-dimensional muscle loss; 114
3DMM: three-dimensional muscle mass; 114

A

ABS: Acrylonitrile–butadiene–styrene; 5
AC: Achieved correction angles; 93
ACA: Angular Correction Axis; 47
AHI: acromiohumeral interval; 112
AM: Additive Manufacturing; 5
ANOVA: Analysis of Variance; 69

B

BIA: Bioelectrical Impedance Analysis; 119
BMC: bone mineral content; 120
BMD: Becker muscular dystrophy; 123; bone mineral density; 116
BTM: Musculoskeletal Tissue Bank; 1

C

CAD: Computer-Aided-Design; 4
CCD: Central Composite Design; 80
CORA: Center of Rotation of Angulation; 16
CSA: cross-sectional area; 112
CT: Computed Tomography; 1
CTA: cuff tear arthropathy; 110

D

DICOM: Digital Imaging and Communications in Medicine; 7
DMD: Duchenne muscular dystrophy; 120
DXA: Dual-energy X-ray Absorptiometry; 112

F

FDA: Food and Drug Administration; 8
FDM: Fused Deposition Modelling; 5
FI: Fatty infiltrations; 113

G

GMFCS: Gross Motor Function Classification System; 122
GMFM: Gross Motor Function Measure; 120
GSIs: Graft-Specific Instruments; 1

H

HTPLA: High-Temperature Polylactic Acid; 36
HU: Hounsfield Units; 12

L

lBL: longitudinal bisector line; 59

M

MDP: Maximum Deformity Plane; 16
MRCT: massive rotator cuff tears; 110
MRI: Magnetic Resonance Imaging; 1

O

OA: glenohumeral osteoarthritis; 110

P

PC: Planned correction angles; 92
PLA: polylactic acid; 5
PoC: Point-of-Care; 8
PSIs: Patient-Specific Instruments; 1

R

ROM: range of motion; 110
RSA: Reverse Shoulder Arthroplasty; 110
RSM: Response Surface Methodology; 80

S

SCPE: Surveillance of Surveillance of Cerebral Palsy Europe; 122
SLA: Stereolithography; 5
STL: Standard Tessellation Language, or STereoLithography; 6
SWE: Shear Wave Elastography; 119

T

tBL: transverse bisector line; 52
TDC: typically developing children; 120
TSA: Total Shoulder Arthroplasty; 110

V

VSP: Virtual Surgical Planning; 7

X

XR: X-rays; 112

1. INTRODUCTION

1.1. Collaboration between the University of Bologna and the IRCCS Rizzoli Orthopaedic Institute

The application of design, modelling, and 3D printing technologies to orthopaedics at the Rizzoli Orthopaedic Institute originated in 2018 with the establishment of a collaboration between the Department of Industrial Engineering at the University of Bologna and the Paediatric Orthopaedics and Traumatology Unit. However, the experience, workflows, and the majority of the applicative and process-related data presented in this thesis were developed directly by the author during the PhD programme, which started in 2022.

Since 2018, various research projects have been carried out between these two institutions in Bologna, gradually evolving from basic understanding of how to obtain skeletal models from CT (Computed Tomography) or MRI (Magnetic Resonance Imaging) scans [1]. Over time, the process has been progressively refined step by step into a well-established workflow [2–5], schematically illustrated in Figure 3 of Chapter 2. Today, this workflow enables the virtual 3D reconstruction of patient anatomy from CT or MRI scans, the 3D printing of patient-specific bone models, personalized preoperative planning, and the design and 3D printing of Patient-Specific Instruments (PSIs) [6–9]. Furthermore, thanks to the Musculoskeletal Tissue Bank (BTM) at the IRCCS Rizzoli Orthopaedic Institute in Bologna, the collaboration has expanded to include research activities involving the reconstruction of 3D anatomical models from CT scans taken from cadaveric bones from donors. When necessary, this also includes preoperative planning and the design and 3D printing of Graft-Specific Instruments (GSIs) tailored to the donor bone.

All developments and applications have been conducted under the framework of three clinical protocols approved by the Area Vasta Emilia Centro Ethics Committee (CE-AVEC) of the Emilia-Romagna Region. The first, now completed, was the 3D MALF study (CE-AVEC 356/2018/Sper/IOR). This was followed by two ongoing protocols, 3D MALF II (CE-AVEC: 301/2022/Sper/IOR; ClinicalTrials.gov ID: NCT05700526, https://clinicaltrials.gov/study/NCT05700526) and SIMULA (CE-AVEC: 643/2023/Sper/IOR; ClinicalTrials.gov ID: NCT06380530, https://clinicaltrials.gov/study/NCT06380530), each focusing on increasingly advanced aspects of virtual planning and surgical simulation, as well as on the design and 3D printing of PSIs and GSIs.

What began as a collaboration with the Paediatric Orthopaedics and Traumatology Department has gradually attracted growing interest. An increasing number of surgeons from other units of the Rizzoli Institute are becoming involved, and the range of clinical applications continues to expand. While initially the focus was solely on the treatment of paediatric lower limb deformities, the workflow is now frequently applied to upper limb and other anatomical area cases as well. Most notably, there is increasing interest in complex oncological cases involving paediatric patients undergoing tumour resection and limb reconstruction, where the BTM plays a central role in the process [10].

1.2. Musculoskeletal disorders in paediatric age

Paediatric care focuses on the dynamic growth of each individual from birth to adolescence. During this period, growth and development takes place for different aspects, such as gross and fine motor skills, body size, gait, sexual characteristics and social and verbal skills. Many paediatric orthopaedic problems results from disorders or conditions that adversely affect normal growth and development. The four major failures of normal growth and development are malformations, deformations, disruptions and dysplasia [11].

Long bone growth occurs through endochondral ossification at the epiphyseal growth plates (physes), where cartilage is progressively replaced by bone. Each physis contributes a specific proportion to longitudinal growth in the upper and lower limbs [11]. This process is regulated by systemic hormones, local growth factors, and nutritional status [12,13]. During puberty, growth plates progressively mature and close through epiphyseal fusion, a process largely driven by sex hormones, particularly estrogen in both sexes, marking the end of longitudinal growth, typically between 12–16 years in females and 14–18 years in males, with relevant individual variability [14]. Alterations of this mechanism may lead to clinically significant growth abnormalities.

Both in children and adults, bone is capable of regeneration after fractures or osteotomies, and it can also be lengthened in a controlled manner through distraction osteogenesis (approximately 1 mm/day), a principle introduced by Codivilla and later popularized by Ilizarov, now widely used for limb length discrepancies, deformities, and bone defects [15–18].

Paediatric musculoskeletal diseases may involve bone deformities and bone tumours. This thesis focuses on the use of 3D technologies in treating mainly skeletal deformities and bone tumours of the long bones, with particular emphasis on those of the lower limbs [19].

1.2.1. Musculoskeletal deformities

Bone deformities can develop in different areas of the body and present in various types. A bone deformity is defined as the deviation of a bone from the parameters and limits of normal alignment, shape or size [20]. Deformities can arise from various causes, such as congenital factors (present at birth), developmental factors (resulting from abnormal growth during childhood) and acquired conditions, such as infections, trauma, or tumours [11].

Despite the complex three-dimensional structure of bones and joints, all bone deformities can be analysed as a combination of four fundamental parameters: angulation (bending of the bone), rotation (twisting of the bone), translation (displacement of bone segments), and length discrepancy (abnormal bone length). The last two parameters, although geometrically equivalent as they both describe a spatial translation, must be distinguished, since from a biological perspective soft tissues (muscles, nerves, blood vessels) impose limits on the extent to which a body segment can be lengthened or shortened. This framework represents the current universal approach to deformity analysis, offering a standardized system for accurate description and surgical planning [21].

Various surgical techniques are available, including growth modulation, which involves the temporarily or permanently stopping growth by the pinning of the physis, gradual correction through distraction osteogenesis, using external or internal lengthening devices that can address all parameters of the deformities including length discrepancies, and acute correction, typically performed with osteotomies.

To better understand these 3D complex characteristics, bone and joint are simplified to basic line drawings that are the mechanical and anatomic bone axes. Each long bone has a mechanical and an anatomic axis. The mechanical axis of a bone is always defined as the straight line connecting the joint centre points of the proximal and distal joints, whether in the frontal or sagittal plane. The anatomical is defined as the mid-diaphyseal line, which can be straight in the frontal plane but curved in the sagittal, as in the femur (Figure 1) [15].

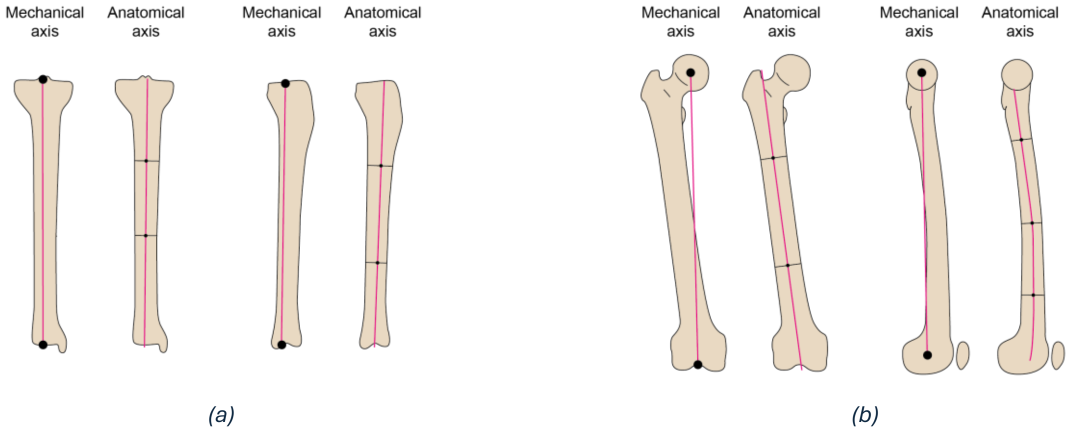

Figure 1. Mechanical and anatomic axes of bones. (a) In straight bones like the tibia, the anatomical axis follows a straight mid-diaphyseal path and the tibial mechanical and anatomical axes are parallel but not coincident. (b) In curved bones like the femur, the anatomical axis follows a curved mid-diaphyseal path, and the mechanical and anatomical axes are not parallel.

1.2.2. Musculoskeletal tumours

Primary bone tumours are rare (<1% of all cancers). Symptoms include pain and swelling in a bone or joint, with symptoms that may initially be mistaken for sports injuries in active adolescents. However, night pain, systemic fever, weight loss, or failure to respond to conservative treatment should raise suspicion of a more serious underlying condition. Among malignant bone tumours in children and adolescents, osteosarcoma has an incidence of 4.4 per million [22], with a peak in the second decade of life, while Ewing sarcoma has an incidence of 2.9 per million [23].

The treatment of these pathologies must be approached in a multidisciplinary manner [24]. For example, both chemotherapy planning and biopsy procedures require close coordination. In the case of biopsy, the needle used for diagnosis should be positioned so that its path can be included in the final surgical excision, and its planning must be jointly coordinated by the radiologist and the surgeon [25]. The initial evaluation typically includes radiography and MRI or CT to assess the primary tumour, followed by additional investigations to detect possible metastatic disease. Curative treatment generally requires surgical removal of the entire tumour, usually through wide excision. Advances in imaging and surgical techniques have significantly increased the feasibility of limb-salvage procedures, reducing the need for amputation [26].

Surgical resection of bone tumours during growth presents several challenges. Most tumours arise in the metaphyseal region and may involve the growth plate. As a result, tumour removal can lead to limb length discrepancies in growing children. This issue can be managed through preventive lengthening during resection, shoe lifts, or, in cases of greater discrepancies, the use of expandable prostheses [27]. Innovative approaches include, for example, the use of intercalary allografts, which can lead to excellent outcomes [28].

1.3. Computer-Aided-Design and 3D Printing technologies

1.3.1. Computer-Aided-Design

In general, Computer-Aided-Design (CAD) is a concept which implies all software tools able to develop digital representations to support the creation, development, and revision of designs. Originally developed for architectural applications, CAD has its roots in the early 1960s, with pioneering systems such as Sketchpad, presented in 1963 by Ivan Sutherland at the Massachusetts Institute of Technology [29]. Today, CAD is essential for designing a wide range of objects and systems, enabling faster development, higher precision, and improved visualization of objects. It also supports simulations to evaluate the effects that would be difficult or costly to test in real conditions. Thanks to its versatility, CAD is well suited for multidisciplinary projects, allowing data integration and process optimization across different domains [30]. One of the earliest applications of CAD technology in medicine was introduced in the mid1980s by Vannier et al., who used it for craniofacial surgical planning and evaluation based on surface contours derived from CT scans [31].

Since then, CAD has been increasingly adopted in medicine, particularly in cranio-maxillofacial surgery, where it enabled the generation of accurate 3D reconstructions from CT data [32,33]. These virtual models allowed surgeons to simulate osteotomies, bone realignment, implant positioning, and tumour resections before the actual operation. Although transferring such precise virtual plans into surgery remains challenging, CAD applications have markedly advanced diagnostic accuracy and preoperative planning beyond the limits of conventional 2D imaging. Similarly, in orthopedics, deformity analysis and correction are integral to many procedures, traditionally based on standard 2D radiographs and reference parameters [34,35]. The introduction of CAD and 3D imaging has therefore provided orthopaedic surgeons with powerful tools for more accurate visualization, simulation, and preoperative planning, as well as integration with intra-operative navigation systems and the development of training platforms for surgical education [32,36–38].

1.3.2. 3D Printing

3D printing, or additive manufacturing (AM), is a process based on the layer-by-layer addition of material to build objects directly from digital models. It first emerged in the 1980s with the development of stereolithography (SLA) by Chuck Hull, who founded 3D Systems and patented the technology in 1986 [39]. Since then, 3D printing has rapidly advanced, introducing diverse techniques and materials that enable high precision, design flexibility, and the fabrication of complex geometries. Initially applied in rapid prototyping [40], 3D printing is now widely used in aerospace, automotive, fashion, and, increasingly, medicine [41–45].

3D printing systems include several different processes that can be categorized as follows, according to the definitions provided by the ISO/ASTM 52900 standard, which classifies AM technologies into seven main process categories [46]:

- Binder Jetting: uses a liquid binding agent, deposited through an inkjet print head, to join powder materials within a powder bed.
- Directed Energy Deposition: uses focused thermal energy, typically from a laser, to fuse materials by melting them as they are deposited.
- Material Extrusion: pushes material, typically a thermoplastic filament, through a heated nozzle onto a platform that moves along horizontal and vertical axes.
- Material Jetting: deposits droplets of build material across the build area using a moving inkjet print head.
- Powder Bed Fusion: uses thermal energy from a laser or electron beam to selectively fuse powder particles within a powder bed.
- Sheet Lamination: bonds sheets of material together to form a 3D object.
- Vat Photopolymerization: selectively cures a liquid photopolymer in a vat using a light source.

The main materials used in 3D printing are plastics and metals, followed by ceramics, composites, and other less common options. The choice of material defines the most suitable printing process, and, conversely, the selected process influences the range of applicable materials.

AM offers several advantages, such as reduced overproduction and transportation costs, shorter supply chains, and lower material waste. These benefits are particularly evident with plastic materials, which are ideal for small, customized productions. Among the various 3D printing technologies, the most accessible and cost-effective is the material extrusion process known as Fused Deposition Modelling (FDM) [47].

FDM combines design flexibility, low equipment and material costs, and the ability to process a wide range of thermoplastics [48,49]. Over the past years, this technology has evolved considerably, with the introduction of numerous filament types and materials that have improved both manufacturability and aesthetic quality. Acrylonitrile–Butadiene–Styrene (ABS) and Polylactic Acid (PLA) are among the most commonly used. In particular, PLA, a semicrystalline biopolymer, finds applications ranging from biodegradable packaging and disposables to medical implants and personal care products [50].

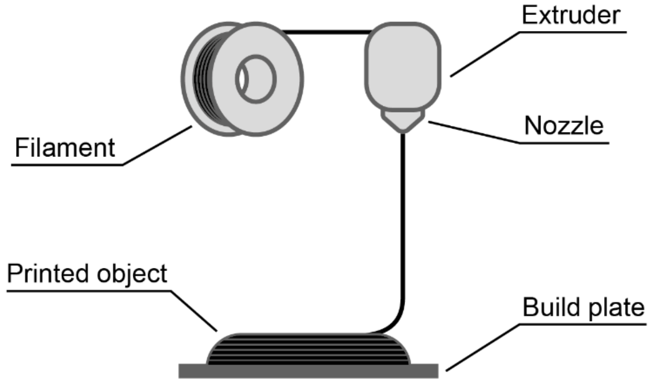

Figure 2. Simplified diagram of the FDM 3D printing process.

The printing principle of FDM is based on the extrusion of a thermoplastic filament through a heated nozzle. The material is pushed by an extruder and deposited line by line onto the build plate. After each layer is completed, the platform lowers by the layer height, and the process repeats until the final object is formed. A schematic representation is shown in Figure 2.

FDM also has some limitations compared to other 3D printing technologies, such as visible layer lines, reduced surface quality and detail, and part anisotropy due to layer bonding [51,52].

To prepare a model for 3D printing, it must be converted into an STL (Standard Tassellation Language, or STereoLithography) file format, which can be directly read by the slicer software used for the slicing process. The slicer divides the model into layers according to the desired layer height and sets printing parameters such as infill, extrusion temperature, and speed. STL is the most common file format used in CAD and 3D printing. It represents the 3D geometry of an object through a surface composed of numerous small triangular facets, which together form a mesh describing its shape and contours [53,54]. This process, known as tessellation, gives the file format its name. The model's resolution determines the number of triangles: higher resolution provides greater surface detail and smoother geometry representation but also increases file size [55].

In healthcare, 3D printing has played a pivotal role since its first medical application in the 1990s, when a 3D model of the cranial bones was reconstructed from CT imaging [56]. Since then, the technology has been increasingly integrated into several surgical specialties, including oral and maxillofacial, cardiothoracic, plastic, neurosurgical, and orthopaedic surgery [57–62]. 3D printing enables the cost-effective fabrication of customized prosthetics, implants, and dental devices, as well as anatomical models to support surgical planning [45,63]. More recently, it has also facilitated the production of patient-specific surgical guides and implants, further enhancing precision and personalization in clinical practice [64].

1.4. Integrating CAD and 3D Printing in Healthcare: from design to bedside

The integration of CAD and AM technologies with 3D medical imaging, such as CT and MRI, has significantly transformed clinical practice. These imaging modalities provide detailed cross-sectional views of patient anatomy, containing both quantitative and qualitative information, including tissue density data [65,66]. Combined with advanced medical image analysis software, the use of CAD and 3D printing has revolutionized surgical planning, first in craniomaxillofacial surgery and progressively across almost all medical fields, with consistent evidence of significant clinical benefits [67]. In orthopedics, and particularly in paediatric orthopaedic surgery, reductions in operating time, fluoroscopy exposure, bleeding, and complication rates, together with improved surgical precision, are among the most frequently reported advantages [68–71].

High-resolution, cross-sectional imaging data from CT and MRI are the main sources used for 3D reconstruction of virtual anatomical models. CT is based on X-ray attenuation, where a rotating source measures tissue density to produce cross-sectional images [72]. MRI, instead, uses magnetic fields and radiofrequency pulses to detect signals from hydrogen nuclei, generating highly detailed images of soft tissues [73]. These imaging datasets are typically stored in the DICOM (Digital Imaging and Communications in Medicine) format, which must be processed before being used for CAD and 3D printing technologies [74–76]. Each DICOM file is composed of voxels, three-dimensional elements that contain spatial and intensity information. The images are segmented to isolate the anatomical regions of interest by outlining tissue boundaries across consecutive 2D slices, from which a 3D reconstruction of the segmented anatomy is generated, producing a closed surface for each structure. The voxel data are then converted into a 3D surface mesh, usually in STL format, using interpolation algorithms that preserve anatomical accuracy, resulting in a 3D digital model of the anatomy [77–79].

Virtual Surgical Planning (VSP) uses 3D reconstructed models to simulate surgical outcomes by manipulating patient-specific anatomies. It allows clinicians to perform virtual osteotomies, bone repositioning, and optimize fixation points while practicing procedures in a risk-free digital environment. These tools enhance anatomical understanding, support surgical simulation, and enable the prediction of postoperative outcomes, while simultaneously allowing the translation of virtual planning into physical 3D printed biomodels, which are valuable for surgical planning, training, and patient communication [80–83]. The process, typically developed in collaboration with technical specialists, leads to the design and fabrication of custom cutting or drilling guides. The impact of medical 3D printing is greatest when it enables the production of patient-specific, also called custom-made, implants for cases unsuitable for standard solutions. CAD software plays a key role in ensuring accurate design of these implants tailored to each patient's anatomy [77].

3D printed PSIs, that is, all systems that guide bone cuts and/or drilling to prepare the bone to receive the implant or fixation devices (e.g., for osteotomies), assist surgeons, particularly in orthopedics, by defining screw direction and depth, osteotomy angle and range [84,85], and by helping achieve adequate margins in bone tumour resections [86–88]. They improve the precision, safety, and reliability of surgical procedures, simplifying complex steps and enabling accurate reproduction of the intended outcome. Moreover, these guides support the training of younger surgeons by providing structured intraoperative assistance and enhancing confidence during challenging procedures [89–92].

3D printed surgical instruments must undergo sterilization, a key step in producing any device intended for human contact, in particular in an operating theatre during surgery. The process must eliminates all microbial life, including viruses, bacteria, and fungi, without altering the material's physical, chemical, mechanical, or biocompatibility properties, thus preventing infections or rejections [93,94]. The most common sterilization methods for medical devices include ethylene oxide (EtO), gamma irradiation, and steam sterilization. For FDM-printed plastics, gamma irradiation can degrade polymers, while ethylene oxide is increasingly restricted due to its toxicity and carcinogenicity [95]. Consequently, steam sterilization remains the preferred and most widely used method in hospitals for sterilizing 3D printed parts. Although high temperatures may alter or deform polymeric materials, its use is gaining relevance in 3D printing applications, where other methods are often less suitable [96].

Efficient sterilization remains one of the main challenges for the clinical use of 3D printed medical devices, particularly those made of PLA. Interest in PLA-based devices has grown rapidly, as this bioabsorbable, biodegradable, and biocompatible polymer can be produced from renewable sources and offers a sustainable alternative to traditional biomaterials [97]. PLA degrades through hydrolysis or enzymatic activity into lactic acid, a naturally occurring compound in the body, thus preventing inflammatory reactions and allowing safe resorption. For these reasons, it is also widely used in tissue engineering, particularly for scaffolds in bone tissue replacement [98,99]. Its proven biocompatibility has led to FDA (Food and Drug Administration) approval for various applications, including orthopedics, cardiology, dentistry, plastic surgery, and drug delivery systems [100].

Among all available materials, PLA is particularly suitable for emerging technologies such as 3D printing, which is increasingly integrated into the biomedical field and now commonly found in hospitals. Among the available techniques, FDM is the most widespread, enabling the rapid fabrication of customized, complex, and reproducible structures. It supports personalized medicine and is widely applied in both research and clinical practice for patient-specific implants, surgical guides, and instruments, improving surgical outcomes and reducing radiation exposure [67].

Advances in 3D printing have led to the creation of Point-of-Care (PoC) centres that produce anatomical models, surgical instruments, and other devices directly in hospitals using patient imaging data to enhance accessibility and user-friendliness, notably cutting management costs [101,102]. While 3D PoC printing can improve patient outcomes and reduce operative time and costs, it also transforms medical device production and remains a regulatory grey area, as the overlap between hospitals and manufacturers challenges current legislation. PoC centres should therefore follow key quality system principles applied to medical device production, implementing internal regulations that cover process monitoring, maintenance protocols, imaging standards, material selection and documentation, layering and meshing accuracy, post-processing, sterilization, biocompatibility, and labelling for unique device traceability [103].

Medical devices manufactured using additive manufacturing (AM) technologies can be either “mass-produced” or “custom-made”, depending on whether they are designed for the general population or tailored to the specific needs of an individual patient. AM medical devices can be classified according to their level of invasiveness, as defined by the Medical Device Regulation [104,105]. Within the orthopedic field, which is the focus of this work, the following categories can be identified:

- **Anatomical biomodels**: bone or bone–soft tissue models used for training, planning, and patient communication. They are subject to the regulation only when intended to support diagnostic or therapeutic decisions. In such cases, the reconstruction software must be certified according to the associated clinical risk.
- **External devices**: such as braces, orthoses, sockets, insoles, and shoes. These devices are manufactured based on patient-specific anatomical characteristics and are intended to be worn by the patient, coming into contact with skin or mucosa for a limited duration.
- **Patient-Specific Instrumentation (PSI)**: devices designed to enable accurate positioning of surgical instruments or implantable medical devices during surgery. They are manufactured based on patient-specific anatomy, used intraoperatively for the duration of the procedure, and removed at the end of surgery, without permanent implantation.
- **Fully Custom-Made implants**: devices designed to be temporarily or permanently implanted within the patient for fixation or reconstruction purposes. These implants are

tailored to individual anatomy and are typically manufactured from metallic materials such as titanium or cobalt–chromium alloys.

- **Implantable grafts**: donor-derived bone grafts that are appropriately shaped and adapted to match the anatomical and therapeutic requirements of a single patient.
- **Engineered tissue and scaffolds**: trabecular or porous structures fabricated through AM, combining biomaterials and, in selected applications, living cells to create bioengineered constructs intended for implantation or in vitro modelling.

2. IN-HOSPITAL 3D PRINTING POINT-OF-CARE FOR PAEDIATRIC ORTHOPEDICS AT THE RIZZOLI INSTITUTE

2.1. Context and Aims

3D anatomical models derived from CT or MRI have become an integral component of modern clinical practice, particularly in surgery. They support diagnosis, education, patient communication, VSP, and the design of personalized implants and instruments such as PSIs and GSIs. To facilitate these applications, many hospitals are establishing in-house 3D printing facilities, commonly referred to as Point-of-Care (POC) centres. Compared to outsourcing, POC settings enable faster and more cost-effective production while fostering close collaboration between surgeons, clinicians, and technical experts, accelerating the adoption of personalized medicine and new 3D technologies. This approach is now widely applied across several specialties, with maxillofacial and orthopaedic surgery among the most active. In paediatric orthopaedics, where congenital and acquired deformities must be corrected while preserving growth, procedures such as osteotomies and reconstructions require accurate planning and the selection of appropriate fixation devices. Given the complexity and rarity of many conditions, VSP is particularly valuable to manage the intricate 3D anatomy of the growing skeleton.

The workflow presented below summarizes the process developed and continuously refined since 2018 at the Pediatric Orthopedics and Traumatology Unit of the Rizzoli Orthopedic Institute, in collaboration with the Department of Industrial Engineering of the University of Bologna. Within this collaboration, the tools supporting the workflow evolved over time in parallel with clinical experience. In the early phase, segmentation and preliminary analyses were mainly performed using open-source software, such as InVesalius (CTI Renato Archer, Brazil), 3D Slicer (open-source platform developed by an international academic consortium, United States), and Meshmixer (Autodesk Inc., United States), while the transition to routine clinical application led to the adoption of certified, industry-grade solutions, including Materialise Mimics (Materialise NV, Belgium) for image processing, Blender (Blender Foundation, The Netherlands) for VSP and PTC Creo (PTC Inc., United States) for parametric CAD design of PSIs and GSIs.

The goal of this collaboration was to establish an in-house framework integrating CAD design and 3D printing to support surgical practice through their application in VSP and in the design and manufacturing of PSIs and GSIs, thereby minimizing dependence on external services and reducing overall costs.

2.2. Workflow Architecture and Operational Phases

The workflow (Figure 3) consists of several phases, involving different specialized professionals who contribute according to their specific role, starting from patient identification and ending with the surgical treatment of that patient.

The process begins with patient identification and enrolment in the protocol, if consent is obtained. It then proceeds to the imaging acquisition phase, followed by data processing and imaging study preparation. The VSP phase follows, involving anatomical 3D virtual model analysis and simulation of the surgical approaches that the surgeon intends to evaluate, including the decision whether PSIs or GSIs are required. If so, once the final simulation is defined, the design and production of the instruments are carried out, followed by sterilization.

A summary report containing the main VSP information, surgical plan, and design specifications is then provided to the surgeon and used intraoperatively to trace the process and guide the use of the instruments, when applicable. Figure 3 illustrates the overall workflow, highlighting the main process phases and the key professional figures involved, which are described in more details in the following sections.

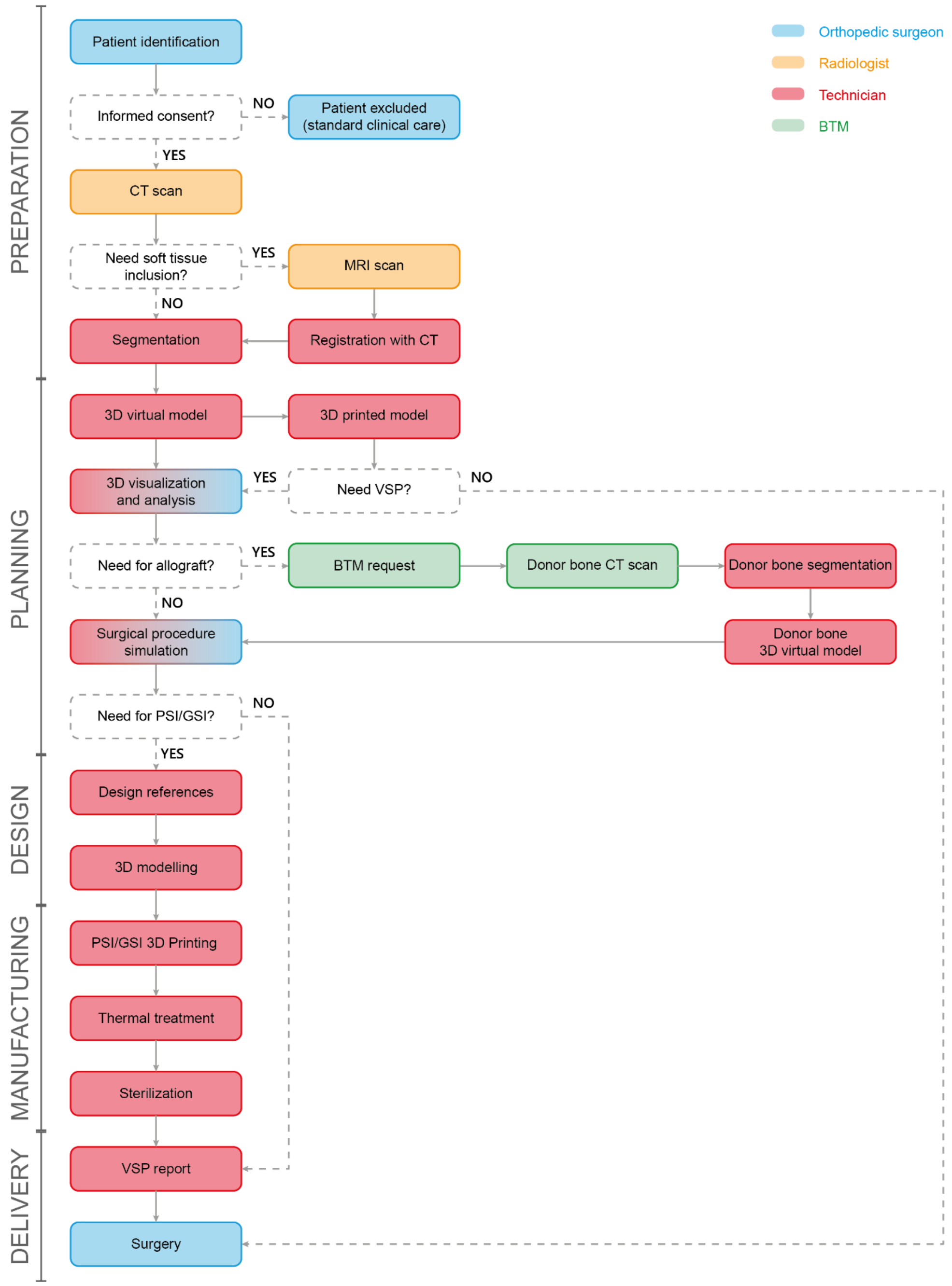

Figure 3. Overview of the workflow from patient selection to 3D printing and surgery (colour map on top right).

2.3. Preparation phase

2.3.1. Patient Identification, Enrolment, and Imaging Acquisition

The process begins with the clinicians during their routine clinical practice. When they visit a patient presenting with a complex deformity or an unusual condition, they evaluate the magnitude and complexity of the treatment and decide whether 3D reconstruction and VSP could support a better understanding of the case and assist in defining the optimal surgical approach.

Once the clinical indication is established, the patient is informed about the proposed use of 3D planning, and written consent is obtained for participation in the clinical trial and for personal data processing, with parental consent required in the case of minors.

After obtaining consent, the surgeon requests the necessary imaging examinations for the anatomical region of interest, typically low-dose CT scans (especially for paediatric patients), usually with a slice thickness of ≤ 1mm, and standard radiographs. In cases involving soft tissue assessment or oncological investigation, MRI scans may also be prescribed. Particularly in cases of unilateral bone deformity, it is preferable that imaging includes both limbs whenever possible, allowing an anatomical comparison with the contralateral healthy side to guide analysis and planning. In bilateral deformities, normal joint orientation angles are used instead. When multiple body segments are involved, the entire region, for example the thigh, the shank and the foot, should be included within the CT scan to ensure comprehensive visualization and more accurate modelling and planning.

Afterward, the surgeon provides the 3D PoC team with the patient's information, including demographic data and clinical details such as the affected segment, side, and type of deformity (e.g., varus or valgus). Once the imaging study is available, the DICOM files, which is the standard format for radiological data, are imported into Materialise Mimics, a certified software for medical use, and anonymized. Anonymization is performed by assigning a unique patient ID, ensuring that personal information such as name, sex and date of birth remains protected.

2.3.2. Segmentation

The process of generating the 3D model then begins, using the same software employed for anonymization. If necessary, image pre-processing can be performed to reduce noise, which may be present due to previously implanted metal fixation devices such as screws or plates. Denoising improves image quality, as noise, seen as unwanted random variations in pixel intensity, can degrade the accuracy of 3D reconstruction and subsequent surgical planning (Figure 4). If no noise is detected, segmentation can proceed directly.

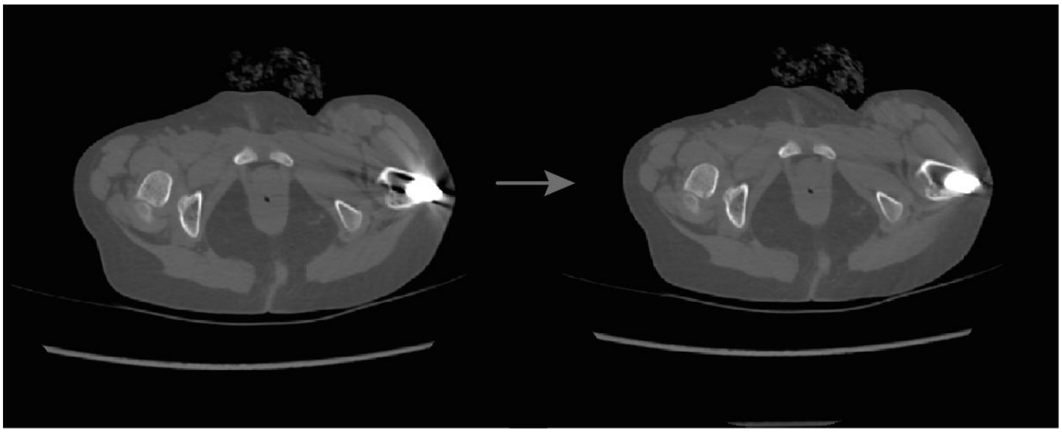

Figure 4. Example of image denoising from original CT images to noise reduction application.

Segmentation allows the partitioning of images into regions that share similar properties such as intensity, texture, or contrast, based on the information contained within voxels (the three-dimensional equivalents of pixels that constitute the original DICOM images). This represents a crucial step for accurate anatomical representation and precise 3D model reconstruction. Segmentation can be performed manually by various professionals, often engineers and radiologists. However, it is essential that the final reconstruction is validated by the clinician, who confirms the delineation of the regions of interest slice by slice. Although this approach ensures accuracy, it is time-consuming. More commonly, semi-automatic algorithms are used, combining manual input for initialization and correction with automated processing to balance efficiency and accuracy. This approach is particularly effective in our context, as bone, being a high-contrast tissue, is easily recognized by the algorithm. Once segmentation is completed, the result is reviewed and validated by the clinician. The main segmentation algorithms used are:

- Thresholding: image segmentation is performed based on Hounsfield Units (HU), which are intensity values calibrated to the density of water (each CT scanner is by default calibrated to water [106]). The threshold is derived from the image histogram. This method does not consider spatial information but includes everything within the selected intensity range, which may also contain unwanted elements and is therefore sensitive to noise. For this reason, it is usually used as a first tool to make an initial identification of the tissues (Figure 5).

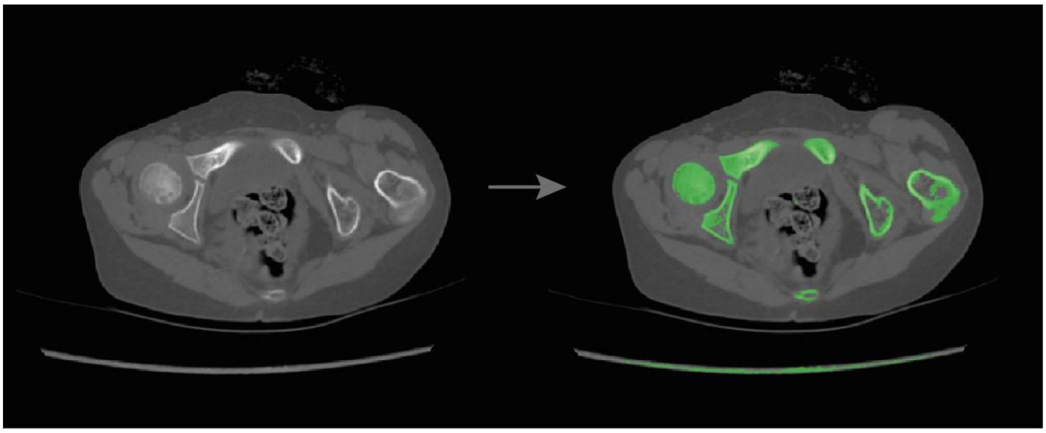

Figure 5. Example of threshold tools for segmentation showing the initial selection of voxels within the chosen intensity range.

- Split mask: this method refines segmentation by dividing an existing threshold-based mask into distinct anatomical regions. By manually outlining different areas in separate colours, it identifies and enables the semi-automatic generation of individual masks for each structure, such as the femur or tibia, allowing quick and efficient separation of anatomical components and significantly speeding up the segmentation process (Figure 6).

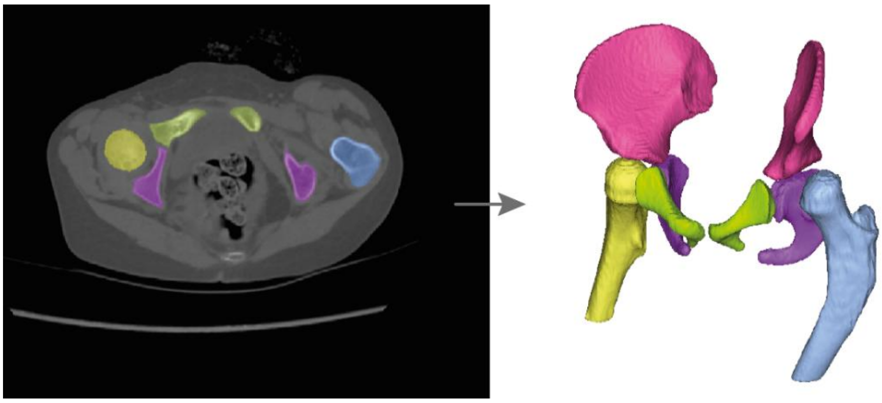

Figure 6. Example of the application of split masks in the segmentation of the pelvis in a 6-year-old female patient with recurrent left hip subluxation in the context of cerebral palsy, previously treated with proximal femoral osteotomy. On the left, manual slice-by-slice selection on CT images is shown; on the right, the corresponding 3D reconstructed model is displayed. Different colours highlight the various bony components of the pelvis.

- Region growing: this method is used to refine segmentation by expanding predefined regions through the addition of neighbouring pixels that meet specific criteria, such as similar intensity values. It utilizes spatial information, but its performance strongly depends on image quality and accurate denoising, as it preserves all neighbouring pixels connected to the selected regions. Therefore, it is ideal for separating distinct anatomical structures, provided that the regions are well connected and not affected by noise. Otherwise, manual refinement is required to remove unwanted connections before using it (Figure 7).

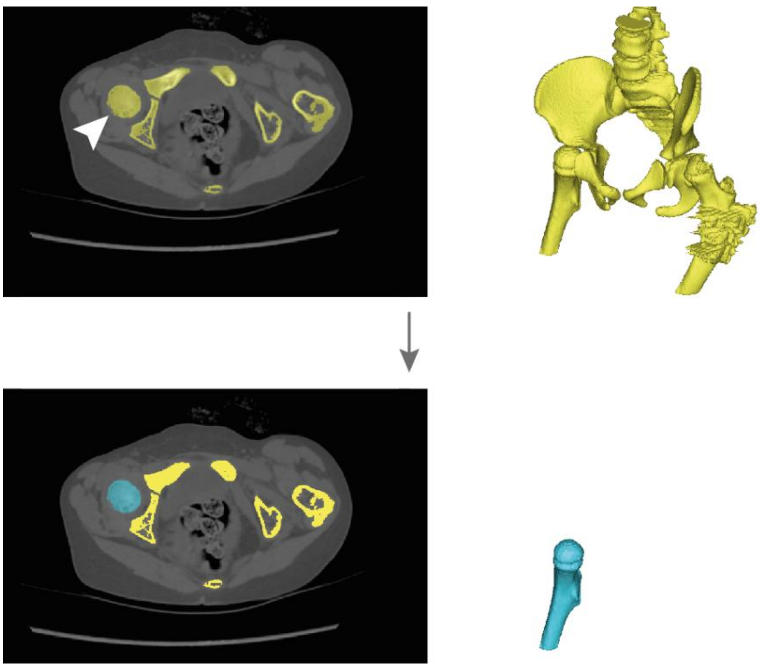

Figure 7. Example of region growing refinement before tool application and after selecting the area of interest and expanding the selected area by including only neighbouring pixels with similar intensity.

Once segmentation is completed and all anatomical regions of interest are identified and named, the 3D model is generated. From the segmented 2D DICOM images, a surface mesh is created based on the voxel values within the segmented mask, where triangular elements define the corresponding 3D geometry. The resulting mesh provides an accurate representation of the surface topology of bones, and eventually of other segmented structures if required, such as muscles or organs.

Using the Materialise Mimics software, a smoothing technique is then applied to reduce artifacts and enhance anatomical realism, since real anatomical surfaces are continuous rather than tessellated. This process minimizes noise and irregularities that could otherwise affect the model's accuracy or hinder its usability.

Each anatomical element is then exported as an STL file and imported into Blender for further optimization. Optimization consists of simplifying the 3D mesh to improve computational efficiency and visualization speed without compromising essential anatomical accuracy. In our workflow, the 'Decimate' modifier in Blender is applied to reduce the number of triangles, particularly for models used solely for analysis or visualization. For instance, in cases of distal humerus deformity (Figure 8), the CT scan includes the entire limb for anatomical context, but during reconstruction the distal segments (e.g., forearm bones) can be simplified, as high precision is only required in the treated area. The refined mesh is now suitable for real-time interaction, a crucial requirement for VSP.

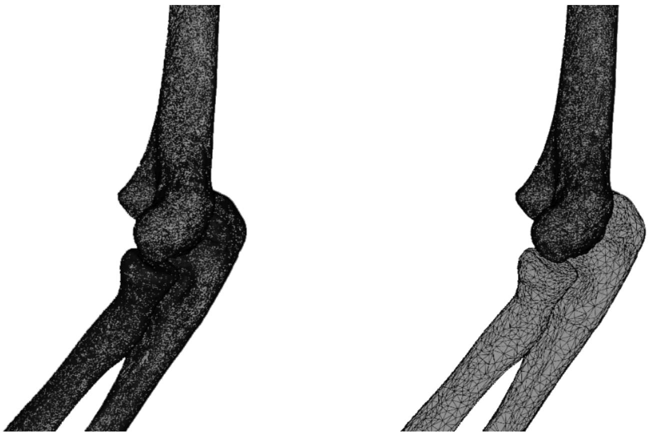

Figure 8. 3D reconstruction for a distal humerus deformity. The humerus is preserved in high detail to retain anatomical accuracy in the region of interest, while distal segments such as the forearm and hand are simplified to optimize model performance and concentrate the resolution where needed.

2.3.3. Registration

In some cases, it may be necessary to integrate 3D information obtained from different imaging modalities, such as MRI, to accurately represent patient anatomy. This requires the registration and alignment of 3D models derived from multiple imaging sources. Image registration defines the spatial correspondence between datasets, establishing the correct mapping of points from one image to their matching positions in another. This step is performed in Mimics software to ensure proper alignment of the images, allowing the 3D reconstruction to be correctly superimposed and the final model to be exported with fused and unified data containing all the required information. The process begins with the standard upload of DICOM images, typically starting from CT scans, followed by the import of additional image sets, such as MRI. The CT dataset is kept as the reference coordinate system, while the secondary dataset is registered onto it. During registration, the two image sets are temporarily overlaid and manually aligned by the operator across the three anatomical planes. Once satisfactory alignment is achieved, the software calculates a transformation matrix, usually consisting of translation and rotation parameters. This matrix is stored within the secondary DICOM dataset and can be used when needed.

Activating the transformation matrix during segmentation of the second imaging dataset (usually MRI) allows the segmented masks to be automatically adjusted according to the defined spatial alignment. Consequently, during 3D model generation, the reconstruction can combine bone structures from CT with soft-tissue components (such as muscles, tumours, or other tissues) from MRI, perfectly matched in their correct anatomical position. The final STL models can then be exported for each segmented bone structure and imported into Blender, providing a complete and spatially coherent dataset derived from both imaging modalities (Figure 9).

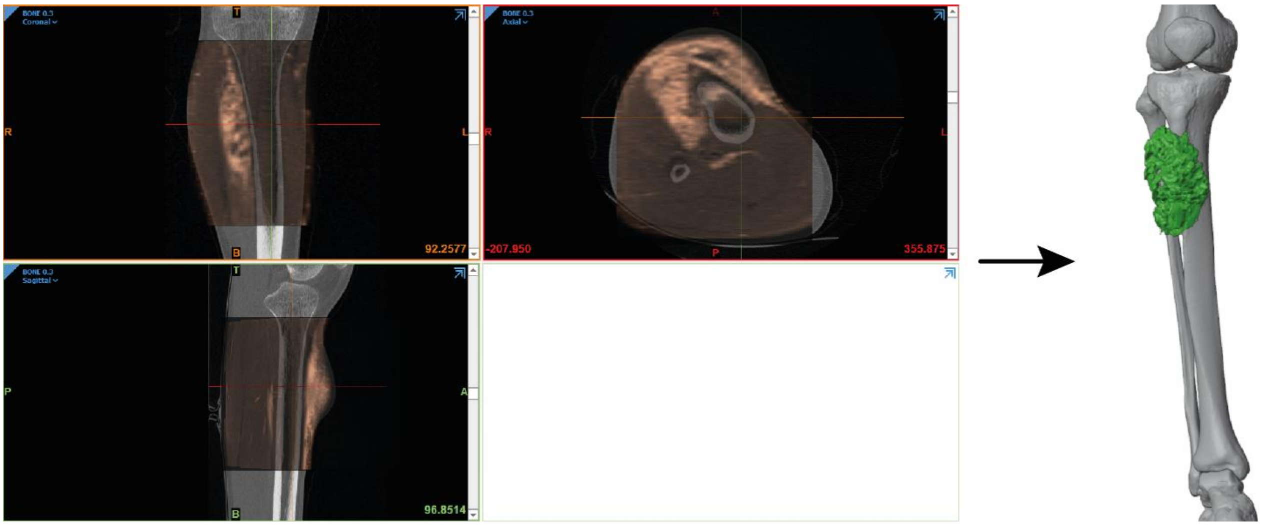

Figure 9. Overlay of MRI and CT datasets during the registration process to ensure correct spatial alignment and final 3D reconstruction combining CT-derived bone structures and MRI-derived structures.

2.4. Virtual Surgical Planning phase – deformity correction

2.4.1. 3D Visualization and Deformity Analysis

Once the model is obtained and optimized, VSP can be carried out in Blender. The digital 3D model can also be 3D printed to obtain a physical anatomical replica, enhancing tactile understanding of morphology and improving communication between surgeons, technicians and patient's family. The model is usually printed at a 1:1 scale to provide accurate dimensional awareness. For large anatomical structures, such as entire long bones or major skeletal segments, the maximum build volume of the printer must be considered, as it may be necessary to divide the model into multiple parts. In such cases, attachment pegs and holes are manually added to the 3D model to allow correct reassembly after printing. Figure 10 shows an example in which, due to the model geometry, the object was subdivided into two interlocking parts to ensure an accurate print of the ankle region. 3D printed anatomical models are also used to illustrate deformities and surgical procedures for training residents and students, as well as to improve communication with patients and their families.

(a) (b)

Figure 10. (a) Disassembled 3D model of an ankle with the connecting pin placed on the talus; (b) 3D model assembled.

On the digital 3D model, the deformity analysis is performed by tracing the anatomical axes of the involved bone segment and identifying the corresponding articular planes. Each anatomical axis is defined in 3D space as the straight line that best approximates the central axis of the bone segment geometry. Typically, one axis is defined on the proximal side and one on the distal side of the segment. This approach is particularly suitable for deformities involving the diaphyseal region. Conversely, when the deformity is located closer to the joint, joint orientation is defined using joint-specific methodologies. A reference plane is approximated by applying a best-fit approach to the articular surface, and an axis, typically corresponding to anatomical axis of the bone, is defined from a reference point, usually the geometric centroid of the articular surface. Both the plane and the axis are defined and validated under the surgeon's control and are then used as geometric references for deformity evaluation and surgical planning. The point where the two anatomical axes intersect is called the Center of Rotation of Angulation (CORA), which represents the apex of the deformity. Figure 11 illustrates an example of CORA identification, defined by the intersection between the distal axis of the radius and the proximal axis of the radius. The two axes intersecting at the CORA (in 2D projections) define a single plane, referred to as the Maximum Deformity Plane (MDP), on which the entire deformity lies.

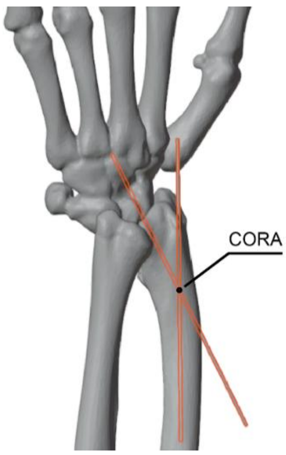

Figure 11. Identification of the CORA by intersecting anatomical axes of a bone segment.

This 3D approach allows a comprehensive evaluation that extends beyond the traditional two-dimensional assessment based on varus/valgus (coronal plane) and procurvatum/recurvatum (sagittal plane) deviations, also including torsional or rotational deformities (axial plane), which cannot be adequately appreciated on standard radiographs.

Once all these elements are defined, the bone morphology can be objectively evaluated to determine the presence, direction, and magnitude of the deformity. This geometric analysis provides an objective and reproducible reference, in contrast to the surgical approach, which may vary depending on the patient's characteristics and the surgeon's preferences.

2.4.2. Surgical Procedure Simulation

Once the model has been analysed, the surgical procedure can be simulated. In most cases, surgical simulation is performed to plan procedures that require one or more osteotomies. Different techniques can be applied to define the extent of the correction.

When a healthy contralateral side is available in the 3D model, it can be mirrored and superimposed onto the affected side to serve as a reference for correction, thereby simulating the morphology of the unaffected limb to be achieved. Figure 12 illustrates Case #1, involving a 4-year-old female patient with a complex deformity of the right lower limb affecting the femur, associated with a markedly altered gait pattern. While the left limb showed normal function, the deformed right limb was used with an inverted orientation, leading to abnormal foot progression and compensatory crouched walking to accommodate limb-length discrepancy. To facilitate deformity interpretation and definition of the target correction, the healthy left femur was mirrored and overlaid onto the affected right side. Deformity analysis identified the condition as a severe valgus deformity of 151°, which was treated with a corrective osteotomy to restore alignment of the right lower limb. The 3D reconstruction and surgical planning were performed following multidisciplinary counselling to ensure respect of vascular structures and surgical access, with the involvement of orthoplastic surgeons from the Orthoplastic Unit of the Rizzoli Orthopedic Institute. At the latest follow-up, a residual limb-length discrepancy was still present. However, limb alignment has been restored, and the patient is progressively regaining a normal gait pattern. The corrective alignment is expected to enable a future limb-lengthening procedure, which was not feasible prior to deformity correction.

Conversely, when both sides are affected or a healthy contralateral model is unavailable, the correction is defined based on the angular parameters derived from segmental deformity analysis and compared with established normal reference values for the corresponding anatomical region.

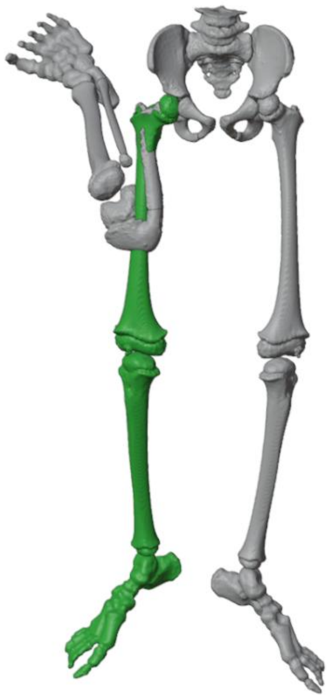

Figure 12. Example of contralateral mirroring applied during virtual surgical planning. In Case #1, the healthy left femur was mirrored and superimposed onto the affected right femur to guide deformity interpretation and target correction definition.

Depending on the surgeon's needs and preferences, it is essential to evaluate and identify the position, orientation, and type of procedure to be simulated. In some cases, multiple approaches can be virtually tested to determine which configuration provides the most suitable outcome for the surgeon. In particular, the main types of procedures that can be simulated include (Figure 13):

- No correction: simulation performed only to define the appropriate fixation device (screws or plates) in terms of fit, size, and positioning. This approach is typically used in fracture cases or in procedures requiring stabilization without correction;
- Closing-wedge osteotomy: removal of a bone wedge while maintaining a cortical hinge on the side corresponding to the wedge apex. This configuration allows for a pure angular correction in closure;
- Opening-wedge osteotomy: addition of a bone wedge while maintaining a cortical hinge on the side corresponding to the wedge apex. This technique provides a pure angular correction in opening;
- Dome osteotomy: complete cortical-to-cortical osteotomy dividing the bone in two segments with a dome cut to provide angular correction;
- Derotative osteotomy: complete cortical-to-cortical osteotomy dividing the bone into two segments, followed by rotation of either the proximal or distal portion around its longitudinal axis to correct torsional deformity;
- Oblique osteotomy: complete cortical-to-cortical osteotomy performed along an oblique plane, allowing for both angular and rotational correction depending on the inclination of the cut;
- Shortening and/or translation osteotomy: complete cortical-to-cortical osteotomy that enables length reduction or segment translation. In some cases, removal of a bone wedge may also introduce angular correction;

- Intercalary bone graft: complete cortical-to-cortical osteotomy in which a bone wedge or graft is interposed between the two segments. When the graft is angled, it can simultaneously provide angular correction.

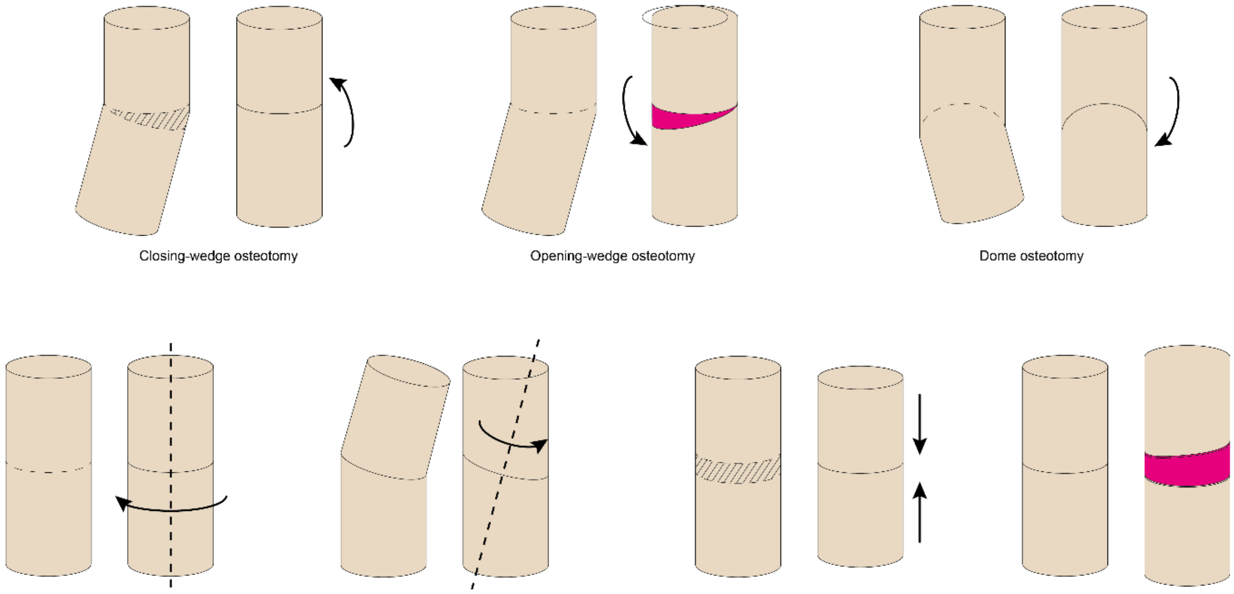

Figure 13. Overview of the main osteotomy types that can be virtually simulated to plan deformity correction, including closing- and opening-wedge, dome, derotative, oblique, shortening, and intercalary bone graft techniques.

After the correction parameters have been defined, the osteotomy planes are positioned accordingly, usually following the reference system derived from the deformity analysis (for example, the osteotomy plane is generally placed perpendicular to the MDP). Figure 14 illustrates the final deformity analysis of Case #1, which identified a severe valgus deformity of 151°. The figure shows the definition of reference planes and cutting planes, together with the corresponding 3D models before treatment and after the simulated correction. The planned correction involved a diaphyseal osteotomy to release the distal segment of the affected bone, followed by flattening at the point of maximum deformity to create a contact plane suitable for stable fixation after correction. A more detailed description of deformity assessment and possible surgical approaches, including osteotomy planning and correction strategies, will be further discussed in Chapter 3.

(a) *(b)* *(c)*

Figure 14. (a) Reference and cutting planes defined in the VSP; (b) 3D printed model before treatment; (c) 3D printed model after simulated correction.

2.4.3. Bone Bank Request

If the treatment involves an opening-wedge osteotomy or an intercalary bone graft, it is necessary to request donor bone from the BTM. In some cases, an autologous graft can be harvested directly from the patient. This represents a specific scenario managed entirely during the surgical planning phase, without the need for a BTM request, and will be discussed in Chapter 3.

When donor bone is required, the internal BTM of the Institute is usually contacted. The BTM operates within the hospital and is responsible for the procurement, processing, and distribution of different types of donor bone tissue. Donor retrieval procedures and donor eligibility assessments are performed internally, and all donor bones are routinely scanned with CT, allowing systematic cataloguing based on donor-specific characteristics.

The BTM can either deliver the donor bone directly to the operating room, allowing the surgeon to manually shape it intraoperatively, or perform the shaping process in a cleanroom environment, providing a pre-shaped graft ready for implantation.

In both situations, the bone cut may be performed freehand. In this case, the VSP serves as a reference to predefine the graft dimensions required to achieve the desired correction. Alternatively, GSIs can be designed to assist in accurately shaping the donor bone according to the VSP. Figures 15 and 16 show bone pre-shaping performed in the clean room by the BTM, and bone shaping performed in the operating room by the surgeon, respectively.

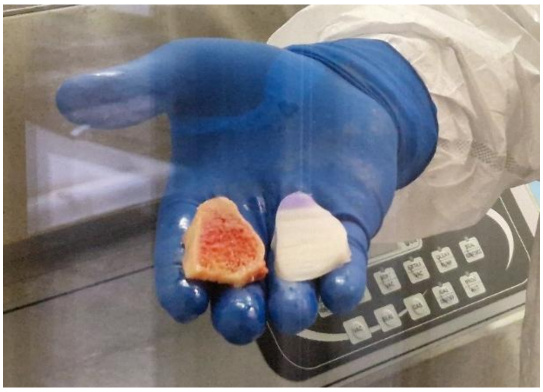

Figure 15. Donor bone pre-shaping performed in the clean room by the BTM, guided by the VSP and a sterile 3D printed reference model reproducing the final desired shape for donor bone cutting.

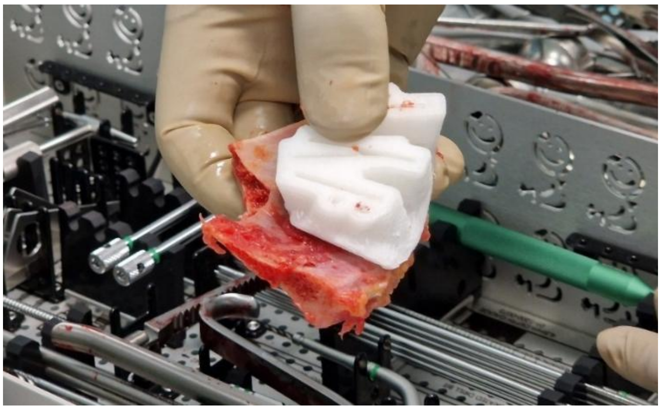

Figure 16. Bone shaping performed in the operating room by the surgeon, using specific GSIs designed for the donor bone according to the VSP.

In both scenarios, the BTM provides the available CT scan of the donor bone (or of the relevant portion), as only a limited section is generally required to obtain the necessary bone wedge. The donor bone is then segmented and optimized following the same process previously described for the patient's CT scan and subsequently imported into Blender and added to the VSP scenario of the corresponding patient. The VSP is then employed to identify the most appropriate region within the donor bone from which to harvest the graft, ensuring that the obtained wedge matches the dimensions and orientation defined during the surgical planning phase (Figure 17).

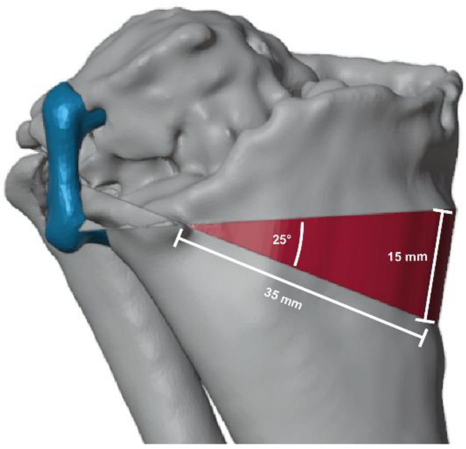

(a)

(b)

Figure 17. (a) Custom bone allograft identification with VSP; (b) Virtual identification of the optimal region within the donor bone for graft harvesting, matching the wedge dimensions required according to the surgical plan.

2.4.4. Fixation Strategy Definition

At this stage, the surgeon may request verification of the fixation system to determine the most appropriate type, size, and positioning of screws or plate, which may be standard (off-the-shelf) or custom-made, precisely conforming to the bone anatomy with which they interface. This is a crucial step, particularly in cases involving small or anatomically complex bones, where selecting the most suitable fixation device is essential to ensure an optimal match with the patient's anatomy.

The fixation components can either be modelled based on the technical drawings provided by the selected company or, preferably, obtained directly as confidential 3D models from the manufacturer upon the surgeon's request. The latter option is recommended, as it ensures higher model accuracy and significantly reduces design time.

The fixation system is usually positioned at the final stage of the VSP, since it must account for the fixation of all components (Figure 18), including potential bone grafts. For this reason, the final configuration of the treatment must be fully defined before proceeding with the placement of the fixation system.

Figure 18. Selected fixation device placed with placeholders to identify screw and K-wires positioning.

2.4.5. Design Reference Definition

If the surgeon requests only the VSP, the process proceeds directly to the preparation of the surgical report (as described in the 'Delivery Phase' paragraph).

When PSIs are also required to support the intraoperative execution of the plan, the subsequent steps are defined in close collaboration with the surgical team. This phase involves identifying critical anatomical structures to be preserved, determining the patient's positioning, selecting the most appropriate surgical approach, and assessing the extent of bone exposure required at the access site. Eventually, this can also be supported by the 3D virtual model, as the skin surface can be preserved during segmentation and used as an external anatomical reference to accurately identify the target bone region, optimize surgical access, and preliminarily hypothesize the most appropriate approach for dermal or plastic reconstruction (Figure 19).

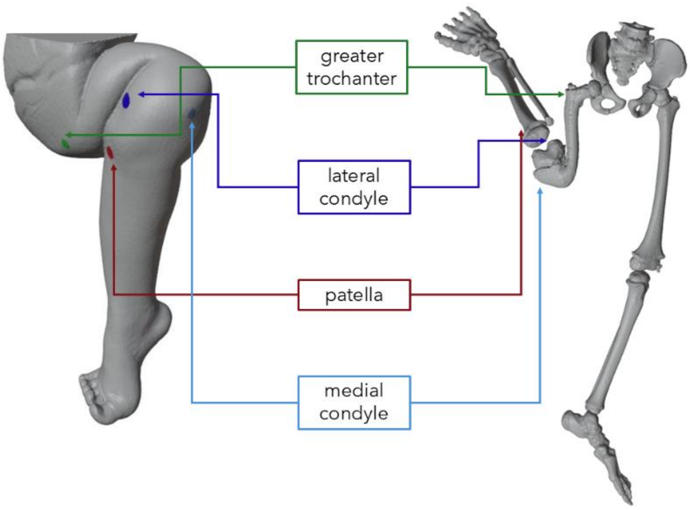

Figure 19. Example of 3D virtual model of Case #1 used as visual aid for anatomical referencing. The skin surface was preserved during segmentation to provide external landmarks for orientation.

This phase is also essential for determining the optimal placement of fixation pins, most commonly Kirschner wires (K-wires) in pediatric cases, which are thin metallic elements widely used in orthopedics to stabilize bone fragments or to guide and secure patient-specific cutting guides during surgery.

Throughout this thesis, the term pin is used in a broad, functional sense to indicate temporary fixation or positioning elements, including K-wires, smooth pins, and, in some contexts, screws, depending on the surgical application. Although these terms are not strictly interchangeable from a technical standpoint, the primary distinction between pins and wires is largely related to diameter, with pins typically ranging from approximately 1.5 mm to 6.5 mm and K-wires from 0.9 mm to 1.5 mm, while both may vary in length and end geometry [107]. Screws are generally larger, threaded devices that provide greater compression and more rigid fixation, often associated with lower rates of non-union but requiring a secondary procedure for removal [108]. In contrast, K-wires allow easier insertion and removal without a second operation, making them particularly suitable for pediatric patients, small fracture fragments, or comminuted cases [109].

It should be noted that many fixation systems are developed for specific osteotomy or treatment types and are accompanied by standardized surgical protocols provided by the manufacturer. These protocols usually describe in detail how the plate should be positioned on the bone and include the use of K-wires for temporary alignment and stabilization during surgery. When the surgeon plans to use a specific fixation system, its standardized surgical technique can be carefully reviewed and incorporated into the PSI design phase. In this way, the predefined pin positions used for plate alignment can also serve as reference points for the design of the guide's pin holes. Aligning the PSI design with the manufacturer's recommended fixation protocol helps avoid unnecessary additional bone perforations, ensures compatibility between the guide and the selected fixation system, and contributes to a more streamlined and efficient surgical workflow (Figure 20).

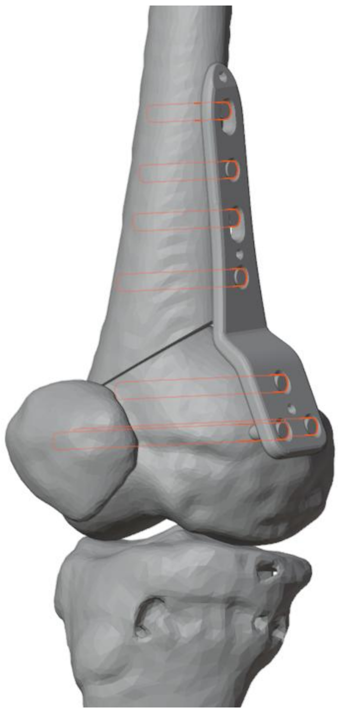

Figure 20. Pin positioning (highlighted in orange) during PSI reference setup, aligned with the selected plate's final screw holes.

In cases where GSIs are also planned, the procedure is very similar but involves fewer constraints. Since the VSP is performed on donor cadaveric bone, there is no need to consider critical anatomical structures, surgical access paths, or the positioning of fixation devices. The entire surface of the donor bone is already exposed and can be freely used without risk. The main task is to correctly position the cutting planes according to the corresponding surfaces of the grafts to be obtained, based on the region identified through the VSP as the most suitable for harvesting the required graft. It is also considered good practice, when positioning the pins for stabilizing the cutting guide used to shape the donor bone, to place them outside the effective area of the graft to be extracted. Naturally, this phase should still be guided by good judgment, aiming to optimize the use of the donor bone material and to minimize unnecessary waste (Figure 21).

Figure 21. VSP of graft harvesting from a donor bone: two bone wedges (highlighted in orange) were planned and extracted from the same tibia specimen to optimize material use and minimize donor bone waste.

2.5. Virtual Surgical Planning phase – tumour resection

2.5.1. 3D Visualization and Analysis of Tumour Extension

As for VSP for tumour resection, the workflow shares several similarities with deformity correction but also requires specific considerations. Once the anatomical model is obtained (usually already incorporating the 3D tumour model derived from the image registration process) the VSP can be initiated in Blender. As previously described for deformity correction, the digital 3D model can also be 3D printed at a 1:1 scale to enhance spatial understanding and preoperative visualization.

In this context, deformity analysis is not required, since the treatment involves the resection of the bone area affected by the tumour. However, anatomical axes and articular planes are still defined to provide a consistent reference system for the planning and alignment of the cutting planes.

A key element of the 3D model is the accurate representation of the tumour. Its size, shape, and spatial extension are carefully evaluated together with the surgeon, who verifies its accuracy using MRI data to ensure full correspondence between imaging and 3D reconstruction. This three-dimensional assessment enables an objective evaluation of the lesion’s morphology and its relationship with surrounding anatomical structures, while also allowing verification of the resection margin feasibility, typically planned with an offset of approximately 1 cm around the tumour to define the bone volume to be removed.

2.5.2. Surgical Procedure Simulation

Once the model has been analysed, the surgical procedure can be virtually simulated. Based on tumour longitudinal extension, proximity to the joint, and residual bone stock, four main resection and reconstruction strategies were experienced during this project (a total of 22 oncologic resections were performed):

- **Complete resection**: typically performed when the tumour is located in the diaphyseal region. In such cases, the entire diaphysis or a portion of the diaphyseal segment is removed through two transverse osteotomies, one proximal and one distal to the lesion, allowing complete excision of the affected bone segment. A size-matched allograft is subsequently implanted to restore the resected portion (Figure 22a). This was the most frequently employed strategy, accounting for 11 out of 22 cases.
- **Partial resection**: generally performed when the bone dimensions are sufficient to allow a more conservative approach. Depending on the tumour's location and extension, it may not be necessary to remove the entire segment; instead, a more limited resection can be carried out, preserving one of the cortical walls along its length. The resulting bone defect is then filled with a massive donor graft (Figure 22b). This approach was applied in 4 out of 22 cases.
- **Composite prosthesis reconstruction**: indicated when the tumour extends very close to the articular region and the resection is particularly extensive. In these cases, reconstruction requires both a prosthesis and a supporting massive allograft. The graft acts as a structural interface between the prosthesis and the host bone, providing additional stability and allowing proper fixation through the selected osteosynthesis system (Figure 22c). This approach was applied in 4 out of 22 cases.
- **Prosthesis only**: indicated when the tumour is located near the joint, but the resection remains limited, allowing preservation of a sufficient portion of healthy bone for direct prosthesis implantation. In this case, only a simple complete osteotomy cut is planned, and reconstruction is performed with the prosthesis alone, without the need for an additional bone graft. This strategy was used in 3 out of 22 cases.

Once the resection type has been defined, the osteotomy planes are positioned under the supervision of the surgeon. These are usually placed to ensure simplicity and reproducibility, using a reference system derived from the anatomical axes and joint-specific reference planes approximated from the articular surface geometry. Resection cuts generally do not require specific angulation but are instead designed as straight, simple cuts perpendicular to the anatomical long axis of the bone, facilitating both planning and surgical execution. Examples of resection approach can be seen in Figure 22.

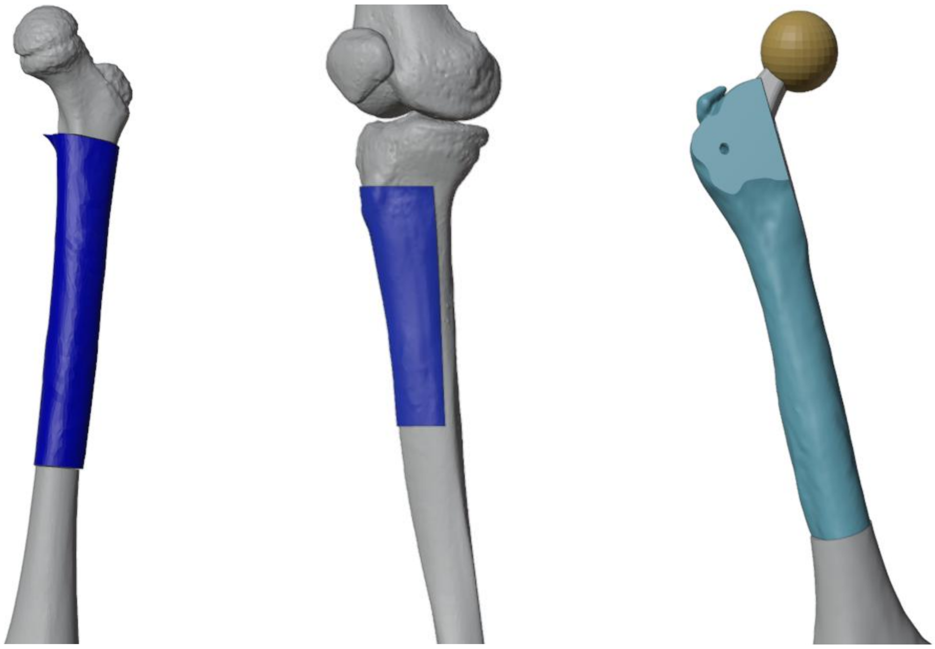

(a) (b) (c)

Figure 22. Examples of tumour resection and reconstruction strategies based on tumour extension, cortical preservation, and proximity to the articular region: (a) complete resection with segmental excision; (b) partial resection preserving a posterior continuous cortical wall; (c) composite prosthesis reconstruction, combining a prosthetic component with a supporting massive allograft.

2.5.3. Bone Bank request

If the treatment involves a complete resection, a partial resection, or a composite prosthesis reconstruction, donor bone must be requested from the BTM. In oncologic cases, the use of autografts is uncommon because the bone segment to be replaced is often extensive, making it unsuitable for harvesting from the patient. However, in selected cases involving smaller bones, such as the metatarsal, autologous grafts (e.g., fibular grafts) can be considered (Figure 23).

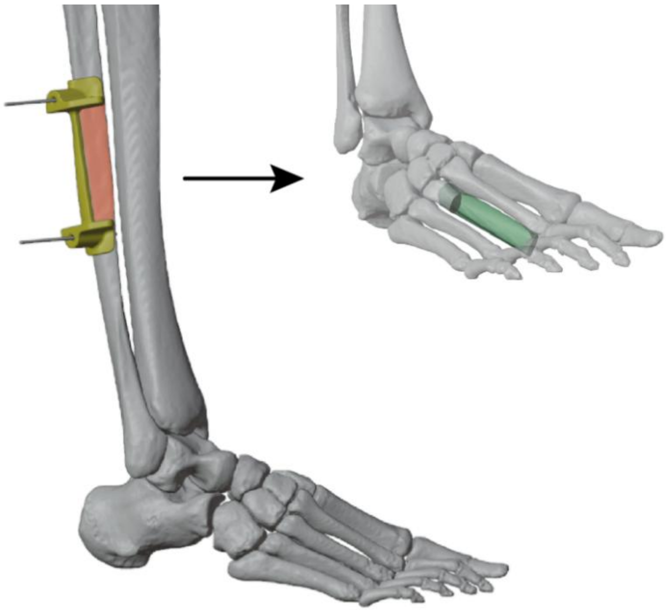

Figure 23. Example of autologous fibular graft for reconstruction of metatarsal bone.

To reconstruct the resected bone segment, the internal BTM of the Institute is contacted. Similarly to deformity correction procedures, the BTM can deliver the donor bone directly to the operating room or provide it already pre-shaped. However, in oncologic cases this option is rarely used, as surgeons generally prefer to shape the graft directly during surgery. This approach minimizes donor bone waste and avoids possible inconveniences for the patient, such as having an unusable graft in the operating room, since updated imaging performed the day before surgery may reveal tumour progression requiring real-time adjustment of the resection and graft dimensions.

The donor bone can be shaped freehand, using only the measurements defined during VSP, or with the aid of GSIs. In both cases, the BTM provides the CT scans of several available donor bones. These undergo the same segmentation and model optimization process described for the patient's imaging data. Once the donor bone models are obtained, they are imported into the patient's VSP in Blender and virtually matched with the patient's anatomy. Together with the surgeon, the most suitable donor, based on anatomical compatibility and the chosen treatment, is selected. After selection, the chosen donor is formally assigned to the patient by the BTM, and the resection planes defined on the patient's model during VSP are transferred onto the corresponding area of the donor bone model. Figure 24 presents Case #2, a 44-year-old female patient with osteosarcoma of the posterior right distal femur. Partial resection of the posterior femoral segment was performed and reconstructed with a massive donor bone allograft, while preserving the unaffected anterior cortical wall to maintain native bone continuity and enhance stability and healing. Donor selection was carried out by best-fit superposition of the patient's 3D model with donor reconstructions provided by BTM, followed by transfer of the cutting planes from the patient's 3D model to the selected donor model to optimize graft fit.

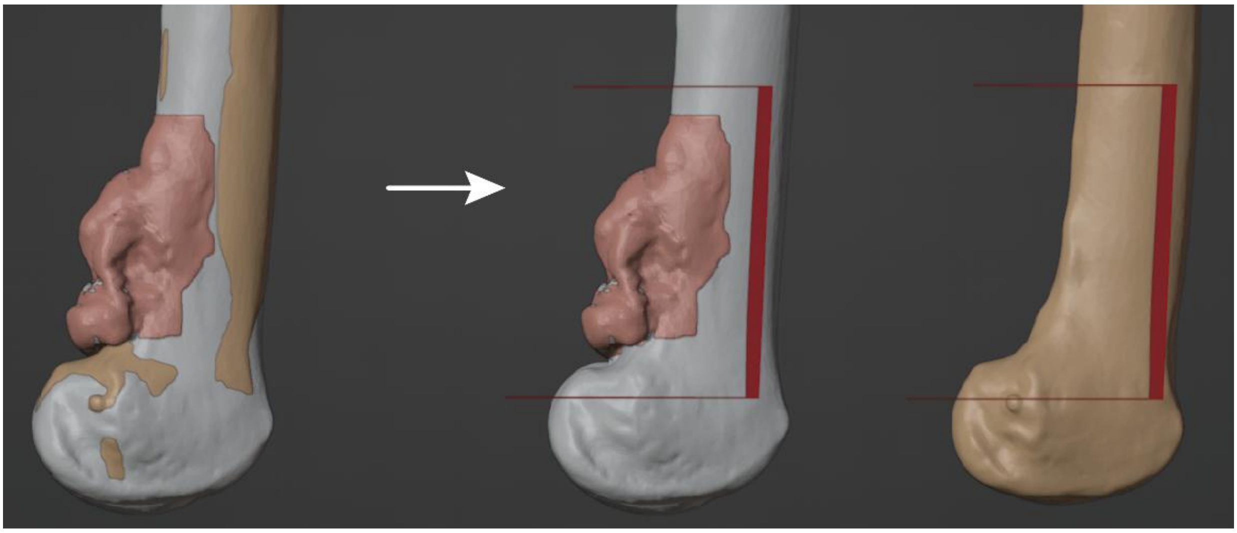

Figure 24. Virtual matching of available donor bones with the patient's anatomy (in grey) in Case #2, followed by transfer of the planned resection planes (in red) from the patient's model to the selected donor bone (in orange) for graft preparation.

2.5.4. Fixation Strategy Definition

The final step of the simulation phase is defining the most suitable fixation system. Large bone reconstructions are challenging to be stabilized, as they must ensure structural strength over extended segments. It is therefore essential to evaluate in advance the planned resection length and the corresponding fixation plate, verifying its availability in the surgical set and its suitability for the patient's anatomy. This is particularly important for long resections, such as distal femoral reconstructions, where the plate may extend to the condylar region. In such cases, it must be assessed preoperatively whether the plate conforms to the bone shape or requires intraoperative bending to achieve proper fitting.

To ensure dimensional accuracy, 3D models of the fixation components are usually obtained directly from the manufacturer, since such large plates are not routinely available in the operating room, leaving little margin for intraoperative adjustment.

The fixation system represents the final step of the VSP process and is positioned on the reconstructed model, after simulating both the resection and the placement of the selected donor graft, to evaluate the final morphology and mechanical feasibility of the construct. Figure 25 shows Case #3, a 10-year-old male patient with distal tibial osteosarcoma. VSP was used to define the fixation strategy, including selection and positioning of the fixation plate during tumour resection and massive allograft reconstruction, while preserving the ankle joint. The procedure was supported by PSIs, and the donor graft was selected with the surgeon and shaped intraoperatively using GSIs.

Figure 25. Virtual positioning of the fixation plate on the reconstructed model after donor graft placement.

2.5.5. Design Reference Definition

Similarly to the VSP for deformity correction, even in this case if the surgeon requests only the VSP, the process proceeds directly to the preparation of the surgical report (as described in the 'Delivery Phase' paragraph).

When PSIs are also required to support the planned treatment, the procedure follows the same workflow described above, in close collaboration with the surgeon. In this phase, critical anatomical structures to be preserved are identified, patient positioning are defined, and the necessary bone exposure is evaluated. Compared to deformity correction, the surgical incision is usually more extensive, as tumour resections and graft implantations require wide access to remove the affected bone and surrounding tissues.

Fixation pin positioning is defined as previously described, always considering the surgical technique associated with the selected fixation plate, when present and applicable. Care must be taken to ensure that the pins do not come into contact with the affected bone. Therefore, their placement must be evaluated exclusively in healthy regions, outside the resection area delimited by the planned cutting planes.

Usually, when PSIs are required, GSIs are also requested to ensure a perfect match between the patient and the donor bone. The procedure for defining the design references is very similar, although it involves fewer constraints, as previously described for deformity correction procedures. As mentioned earlier, the cutting planes must be accurately positioned according to the orientation and harvesting site on the donor bone, defined during the donor bone selection phase, in relation to the morphology and requirements of the patient's reconstruction site. In cases involving massive grafts, particular attention must be paid to the positioning of the fixation pins used to stabilize the cutting guide for donor bone shaping.

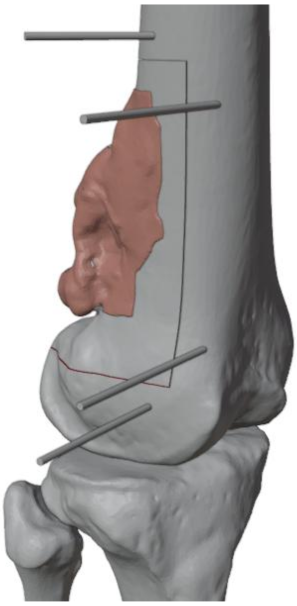

(a)

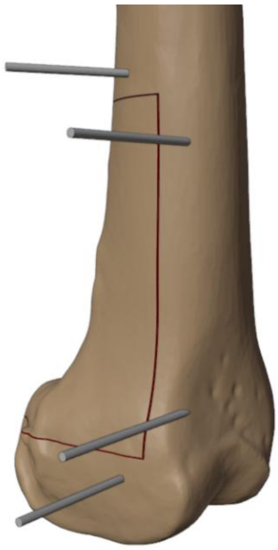

(b)

Figure 26. Fixation pin positioning used as references for PSI and GSI design for Case #2: (a) Positioning of fixation pins on the patient's bone outside the resection planes to avoid interference with the tumor-affected area; (b) Placement of fixation pins on the donor bone outside the selected graft segment to preserve its structural integrity.

Pins must always be placed outside the effective graft area to avoid compromising the structural integrity of the donor bone, which serves a crucial load-bearing function. Figure 26 shows, for Case #2, the placement of fixation pins used as references for the design of the PSI and GSI, positioned outside the planned resection and reconstruction area.

2.6. Design phase

2.6.1. General Evaluation

Upon the surgeon's approval of the final VSP, if PSIs or GSIs are required, the design phase can begin. This phase is developed according to specific clinical needs and surgical approach, and is therefore highly customizable, varying across patients, treatments, and surgeons. Based on these considerations, some general guidelines can be defined.

As previously mentioned, the possible locations for inserting fixation pins to stabilize the surgical guide are evaluated together with the surgeon. Regarding their orientation, several configurations can be considered depending on the surgical requirements (Figure 27):

- **Parallel pins**: the use of parallel pins allows a small degree of freedom for the cutting guide, as the guide holes act similarly to sliding joints along the pin axis. At least two pins are required, especially when the guide has limited surface contact with the bone, to prevent rotational clearance around a single pin axis. This configuration is chosen when the guide needs to be removed while keeping the pins in place. This may be necessary to preserve positional references for subsequent surgical steps or to insert additional guides, for example when two separate osteotomies are required and cannot be incorporated into a single PSI (or GSI). In these cases, the same parallel pins serve as reference points for positioning the subsequent guides;
- **Divergent pins**: when there is no need to remove and reinsert the same or different guides during surgery, the pins can be positioned divergently (again, at least two are required). This configuration ensures complete stability and prevents movement of the cutting guide, including along the pin axis. However, to remove the PSI (or GSI), the pins must first be extracted. This setup provides maximum fixation stability but less flexibility for multi-step procedures;
- **Mixed pins**: in certain procedures, particularly those involving torsional corrections, pins may be placed in a mixed configuration. Typically, two parallel pins are used to stabilize the guide, while an additional divergent pin is placed on the opposite side of the osteotomy to indicate the torsional angle that must be reproduced during correction. After inserting the pins, the cutting guide is removed to perform the osteotomy. Therefore, during the design phase, the slot for the divergent pin should be partially open: this ensures accurate guidance during insertion while allowing the guide's removal along the direction of the parallel pins once fixation is complete.

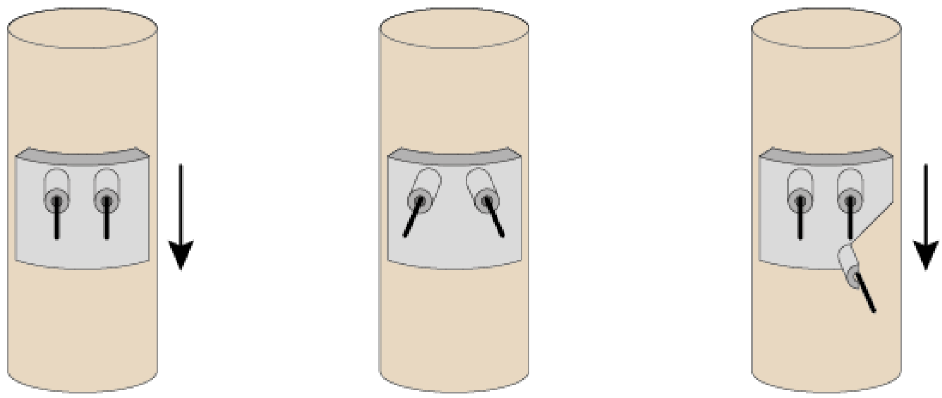

Figure 27. Parallel pin configuration allowing guide removal and repositioning for subsequent surgical steps (left); divergent pin configuration ensuring complete guide stability during cutting (centre); mixed pin configuration used in torsional corrections, with one divergent pin indicating the required rotation angle (right).

Usually, especially when the fixation system is associated with a specific surgical technique, a reverse planning approach can be adopted. For example, in the case of fixation systems such as blade plates or screw-plate constructs, the providing company typically supplies the corresponding surgical instrumentation. This often includes tools such as guiding cannulas that can be mounted onto the plate to assist with the correct insertion of wires or screws. The step-by-step surgical technique is usually detailed in a dedicated brochure provided with the implant system.

In such cases, to ensure the correct placement of fixation elements to be used as design references during VSP, a reverse planning workflow is applied. A common example is the use of a screw-plate system for proximal femur procedures, which is typically accompanied by a detailed surgical technique. The process begins by defining and simulating the desired correction. The fixation plate is then virtually positioned on the corrected model, and placeholders are added to indicate the trajectory and location of the screws, details that may vary depending on the specific implant design. So, once the correct plate is chosen and placed, the final configuration of the correction and the fixation can be evaluated, including estimating the appropriate screw lengths. However, this step alone is not sufficient. It is essential to then reverse the correction, anchoring the placeholders to the model and restoring the preoperative, deformed anatomy. In doing so, the initial reference positions for K-wires or screws are retrieved, allowing the surgeon to know precisely how to place them intraoperatively to reproduce the planned correction (Figure 28). These reference points are critical for achieving the intended outcome.

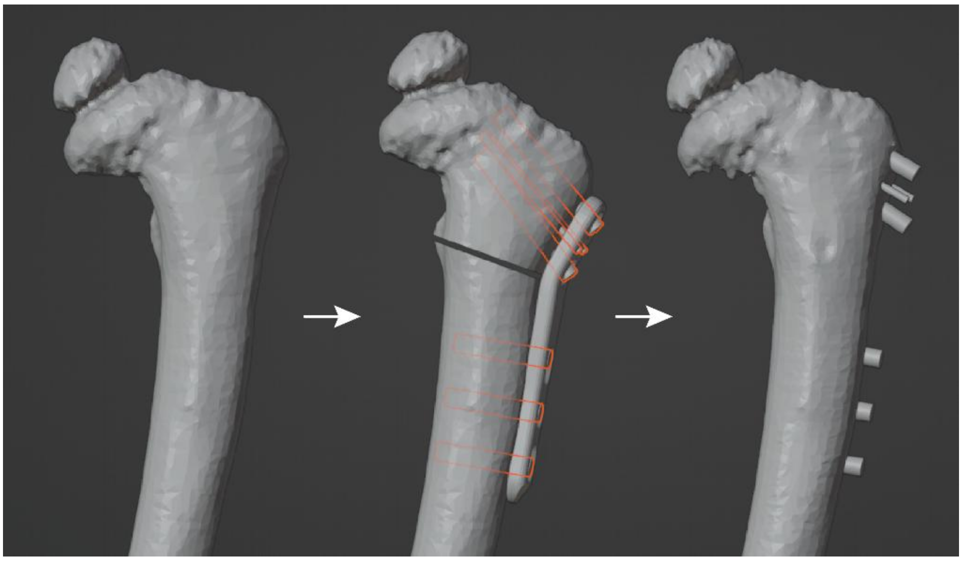

Figure 28. Preoperative reverse planning workflow: preoperative 3D model showing the initial deformity (left), simulation of the desired correction with virtual placement of fixation plates and screw placeholders (centre) and, finally, correction reversed to restore the original anatomy while preserving the planned fixation elements, enabling the definition of initial pin or screw trajectories (right).

This reverse planning technique can also be applied regardless of the specific fixation system used and is particularly valuable in anatomically challenging regions, such as areas with limited bone stock or close proximity to critical structures, where optimal screw or wire placement is crucial to ensure stable and safe fixation.

Not only fixation or reference pins must be considered during the design phase. When additional instruments are required according to the selected surgical technique or fixation system (mainly for PSIs), their positioning and orientation must also be integrated into the guide design. An example is the chisel used for inserting the blade plate, a parallelepiped-shaped tool introduced with a mallet to guide the insertion path of the plate blade. In these cases, the chisel is incorporated into the cutting guide design to ensure proper alignment, tilt and sizing. Its orientation is strictly defined according to the direction of the blade selected during planning, and all pin directions are consequently evaluated with respect to it (Figure 29).

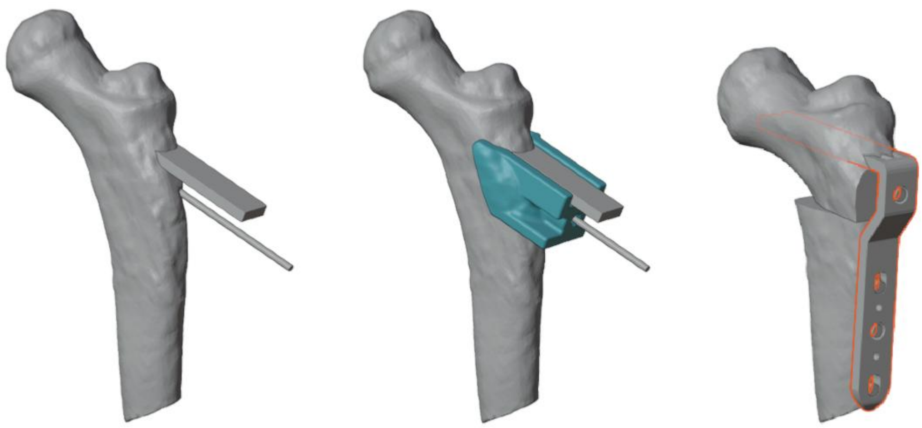

Figure 29. Chisel integrated for blade plate positioning (left), with pin orientation allowing surgical guide (in light blue, at the centre) removal for next steps to support final fixation with blade plate (highlighted in orange, on the right).

Regarding the cutting planes, these are directly imported from the VSP approved by the surgeon. During the design phase, when multiple osteotomy cuts are planned, it is important to consider their sequence to ensure proper intraoperative management of the guides.

For example, in a wedge resection involving two cuts, one defining the distal and one the proximal surface of the wedge, the order of execution must be planned carefully. If the cutting guide rests on the proximal side of the bone, the distal cut should be performed first, followed by the proximal one. Executing the proximal cut first would result in bone separation and the loss of the reference bone surface needed to perform the distal cut accurately (Figure 30). In general, when two cuts are required, the first should always be made on the side farthest from the guide's contact surface: distal first if the guide is positioned proximally, and proximal first if the guide is positioned distally.

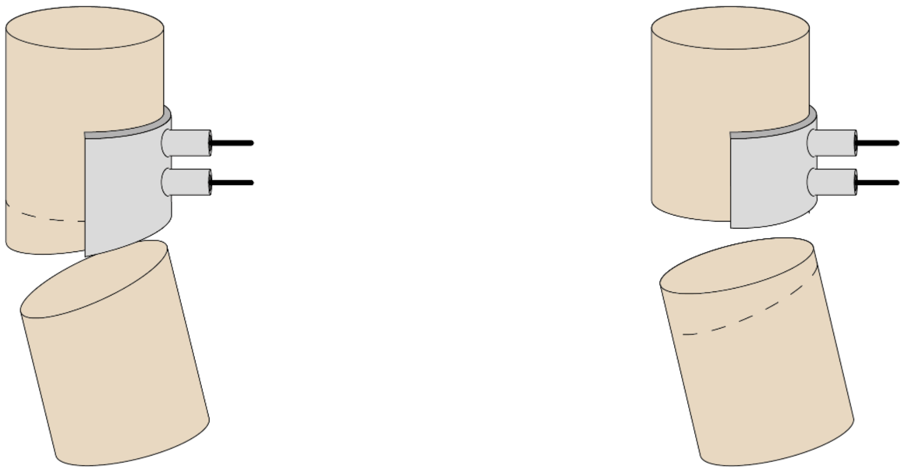

(a) *(b)*

Figure 30. Example of a proximally positioned cutting guide, with dashed lines indicating the planned cutting planes: (a) Distal cut executed first, preserving the reference surface under the guide and allowing accurate positioning of a subsequent guide for the second cut; (b) Proximal cut executed first, causing bone separation and loss of the reference surface needed to perform the distal cut correctly.

2.6.2. Working Area and Design References

To begin the design phase, the working area must first be defined. During the VSP, several aspects are evaluated together with the surgeon, since soft tissues are not clearly distinguishable on CT images. These include the selected surgical approach, the expected degree of bone exposure, which determines the available surface area for the guide to rest on, and the bone regions free from tendon, nerve, or other soft-tissue insertions. These considerations, along with the planned incision site, help identify on which bone surface (lateral, medial, anterior, etc.) the PSI or GSI will be placed and how far the bone–contact surface of the guide can extend. For GSIs, these constraints are generally less critical, except in cases where tendinous insertions from the donor bone must be preserved. In such cases, the guide design and positioning are adapted accordingly to the anatomical characteristics also for the donor bone.

Once defined, the portion of bone suitable for guide placement is selected and exported for 3D modelling in Creo. In Creo software, the imported bone surface serves as the base geometry to which all design references from the VSP are added. Cutting planes, fixation pins, and other reference elements (such as the chisel) are exported as STL files from Blender and then imported into Creo (Figure 31).

These features are then used to create construction elements, placing axes at the pin locations and planes corresponding to the cutting planes to proceed with 3D modelling.

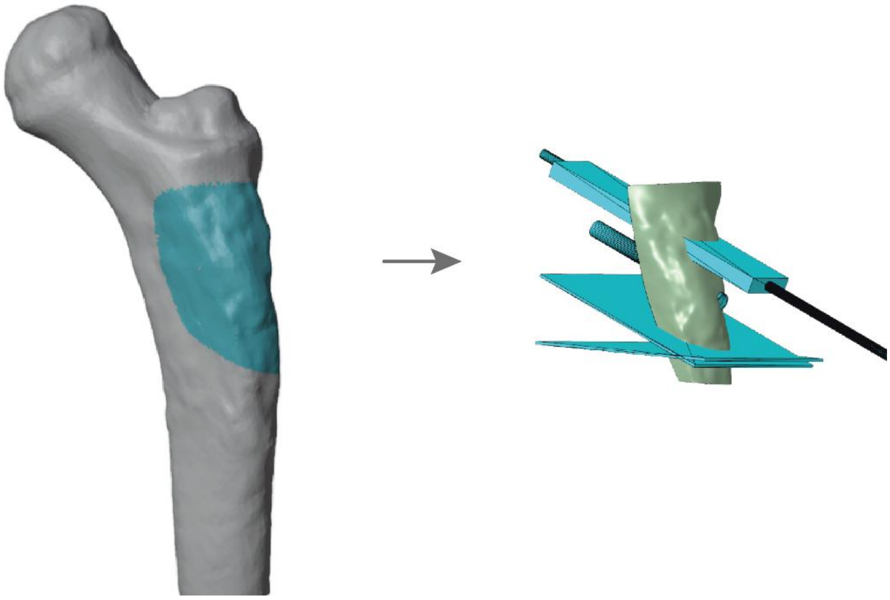

Figure 31. Selection of the working area based on the surgical approach and expected bone exposure during VSP (highlighted in blue on the left), followed by export and insertion of design references (planes and screw/K-wire highlighted in light blue on the right) for 3D modelling in Creo.

2.6.3. Design steps

The design of the guides must take into account the technical constraints of the 3D printing process. Since printing is performed with a 0.4 mm nozzle and 0.2 mm layer height, very small details cannot be reproduced. The guide should therefore be designed to be compact yet stable, ensuring adequate thickness and support while maintaining usability and accessibility to the surgical site (these aspects are further detailed in the 'Printing Phase' paragraph).

Cutting guides are generally characterized by three main features (Figure 32):

- **Body**: the main structure of the guide, obtained from the bone surface previously selected and defined as suitable for guide placement. It provides an accurate fit onto the bone by replicating the geometry of the corresponding anatomical segment.
- **Pin holes**: hollow cylindrical features designed to accommodate K-wires or screws, which serve both to secure the guide in place and to assist in the correct positioning of fixation plates or screws, as previously described.
- **Saw slot**: the functional part of the guide dedicated to guiding the surgical saw during the osteotomy, ensuring the correct position, orientation, and direction of the planned cut.

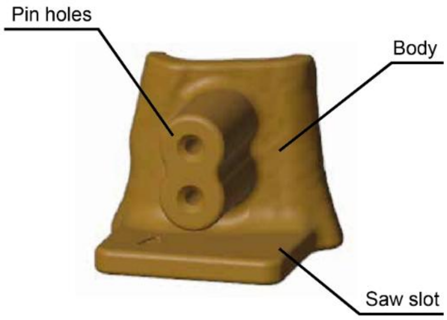

Figure 32. Main structural features of a surgical guide.

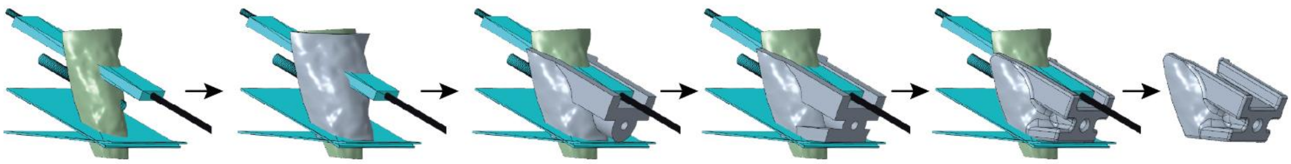

Figure 33. Step-by-step creation of the surgical guide (from left to right): definition of VSP reference surfaces on the target bone region for guide positioning, generation of the guide body, integration of pin holes and additional features (e.g., chisel and saw slots), edge filleting, and finalization of the completed guide.

The design process (Figure 33) starts with the body, obtained by offsetting the imported bone surface by 3 mm to create a solid structure. Due to the freeform, anatomy-driven geometry of the bone, local variations in surface thickness may occur. Therefore, the model must be carefully checked to ensure that no areas are thinner than 3 mm.

Once the bone-contacting base is defined, the pin holes are designed using the axes previously created from the VSP pin placement references. Initially, a standard configuration was used, consisting of a 3 mm internal hole diameter and a 4 mm outer cylinder thickness. This setup ensured that K-wires of various diameters (selected at the surgeon's discretion) could be accommodated in most cases. However, this approach proved to be somewhat inaccurate: thinner wires tended to fit loosely, while in other cases a precise match between the hole and the chosen wire diameter was necessary. Two possible solutions were considered to improve the accuracy of wire fitting: either increasing the length of the cylindrical features or refining the hole diameter definition.

From a geometric standpoint, when guiding K-wires or pins through cylindrical features, angular instability may occur due to the clearance between the wire and the hole. In addition to hole diameter, the length of the guiding feature plays a key role in constraining wire orientation: shorter holes allow larger angular deviations, whereas longer guiding features limit wire tilt and improve directional stability. This effect is schematically illustrated in Figure 34.

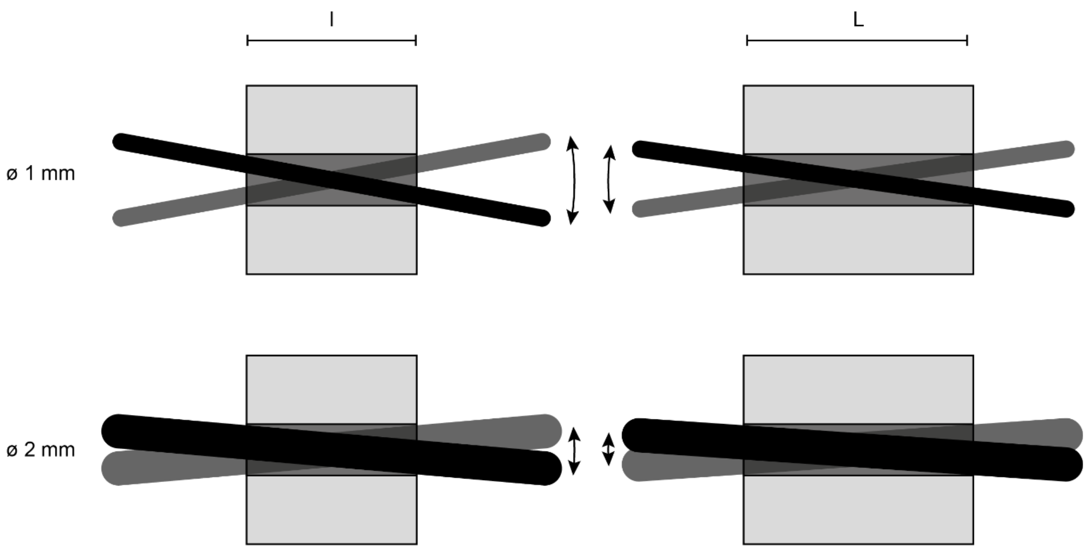

Figure 34. Example showing variable clearance of 1 mm and 2 mm K-wires inside a 3 mm guide hole, at different hole lengths (l<L).

Since increasing the length of the cylindrical features was not feasible due to the often limited available surgical space, the issue was addressed by optimizing the hole diameters to achieve a more accurate fit. The optimal wire diameter is now defined together with the surgeon directly during the VSP phase, providing the designer with precise input parameters. To determine the corresponding hole dimensions, an experimental study was conducted to develop a predictive algorithm that accounts for dimensional variations induced by 3D printing and subsequent heat treatment. This approach makes the design independent from the hole length, which may vary according to the anatomical site and surgical requirements. These aspects and the related experiment are discussed in detail in Chapter 4, in the paragraph 'Design Parameters Tuning for 3D Printing'.

Finally, the saw slots are designed. To prevent problems related to frictional heating between the saw blade and the guide, since the generated heat may deform the plastic material, and to provide greater surgical flexibility, the slot is not designed as a closed channel. Instead, flat "balcony-type" support surfaces are created to define the correct direction and position of the saw. This open configuration allows the use of different cutting tools, such as saw blades of various thicknesses or osteotomes, depending on surgical needs and surgeon preference. It also reduces heat generation and limits debris formation. This aspect is particularly relevant because, although cutting guide materials are classified as biocompatible when used according to the manufacturer's protocol, polymer debris generated during jaw cutting may persist in the body beyond the intended exposure time. Previous studies have shown that debris from surgical-grade polypropylene and polyamide can be cytotoxic and impair bone healing [110]. In contrast, a separate study reported pure and steam-sterilized PLA-based materials have been reported as non-cytotoxic, supporting their suitability for surgical guides [111,112]. Surgeons should therefore be aware of the potential risks associated with residual material during and after surgery.

As a design guideline, a balcony-type guide helps reduce mechanical constraints and debris accumulation during osteotomy, ensuring a complete and correctly oriented bone cut (Figure 35).

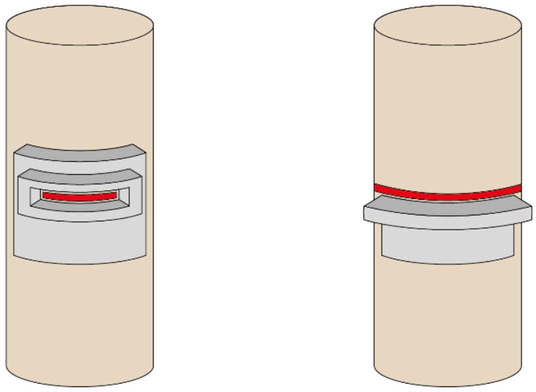

Figure 35. "Balcony-type" saw guide design (right), compared to traditional closed slots (left), allowing complete bone cutting with the correct angular orientation and compatibility with different saw or osteotome types. In red, the area reachable by the saw blade without removing the guide in the two configurations.

The final refinement of the surgical guide design includes chamfering and filleting sharp edges to prevent fragile corners that could chip or concentrate stress. Additionally, it is recommended to embed an identification label directly on each guide, especially in procedures involving multiple surgical steps and the use of several consecutive guides, to ensure easy intraoperative recognition and proper traceability, as each label is uniquely associated with the corresponding patient ID (Figure 36). All these design principles apply equally to both PSIs and GSIs. However, GSIs permit greater manoeuvrability and bulk, as they are applied to donor bone allografts rather than directly to patients.

After completing the 3D modelling phase, the finalized cutting guide models are exported in STL format for 3D printing.

Figure 36. Embedded identification labels are incorporated into each guide to ensure clear differentiation: number 1 (left) indicates the first guide to be used, and number 2 (right) indicates the second guide in the surgical sequence.

After completing the guide design, non-sterile prototypes are 3D printed to verify fit and functionality on the bone model with the surgeon (Figure 37). Once validated, the manufacturing phase to produce the sterilizable final parts begins.

Figure 37. Non-sterile 3D printed guide (white) tested on the bone model (orange).

2.7. Manufacturing phase

2.7.1. Material and 3D Printing Technology

The cutting guides are manufactured using High-Temperature Polylactic Acid (HTPLA) filament with a diameter of 1,75 mm (Table 1). Polylactic acid (PLA) is a biodegradable polymer obtained from renewable resources, characterized by good mechanical properties and low cost compared with other biodegradable polymers traditionally used in medical applications [97]. However, conventional PLA, although providing good printing quality and stiffness, has a low glass transition temperature, which compromises its ability to maintain shape at moderate temperatures and makes it unsuitable for thermal or sterilization processes. HTPLA, previously identified in a study of our team as the most suitable material for surgical guide fabrication, is a modified PLA filament containing a crystallization compound that allows the polymer to stabilize at higher temperatures and further enhance its mechanical performance [8]. After thermal annealing, HTPLA exhibits improved strength, dimensional stability, and heat resistance, making it compatible with autoclave steam sterilization. In paediatric deformity correction cutting guides, no clinically relevant post-sterilization deformation affecting fitting accuracy or intraoperative usability was observed.

The cutting guides were produced using FDM technology with a Bambu Lab X1 Carbon printer (Bambu Lab, Shenzhen, China) (Figure 38). This process was selected for its high reliability, dimensional accuracy, and cost-effectiveness, enabling rapid in-office production with desktop-grade equipment. It also allows easy customization of design parameters and quick iteration during the design and validation phases.

Table 1. Main Properties of HTPLA (PLA Crystal Clear, Fillamentum Manufacturing Czech).

Thermal properties	Glass transition temperature	55-60 °C
	Melting point	150-230 °C
	Decomposition temperature	>230 °C
Printing properties	Print temperature	210-230 °C
	Hot pad	50-60 °C
Physical Properties	Material density	1.24 g/cm3
Mechanical properties	Tensile strength	50 MPa

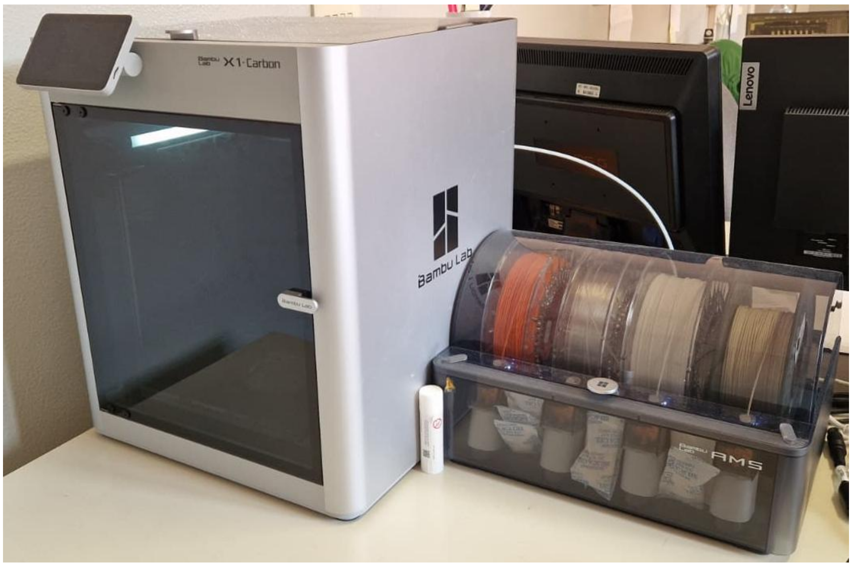

Figure 38. Bambu Lab X1 Carbon 3D printer used for cutting guide fabrication.

2.7.2. Working Environment Overview

The working environment is organized by considering basic requirements related to safety and material handling. The equipment in use, including the 3D printer, complies with applicable regulations in terms of CE marking according to the Machinery Directive, and all materials are accompanied by technical data sheets and safety data sheets provided by the manufacturers.

Printing materials are stored either under vacuum or in controlled-humidity environments. No dedicated storage rooms are in place, as they are not required for materials commonly used in FDM processes. Once opened, filament spools are kept in closed containers with humidity control. After the printing and post-processing steps, the operator manually removes printing residues (e.g., support structures), using basic personal protective equipment such as gloves and safety glasses.

2.7.3. Printing settings

Printing parameters were optimized in previous studies of our team [8,113] to obtain the best printing configuration for HTPLA, ensuring minimal air voids and a dense, compact internal structure. This setup is adopted for all guide production to guarantee consistent quality and reproducibility (Table 2).

During slicing, the digital mesh is imported into the slicing software Bambu Studio (Bambu Lab, Shenzhen, China) with the bone-contact surface oriented upward (Figure 39) to avoid contact with support structures that, once removed, could compromise the smoothness and accuracy of the contact area. The mesh is then divided into successive layers according to the defined nozzle diameter and layer height, generating the corresponding toolpath on the build platform. The printing process is continuously monitored to maintain stability and prevent manufacturing errors.

Printing is performed using a 0.4 mm nozzle and a 0.2 mm layer height, providing an optimal balance between dimensional accuracy, surface quality, and printing time. These parameters directly define the minimum printable feature size and therefore influence the design constraints. Features smaller than 0.2 mm and wall thicknesses below 3 mm are avoided to ensure the presence of at least three wall loops and a solid infill throughout the model. This configuration minimizes internal voids and surface defects [113], ensuring adequate mechanical strength, dimensional stability, and high-quality surface finishing.

Once printed, the guides are allowed to cool down at room temperature, then carefully removed from the build platform to undergo a post-processing phase consisting of thermal treatment, called annealing, and support removal to further enhance structural integrity and dimensional stability. All technical specifications of the printer are summarized in Table 1, and the optimized printing parameters for HTPLA are listed in Table 3.

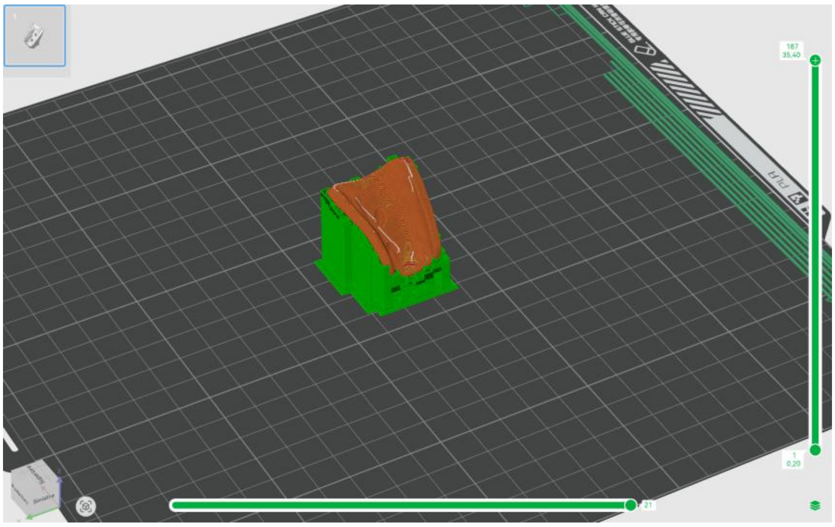

Figure 39. 3D printing setup for a proximal femoral cutting guide. The guide is oriented with the bone-contacting surface facing upward to avoid supports on the functional interface. Dense support structures (green) are used to support undercut regions during printing and to constrain the guide (orange) during heat treatment, thereby limiting deformation.

Table 2. Technical specifications of the Bambu Lab X1 Carbon 3D printer.

Printing Technology	FDM (Fused Deposition Modelling)
Build Volume (W x D x H)	256 x 256 x 256 mm^3
Max Hot End Temperature	300 °C
Max Build Plate Temperature	110 °C
Max Speed Tool head	500 mm/s
Nozzle Diameter	0.4 mm
Filament Diameter	1.75 mm
Multimaterial	Yes
Supported Filament	PLA, PETG, TPU, ABS, ASA, PET, PA, PC, Carbon/Glass Fiber Reinforced Polymer
Connectivity	Wi-Fi
Formats	G-code
Software slicing	Bambu Studio
Weight	14.13 kg

Table 3. Optimized printing parameters defined for HTPLA cutting guide 3D printing.

	Layer (mm)	Line Width (mm)	Infill (%)	Infill pattern	Infill/Wall Overlap (%)	Wall loops	T Nozzle (°C)	T Bed (°C)
HTPLA	0.2	0.4	100	Monotonic	30	3	220	60

2.7.4. Thermal treatment, packaging and labelling, sterilization

After printing, the models undergo a post-processing phase consisting of thermal treatment and support removal. Annealing is a post-printing procedure commonly applied to polymeric materials, as it improves their mechanical performance by promoting re-crystallization, relaxing internal stresses and enhancing stability at temperatures above the polymer's glass transition temperature. This process is one of the most effective ways to relieve internal material tensions, improve interlayer adhesion, and reduce geometric imperfections, resulting in increased overall stability and dimensional accuracy of the final part.

The annealing cycle parameters (Table 4) were defined based on previous studies [8,9,114]. The process is performed in a static oven with the 3D printing supports still attached to the model to preserve dimensional accuracy and mechanical consistency during heating. After annealing, the parts are cooled gradually to room temperature to prevent the formation of residual stresses, after which the supports are carefully removed.

Following the increasing number of oncological cases requiring large resections and massive cutting guides, significant geometric deformations were in some cases observed in these parts after thermal treatment. The manufacturing process was therefore further investigated, with the aim of minimizing these defects by analysing additional printing parameters. These aspects and the related experimental analysis are discussed in detail in Chapter 4, in the paragraph ‘Reducing Deformation in 3D Printing’.

Table 4. Temperature and time cycle for the annealing process for HTPLA. The treatment is performed in a single cycle with two thermal phases.

Phase1	Time (minutes)	Temperature (°C)
1st	10	80
2nd	40	100

Once finalized, the cutting guides are prepared for delivery to the Pharmacy Unit of the Rizzoli Institute for sterilization. Each guide, or set of guides (e.g., multiple surgical guides intended for the same patient), is packaged together (Figure 40). If donor-specific GSIs are also required, they are delivered in a separate package. Each package is properly labelled with the following information:

- **Protocol name**: the number and ID of the clinical trial approved by the Ethical Committee under which the cutting guide was produced.
- **Patient ID**: unique identifier for association with the corresponding patient case.
- **Date**: the scheduled date of surgery.
- **Surgical Unit**: the clinical department to which the requesting surgeon belongs.
- **Surgeon**: name of the requesting surgeon, corresponding to the primary operator in the operating room.
- **Package number**: sequential numbering of the packages (e.g., 1 of 2), used when multiple guides must be sterilized and kept separate (for instance, one package containing PSIs and another containing GSIs.
- **Number of items**: total number of PSIs or GSIs included in each package (i.e., the number of individual components included in the set and intended to guide the surgical procedure).

Figure 40. Sealed pouch with case-specific identification label, ready for insertion of the treated cutting guide and delivery to the hospital pharmacy for sterilization.

All labelled packages were sent to the Pharmacy Unit. A total of 119 packages, including both PSI and GSI sets, were delivered and sterilized using the standard steam sterilization protocol of the Rizzoli Orthopedic Institute in a CISA 6410 autoclave (CISA Production Srl, Lucca, Italy). The sterilization cycle includes conditioning, heating, washing, and drying phases, with a total duration of approximately 50 minutes and maximum temperatures ranging between 134.7 °C and 134.9 °C, ensuring that each guide is ready for intraoperative use under sterile conditions.

2.8. Delivery and Surgery phase

Before the day of surgery, a summary report is prepared containing all information related to the VSP. The report includes all measurements, anatomical references, and surgical indications defined during the planning phase, as well as details regarding the type of cutting guides produced (PSIs and/or GSIs). It also provides visual references to verify the correct positioning of the guides, including transparent overlay images that illustrate how the intraoperative fluoroscopic check should appear during surgery.

The report further specifies whether a bone graft from the bone bank is required, including the corresponding donor ID, the type of fixation device to be used, and all additional information already included on the guide label used for delivery to the Pharmacy Unit, such as the patient ID, clinical protocol, and surgeon name. This report is provided to the surgeon and brought into the operating room on the day of surgery as a reference for guide placement and verification. A facsimile of the summary report provided to the surgeon is shown in Figure 41, illustrating the information and visual references included for intraoperative verification.

On the day of the procedure, the cutting guides are delivered directly to the operating room with their corresponding labels and are used according to the VSP plan (Figure 42). The labels produced for delivery are also used to trace the actual use of the cutting guides in the operating room, following the same procedure applied to standard surgical instruments. Figure 43 shows the comparison between the planned outcome and the postoperative radiographic result in Case #4, a 4-year-old child with Ewing sarcoma of the right proximal femur, treated with tumour resection and reconstruction using a composite prosthesis and managed with virtual VSP, PSIs, and GSIs. The graft was designed slightly longer to compensate for the expected loss of future growth due to resection of the proximal femoral growth plate, based on patient-specific growth data.

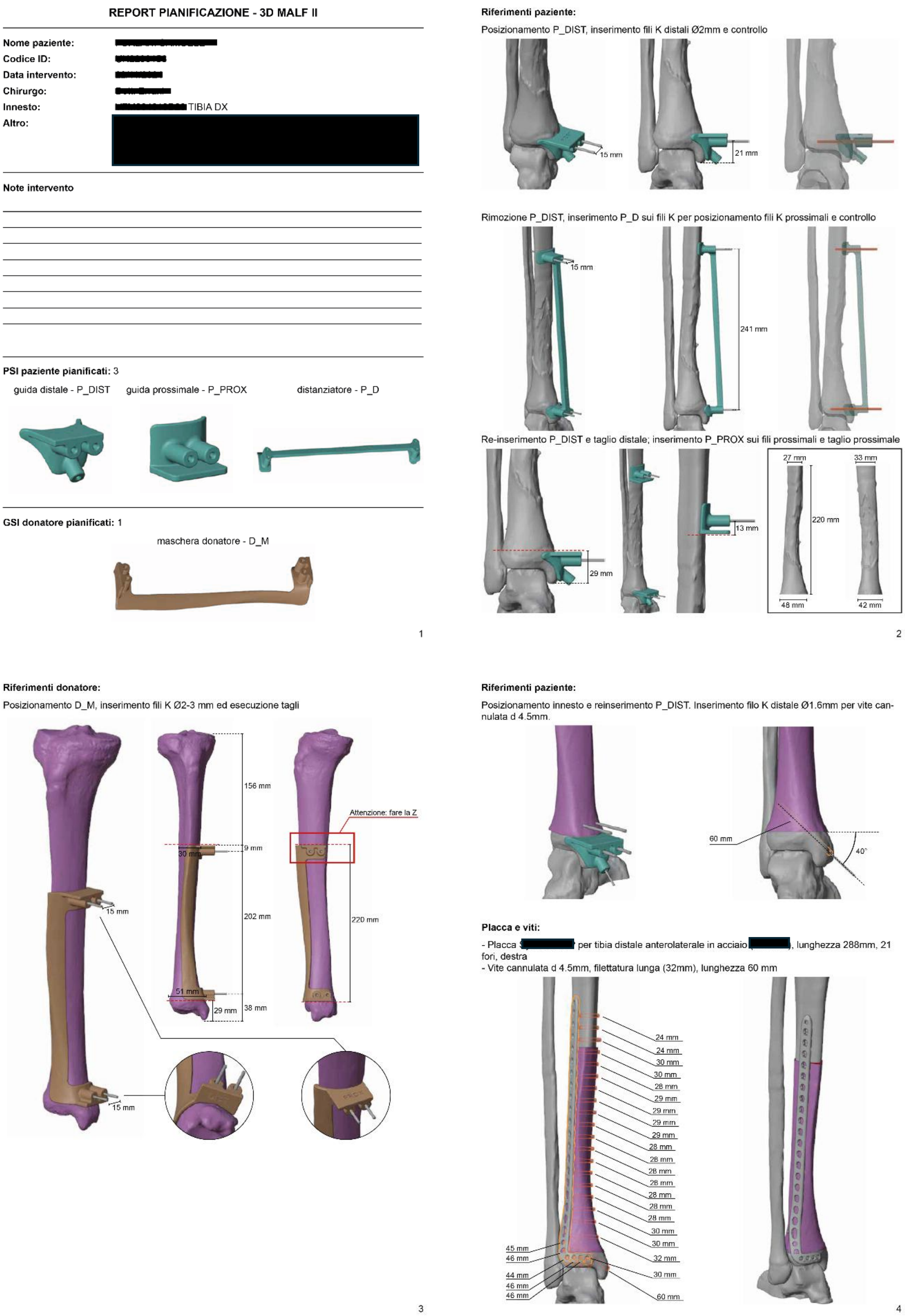

Figure 41. Example of the summary report for Case #3 delivered to the surgeon before surgery, containing VSP data, guide type (PSIs/GSIs), surgical indications, and visual fluoroscopic references for intraoperative verification. The patient's bone is shown in grey, while the donor bone is shown in pink. All information has been blurred for privacy reasons.

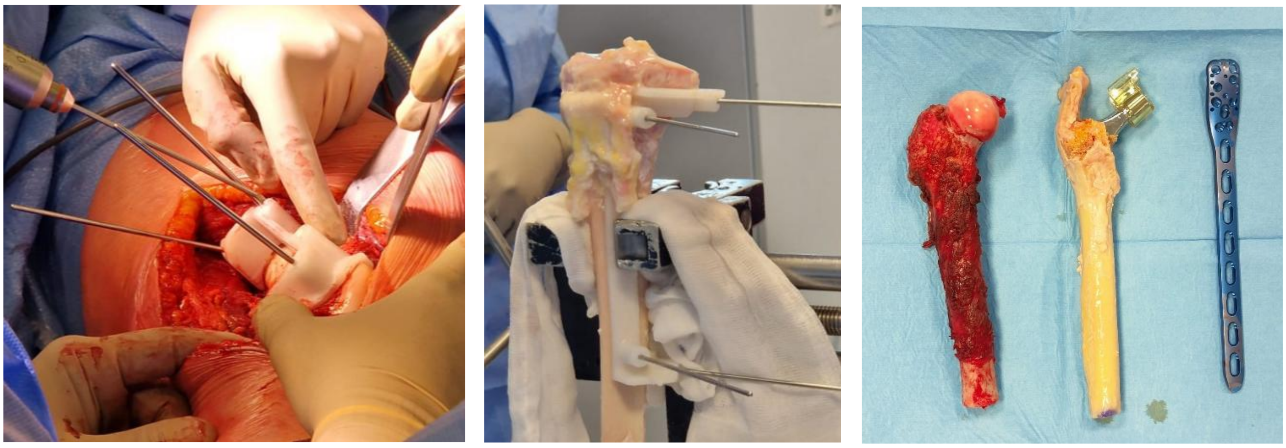

(a) (b) (c)

Figure 42. Example of intraoperative application in an oncological case involving resection and reconstruction with a composite prosthesis, planned through VSP and supported by PSI and GSI: (a) PSI positioned on the patient; (b) GSI used intraoperatively to shape the donor bone; (c) resected patient bone alongside the shaped donor graft and the selected fixation hardware ready for assembly.

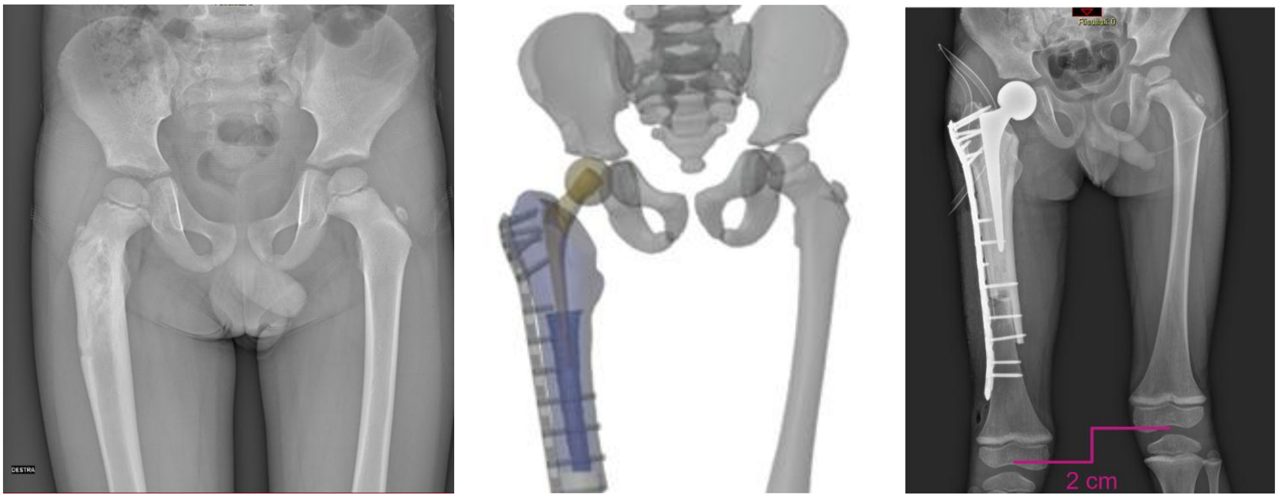

(a) (b) (c)

Figure 43. Case #4 managed with VSP, PSIs, and GSIs. (a) Preoperative radiograph of a 5-year-old male diagnosed with Ewing sarcoma; (b) virtual planning for tumour resection and composite prosthesis reconstruction; (c) postoperative radiographic follow-up showing a final limb length discrepancy of approximately 2 cm, as the graft was intentionally planned longer to compensate for the expected growth arrest of the resected proximal femoral physis.

3. VIRTUAL SURGICAL PLANNING AND OPTIMIZED PROCEDURES

3.1. Preoperative Planning Procedure

This work does not aim to provide a detailed account of the clinical and surgical specificities of each condition in which the method has been applied. As outlined in the introduction, its applications can be broadly divided into two domains: bone deformities and bone tumours. The primary treatment objectives were bone realignment in the former and complete tumour resection with subsequent limb reconstruction in the latter, as explained previously.

This chapter focuses on the methodology directly applied by the author and progressively consolidated over the course of the PhD program, from imaging analysis to the design and fabrication of cutting guides.

Clinical outcome analyses on the broader cohort, which also includes additional cases not directly managed by the author, are presented in a dedicated Chapter 5. Case planning was supervised by the treating orthopaedic surgeon, who frequently adjusted correction parameters according to personal preferences or surgical/clinical experience. For example, in deformities with a high risk of recurrence, overcorrection of selected parameters identified during analysis may be required. Nevertheless, in complex deformities, this approach has become an irreplaceable tool for both understanding and management.

3.1.1. Clinical Assessment, Gait Analysis and Radiographic Imaging

In the setting of deformities, beyond establishing the diagnosis and determining the most appropriate treatment, it is essential for the orthopaedic surgeon to perform a systematic clinical examination of the affected limb [115]. This should assess not only overall weight-bearing alignment but also the preoperative mobility and stability of the involved joints. These findings, which can be documented in written form as well as with photographs or videos, are crucial in guiding the choice of corrections to be applied and require a precise assessment that minimizes confounding factors. In certain conditions, even with advanced imaging available, it may remain difficult to accurately evaluate torsional deformities of a segment or abnormal joint motion (e.g., elbow or knee recurvatum). Furthermore, it is important for the surgeon to determine the need for adjunctive soft-tissue procedures to be performed in conjunction with the bony corrections (e.g., lengthenings, transpositions), whose detailed planning would require more complex 3D models incorporating soft-tissue anatomy and is therefore beyond the scope of this work.

As a complement to clinical assessment, gait analysis provides an objective evaluation of joint kinematics and muscle function and supports surgical decision-making, particularly in patients with neuromuscular disorders and complex gait alterations. This integrated approach has been shown to provide promising levels of accuracy and clinical applicability, which vary depending on the specific technology and acquisition modality adopted [116]. At the Rizzoli Orthopaedic Institute, gait analysis is supported by a dedicated laboratory and is routinely used in clinical practice for patients with altered motor function. Several studies have investigated its application, for example to evaluate the effects of high tibial osteotomy on motor function (walking, stair ascent, and stair descent) in patients with knee osteoarthritis, severe varus deformity of the knee or plano-valgus foot, as well as to assess postoperative lower-limb biomechanics during gait following total knee arthroplasty or arthroereisis [117–123]. Within the collaboration between the two institutions, selected cases have integrated three-dimensional skeletal reconstructions with gait analysis data to generate animated skeletal models [124]. However, despite its potential, this integrated approach, requiring the combination of imaging and gait analysis within a single session, has not yet been implemented within the workflow adopted in the present study.

A complete radiographic assessment of the body segment of interest remains fundamental, particularly for evaluating lower limb alignment under weightbearing conditions [15]. It can be regarded as a 2D orthographic view of the segment of interest. This exam, if performed with proper patient positioning, may be sufficient to characterize the nature of a mild to moderate angular or translational deformity (whether lateral or longitudinal), but it provides no information on possible rotational abnormalities. Moreover, in deformities where one or more parameters are severely altered, thus defined as complex, the analysis may become entirely unfeasible.

Second-level imaging is essential for the evaluation of complex deformities and bone tumours, and it usually encompasses both CT and MRI. CT or CBCT (cone-beam CT) enable high-resolution visualization of bone morphology, with CBCT offering reduced radiation dose and weight-bearing acquisition, making them suitable for detailed anatomical reconstructions without contrast agents [72,125]. MRI, on the other hand, offers exceptional contrast for soft tissues, allowing accurate evaluation of muscles, cartilage, and pathological changes within bone. Together, these modalities provide a comprehensive understanding of both osseous and soft-tissue anatomy, essential for accurate diagnosis and surgical planning, and can be spatially overlaid through registration procedures (e.g., best-fit algorithms) to combine complementary datasets, which is especially useful for reconstructing tumour-related anatomical models [73,126].

The imaging data are subsequently processed to generate a 3D virtual bone model of the patient's anatomy, obtained by converting DICOM files into STL format as previously described. This model serves as the basis for deformity analysis.

3.1.2. Three-Dimensional Analysis of the Deformity

Deformity analysis serves a dual purpose: on the one hand, it allows for a detailed understanding of the problem being addressed, and on the other, it provides a framework for planning its correction. This stage of the workflow relies on objective data, and analyses performed by different operators are generally reproducible.

A limb can be conceptualized as a chain of mobile joints connected by rigid segments (bones) according to optimal geometric relationships. The purpose of deformity analysis is to determine the misalignment between joints by precisely identifying the point or points along the bone where the deviation is most evident. These points indicate the most suitable sites for performing deformity correction.

To assess these deviations, a principal joint plane and a centroid can be identified for each joint, both defined according to the specific anatomical region. A recent Delphi consensus outlined the most commonly used anatomical landmarks for determining joint planes, centroids, and reference coordinate systems for 3D lower-limb alignment analysis, focusing on the hip, knee, and ankle joints [127]. From each centroid and plane, an axis emerges, forming in each bone segment a peculiar angular relationship with the anatomical axis of the bone (Figure 44). In a normal limb, these axes are collinear with the anatomical axis, whereas in a deformed limb they deviate as a result of angular, translational, and/or rotational abnormalities. The following section analyses each of these components and explains how they can be identified on the models using the CORA method described by Paley et al [15].

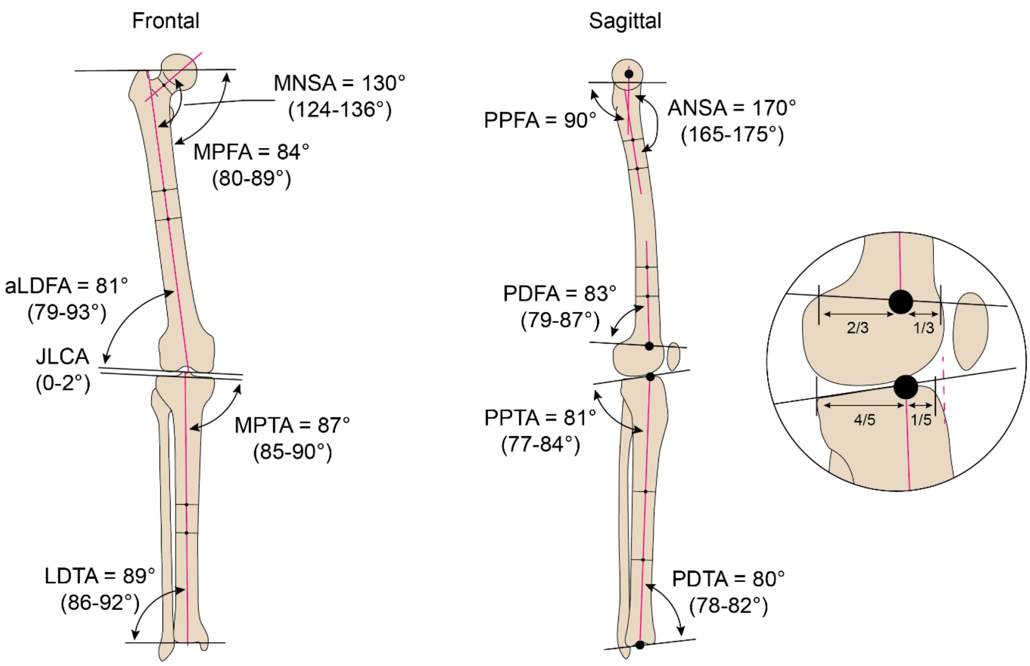

Figure 44. A diagram with the nomenclature for joint orientation angles in the frontal and sagittal plane. MNSA: Mechanical Neck–Shaft Angle; aLDFA: Anatomical Lateral Distal Femoral Angle; JLCA: Joint Line Convergence Angle; MPTA: Medial Proximal Tibial Angle; LDTA: Lateral Distal Tibial Angle; PPFA: Posterior Proximal Femoral Angle; ANSA: Anatomical Neck–Shaft Angle; PDFA: Posterior Distal Femoral Angle; PPTA: Posterior Proximal Tibial Angle; PDTA: Posterior Distal Tibial Angle.

Angular deformity is the most important among deformity parameters. Compared to other parameters, it is the one that most significantly compromises limb function, and it is usually the source of discomfort and pain for the patient [34]. For example, in the lower limbs, even a small angular deformity of a few degrees near the articular surface of the knee will markedly shift the load-bearing axis (defined as the mechanical axis, through which the body's centre of mass passes during gait) outside the articular surface, generating an eccentric overload that disturbs growth at the knee and accelerates its degeneration.

The identification of these axes in each anatomical segment is highly specific and should be carried out in collaboration with the surgeon, following standard measurement nomenclature and, when possible, referencing the contralateral "normal" bone. As illustrated in Figure 44, there are no absolute normal values but rather ranges of physiological joint alignment relative to the bone axis. These axes are often straightforward to identify. However, when the deformity is located near a joint surface, localization becomes more challenging, and the use of a method that accounts for normal angular ranges becomes essential.

In any case, the decision-making process is more complex and must always be approached in dialogue with the surgeon, as the final desired correction, as well as the method and type of treatment to achieve it, depends on several factors, including the underlying pathology and the patient’s clinical presentation. For instance, in certain cases the objective may be limited to realigning the mechanical axis, and the use of physiological joint orientation ranges is sufficient. However, this is not universally applicable. A patient may present with aligned anatomical axes, yet clinically exhibit knee recurvatum. In such cases, the correction must be guided by clinical findings. In pathologies such as Perthes disease, the primary goal may instead be to ensure proper femoral head coverage. In some complex pediatric cases, particularly in patients with neuromuscular disorders, the aim may not be anatomical realignment at all, but rather achieving a functional posture that enables basic care activities, such as dressing or hygiene, to be safely performed by caregivers.

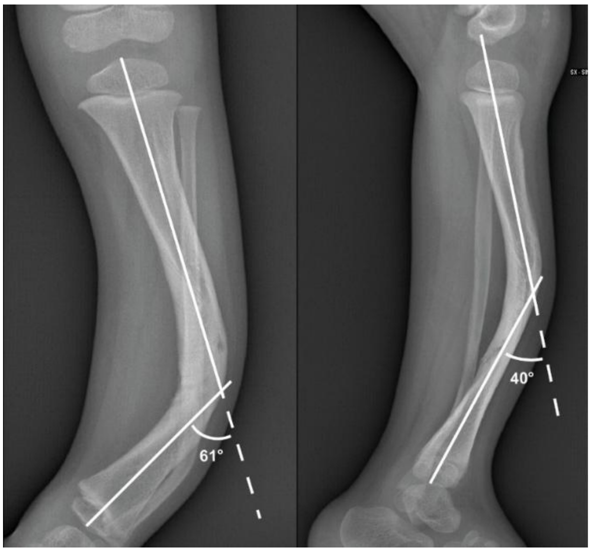

Figure 45. Two-dimensional representation of Case #5 showing the diaphyseal angular deformity of the left tibia as visualized on orthogonal radiographs, in anteroposterior and lateral projections, respectively.

Figure 46. Case #5 CT scan obtained from the hospital PACS (Picture Archiving and Communication System) illustrating a diaphyseal angular deformity of the left tibia and fibula, with three-dimensional visualizations in oblique, frontal, and lateral views, respectively.

Figures 45 and 46 illustrate Case #5, a 6-year-old girl with congenital pseudoarthrosis of the left tibia associated with neurofibromatosis. Although the planned corrective osteotomy with intramedullary nailing was not performed due to a preoperative fracture and the case was excluded from the case series, it is shown here to illustrate the basic concept underlying deformity localization.

Standard assessment relies on the coronal and sagittal anatomical planes, corresponding to anteroposterior and lateral radiographs, respectively. When a uniapical deformity is visible on both projections, it is often incorrectly described as biplanar. In fact, these are typically uniplanar deformities lying in an oblique plane between the coronal and sagittal planes.

When a bone with an angular deformity is rotated 360° relative to a fixed observer, the angle (α) formed between the proximal and distal axes varies between a maximum value (+μ) and a minimum value (−μ). These extrema have the same magnitude but opposite sign, reflecting the mirrored appearance of the same deformity when projected onto a two-dimensional plane from opposite viewing directions. These extreme values are reached by rotating the bone through 180°. In other words, when the deformity appears maximal in one orientation, a 180° rotation reveals the same degree of deformity in the opposite direction. The variation of α during a full 360° rotation follows a sinusoidal pattern, as shown in Figure 47.

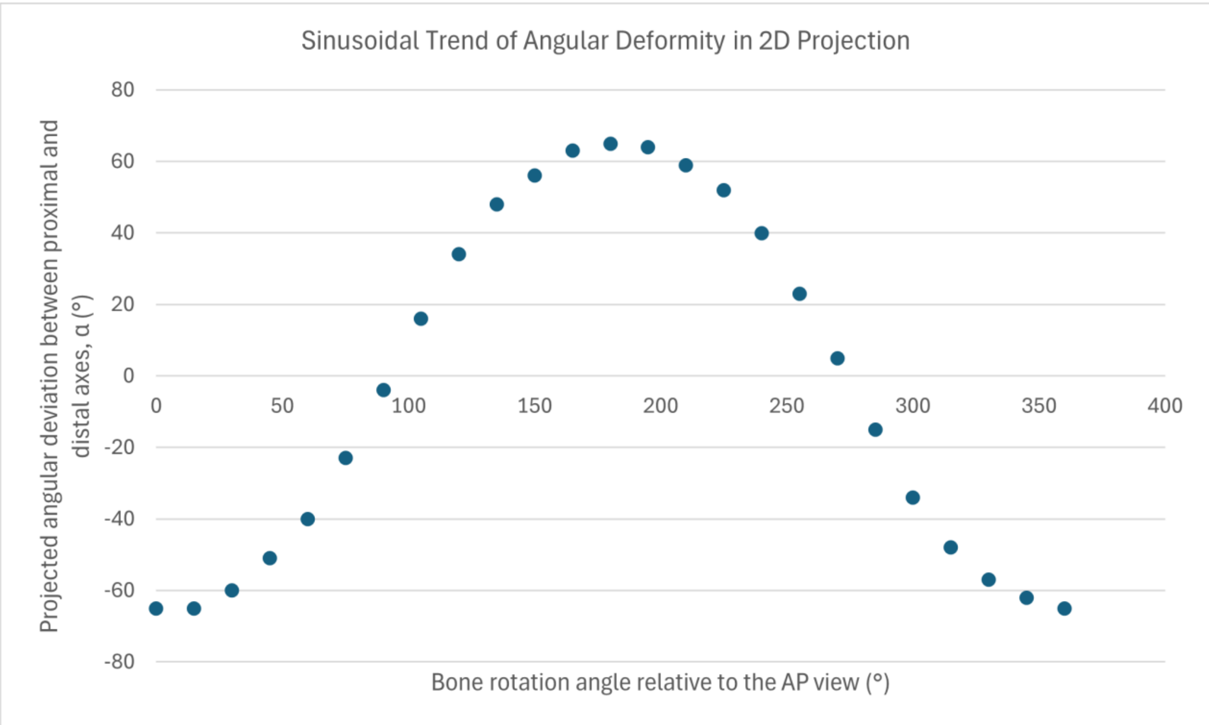

Figure 47. Graph showing the angle between the proximal and distal axes of a diaphyseal angular deformity of the left tibia for Case #5, measured on the CT reconstruction by rotating the bone model in 15° increments starting from the anteroposterior (AP) orientation. The measured deformity increases to approximately +60° and then decreases to –60°, following a sinusoidal pattern. The maximum angulation of the deformity is observed in an oblique plane, about 15° from the AP view. The graph illustrates the sinusoidal variation of the angular deviation (α) as the bone is rotated through 360°, showing equal but opposite magnitudes of deformity (±μ) every 180° of rotation.

The **maximum angular deformity** between the proximal and distal axes (magnitude) is identified by rotating the bone in 3D space until the two axes appear parallel in a 2D projection, corresponding to a null apparent deformity (0°) in the sinusoidal variation of the angle. A 90°

rotation from this projection reveals the plane in which the maximum angular deformity is observed (Figure 47).

In 3D analysis, the proximal and distal axes do not necessarily intersect. Therefore, the MDP is defined as the plane parallel to both axes and oriented along the direction of the maximum angular deformity. This plane shows the true 3D deformity, extending beyond traditional 2D visualization, since angular deviations observed on anteroposterior and lateral radiographs correspond to a single uniapical deformity lying in an oblique plane. As explained before, proximal and distal axes are defined as the lines that best approximate the central longitudinal geometry of the bone segment and are identified on the 3D model using Blender, in agreement with the surgeon.

When projected onto the MDP, the deformity is fully expressed, and the proximal and distal axes intersect at the point known as the CORA. The axis passing through the CORA and perpendicular to the MDP, defined as the Angular Correction Axis (ACA), represents the line around which the bone segments must be rotated by the magnitude angle to realign the proximal and distal axes (Figure 48).

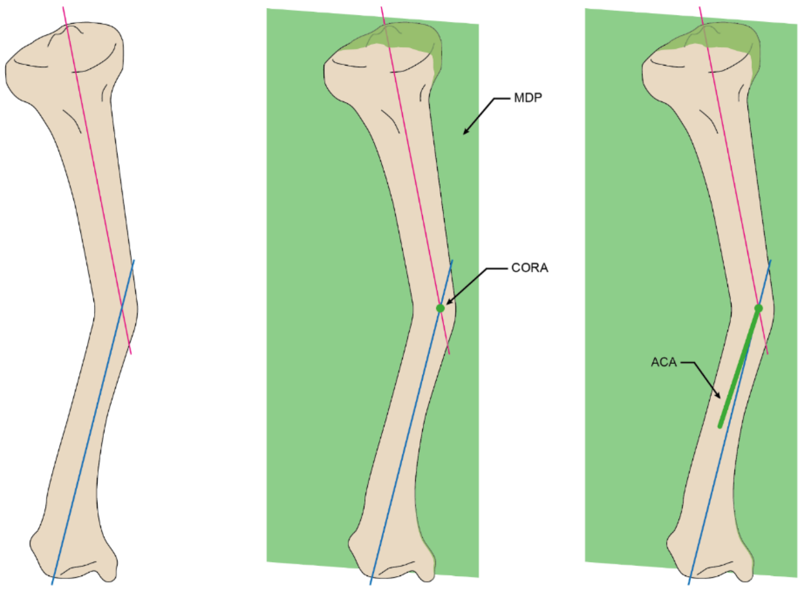

Figure 48. Schematic representation of the proximal and distal axes, the Centre of Rotation of Angulation (CORA), the Maximum Deformity Plane (MDP), and the Angular Correction Axis (ACA). The MDP is defined as the plane containing both the proximal and distal axes, which intersect at the CORA. The ACA, oriented perpendicular to the MDP, represents the axis around which the bone segments are rotated to restore alignment.

In fact, any plane parallel to both axes can be defined as a plane of maximum deformity. The proximal and distal axes may lie in two distinct yet parallel planes, both belonging to this group. The distance between these planes represents the **translational component** of the deformity (Figure 49). In most cases, this component is minimal and rarely occurs as an isolated deformity. However, as will be discussed in the planning section, it must be carefully monitored, as it may increase depending on the selected correction strategy or the fixation devices used.

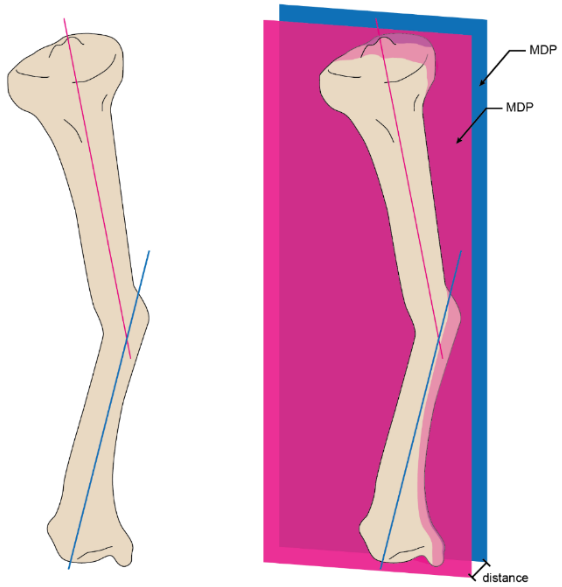

Figure 49. Representation of the translational component of deformity. The proximal and distal axes may lie in two distinct but parallel Maximum Deformity Planes (MDPs); the distance between them represents the translational component.

Suppose that a bone is adjusted so that the proximal and distal mechanical axes are parallel (eliminating angular deformity) and coaxial (eliminating translational offset). Under these conditions, two additional parameters remain to be defined. The first is **bone length**, which may vary due to longitudinal translation between the proximal and distal segments. This parameter is critical to estimate and monitor, as it influences the outcome of the correction. A deformed bone may initially appear shorter than the contralateral side, yet once realigned, this difference can become negligible. However, as will be discussed later, variations in the correction technique can lead to significant differences in the final bone length, which may have clinical implications.

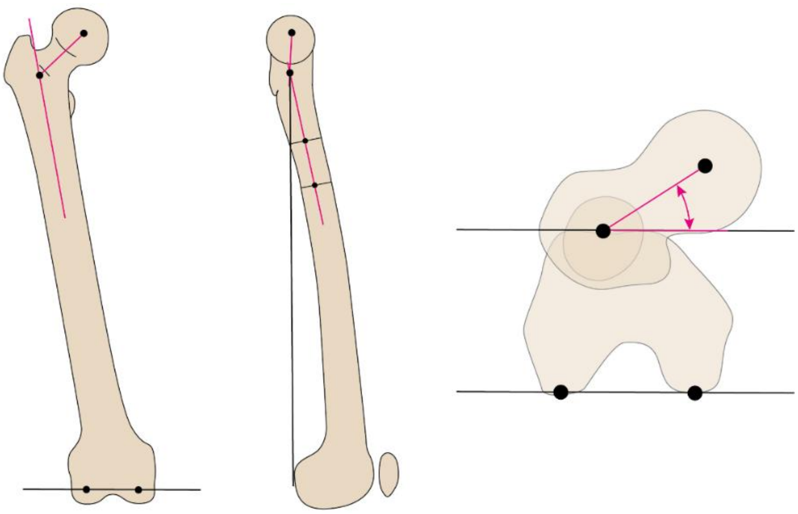

Figure 50. Illustration showing measurement of femoral version: in the frontal and sagittal views (left), the femoral shaft and neck axes (red lines) are shown for anatomical reference. In the transverse view (right), femoral version is defined as the angle between the line connecting the posterior tangent points of the femoral condyles projected onto the transverse plane (black line with two points), and the proximal axis passing through the centre of the femoral neck (red line). The angle between these two axes represents femoral anteversion.

Finally, another important parameter that can affect limb function is **torsional deformity**, which in some cases may represent the only major abnormality. It is evaluated with respect to age-specific normal ranges by measuring angular reference points between proximal and distal articular structures and assessing their angular relationship to the bone's longitudinal axis (Figure 50). Several methods are available for evaluating bone torsional alignment, most of which rely on CT or MRI, which are considered the current gold standard [128].

In summary, bones deformity analysis consists of identifying two axes (proximal and distal) that should ideally be coaxial, and measuring the extent to which they are angulated, translated, shortened or lengthened, and rotated relative to each other. Having a model of the contralateral healthy bone is highly useful for determining the bone's normal alignment. Some authors, such as Dobbe et al. [129] in computer-assisted planning of distal radius osteotomy, have even proposed automated systems that compare the deformed bone model with a mirrored reconstruction of the contralateral normal bone.

3.1.3. Planning Deformity Correction

Although deformity analysis objectively and reproducibly defines the altered parameters, it does not prescribe a single corrective solution. In practice, multiple (and theoretically infinite) strategies can achieve the same geometric realignment [130]. Accurate identification of which parameters to adjust and the selection of reliable reference points are therefore essential to guide surgical decision-making. In cases of deformities prone to recurrence, particularly in skeletally immature patients, intentional "overcorrection" of one or more parameters may be advisable [131]. This stage of planning thus demands close surgeon supervision [132].

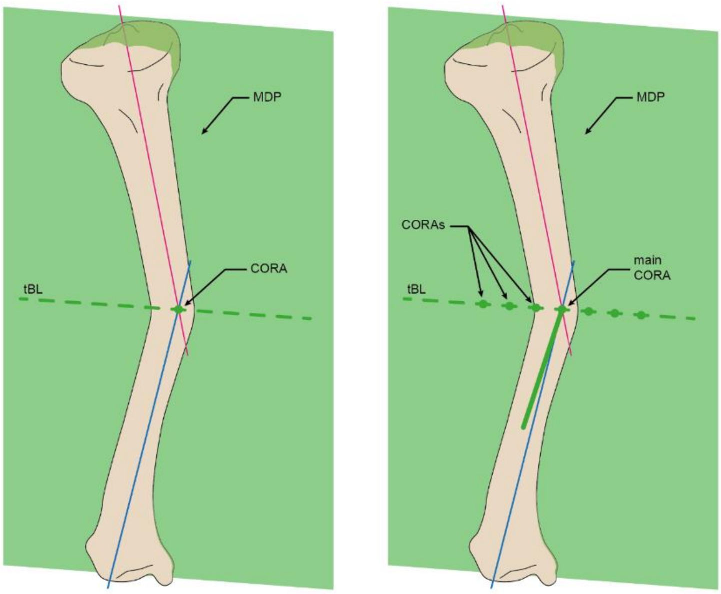

Figure 51. Schematic representation of the Maximum Deformity Plane (MDP), the transverse bisector line (tBL), and the corresponding Centers of Rotation of Angulation (CORAs). The main CORA is located at the intersection of the proximal and distal axes (left), while the Angular Correction Axis (ACA), perpendicular to the MDP, can pass through any of the CORAs along the tBL (right).

The most important element in planning corrections is the CORA, that is the center of rotation of the angular deformity located at the intersection of the proximal and distal reference axes in the plane of projection [15]. As previously noted, the ACA is the line perpendicular to the MDP passing through the CORA. In practice, an infinite number of CORAs can be defined, all lying along the transverse bisector line (tBL), which bisects the angle between the proximal and distal axes within the MDP. The CORA located at the intersection of the two axes is referred to as the main CORA. The same principle applies to the ACA, which is perpendicular to the MDP and can pass through any of these CORAs (Figure 51).

Positioning the ACA exactly at the main CORA and rotating one bone segment by the angular magnitude realigns the proximal and distal axes without changing the overall bone length. This property of achieving realignment is shared by all points lying on the tBL. However, selecting an ACA at a different position along the tBL will modify the final bone length by twice the product of the distance (d) from the main CORA and the sine of half the deformity angle (α/2). The final bone length decreases if the ACA is placed on the concave side and increases if it is placed on the convex side of the deformity (Figure 52). This principle underlies the simplest osteotomy corrections (opening- and closing-wedge osteotomies) in orthopaedic surgery. The classic method for geometric deformity planning along mechanical or anatomical axes was developed by Paley et al. [15] and remains fundamental in current practice.

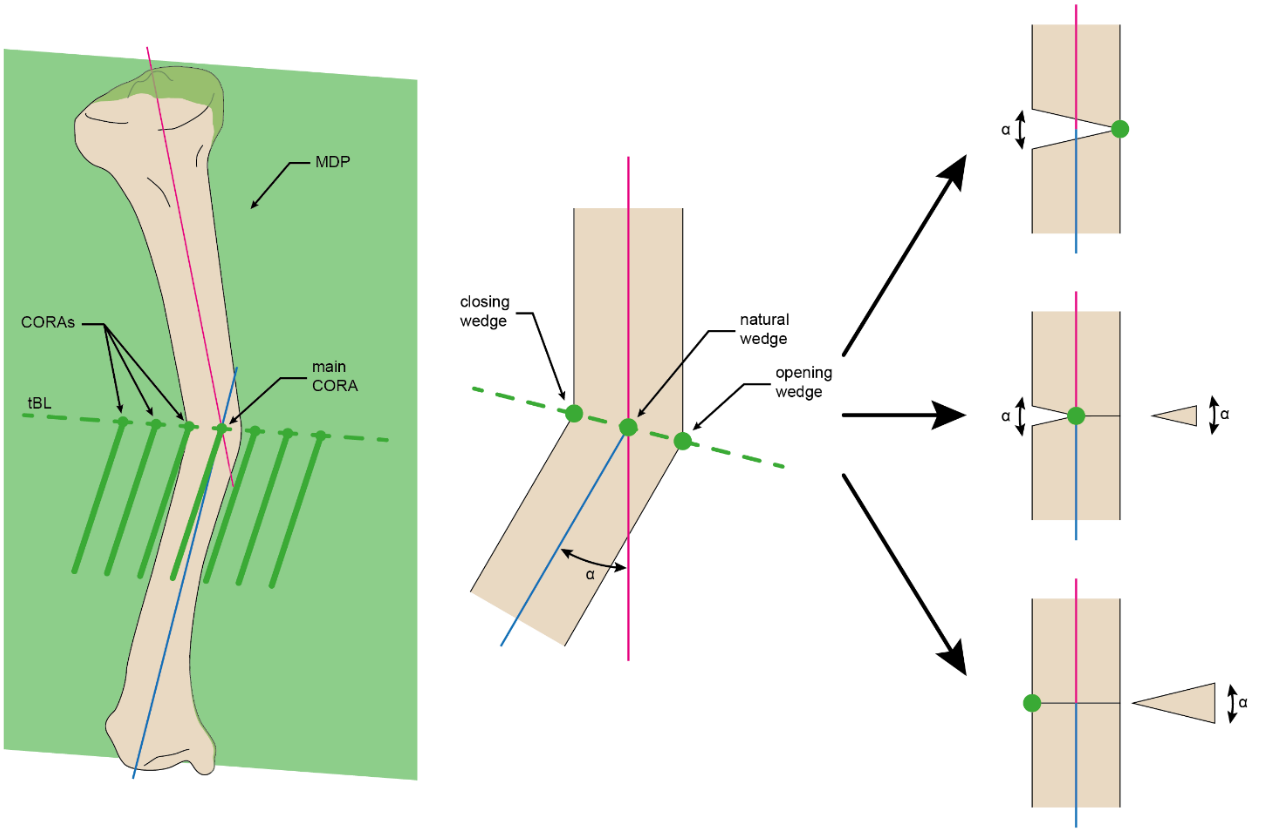

Figure 52. All points (green) lying on the transverse bisector line (tBL, dotted green) are equivalent centres of rotation of angulation (CORA) and achieve coaxial alignment of the proximal (red) and distal (blue) axes without inducing length changes (left). Conversely, selecting a pivot displaced from the true CORA to correct an angular deformity of α introduces a longitudinal effect (centre), resulting in bone lengthening in an opening-wedge osteotomy (top right) or bone shortening in a closing-wedge osteotomy (bottom right).

These closing- and opening-wedge osteotomies represent the technically simplest approaches for correcting pure angular deformities. They involve an incomplete bone cut, preserving a thin final cortical bone at the end of the osteotomy, the so called 'hinge', an intact cortex that acts as the fulcrum for correction. The hinge must be thin enough to allow controlled bending of the bone, yet thick enough to prevent unintended fracture [133]. Provided that the hinge remains intact, very precise correction can be obtained, and fixation can usually be obtained with minimal hardware, such as plates or screws. However, these classic wedge techniques cannot address torsional alignment of the bone. Moreover, they are poorly suited to diaphyseal bone segments, as the thick cortical bone does not allow preservation of a flexible hinge, and for angular corrections over 15–20°, the risk of hinge fracture becomes significant.

Closing-wedge osteotomy is performed by making two convergent subcomplete osteotomies (often perpendicular to the proximal and distal reference axes) while leaving a hinge of bone at the apex of this wedge. The deformity is corrected by removing the bone wedge between these cuts and closing the gap. The final bone length is shortened by approximately half the maximal height of the bone wedge removed (Figure 53).

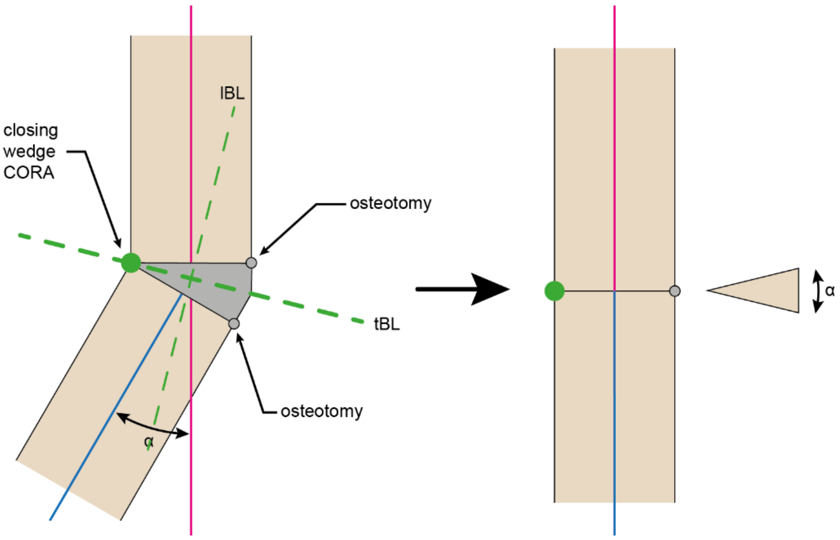

Figure 53. Closing-wedge osteotomy: correction obtained by removing a bone wedge (grey area) between two cuts while preserving a hinge at the apex (left), resulting in slight bone shortening (right).

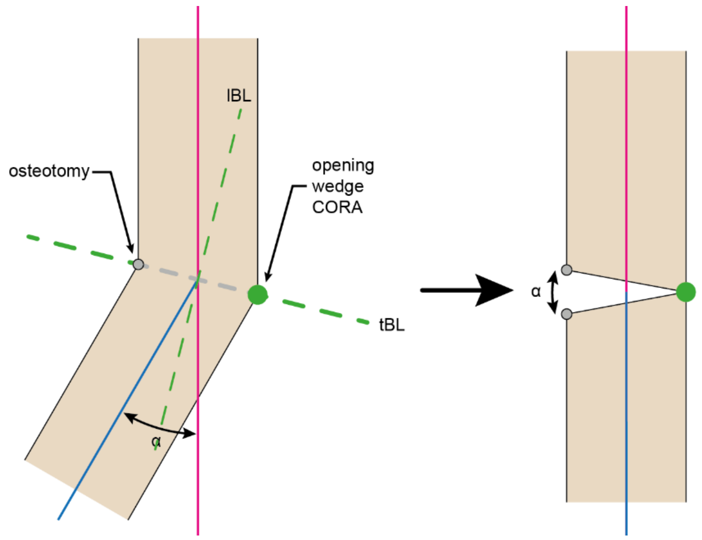

Figure 54. Opening-wedge osteotomy: correction achieved by distracting bone segments around a preserved hinge (grey dot) (left), leading to slight increase in overall bone length (right).

Opening-wedge osteotomy ideally involves a single subcomplete cut on a plane passing through tBL and perpendicular to the plane of maximum deformity. By distracting between the bone segments about a hinge, one correction of the deformity is obtained. The final length increases by about half the maximum diastasis between the segments. If the hinge is preserved, the correction may be stable with just a bone graft wedge, though fixation and/or postoperative immobilization in a cast is often recommended (Figure 54).

Both osteotomy techniques should ideally be performed as close as possible to the CORA position, or more precisely, along the transverse bisector line (tBL) on which the CORAs lie. The farther the osteotomy is placed from the CORA, the greater the secondary translation is induced between the proximal and distal axes [134]. In some cases, anatomical or technical limitations preclude placing the osteotomy precisely at the CORA. However, the evaluation of the induced translation allows the surgeon to judge whether the resulting displacement remains acceptable given the advantages of a simpler approach. Therefore, use of alternative correction techniques beyond basic wedge methods should be justified by one or more of the following reasons: (1) the osteotomy plane cannot be placed sufficiently near the CORA; (2) a torsional or translational adjustment is also needed; (3) the angular deformity to correct is severe (angular deformity over 15°-20°); (4) the osteotomy would be located in the diaphyseal region, where the cortical bone is too thick to preserve a bone hinge [135].

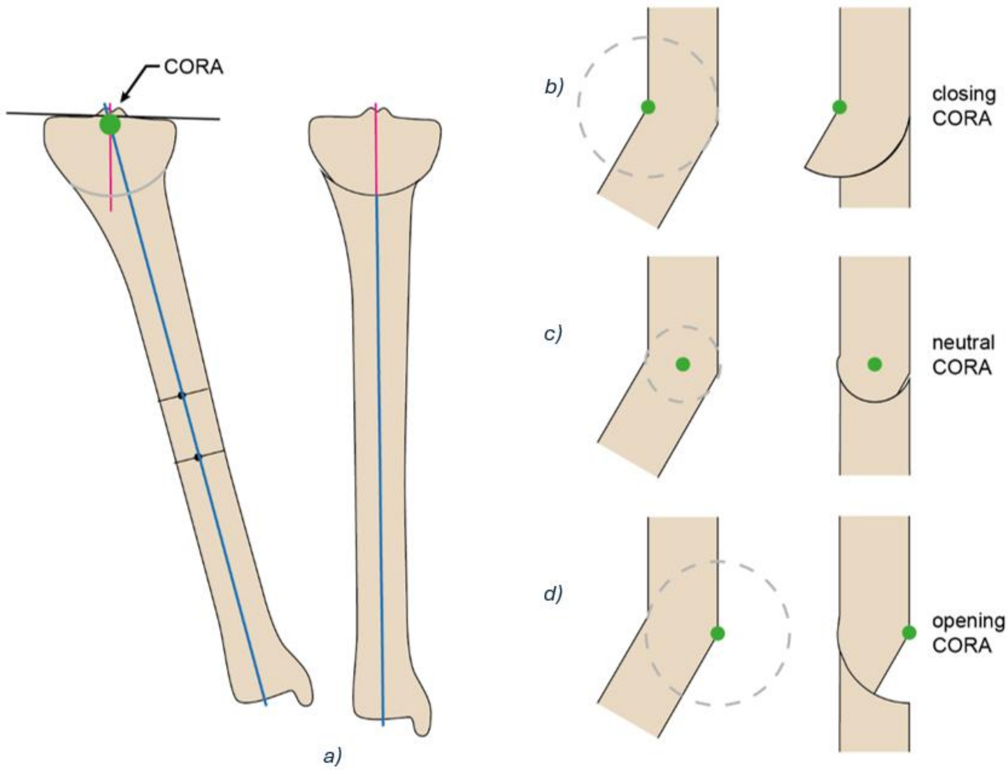

Figure 55. Dome osteotomy is useful when the CORA is located close to a joint (a). The final bone length can be modulated by shifting the centre of the cylindrical cut along the tBL: when centred, bone length remains unchanged (c), whereas shifting the centre toward the concave or convex side results in shortening (b) or lengthening (d), respectively.

The **dome osteotomy** is one option when the osteotomy cannot pass through the CORA. The surgeon creates a cylindrical cut whose axis passes through the CORA and is perpendicular to the plane of maximum deformity. This osteotomy is technically demanding, even with specialized tools, as it requires a precisely cylindrical cut. This technique allows correction of large angular deformities, but it can be applied only in large metaphyseal bone and does not permit torsional or translational adjustments. Some control of final length is possible by shifting the center of the cylinder toward the concave or convex side (analogous to wedge methods, see Figure 55).

To correct pure torsional deformities, the standard technique is the **derotational osteotomy**, defined as a complete linear osteotomy performed on a plane as perpendicular as possible to the mechanical axis connecting the proximal and distal joint centroids [136]. The bone fragments are aligned as needed and fixed. This osteotomy may be placed anywhere, but its orientation must be precise to avoid introducing secondary angular deformities. Note that in the lower limb, a torsion correction near the knee may also affect patellar tracking, either beneficially or adversely. During this procedure, torsional alignment of the bone axes should always be carefully monitored using at least two large pins.

If the torsion correction is truly pure, the osteotomy plane should be perpendicular to the mechanical axis (0° inclination), otherwise an angular parasitic deformity will be introduced after the torsional correction. More advanced planning techniques allow the surgeons to exploit the parasitic angulation to design a single **oblique osteotomy** that corrects both angular and rotational deformities with one cut. This requires precise quantification of both the angular and torsional components, as well as accurate localization of the angular CORA.

When the angular deformity greatly exceeds the torsional one, such an oblique correction is generally discouraged, as an excessively steep osteotomy plane may create dangerously sharp bone edges. To illustrate the geometric relationship between angular and torsional deformities, Figure 56 shows an experimental example using a banana model, taken from Paley et al. [15], representing a varus deformity combined with intrarotation.

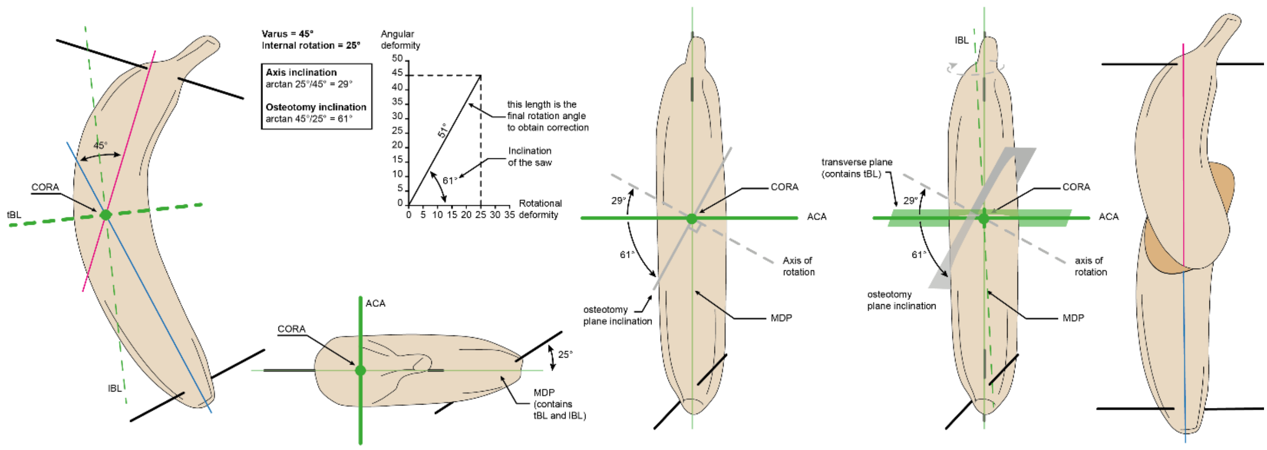

Figure 56. Example of oblique osteotomy planning for a combined angular (45°) and torsional (25°) deformity. The calculated osteotomy inclination is 61° with a 51° rotational correction. When the angular component predominates, the plane becomes excessively steep, making this approach less suitable, as shown [15].

In this example, a 45° varus deformity is associated with 25° of internal rotation. By applying geometric combination principles, the orientation of the osteotomy plane relative to the plane of maximum deformity can be determined, resulting in a saw inclination of 61° and a rotational adjustment of 51°. Before performing the osteotomy, the cutting plane must be reoriented by half of the torsional deformity (12.5°) in the opposite direction to ensure proper alignment. After cutting, rotating the distal segment by 51° around the osteotomy axis allows full correction of both angular and torsional components. However, as shown in this example, when the angular deformity predominates, the osteotomy plane becomes too steep, producing sharp bone edges and reducing the contact area between fragments. Therefore, this approach is not recommended in cases with a dominant angular deformity. As the example shows, oblique osteotomy demands very precise identification of the osteotomy plane, and thus the use of PSIs is mandatory. Because of the complexity of the required calculations, intraoperative modifications are generally not feasible.

The last two techniques, shortening/translation osteotomy and osteotomy with intercalary bone graft, enable correction of all deformity components (angulation, torsion, translation, and length). They can be considered, respectively, as modified closing- and opening-wedge osteotomies in which the bone hinge is sacrificed to allow additional torsional, translational, and/or length adjustments.

In a **shortening or translation osteotomy**, the bone ends are brought into direct contact, sometimes requiring the removal of a wedge or trapezoid, usually along planes perpendicular to their respective reference axes. The resulting shortening may produce a clinically significant limb length discrepancy, which must be carefully evaluated. The osteotomy plane can be shaped using various configurations described for specific bone regions, allowing the surgeon to optimize stability or minimize bone loss. For instance, oblique or chevron (V-shaped) osteotomies can be used to enhance final stability and to reduce shortening. In particular, the reverse V-shaped osteotomy of the distal humerus (Figure 57) enables correction of cubitus varus while minimizing instability and medial displacement compared to the classic closing-wedge technique [137]. Another example is the Morscher technique, in which the femoral neck is lengthened by sliding it along an oblique osteotomy plane [138]. Numerous other techniques involve local rearrangement of bone segments, but they share the common feature of maintaining direct contact between proximal and distal fragments, thus eliminating the need for bone grafting.

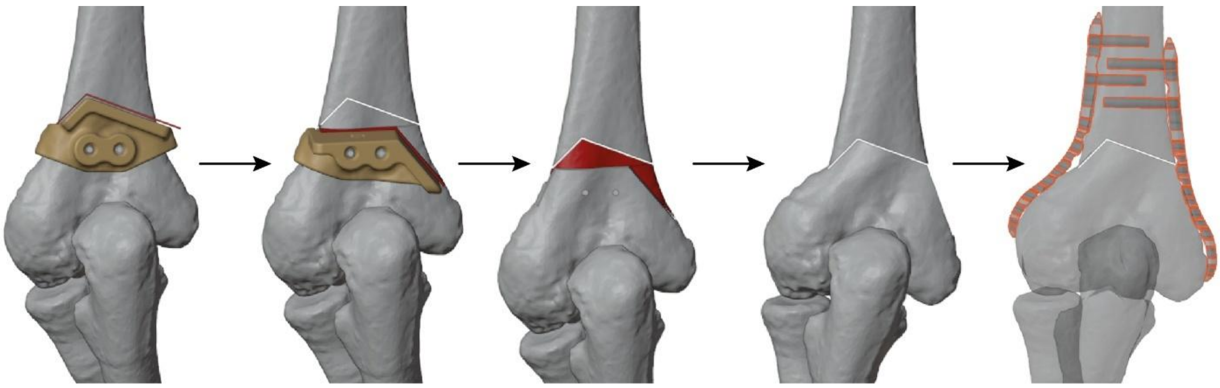

Figure 57. Example of reverse V-shaped osteotomy of the distal humerus for cubitus varus correction, with design of PSIs. This configuration improves stability and reduces medial displacement compared with the traditional closing-wedge technique.

In an **intercalary graft osteotomy**, the proximal and distal bone segments are not in direct contact, and shortening is compensated, or in some cases acutely converted into lengthening, by interposing an autologous or homologous bone graft. This configuration can reduce mechanical stability, making proper fixation essential to minimize the risk of non-union.

Although the inclination of the osteotomy planes may vary, it is generally advisable for at least one plane to remain perpendicular to the mechanical axis, allowing torsional correction without introducing parasitic angular deformities. In an intercalary graft osteotomy, the proximal and distal bone segments are not in direct contact, and shortening is compensated, or in some cases acutely converted into lengthening, by interposing an autologous or homologous bone graft. This configuration can reduce mechanical stability, making proper fixation essential to minimize the risk of non-union. Although the inclination of the osteotomy planes may vary, it is generally advisable for at least one plane to remain perpendicular to the mechanical axis, allowing torsional correction without introducing parasitic angular deformities. Finally, all acute lengthening manoeuvres are limited by soft-tissue tolerance. Lengthening beyond the physiological capacity of the surrounding tissues increases the risk of neurovascular or soft-tissue injury. When the planned acute lengthening exceeds commonly accepted safe thresholds (approximately 1 cm for the upper limb and foot [139], and 2 cm for the femur [140]) it is advisable to adopt gradual correction techniques using external fixation or lengthening intramedullary nails.

Distraction osteogenesis is a technique used to achieve progressive bone lengthening. It involves placing an internal or external fixation device proximal and distal to an osteotomy and applying gradual distraction, typically 0.5–1 mm per day.

From a biomechanical and planning perspective, these procedures are characterized by a high sensitivity to initial implant positioning, spatial alignment, and axis definition, as gradual distraction amplifies even small residual angular, translational, or torsional errors over time.

External fixation systems capable of multiaxial correction, such as hexapod (Taylor Spatial Frame) configurations, allow postoperative adjustment through predefined correction schedules generated by dedicated software. However, their effectiveness relies on an accurate initial geometric definition of the deformity and reference axes, while prolonged treatment duration (that may extend up to 6–12 months or longer) and patient encumbrance remain major drawbacks. Conversely, simpler unilateral systems represent a similar concept reducing external bulk but offering limited capacity for secondary correction, making precise preoperative alignment critical.

Although distraction osteogenesis procedures are generally not included within the scope of this project, as they are not typically planned through VSP or executed PSIs, some preliminary simulation tests were carried out to support the application of these techniques as well. A biplanar distraction approach was tested on a forearm case, first through VSP and then on a non-sterile 3D printed model, to assess feasibility, spatial configuration, and potential surgical applicability (Figure 58).

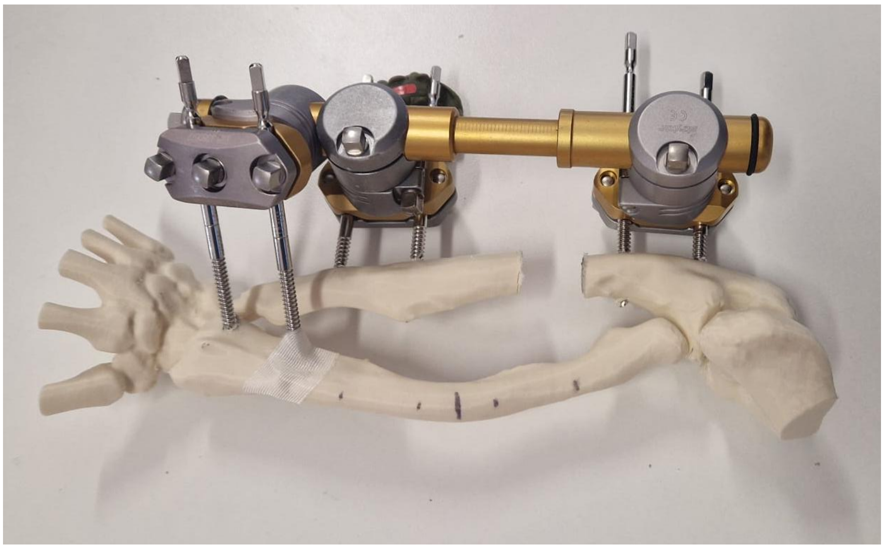

Figure 58. Preliminary simulation of a biplanar distraction osteogenesis using a unilateral external fixator: physical test on a non-sterile 3D printed prototype to assess feasibility and spatial configuration.

The most advanced tool for distraction osteogenesis is the magnetically or radio-controlled lengthening **intramedullary nail**. This fully implantable system uses an internal mechanical actuator controlled by external magnetic fields or radiofrequency signals to gradually change nail length. In these cases, the absence of postoperative adjustability makes surgical accuracy paramount, as angular or torsional errors cannot be corrected without revision surgery [141]. Here, VSP was employed to support the selection of implant dimensions and to define the optimal insertion trajectory, enabling simultaneous control of lengthening and angular correction (Figure 59).

Overall, these exploratory applications highlight how 3D modelling and virtual planning can provide critical support in distraction-based procedures by reducing geometric uncertainty, improving implant positioning accuracy, and anticipating cumulative alignment errors, even in contexts where PSIs are not directly employed.

A schematic overview of the approaches discussed above is summarized in Table 5.

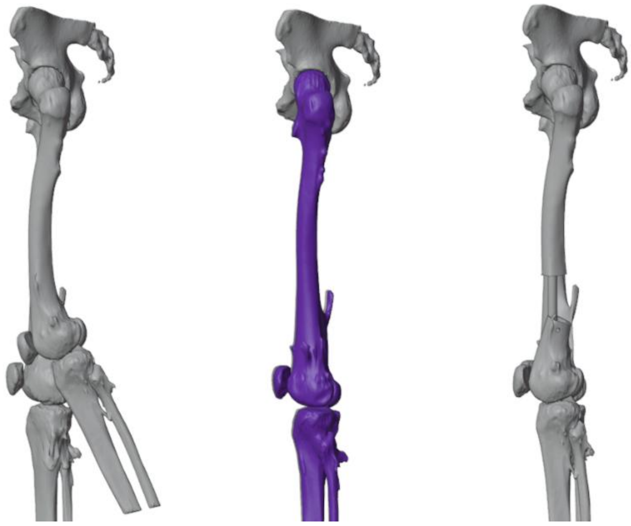

Figure 59. Virtual simulation of a magnetically controlled lengthening nail supported by VSP for sizing and insertion trajectory planning, showing the initial deformity (left), contralateral anatomy used as reference (center, violet), and the planned final correction (right).

Table 5. Summary of the main deformity correction techniques described, indicating the type of correction they allow and the stage at which it can be achieved.

Osteotomy type	Complexity	Corrections	Advantages	Drawbacks
Closing-wedge	Low	Angulation	Minimum fixation required Bone graft not required Low risk of secondary deformities Low risk of non-union	Reduces the final length of the bone No rotation/translation allowed Impossible in diaphyseal bone and in severe angular deformities
Opening-wedge	Medium	Angulation	Minimum fixation required Low risk of secondary deformities Low risk of non-union	Increases the final length of the bone Bone graft recommended No rotation/translation allowed Impossible in diaphyseal bone and in severe angular deformities
Dome	Very high	Angulation	Osteotomy away from the CORA Allow for severe angular deformities correction Bone graft not required	Technically demanding No rotation/translation allowed Impossible in diaphyseal bone
Derotative	Medium	Rotation Translation	Simple single cut Low risk of non-union Bone graft not required	Moderate risk of secondary deformities No angular correction allowed
Oblique	Very high	Rotation Angulation	Multiplanar correction No bone shortening Low risk of non-union Bone graft not required	The torsional deformity should be higher than the angular deformity PSIs use is mandatory Intraoperative modifications not allowed
Shortening	High	Angulation Translation Rotation	Low risk of non-union Bone graft not required	Short final length Moderate risk of secondary deformities
Intercalary bone graft *(e.g. Flipping-Wedge Osteotomy, Side-to-Side Flipping Wedge Osteotomy)*	Very high	Angulation Translation Rotation Length (*)	Allow correction of all parameters Allow length adjustment	Requires appropriate fixation technique Bone graft is mandatory High risk of non-union High risk of secondary deformities Limited maximal lengthening (1 cm in small bones, 2-3 cm in large bones)
Taylor spatial frame (hexapod external fixator)	Medium	Angulation Translation Rotation Length	Allow for contemporary correction of all parameters	Bulky to wear High risk of pin tract infections Expensive
Unilateral external fixator	High	Length Translation (**) Angulation (**) Rotation (**)	Less bulky than circular frames	Limited options to change angulation and rotation after the initial surgery High risk of pin tract infections

Intramedullary lengthening nail	Very high	Length Rotation (**) Angulation (**)	All system under the skin Implant can be removed after complete healing of the bone	All corrections but lengthening must be achieved during the initial surgery Extremely expensive

(*) = limited
(**) = only during initial surgery

3.2. Optimized Case-specific Procedures

Based on the principles of deformity correction previously described, VSP and 3D printing were employed not only as supporting tools, improving the understanding of the deformity and supporting the design of customized instruments, but as enabling technologies for the conceptual development of new surgical strategies. Within this work, two original correction techniques were conceived, formalized, and applied by the authors in selected clinical cases, extending the conventional use of VSP and PSIs and GSIs toward more versatile and geometry-driven correction approaches. These techniques, termed Flipping-Wedge Osteotomy and Side-to-Side Flipping-Wedge Osteotomy, were specifically developed to improve correction accuracy, control bone length, and improve intraoperative feasibility in complex deformities where standard osteotomy strategies are insufficient. These methodologies have been developed using VSP and 3D virtual models, which aid in visualizing and understanding the morphology and geometry. Notably, the strength of these techniques lies in their applicability. Even though they were conceived with the aid of 3D visualization, they can also be effectively utilized in settings where such technologies are unavailable, starting from standard 2D radiographs.

3.2.1. Flipping Wedge Osteotomy

The Flipping-Wedge Osteotomy is a geometric correction technique in which the deformity angle is corrected by rotating a bone wedge by 180° around its longitudinal axis. The wedge has a trapezoidal cross-section, defined by two key cuts: the first (major leg) is performed along the tBL at the CORA, while the second (minor leg) is made perpendicular to one of the reference axes (proximal or distal) at a chosen distance (Figure 60). This configuration allows the wedge to be flipped 180° along the chosen reference axis and repositioned, restoring alignment without bone removal. A crucial prerequisite for this method is the precise assessment of the deformity and accurate identification of the MDP, as described above. It was initially developed for a distal radius deformity case, but the technique can be applied to any long bone [81].

According to the osteotomy techniques reported in Chapter 3, in the paragraph ‘Planning Deformity Correction’, the Flipping wedge osteotomy can be classified as an intercalary bone graft osteotomy that uses a local bone graft. As recommended, it always requires the fixation with an appropriate device (such as plate with locking screws).

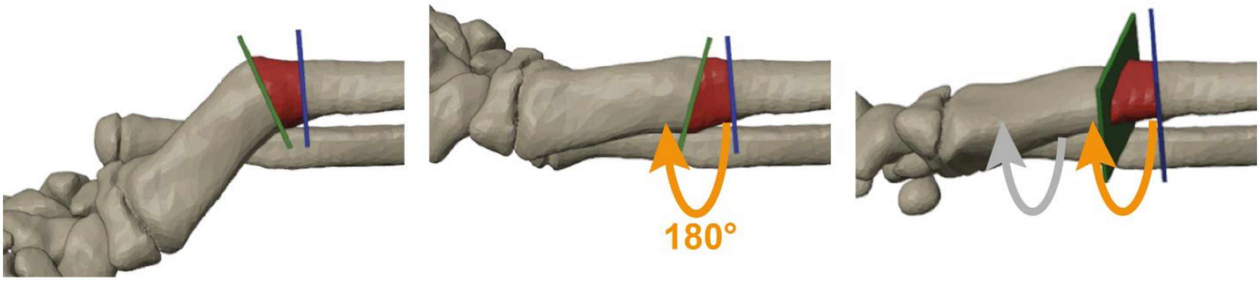

(a) (b) (c)

Figure 60. Simulation of the surgical steps of the Flipping-Wedge Osteotomy on a deformed radius, viewed in the MDP: (a) One cut is made along the transverse bisector line (green plane) and the other perpendicular to the longitudinal axis of the proximal bone (blue plane); (b) the bone wedge between the cuts (red) is flipped 180° around the longitudinal axis (orange arrow); (c) additional correction of the rotational deformity is achieved by rotating all segments distal to the blue plane (grey and orange arrows).

Here, the geometric explanation is defined. Between two lines *a* and *b* intersecting at the CORA, representing the proximal and distal bone axes (Figure 61a), two pairs of opposite angles are formed on the plane containing both axes, typically the MDP. One pair defines the angular deformity (α), while the other corresponds to its supplementary angle (β = 180° − α) (Figure 61b). At this stage, any possible torsional deformity between the axes is not considered, as it will be addressed later. The intersection point of the two axes identifies the CORA, where a concavity angle (γ) and a convexity angle (δ) can be defined and calculated as follows:

$$\gamma = \beta = 180° - \alpha$$

$$\delta = 2\alpha + \beta = 2\alpha + (180° - \alpha) = 180° + \alpha$$

To correct the deformity, both γ and δ must reach 180°. This is achieved by aligning the portion of the *b* axis below the CORA parallel to the *a* axis. The correction can be obtained by mirroring or rotating the *b* axis by 180° around the longitudinal bisector line (lBL). Since only the segment distal to the CORA is involved, the tBL (perpendicular to the lBL) is defined as the cutting plane, allowing the lower portion to be flipped. Once this rotation is completed, *γ'* and *δ'* both equal 180°, and the *a* and *b* axes become coincident.

$$\gamma' = \gamma + \alpha = 180° - \alpha + \alpha = 180°$$

$$\delta' = \delta - \alpha = 180° + \alpha - \alpha = 180°$$

These geometric principles, defined in two dimensions, can be extended to a three-dimensional system by applying them on the MDP in which the deformity reaches the highest magnitude. The axes and CORA are identified as previously described (Figure 61a and 61b). By idealizing the bone as a rectangle with sides parallel to the axes, the corresponding angles theorem can be applied (Figure 61c). Cutting along the tBL corrects the angular deformity, while a second cut (perpendicular to either axis and positioned at any chosen distance) completes the wedge without influencing the correction (Figure 61d and 61e).

If a rotational deformity is also present, it can be addressed by rotating the diaphyseal segment on the side of the perpendicular cut, correcting the torsion independently from the achieved angular realignment (Figure 61f).

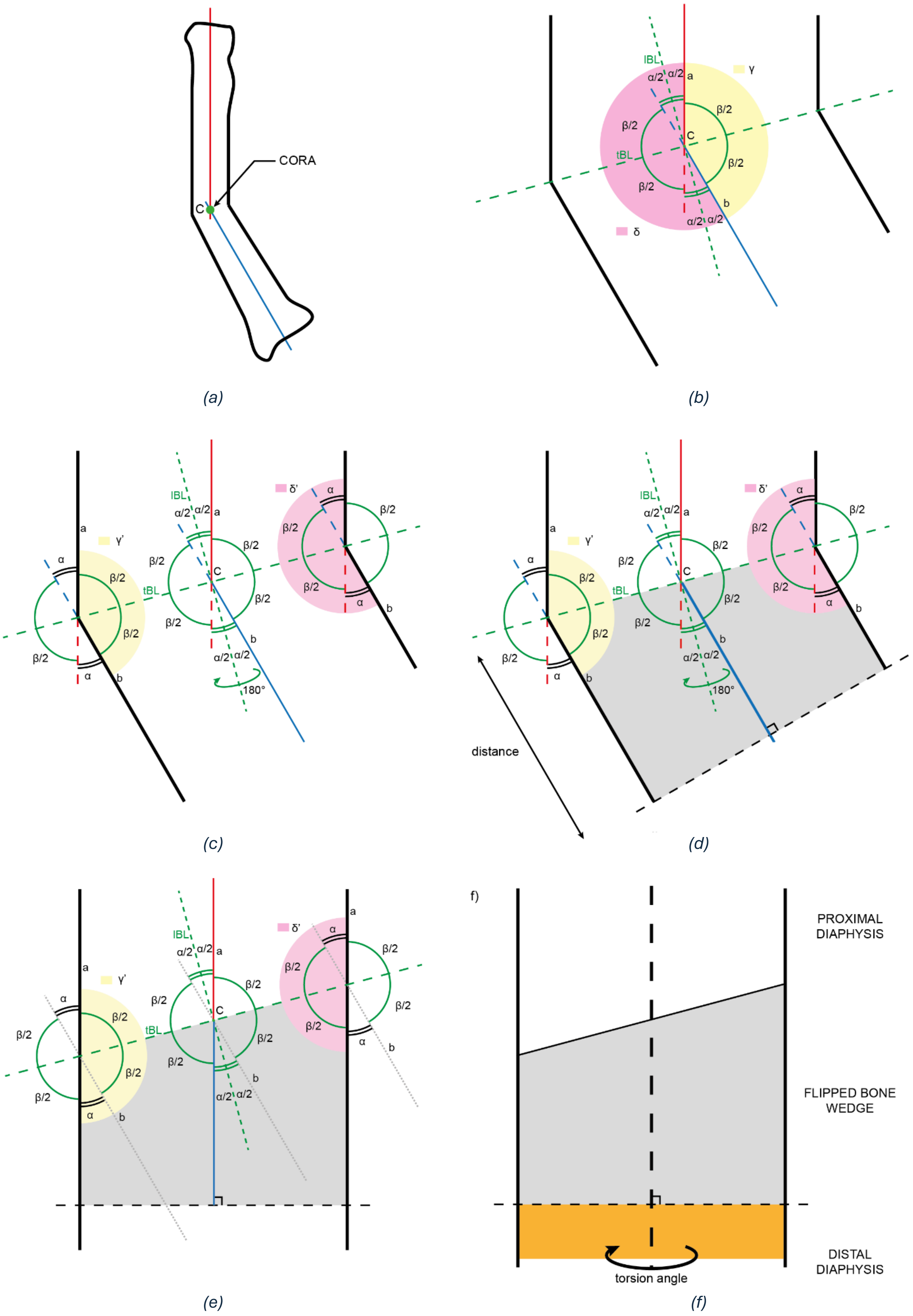

Figure 61. Schematic representation of the flipping-wedge osteotomy and its geometric rationale: (a) Deformed radius sectioned along the plane of maximum deformity, with proximal (red) and distal (blue) axes intersecting at the CORA; (b) identification of the angular deformity (α), its supplementary angle (β), and construction of the longitudinal (lBL) and transverse bisector lines (tBL) (dotted lines); concavity (γ) and convexity (δ) angles are highlighted in yellow and pink; (c) correspondence between γ and δ and the concave/convex bone contours; (d) definition of the bone wedge (grey) between the tBL and a line perpendicular to axis b (black dotted line); (e) flipping the wedge 180° results in γ' and δ' = 180°, restoring alignment; (f) torsional correction is achieved by rotating the distal (orange) segment on the perpendicular plane.

Preoperative clinical and radiographic views of the distal forearm showing a severe angular deformity of the distal meta-diaphysis of the radius, for which this technique was developed, and the postoperative outcomes are presented in Figure 62 and 63.

The Flipping-Wedge Osteotomy presents several advantages and limitations that should be considered when selecting it as a correction strategy. Among its main advantages:

- Preservation of bone length: the final bone length remains unchanged. If a shortening is desired, a small cylindrical slice can be removed from one end of the segment.
- Combined angular and rotational correction: since one of the osteotomy cuts is perpendicular to the longitudinal axis, torsional adjustment can be performed in addition to angular correction.
- Conceptual applicability beyond VSP and 3D printing technologies: the technique can be planned and executed even in the absence of 3D modelling software or PSIs, provided that the MDP is accurately identified during preoperative assessment.
- Suitability for diaphyseal regions and intramedullary fixation: it offers a straight path for intramedullary nails, and the use of compression or Poller screws can ensure good stability and alignment.

Although applied in few cases and requiring further validation, the flipping-wedge osteotomy has proven to be a technique that enables accurate realignment while preserving bone length.

Figure 62. Clinical and radiographic appearance of the distal forearm. A severe angulation of the distal meta-diaphysis of the radius is visible in both anteroposterior and laterolateral projections.

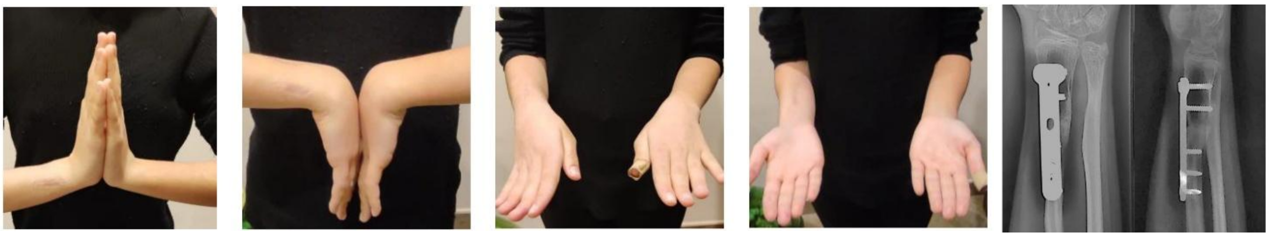

Figure 63. Postoperative clinical and radiographic images at 5-month follow-up following a Flipping Wedge Osteotomy, showing wrist and forearm range of motion and progressive consolidation at the osteotomy site.

3.2.2. Side-to-Side Flipping Wedge Osteotomy

The Side-to-Side Flipping Wedge Osteotomy represents a possible application of VSP, PSIs, and GSIs to correct multiple deformities in a single surgical procedure, using an autograft harvested from the contralateral deformity, thereby employing the graft from one correction, that is shaped a reoriented, to treat anther deformity if present [82]. It was developed to treat a case of windswept deformity, defined as the phenotypical presentation of concurrent varus and valgus deformities with variable localization and underlying pathologies [142], managed through a single-stage acute bilateral osteotomy. This innovative approach highlights how VSP, PSIs, and GSIs can serve as valuable resources for streamlining surgical procedures, fostering technical innovation, and promoting more rational use of bone grafts [2].

The approach involves a medial closing-wedge distal femoral osteotomy on the right side and a medial opening-wedge osteotomy on the left. The wedge removed from the valgus side was rotated 180° and used as a cortico-cancellous autograft on the varus side. The procedure was entirely planned through VSP, with 3D printed PSIs (also serving as GSIs) ensuring precise correction and optimal plate placement. In literature it was not possible to find any previous instances of a similar intervention, making it essential to conduct a simulation in a virtual environment to assess the feasibility of this novel procedure (Figure 64).

According to the osteotomy techniques described in Chapter 3, in the paragraph ‘Planning Deformity Correction’, the Side-to-Side Flipping Wedge Osteotomy, similarly to the Flipping Wedge Osteotomy, can be classified as an intercalary bone graft osteotomy utilizing a local bone graft. As in the previous case, fixation with an appropriate device is recommended.

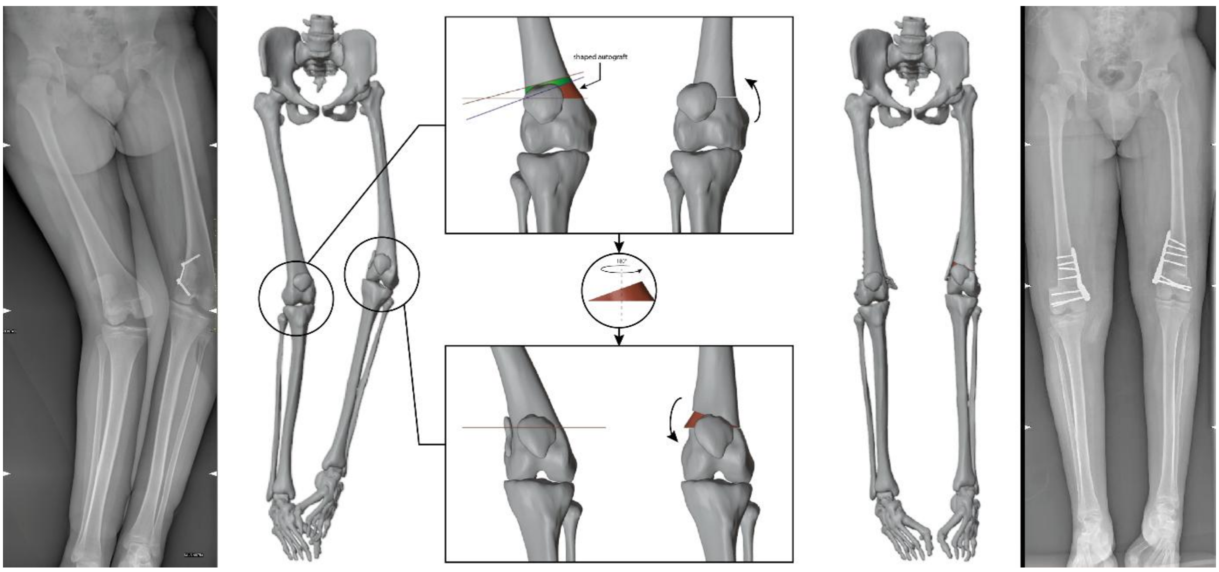

Figure 64. Planning process of valgus and varus correction, with shaping of the wedge removed from the right side to correct the valgus deformity (top central) and its rotated implantation on the left side to correct the varus deformity (bottom central). Preoperative (left) and postoperative (right) radiographs are also shown.

In this procedure, the PSIs and GSIs coincide. Specifically, the VSP enabled analysis of the required corrections and identification of the appropriate cutting planes, on which the surgical guides were consequently designed. In this case, the fist cutting guide was a GSI that was directly used on the patient (acting more like a PSI) to shape the graft, followed by a second PSI used to perform the actual corrective osteotomy. This approach was also feasible because of a slight pre-existing limb length discrepancy, with the right limb being marginally longer. By removing the graft and implanting it on the left side, followed by the corrective cut on the right side, this difference was effectively equalized. The use of the designed cutting guides is shown in Figure 65, 66 and 67.

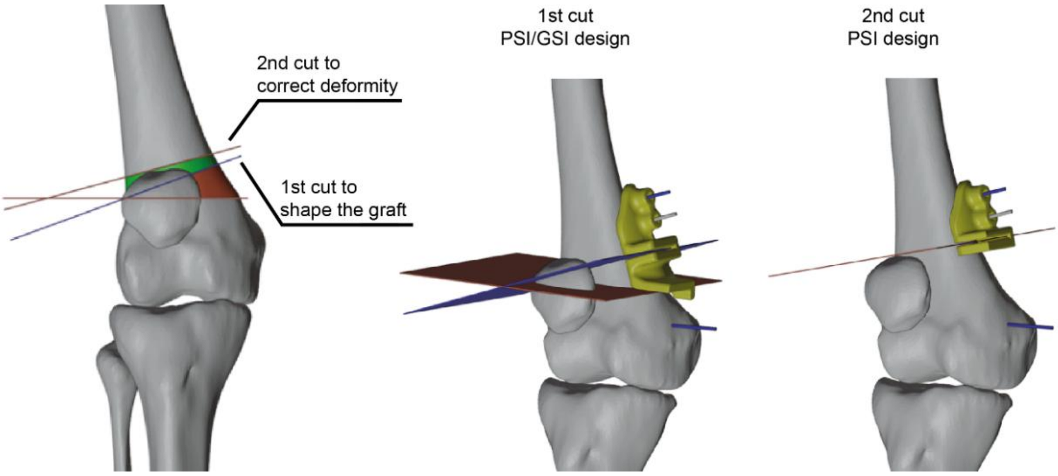

Figure 65. Planned osteotomy cuts for graft shaping and correction on the right side, illustrating the use of the PSI/GSI for graft shaping (blue plane) and the PSI for the corrective osteotomy (red plane).

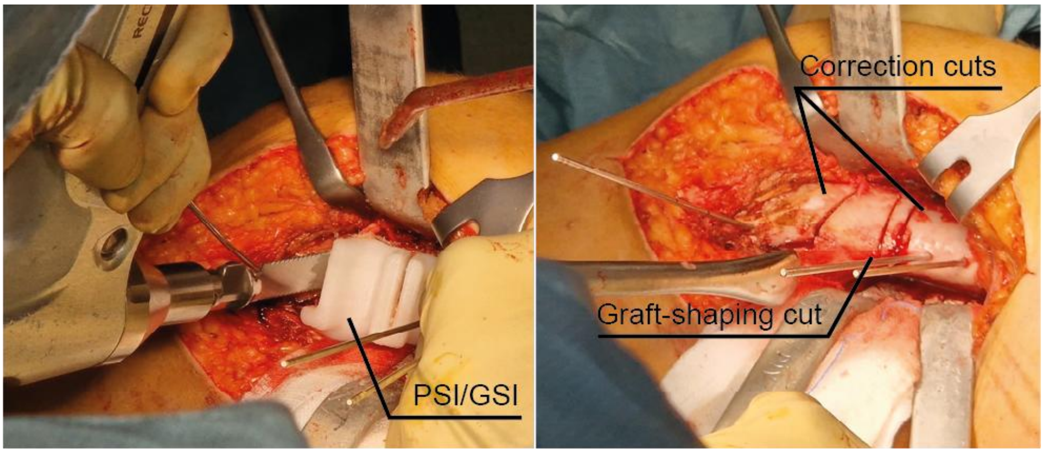

Figure 66. Intraoperative view showing the application of the PSI/GSI (left) and the resulting osteotomy cuts for deformity correction and autologous graft shaping (right) on the right femur.

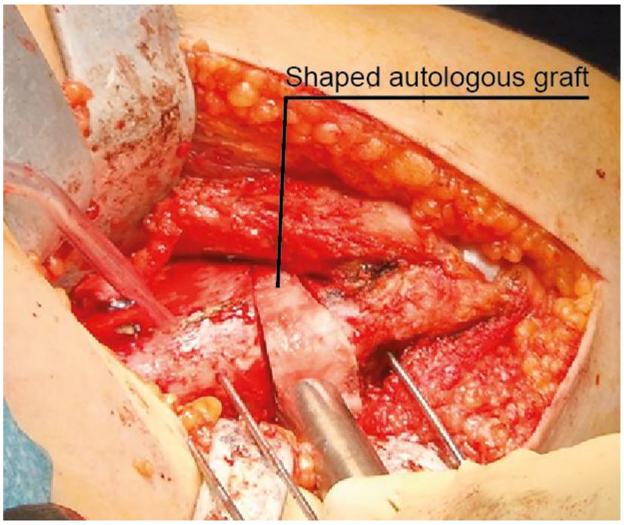

Figure 67. Intraoperative image showing the implantation of the shaped autologous bone graft to correct the left femur.

This case demonstrates how VSP and 3D printing can be effectively employed to simulate and plan innovative approaches for correcting windswept knee deformities, ensuring both feasibility and patient safety. To the best of our knowledge, this represents the first reported case of a child with windswept deformity treated through simultaneous corrective osteotomy of both knees.

Although this is a highly specific and difficult-to-replicate application, the Side-to-Side Flipping Wedge Osteotomy represents a methodological example of how VSP and 3D printed cutting guides can enable precise deformity correction while optimizing biological integration and surgical efficiency. By exploiting one correction to generate an autograft for the contralateral side, this approach allows multiple deformities to be treated within a single procedure using the patient's own bone, which is the gold standard for grafting. Although originally conceived for this specific type of deformity, the same methodological principle could be potentially extended to other scenarios, promoting more efficient and biologically sustainable surgical strategies.

4. 3D PRINTING AND DESIGN PROCESS OPTIMIZATION

The 3D printing and design process plays a central role in ensuring the dimensional accuracy and functional reliability of patient-specific cutting guides. In clinical applications, geometrical distortions induced by manufacturing and post-processing steps cannot always be completely eliminated, particularly in the case of custom-made devices, where geometrical variability is intrinsic. Addressing these effects requires a combined approach, acting both on process parameters for specific guide configurations and on design-stage adjustments to compensate for predictable dimensional variations.

The two experiments presented in this section were guided by two main hypotheses. First, it was assumed that optimizing printing parameters could reduce residual stresses generated during FDM fabrication, thereby limiting stress release and associated distortion during thermal annealing. This aspect is particularly relevant to ensure reliable manufacturing also for larger PSIs/GSIs, as required in oncological resections. Second, it was hypothesized that once a stable manufacturing process is defined, specific design features, particularly pin-hole geometry, exhibit a systematic and measurable behaviour, which can be characterized and exploited to obtain controlled final dimensional outcomes.

Overall, these studies represent initial steps within a broader research framework aimed at establishing evidence-based design and printing guidelines. By addressing selected aspects of the 3D printing and design workflow, they support the progressive definition of robust and clinically applicable processes.

4.1. Reducing Deformation in 3D Printing

After an initial surge of interest in applying these technologies to orthopaedic paediatric patients undergoing surgical treatment for bone deformities, attention gradually expanded to their use in surgeries for paediatric bone tumour resections. In such cases, tumour removal often requires the resection of large bone segments, which are subsequently replaced with a metal implant or prothesis, or more frequently an equally large allograft obtained from a donor through the bone tissue bank. This context may generate the need to plan, design, and manufacture larger PSIs and GSIs than those typically produced.

The established manufacturing workflow, comprising CAD design, STL export, slicing, HTPLA 3D printing, annealing, and sterilization, has generally proven effective, but some limitations emerged, particularly during the annealing step. This process, essential for enhancing thermal and mechanical properties, promoting recrystallization, and ensuring resistance to sterilization, was observed to cause substantial deformation in certain cases. One possible explanation is that with larger components, the scale of deformation may increase, as the recrystallization process releases internal stresses retained during solidification, resulting in visible distortions.

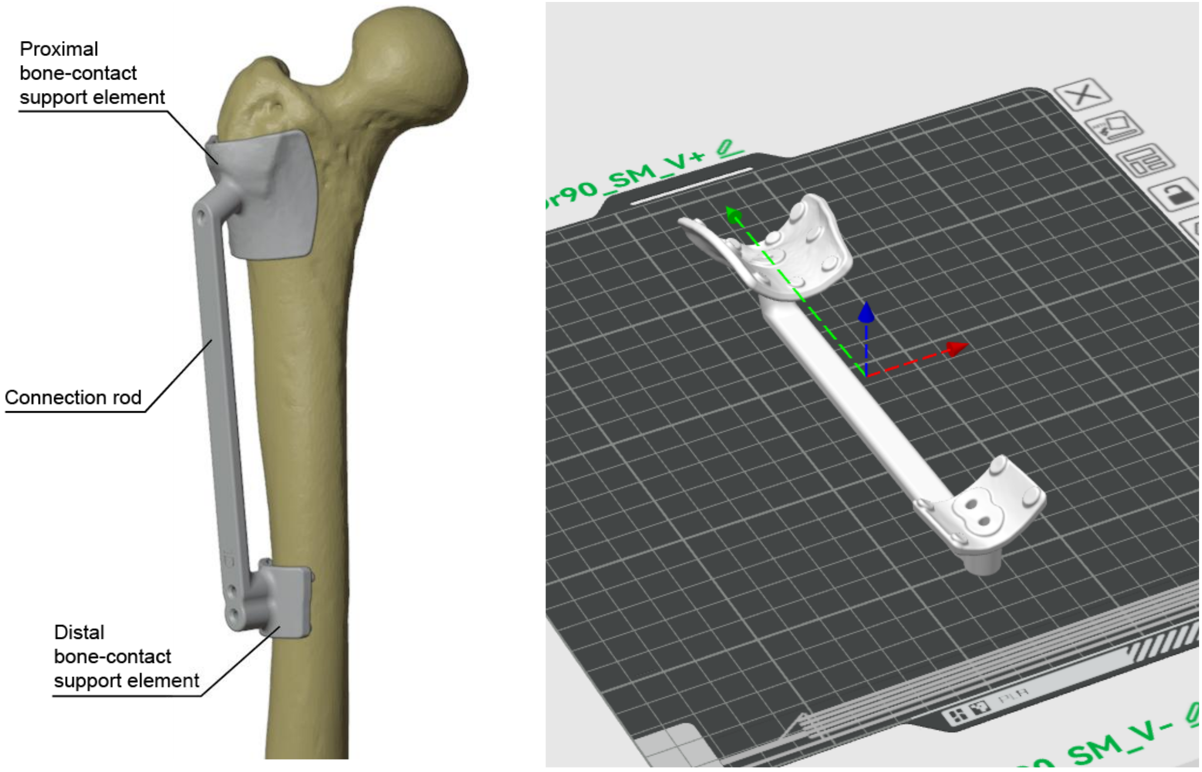

(a) *(b)*

Figure 68. The cutting guide selected for the experiment. (a) Cutting guide and its features; (b) Print bed orientation of the cutting guide, designed to prevent the use of support structures on the bone-contacting surface, the arrow represents the reference system x, y and z (red, green and blue respectively).

The CAD model used in this experiment was a cutting guide designed for a bone resection procedure with a total length of 142 mm. It was selected due to its unusually large dimensions, an uncommon feature in paediatric orthopedics deformity corrections, where guides are typically smaller and, to date, have not shown significant deformation. Its length and bone contact support elements, however, led to considerable warping, which motivated a more in-depth investigation. The guide featured lateral extensions for support and bone contact, connected by a central rod (Figure 68a).

For this study, the basic printing parameters previously described, as well as the guide's orientation on the print bed, were kept consistent across all samples. The guide was positioned centrally on the print bed with its largest flat surface facing downward. This orientation, defined during the design phase, ensured that the bone-contacting surface faced upward as usual, thereby eliminating the need for support structures and minimizing the risk of dimensional inaccuracies (Figure 68b).

Accordingly, the focus of this work was not focused on the design process itself, which remains highly case-specific and cannot be fully standardized, but rather on the evaluation of additional printing parameters, tailored to our in-house workflow, whose influence on deformation has not yet been fully understood. This study therefore aimed to answer two main research questions: What effect do printing parameters have on the deformation of cutting guides after annealing? And is there an optimal parameter combination capable of minimizing geometric deformation to ensure reproducible and reliable outcomes, even for larger geometries?

4.1.1. Design of the Experiment

For this experiment, a factorial design was chosen to investigate the effects of multiple factors simultaneously. This approach evaluates all possible combinations of factor levels, enabling the analysis of both main isolated effects and their interactions. A main effect is the change in response produced by a change in a factor's level, while an interaction occurs when the effect of one factor depends on the level of another [143].

Four factors were selected and tested at two levels ("high" and "low") (Figure 69) to investigate both their individual effects and their interaction: raft thickness, infill pattern orientation, first-layer surface pattern, and cooling fan speed.

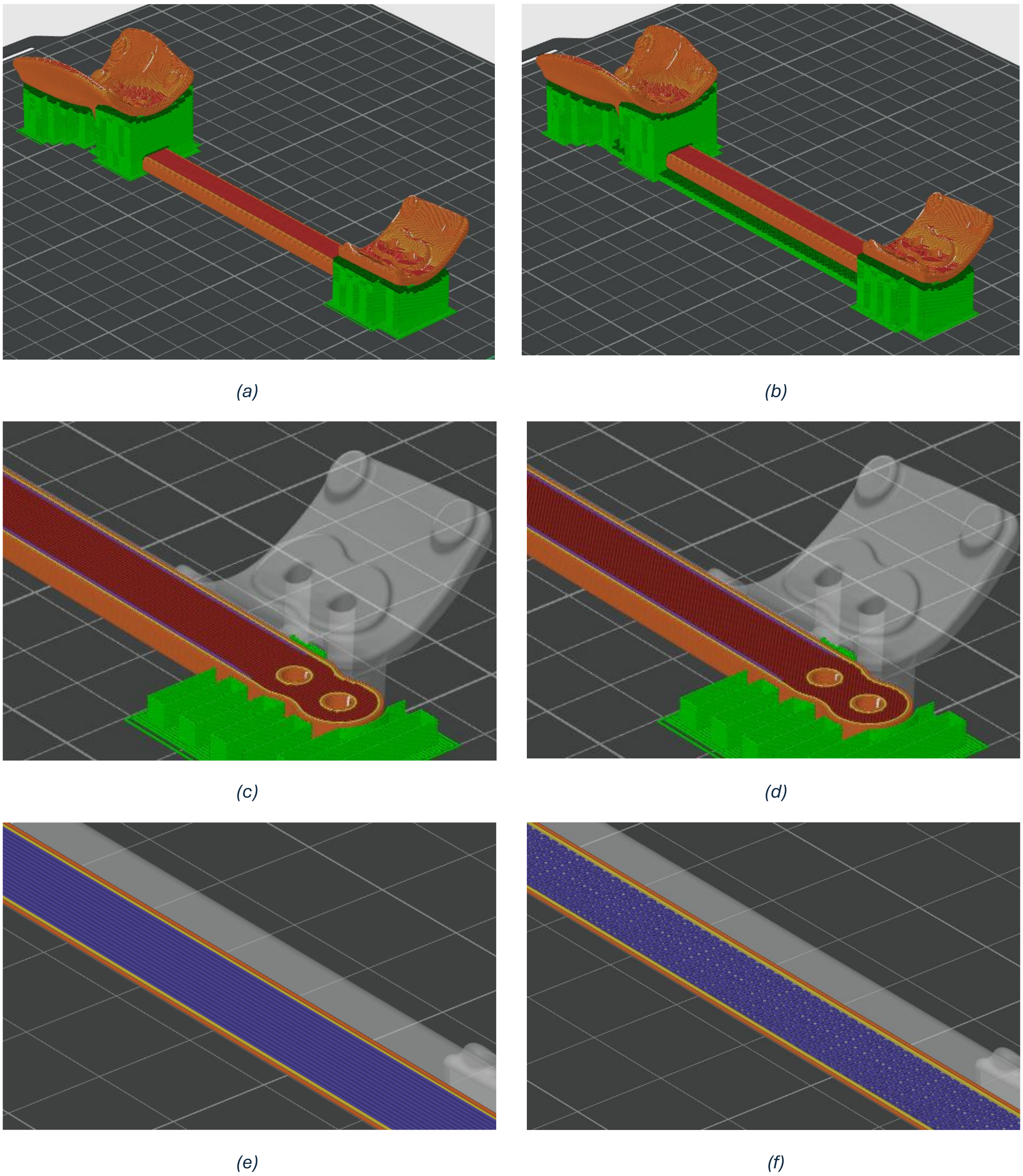

Figure 69. Representative examples of the selected factor levels: raft thickness at 0 (a) and 6 (b) layers, infill pattern at 90° (c) and 45° (d), and first-layer pattern with monotonic (e) and Hilbert curve (f) configurations.

- Raft thickness was included as it is hypothesized to act as a mechanical constraint during annealing, to preserve the geometry by resisting deformation. Two conditions were tested: 0 layers (absence of raft) and 6 layers (presence of raft) (Figure 69a and 69b);
- Infill pattern orientation was selected based on the assumption that different internal geometries influence the distribution of residual stresses during cooling. These stresses are later released during annealing, potentially affecting the final shape. Two orientations were tested: 90° and 45° relative to the longitudinal axis of the cutting guide (Figure 69c and 69d);
- First-layer pattern was included to evaluate whether changing the default monotonic infill to a slower, more intricate deposition path (Hilbert curve) affects residual stress accumulation (Figure 69e and 69f);
- Fan speed was varied to assess its impact on the cooling rate during deposition, which may in turn influence internal stresses. To determine the levels to be tested, five preliminary specimens were printed using the standard process while varying the fan speed (0%, 25%, 50%, 75%, 100%). At 0% fan speed, removing the printing supports has proven to be very difficult; therefore, the lower level was set at 25%. Accordingly, two levels were selected for investigation: 25% and 100% fan power.

The experiment was designed as a 2^4 factorial experiment with a single replicate, and the runs were randomized. The complete factor settings and experimental runs are reported in Tables 6 and 7.

Table 6. Values of the high and low levels for the four factor tested.

Factor		Levels	
		Low (-)	High (+)
Raft thickness (layers)	A	0	6
Infill pattern (°)	B	45°	90°
First-layer pattern (type)	C	M (Monotonic)	H (Hilbert curve)
Fan speed (%)	D	25%	100%

4.1.2. Measurements

The experiment was carried out by comparing the values of the original CAD model with those of the specimens treated prior to sterilization. All 16 specimens were 3D printed using the Bambu Lab X1 Carbon printer (Shenzhen, China) following the randomized order defined by the experimental design matrix (Table 7). They were then subjected to the annealing process described above. After thermal treatment, the specimens were cleaned from all supports (Figure 70) and scanned using a FARO Quantum S arm (with a non-contact accuracy of ± 0,043 mm) in combination with Geomagic Design X to generate STL files for each sample. These files were subsequently analysed by comparing them to the original CAD model.

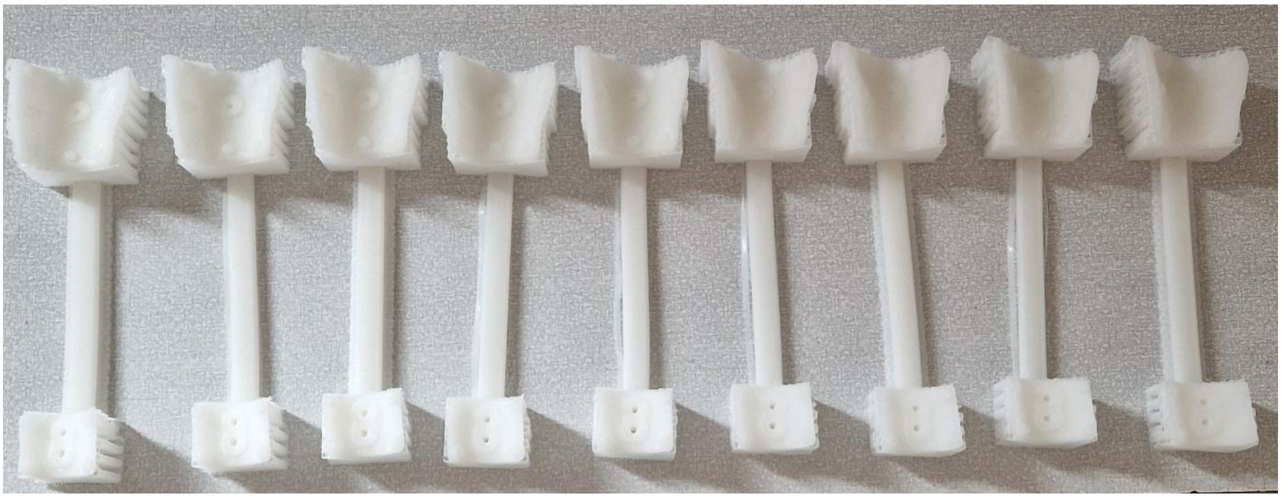

Figure 70. Some of the specimens after printing, annealing, and support removal, ready for scanning.

Deformation analysis was conducted using 3D distance maps generated in Geomagic Control X (Oqton, San Francisco, California) by comparing the original CAD model with the STL files of the 3D printed specimens (Figure 70), complemented by the evaluation of 2D cross-sections along predefined planes: plane A, parallel to the printing bed and intersecting the connecting rod at its mid-height (xy-plane), and plane B, longitudinal and aligned with the cutting guide at the midpoint of the connecting rod (yz-plane) (Figure 71 and 72).

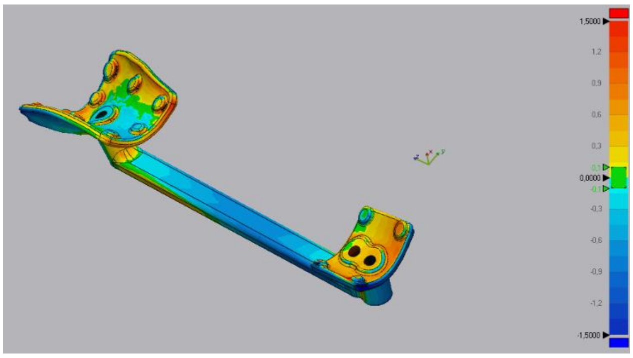

Figure 71. 3D distance map of the STL model of specimen no.1 (0 raft layers, a 45° infill pattern, monotonic first-layer pattern, and a fan speed of 25%) compared with the original CAD geometry for deformation assessment.

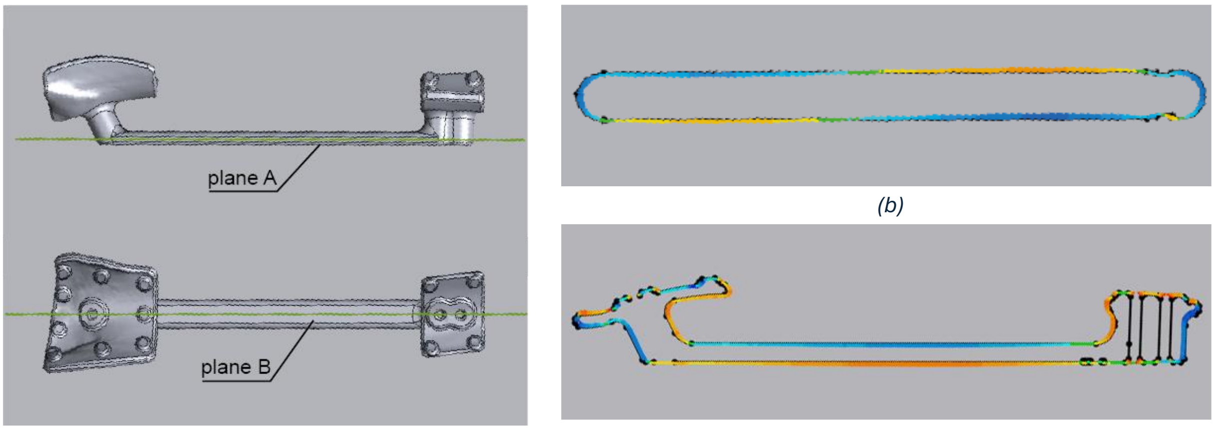

(a) (c)

Figure 72. (a) 3D model showing the planes used for 2D cross-sectional deformation analysis; Representative 2D cross-sectional comparison between the STL model of specimen no. 1 (0 raft layers, 45° infill pattern, monotonic first-layer pattern, fan speed 25%) and the original CAD on planes A (b) and B (c): positive deformation is shown in orange/yellow, while negative deformation is shown in blue/light blue, calculated as point-to-surface distance along surface normals.

The analysed parameters included 3D deformation, deformation on Plane A, and deformation on Plane B. For each parameter, the standard deviation was considered to ensure the detection of actual variations that could not be captured by the mean value alone.

Given the screening objective of identifying the factors influencing deformation, an exploratory data analysis was first conducted, followed by an ANOVA (Analysis of Variance) limited to main effects. A p-value below 0.05 was considered indicative of statistical significance.

Table 7. Design matrix of the experiments, including randomized run order and corresponding response values (in mm). 3d_dev: standard deviation of the 3D distance map comparison; plA_dev: standard deviation of the 2D comparison performed on plane A; plB_dev: standard deviation of the 2D comparison performed on plane B.

Standard Order	Run Order	A	B	C	D	3d_dev	plA_dev	plB_dev
1	1	-	-	-	-	0.63	0.35	0.70
2	7	+	-	-	-	0.47	0.21	0.60
3	10	-	+	-	-	0.48	0.34	0.44
4	6	+	+	-	-	0.65	0.39	0.51
5	15	-	-	+	-	0.59	0.24	0.60
6	11	+	-	+	-	0.55	0.31	0.66
7	5	-	+	+	-	0.56	0.48	0.65
8	4	+	+	+	-	0.54	0.43	0.61
9	9	-	-	-	+	0.82	0.35	0.75
10	3	+	-	-	+	0.80	0.36	0.77
11	8	-	+	-	+	0.61	0.48	0.70
12	13	+	+	-	+	0.53	0.48	0.58
13	14	-	-	+	+	0.65	0.37	0.75
14	12	+	-	+	+	0.84	0.29	0.70
15	16	-	+	+	+	0.57	0.34	0.62
16	2	+	+	+	+	0.83	0.54	1.05

4.1.3. Preliminary results of the Experiment

With four factors varied at two levels, the collected data (Table 7) were initially analysed using a 2^4 factorial design with a single replicate (16 samples in total), given the screening objective of the experiment. To identify the main effects influencing the responses, half-normal probability plots of the effect estimates were constructed (Figure 73, 74 and 75), and the contribution rates of each term to the responses are summarized in Table 8.

Table 8. *Contribution of the main terms for each response (the remaining percentage values corresponded to interaction effects, which were excluded from this preliminary investigation).*

	3d_dev (%)	plA_dev (%)	plB_dev (%)
(A) Raft thickness (layers)	2.57	0.17	**1.68***
(B) Infill pattern (°)	9.09	50.92	3.04
(C) First-layer pattern	**0.41***	**0.14***	7.78
(D) Fan speed (%)	36.72	10.97	30.53

**Values in bold highlight the factors with the lowest contribution.*

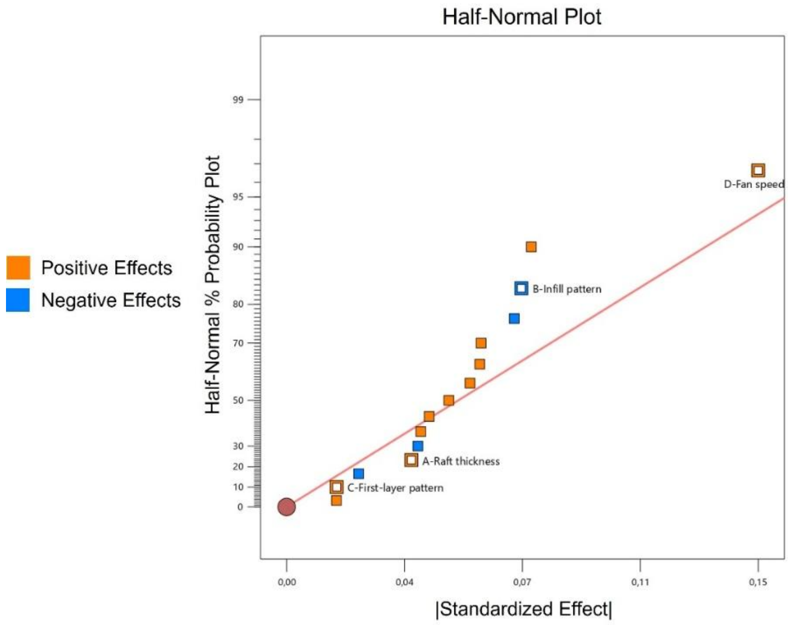

Figure 73. Half-normal probability plots for the 3d_dev response of the effects for the 2^4 factorial design (positive effect in orange, negative effect in blue), with the four main factors highlighted.

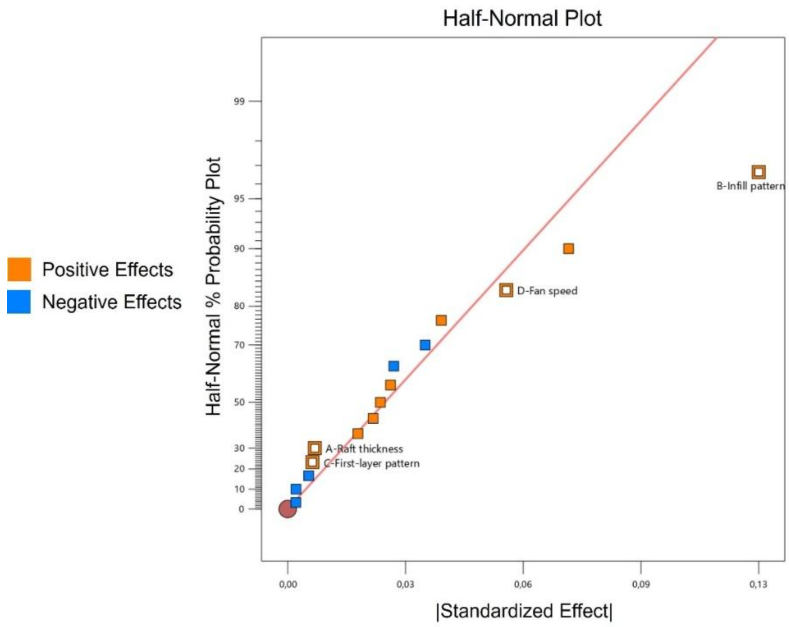

Figure 74. Half-normal probability plots for the plA_dev response of the effects for the 2^4 factorial design (positive effect in orange, negative effect in blue), with the four main factors highlighted.

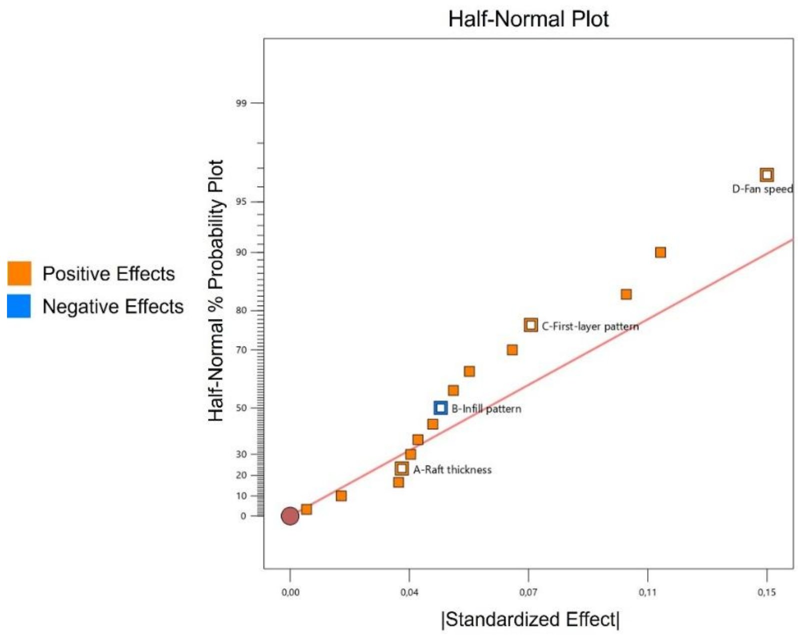

Figure 75. Half-normal probability plots for the plB_dev response of the effects for the 2^4 factorial design (positive effect in orange, negative effect in blue), with the four main factors highlighted.

The normal probability plots of the effects for each analysed response are shown in Figure 73, 74 and 75. Effects lying close to the interpolation line can be considered negligible, whereas large effects deviate markedly from it. The plots indicate that fan speed exerts the greatest influence on both the overall 3D deformation and the deformation observed on cross-sectional Plane B. In contrast, deformation on Plane A is mainly affected by the infill pattern, while raft thickness and first-layer pattern show negligible impact on the responses.

For the 3D deformation, the lowest value of standard deviation was 0.47 mm, while the highest was 0.83 mm, which corresponds respectively to standard order specimen no.2 (raft thickness layer=6; infill pattern degree=45, first layer pattern=M and fan speed percentage=25) and no.14 (raft thickness layer=6; infill pattern degree=45, first layer pat-tern=H and fan speed percentage=100). For the deformation on plane A, the lowest value of standard deviation was 0.21 mm, while the highest was 0.54 mm, which corresponds respectively to standard order no.2 (raft thickness layer=6; infill pattern degree=45, first layer pattern=M and fan speed percentage=25) and no.16 (raft thickness layer=6; infill pattern degree=90, first layer pattern=H and fan speed percentage=100). For the deformation on plane B, the lowest value of standard deviation was 0.44 mm, while the highest was 1.05 mm, which corresponds respectively to standard order specimens no.3 (raft thickness layer=0; infill pattern degree=90, first layer pattern=M and fan speed percentage=25) and no.16 (raft thickness layer=6; infill pattern degree=90, first layer pattern=H and fan speed percentage=100). Overall, the highest deformation is visible in plane B. The specimens are illustrated in Figure 76 and 77.

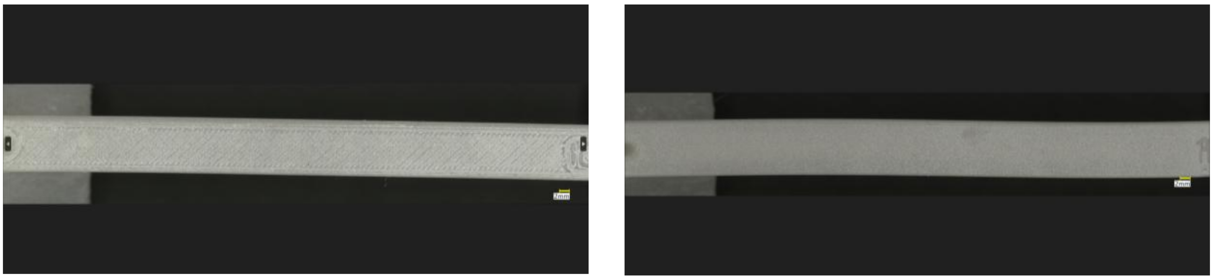

(a) (b)

Figure 76. Specimen no. 2 (a), which exhibited the lowest deformation in both the overall 3D deformation and on Plane A, and specimen no. 3 (b), which showed the lowest deformation on Plane B.

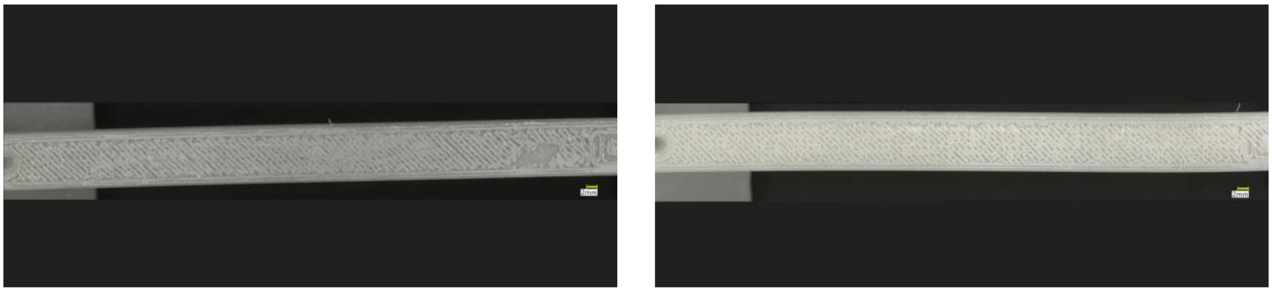

(a) (b)

Figure 77. Specimen no. 14 (a), which exhibited the highest overall 3D deformation, and specimen no. 16 (b), which showed the highest deformation on both Plane A and Plane B.

These data show that plane B experienced the highest deformation, indicating that this plane is more sensitive to shape modifications. Both the 3D deformation and plane A exhibited the lowest deformation in specimen no. 2 from the standard order, which aligns with the initial assumption derived from graphical analysis: lower fan speed and a lower infill percentage result in reduced deformation. The highest standard deviation for 3D deformation was observed in specimen no. 14, which also had a higher fan speed, this agrees with the overall findings. The highest deformation value for both plane A and plane B was found in specimen no. 16, which is consistent with the graphical analysis, showing a 90° infill pattern for plane A and a higher fan speed for plane B. Plane B exhibited its lowest deformation in specimen no. 3, which was printed with a lower fan speed. Clinically, the different sensitivity of the analysed planes suggests that shape modifications may affect surgical references in distinct ways: deformations on plane B may induce convergent or divergent tilting of the references, whereas deformations on plane A may primarily impact rotational alignment.

4.1.4. Projection into a 2^3 design

Since the first-layer pattern was non-significant for all analysed results and showed the lowest percentage contribution across most responses, it was excluded from the experiment. The design was thus reduced to a 2^3 factorial with two replicates for the factors raft thickness, infill pattern, and fan speed, allowing for the estimation of experimental error and the application of ANOVA. The three factors were renamed accordingly to perform the analysis (Table 9).

Table 9. Values of the high and low levels of the renamed three factors.

Factor	Levels	
	Low (-)	High (+)

Raft thickness (layers)	A	0	6
Infill pattern (°)	B	45°	90°
Fan speed (%)	C	25%	100%

The revised half-normal probability plot for the 2^3 design validated the results obtained in the previous analysis (Figure 78, 79 and 80). The main factors with a positive effect on deformation are the infill pattern orientation and the fan speed. This indicates that higher infill orientation angles and increased fan speed lead to greater deformation.

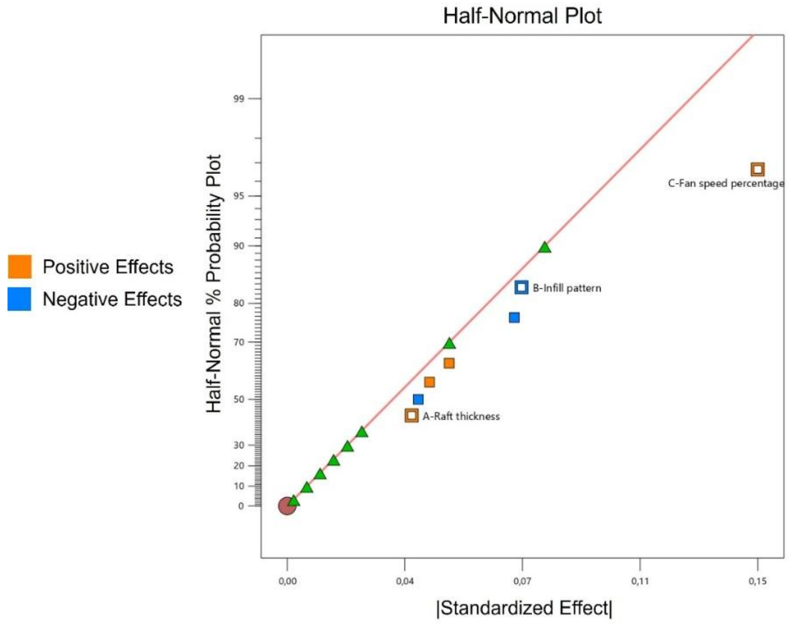

Figure 78. Half-normal probability plots for the 3d_dev response of the effects for the 2^3 factorial design (positive effect in orange, negative effect in blue), with the four main factors highlighted.

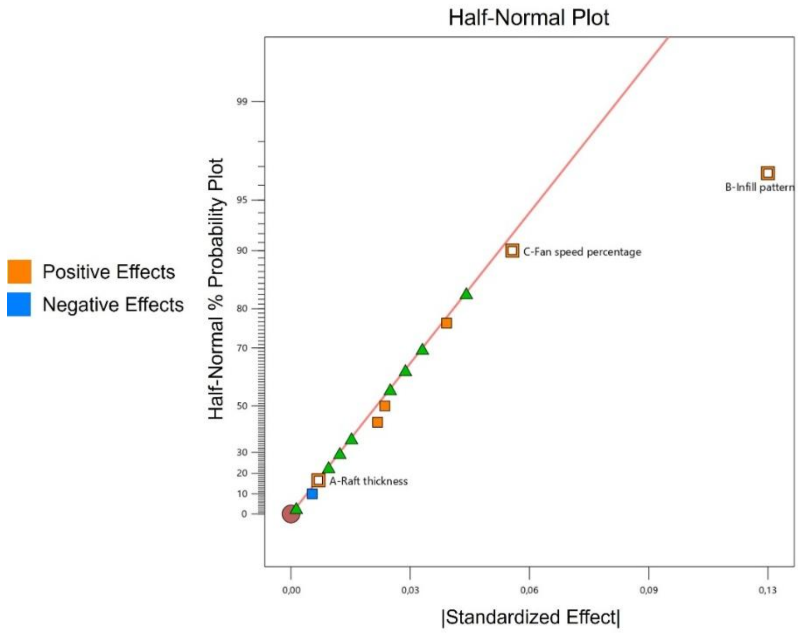

Figure 79. Half-normal probability plots for the plA_dev response of the effects for the 2^3 factorial design (positive effect in orange, negative effect in blue), with the four main factors highlighted.

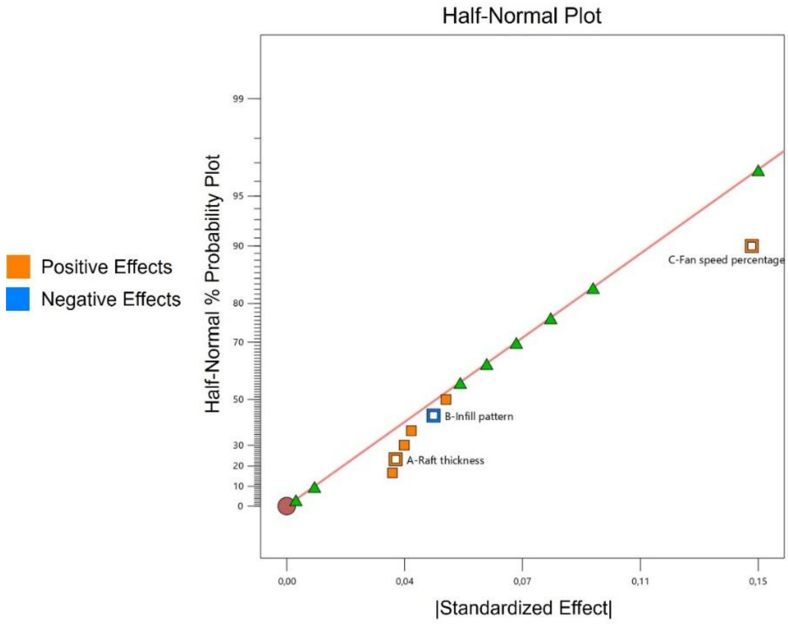

Figure 80. Half-normal probability plots for the plB_dev response of the effects for the 2^3 factorial design (positive effect in orange, negative effect in blue), with the four main factors highlighted.

The ANOVA results show that fan speed and infill pattern have significant main effects, respectively on the 3D deformation and the 2D deformation of plane A. In contrast, plane B does not exhibit any significant factors, and the model itself is not statistically significant. No interaction effects are significant (Tables 10–12).

Table 10. ANOVA analysis for the 3d_dev response.

	Sum of Squares	df	Mean Square	F-value	p-value
Model	0.1581	7	0.0226	2.37	0.1245
A-Raft thickness	0.0060	1	0.0060	0.6330	0.4492
B-Infill pattern	0.0213	1	0.0213	2.24	0.1730
C-Fan speed percentage	0.0860	1	0.0860	9.04	**0.0169***
AB	0.0079	1	0.0079	0.8269	0.3897
AC	0.0102	1	0.0102	1.07	0.3312
BC	0.0200	1	0.0200	2.11	0.1848
ABC	0.0067	1	0.0067	0.7008	0.4268
Pure Error	0.0762	8	0.0095		
Cor Total	0.2343	15			

**Values in bold with an asterisk highlight the factors that are statistically significant ($p < 0.05$)*

Table 11. ANOVA analysis for the plA_dev response.

	Sum of Squares	df	Mean Square	F-value	p-value
Model	0.0889	7	0.0127	2.83	0.0843
A-Raft thickness	0.0002	1	0.0002	0.0470	0.8338
B-Infill pattern	0.0636	1	0.0636	14.15	**0.0055***
C-Fan speed percentage	0.0137	1	0.0137	3.05	0.1189
AB	0.0068	1	0.0068	1.51	0.2547
AC	0.0021	1	0.0021	0.4655	0.5143
BC	0.0001	1	0.0001	0.0283	0.8706
ABC	0.0025	1	0.0025	0.5483	0.4802
Pure Error	0.0359	8	0.0045		
Cor Total	0.1248	15			

**Values in bold with an asterisk highlight the factors that are statistically significant (p < 0.05)*

Table 12. ANOVA analysis for the plB_dev response.

	Sum of Squares	df	Mean Square	F-value	p-value
Model	0.1228	7	0.0175	0.9183	0.5382
A-Raft thickness	0.0046	1	0.0046	0.2417	0.6362
B-Infill pattern	0.0084	1	0.0084	0.4393	0.5261
C-Fan speed percentage	0.0841	1	0.0841	4.40	0.0691
AB	0.0099	1	0.0099	0.5168	0.4927
AC	0.0054	1	0.0054	0.2813	0.6103
BC	0.0060	1	0.0060	0.3165	0.5891
ABC	0.0044	1	0.0044	0.2281	0.6457
Pure Error	0.1528	8	0.0191		
Cor Total	0.2756	15			

**Values in bold with an asterisk highlight the factors that are statistically significant (p < 0.05)*

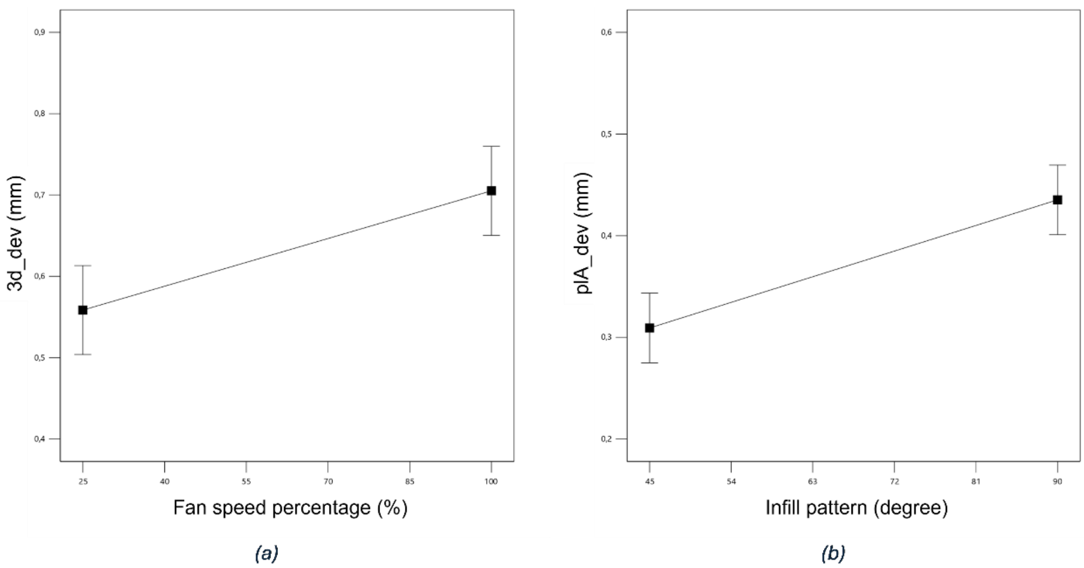

Figure 81. (a) Main effect plot for the fan speed for 3d_dev response; (b) Main effect plot for the infill pattern for plA_dev response.

The graphical representation of the main effects shows that lower deformation is achieved with the fan speed set at its lowest value (25%) and with a 45° infill pattern (Figure 81).

However, the ANOVA for the 3D_dev response yielded a non-significant model p-value ($p = 0.1245$). When the analysis was recalculated excluding raft thickness, which appeared non-significant, the resulting simplified model became significant for both overall 3D deformation ($p = 0.0206$) and deformation on Plane A ($p = 0.0073$). The lack-of-fit test was non-significant ($p = 0.5537$ and $p = 0.6479$), indicating a good representation of the data, while Plane B remained non-significant (Tables 13–15)

Table 13. Recalculated ANOVA without the raft-thickness factor for the 3D_dev response.

Source	Sum of Squares	df	Mean Square	F-value	p-value
Model	0.1274	3	0.0425	4.77	**0.0206***
B-Infill pattern	0.0213	1	0.0213	2.39	0.1479
C-Fan speed percentage	0.0860	1	0.0860	9.66	**0.0091***
BC	0.0200	1	0.0200	2.25	0.1595
Residual	0.1069	12	0.0089		
Lack of Fit	0.0308	4	0.0077	0.8077	0.5537
Pure Error	0.0762	8	0.0095		
Cor Total	0.2343	15			

**Values in bold with an asterisk highlight the factors that are statistically significant ($p < 0.05$)*

Table 14. Recalculated ANOVA without the raft-thickness factor for the plA_dev response.

Source	Sum of Squares	df	Mean Square	F-value	p-value
Model	0.0774	3	0.0258	6.52	**0.0073***
B-Infill pattern	0.0636	1	0.0636	16.07	**0.0017***
C-Fan speed percentage	0.0137	1	0.0137	3.46	0.0874
BC	0.0001	1	0.0001	0.0321	0.8607
Residual	0.0475	12	0.0040		
Lack of Fit	0.0115	4	0.0029	0.6416	0.6479
Pure Error	0.0359	8	0.0045		
Cor Total	0.1248	15			

**Values in bold with an asterisk highlight the factors that are statistically significant ($p < 0.05$)*

Table 15. Recalculated ANOVA without the raft-thickness factor for the plB_dev response.

Source	Sum of Squares	df	Mean Square	F-value	p-value
Model	0.0986	3	0.0329	2.23	0.1376
B-Infill pattern	0.0084	1	0.0084	0.5688	0.4653
C-Fan speed percentage	0.0841	1	0.0841	5.70	0.0343
BC	0.0060	1	0.0060	0.4098	0.5341
Residual	0.1770	12	0.0148		
Lack of Fit	0.0242	4	0.0061	0.3170	0.8590
Pure Error	0.1528	8	0.0191		
Cor Total	0.2756	15			

**Values in bold with an asterisk highlight the factors that are statistically significant ($p < 0.05$)*

The analysis indicates that only the main effects, infill pattern and fan speed, contribute significantly to the overall 3D deformation and to deformation on Plane A, whereas interaction terms do not provide meaningful explanatory power and can therefore be excluded from the model. Deformation on Plane B is not significantly explained by these factors.

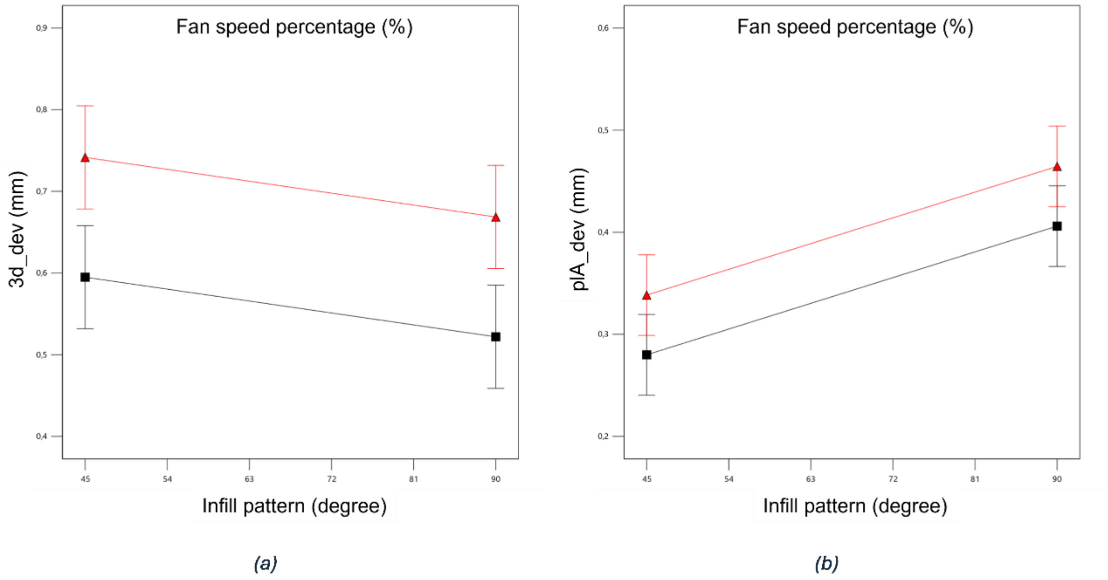

Figure 82. (a) Main effect plot of fan speed for the 3D_dev response; (b) Main effect plot of infill pattern for the plA_dev response. The red line represents high fan speed (100%), while the black line represents low fan speed (25%).

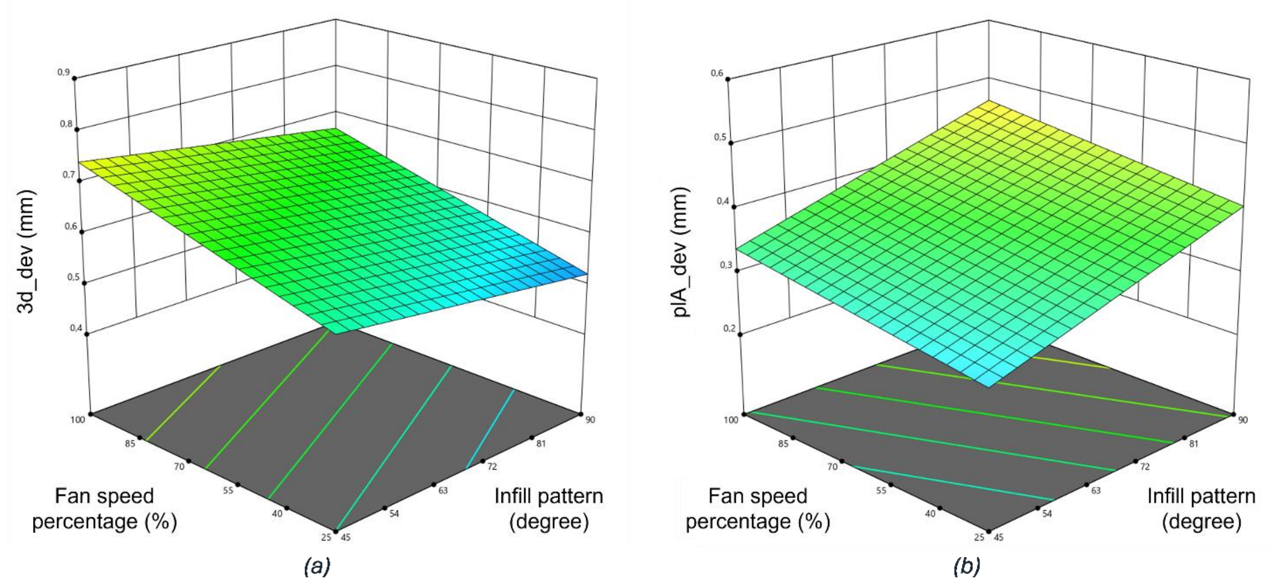

Figure 83. (a) 3D response surface plot for the 3D_dev response; (b) 3D response surface plot of infill pattern for the plA_dev response. Yellow/red areas indicate higher deformation at that point, whereas light blue/blue areas indicate lower deformation.

Finally, from the results and the graphs (Figures 82 and 83), it can be stated with confidence that minimizing overall 3D deformation requires setting the fan speed to its lowest value during printing (even though it is not significant according to the results for Plane A). The effect of the infill pattern, however, appears less straightforward. For deformation on Plane A, the lowest values were observed at 45°, whereas the 3D_dev response showed the lowest deformation at 90°. This apparent contradiction may be explained by the alignment of the 90° linear infill with the vertical connecting rod, which creates longer continuous lines on Plane A. These lines accumulate greater tension during annealing, as their orientation favours stress concentration along the rod. Moreover, during deposition, the longer lines, spanning the entire length of the rod, may cool more rapidly when laid adjacent to one another, since neighbouring lines are already cold, thereby inducing lateral adhesion stresses reflected on Plane A (xy-plane).

Altogether, these findings suggest that the observed differences between 45° and 90° infill orientations result from a complex interplay of geometric alignment, thermal gradients, and stress release during annealing.

While the most robust evidence concerns the reduction of overall 3D deformation at lower fan speeds, the present dataset was likely insufficient to capture the full complexity of the response. This indicates the need for further research with additional factor levels to account for possible non-linear effects, greater statistical power, and more replicates to better characterize experimental variability and strengthen the statistical significance of the model terms. Moreover, other parameters not investigated here (such as infill geometry rather than orientation, the number of walls, etc.) may also play an important role. Therefore, even though the current results are significant, these should be regarded as a starting point for future studies aimed at process optimization.

4.1.5. Discussion

In oncological resections, surgical guides are often bulkier and require larger material volumes than those used for standard deformity corrections, which increases their susceptibility to deformation during thermal post-processing. This experiment was therefore designed to evaluate whether printing parameter optimization can improve dimensional stability after annealing and minimize final geometric distortion.

Literature clearly shows that the mechanical performance and dimensional accuracy of FDM parts are strongly influenced by process parameters, including printing speed, extrusion and bed temperatures, infill density and pattern, and layer settings [144]. Furthermore, the strength of 3D printed components is inherently anisotropic, with its extent largely determined by the selected process parameters [145–148].

Due to rapid heating and cooling during extrusion, FDM is prone to internal stresses, shrinkage, weak interlayer adhesion, and voids, often requiring post-processing to improve part quality [149,150]. Among available techniques, annealing is particularly effective. By increasing crystallinity, it reduces internal stresses, improves interlayer adhesion, and enhances mechanical properties [151–154]. Its effects vary with polymer type: in ABS, quality improves mainly through material reflow and gap filling, while in PLA, flexural strength increases with higher crystallinity, depending on annealing temperature and heating/cooling cycles [155,156]. Annealing can alter the dimensional tolerances of FDM parts, so shrinkage and expansion must be considered during design [157].

In medical applications, steam sterilization at 121–134 °C is a key requirement, but standard PLA may soften and degrade under heat and moisture. Nevertheless, multiple studies show that with appropriate conditioning (material choice, geometry, and pre-annealing), PLA-based materials can better withstand autoclaving with limited dimensional change [8,158–161]. Tarragó et al. [158] reported that PLA bio models showed the best performance at 25% infill, with a mean deformation of 0.41 mm (SD 0.09; 95% CI 0.34–0.47; $p < 0.01$). This is comparable in magnitude to the lowest 3D deformation observed in our study (0.47 mm SD, Table 7), despite differences in metrics and the fact that their evaluation was performed after sterilization without prior annealing. Similarly, Boursier et al. [159] analysed autoclave sterilization on FDM-printed PLA bone models, focusing on the effect of temperature, and reported minimal deformation values. Frizziero et al. [8] demonstrated that optimal performance was achieved with previously annealed HTPLA, confirming the need for accurate control of heating and cooling times to ensure material stability at high temperatures. PLA showed results above expectations, making it a valid low-cost option and a promising alternative for disposable medical tools requiring only a single heat cycle. Similarly, Cerezo et al. [160] found that annealing-induced deformation was mainly expressed along the main length of the part. In our study, the highest deviation was observed on Plane B (1.05 mm, Table 7), while Plane A showed maximum deformation at 90° infill orientation, consistent with directional effects.

Finally, our findings are consistent with the recommendations of Popescu et al. [161], who emphasized that dimensional precision is critical for surgical guides. It is therefore essential to monitor both global and local metrics, as we did by analysing overall 3D deformation together with 2D changes on planes A and B, to capture local deformation and directional shrinkage or expansion. These effects are strongly process- and material-dependent.

rom a practical and clinical perspective, a more predictable manufacturing process reduces reprints, waste, and costs, while improving fidelity to VSP and reducing deformation-related risks in guide positioning and correction accuracy.

4.1.6. Limitations

This study has several limitations. First, not all the possible printing parameters that can be defined during slicing were investigated, due to the high number of possible parameters, which also differ between slicing software. This is the reason why only a few parameters, considered the most impactful by their nature, were selected.

A further limitation is that dimensional variation was assessed on a single custom cutting guide with a total length of 142 mm. Given the high level of personalization, it is difficult to establish a standardized protocol applicable to all models, as could be done with generic or regular geometries. Consequently, the results apply specifically to this design, with its overall length and the defined dimensions of the connection rod.

Moreover, all measurements were taken after annealing and before sterilization. Based on our experience, no clinically relevant deformations were observed after sterilization when annealing was applied, at least nonsufficient to compromise the functional usability of the guides, such as preventing proper positioning on the bone during surgery. For this reason, the effect of sterilization was not included in the present analysis. Measuring only after sterilization would not have clarified whether any deformation was due to annealing or to sterilization and would have required two separate measurement phases, one for each treatment, which would have been excessively time-consuming. Nonetheless, further studies incorporating sterilization are warranted to empirically confirm the absence of additional deformations following this process.

Moreover, measurements were not taken immediately after printing, as the study focused on deformations relative to the original model. The aim was to assess the effect of printing parameters on the dimensional stability of a large-scale object, regardless of the printer's baseline accuracy.

The factorial design was intended as a screening experiment rather than a full optimization. Only two levels per factor were tested, assuming linear relationships between factors and responses, which is an acceptable simplification for preliminary purposes, although higher-order interactions or non-linear effects may exist but were not captured. In addition, no replicates were initially performed due to the large number of specimens and the time required for each test, which prevented the estimation of experimental error and may have introduced some inaccuracy. However, the design was subsequently reduced to a 2^3 factorial with at least one replicate, allowing for error estimation. Further studies with more levels and additional replications are needed to obtain more precise results and move towards parameter optimization.

4.2. Design Parameters Tuning for 3D Printing

The design phase is one of the most critical steps of the process, as a poorly conceived guide may compromise both the surgeon's experience and the accuracy in reproducing the preoperatively planned correction. VSP often relies on cutting guides that support the execution of both standard and complex procedures, performed with either conventional operating room instruments or dedicated systems linked to the fixation devices intended for use. Ensuring a stable positioning of the guide and an accurate reproduction of the surgical plan is therefore essential, and this is typically achieved through the application of K-wires. This requirement highlighted the need to analyse specific design aspects that had not yet been systematically addressed.

Cutting guides are generally characterized by three main features: the guide body, which provides a precise fit onto the bone by replicating the geometric surface of the corresponding segment; the saw slot, which directs the inclination and orientation of the surgical blade; and the pin (K-wires/screw) holes, which serve both to secure the guide in place and to assist in the placement of plates or screws. While the first two elements had already been evaluated in previous studies and through our empirical experience, the design of pin holes remained largely unexplored.

Given their central role in positioning and overall guide performance, we conducted an experiment to investigate their design parameters in relation to the desired design outcomes. It is crucial that the pin remains stable once inserted, without any movement inside the hole. Such stability is fundamental to ensure reliable intraoperative handling and to maintain the planned orientation of the wire within the bone. The experiment therefore focused on identifying the optimal design features of pin holes in relation to the required final wire diameter, while also accounting for the deformations introduced by our manufacturing process described earlier, which frequently results in a narrowing of the initially designed hole.

As mentioned earlier, the design process is highly case-specific and difficult to fully standardize, as each case has its own requirements. Nevertheless, this work focuses on analysing one of the more consistent features of the guides, while acknowledging that exceptional cases may arise where the proposed values are not directly applicable. The study experimentally investigates how the process affects the dimensional accuracy of PSIs and develops a regression model to predict the final dimensions, with the aim of optimizing design parameters during the modelling phase to ensure a precise fit of fixation pins and thereby improve surgical accuracy and overall PSIs stability. In this context, a key question is addressed: what diameter should the pin holes be designed to, given the final diameter of the pin to be used?

4.2.1. Design of the Experiment

For this experiment, a set of samples with different dimensions was produced to collect data and define the relationship between planned and effective values. The specimen height was fixed at 5 mm to standardize the geometry and exclude it as a variable, ensuring that the analysis focused solely on inner diameter and hole thickness (Figure 84). After the 3D printing phase and subsequent annealing, the final dimensions were manually measured with a digital calliper. To derive an empirical formula capable of predicting the final inner diameter of the annealed specimens within the practical range of parameter values, Response Surface Methodology (RSM) was applied. The purpose here is not to identify an optimization plateau, but rather to establish a usable relationship within the specific diameter range employed in practice. For the 3D printing of the specimens, the same material, machine, and process described in the previous chapters of the standard procedure were used.

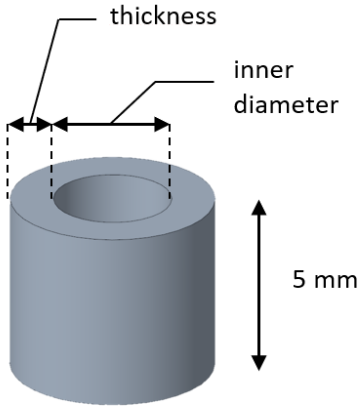

Figure 84. 3D representation of the specimen with a fixed height of 5 mm and variable inner diameter and thickness.

Thirteen 3D printed samples were obtained from the combination of the selected parameters for a comprehensive study. As previously mentioned, the two factors under investigation were the inner diameter and thickness, for which a specific range of levels ("high" and "low") was defined:

1. The inner diameter was included as the main focus of the research, to investigate how it changes from the initial design to the final post-process condition. The values ranged from 1.6 mm to 5 mm, selected based on surgical practice, reflecting the minimum and maximum diameters commonly used in our experience in the operating room, and ensuring they could be reliably measured with a digital calliper at the end of the process, while accounting for a safety margin to accommodate shrinkage;
2. Thickness was the second parameter considered, as the amount of material surrounding the inner diameter is expected to play a key role in the shrinkage results. The values were set between a minimum of 2 mm and a maximum of 6 mm.

For the optimization of design parameters in relation to the dimensional variation caused by annealing, a response surface approach was adopted. The Central Composite Design (CCD) is an extension of the factorial design that incorporates centre points and axial points to estimate curvature. The position of the axial points depends on an alpha (α) value, which is determined by the number of points in the underlying factorial design. In this case, with a two-factor, two-level design (4 points), the corresponding α value is 1,414. Unlike a simple factorial design, which captures only linear effects and interactions, CCD enables modelling of both linear and quadratic terms, making it suitable for response surface analysis [143]. While CCD is typically applied to identify an optimum point, in this study it was used solely to develop a descriptive model, capturing the relationship between planned and effective dimensions within the practical range of values. The variable parameters and their level are described in Table 16.

Table 16. High and low levels of the variable parameters.

	Levels	
	Low (-)	**High (+)**
Inner diameter (mm)	1.6	5
Thickness (mm)	2	6

4.2.2. Measurements

The experiment was conducted by designing the CAD model of each specimen according to the dimensions defined in the design of experiment. The specimens were subsequently 3D printed and annealed (Figure 85 and 86), after which their final dimensions were manually measured with a digital calliper. These measurements were then compared with the initial CAD dimensions, from which also the theoretical volume was calculated (Table 17), to evaluate the dimensional changes induced by the process.

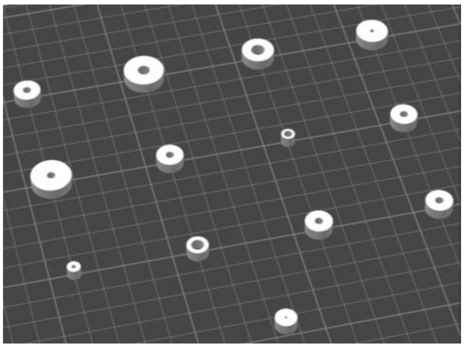

Figure 85. The 13 specimens randomly arranged on the build plate according to the randomized order.

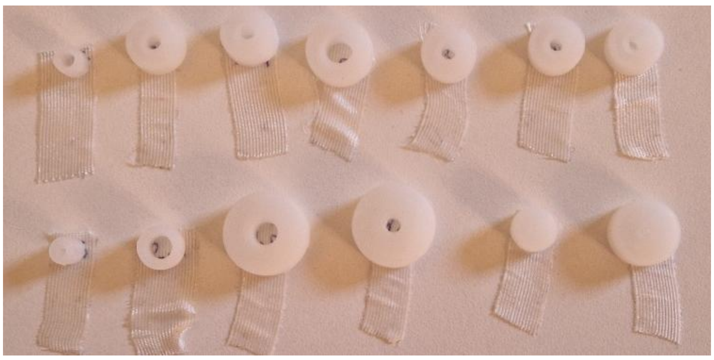

Figure 86. The 13 specimens after annealing, ready for measurement.

Table 17. Central Composite Design of the experiments, including randomized run order, point type and corresponding values (in mm). Please note that the height is maintained constant at 5 mm in the experiment.

Standard Order	Run Order	Point Type	Variables (mm)		Height (mm)	Volume (mm^3)
			Inner Diameter	Thickness		
1	11	Factorial	1.6	2	5.0	163.3
2	8	Factorial	5	2	5.0	376.8
3	3	Factorial	1.6	6	5.0	866.6
4	4	Factorial	5	6	5.0	1507.2
5	1	Axial	0.9	4	5.0	363.7
6	6	Axial	5.7	4	5.0	967.6
7	9	Axial	3.3	1,2	5.0	142.9
8	2	Axial	3.3	6,8	5.0	1439.6
9	7	Centre	3.3	4	5.0	665.7
10	12	Centre	3.3	4	5.0	665.7
11	13	Centre	3.3	4	5.0	665.7
12	5	Centre	3.3	4	5.0	665.7
13	10	Centre	3.3	4	5.0	665.7

After the annealing process, the effective values of inner diameter, thickness, height (although not included in the design, it was monitored as a control), and volume were manually measured and calculated for each specimen. From these, the differences with respect to the designed values were computed (Δinner, Δthickness, Δheight, Δvolume, and Δvolume%) (Table 18).

Table 18. Final measurement and values for each specimen.

Standard Order	Final inner (mm)	Final thickness (mm)	Final height (mm)	Final Volume (mm^3)	Δinner (mm)	Δthickness (mm)	Δheight (mm)	Δvolume	
								(mm)	(%)
1	0.90	2.40	5.20	164.59	-0.70	0.40	0.20	1.31	0.01
2	4.50	2.10	5.20	380.61	-0.50	0.10	0.20	3.81	0.01
3	0.90	6.40	5.30	873.37	-0.70	0.40	0.30	6.73	0.01
4	4.60	6.00	5.30	1517.75	-0.40	0.00	0.30	10.55	0.01
5	0.00	4.30	5.30	307.71	-0.90	0.30	0.30	-56.01	-0.15
6	5.20	4.20	5.20	1001.23	-0.50	0.20	0.20	33.59	0.03
7	2.70	1.50	5.10	165.74	-0.60	0.33	0.10	22.80	0.16
8	2.90	6.90	5.30	1458.34	-0.40	0.07	0.30	18.73	0.01
9	2.80	4.20	5.30	684.98	-0.50	0.20	0.30	19.30	0.03
10	2.80	4.10	5.30	661.85	-0.50	0.10	0.30	-3.83	-0.01

11	2.70	4.20	5.20	658.34	-0.60	0.20	0.20	-7.34	-0.01
12	2.90	4.30	5.20	709.13	-0.40	0.30	0.20	43.45	0.07
13	2.80	4.20	5.30	684.98	-0.50	0.20	0.30	19.30	0.03

The data were analysed based on RSM with a CCD, with inner diameter and thickness as independent factors. Quadratic regression models were fitted to evaluate linear, quadratic, and interaction effects on the measured responses. Model adequacy was assessed through ANOVA, with a significance threshold set at $p < 0.05$. Non-significant terms were removed by stepwise regression where appropriate, in order to refine the predictive model. The resulting equations were used to generate response surface and contour plots, allowing a direct interpretation of the relationship between design parameters and dimensional variations after annealing.

4.2.3. Preliminary results of the Experiment

Preliminary inspection of the data clearly shows that the inner diameter consistently decreases (our data show a range from –0.4 to –0.9 mm), while the thickness systematically increases (data range from +0.1 to +0.4 mm). The height also shows a slight positive shift, even if it was maintained as a constant (from +0.2 to +0,3 mm). Overall, the volume displays only limited percentage variations, suggesting that the dimensional changes mainly result from a redistribution of material rather than an actual loss of volume, with the main dimensional effect being the reduction of the inner diameter, which represents the most critical feature for the correct fit of pins.

The response of interest was the final inner diameter, considering the varied values for the experiment (inner diameter and thickness) as independent factors. The model fit summary (Table 19) indicated that the quadratic model was the most suitable for describing the variation of our response. The linear and 2FI models were not adequate, despite showing high R^2 values, while the cubic model was aliased and therefore not considered. The quadratic model was statistically significant ($p = 0.0129$), with no significant lack-of-fit ($p = 0.7698$), and showed excellent agreement between adjusted R^2 (0.9984) and predicted R^2 (0.9973). Based on these results, the quadratic model was selected.

Table 19. Fit summary for the choice of the model.

Model	Sequential p-value	Lack of Fit p-value	Adjusted R^2	Predicted R^2	
Linear	< 0.0001	0.2086	0.9959	0.9938	Not adequate
2FI	0.6278	0.1723	0.9956	0.9935	Not adequate
Quadratic	**0.0129**	**0.7698**	**0.9984**	**0.9973**	**Suggested**
Cubic	0.6161	0.6433	0.9981	0.9959	Aliased

ANOVA results for the full quadratic model (Table 20) confirmed that the model was statistically significant ($p < 0.0001$), with no significant lack of fit ($p = 0.7698$). Among the individual terms, the factor inner diameter had the strongest effect on the final diameter ($p < 0.0001$), together with its quadratic term ($p = 0.0047$), indicating a non-linear relationship between nominal and final inner diameter. Conversely, the main effect of thickness was only marginally non-significant ($p = 0.061$), while the interaction (Inner Diameter*Thickness) and quadratic effect of thickness were clearly not significant.

Table 20. ANOVA analysis for the full quadratic model.

	Sum of Squares	df	Mean Square	F-value	p-value
Model	26.93	5	5.39	1461.57	**< 0.0001***
Inner Diameter	26.84	1	26.84	7284.95	**< 0.0001***
Thickness	0.0183	1	0.0183	4.97	0.0610
Inner Diameter*Thickness	0.0025	1	0.0025	0.6785	0.4373
Inner Diameter^2	0.0611	1	0.0611	16.59	**0.0047***
Thickness^2	0.0003	1	0.0003	0.0737	0.7938
Residual	0.0258	7	0.0037		
Lack of Fit	0.0058	3	0.0019	0.3861	0.7698
Pure Error	0.0200	4	0.0050		
Cor Total	26.95	12			

**Values in bold with an asterisk highlight the factors that are statistically significant ($p < 0.05$)*

Based on these results, a model reduction was performed to retain only the significant terms. After model reduction, the ANOVA (Table 21) confirmed that the simplified model remained highly significant ($p < 0.0001$) with no lack of fit ($p = 0.8646$). The reduced model retained three terms: the main effects of inner diameter and thickness, as well as the quadratic effect of inner. Among these, inner diameter was by far the dominant factor ($p < 0.0001$), while thickness had a smaller but still significant effect ($p = 0.0397$). The quadratic term of inner confirmed the presence of curvature in the relationship between nominal and final inner diameter. The interaction term and the quadratic term of thickness were excluded as they were not significant. The coefficients of determination confirmed the quality of the fit, with R^2 = 0,9989, Adjusted R^2 = 0.9986, and Predicted R^2 = 0.9982, all in close agreement.

Table 21. ANOVA analysis for the model reduction.

	Sum of Squares	df	Mean Square	F-value	p-value
Model	26.92	3	8.97	2827.3	**< 0.0001***
A-inner	26.84	1	26.84	8457.48	**< 0.0001***
B-thickness	0.0183	1	0.0183	5.77	**0.0397***
A^2	0.0633	1	0.0633	19.94	**0.0016***
Residual	0.0286	9	0.0032		
Lack of Fit	0.0086	5	0.0017	0.3426	0.8646

Pure Error	0.0200	4	0.0050
Cor Total	26.95	12	

$R^2 = 0.9989$ Adjusted $R^2 = 0.9986$ Predicted $R^2 = 0.9982$

**Values in bold with an asterisk highlight the factors that are statistically significant ($p < 0.05$)*

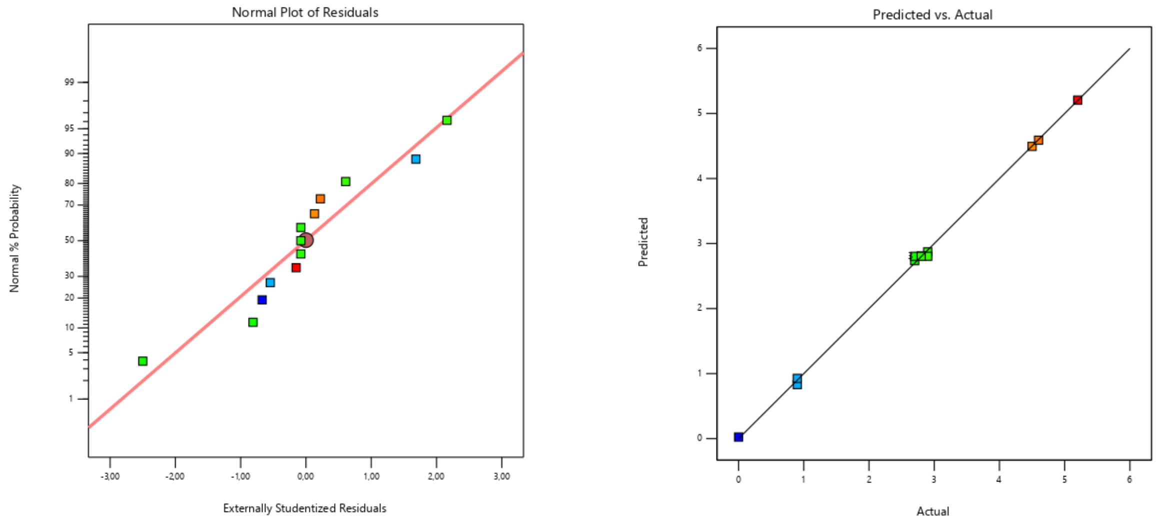

(a) *(b)*

Figure 87. (a) Normal probability plot of residuals confirming the normal distribution of the data; (b) Predicted vs. actual plot demonstrating good predictive accuracy of the model.

Diagnostic plots confirmed the adequacy of the model (Figure 87): residuals were approximately normally distributed and the predicted vs. actual plot showed that the experimental data aligned closely with the bisector, indicating good predictive reliability.

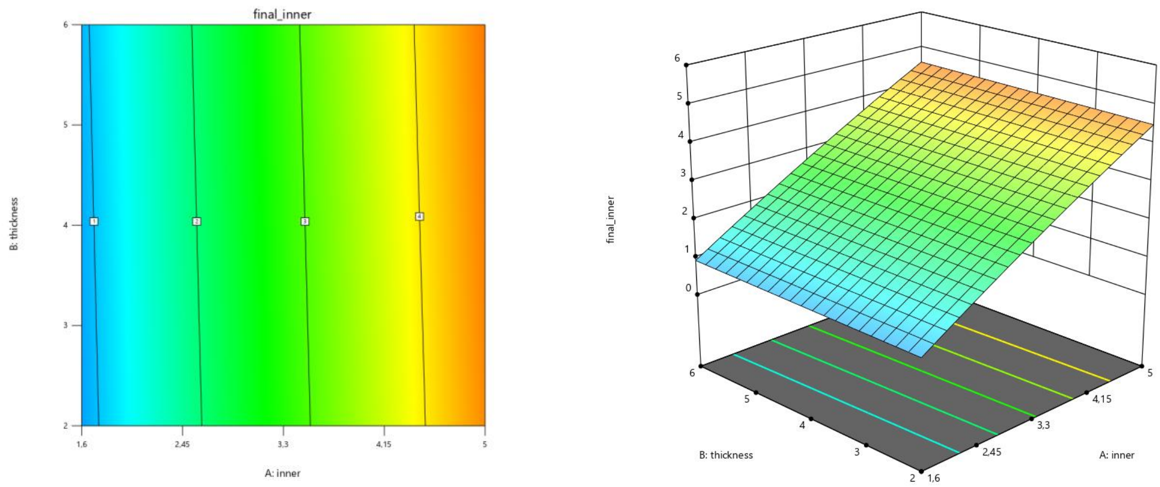

(a) *(b)*

Figure 88. (a) Contour plot and response surface plot (b) illustrating the effect of the factors of the model on the final diameter.

In addition, contour and response surface plots (Figure 88) illustrate the effect of nominal inner diameter and thickness on the final inner diameter. The plots clearly illustrate that inner diameter is the dominant factor, with a non-linear curvature confirmed by the quadratic term, while thickness has a smaller but significant effect. These graphical representations allow a direct interpretation of how dimensional changes evolve across the design space and support the use of the regression model for predictive purposes.

The reduced quadratic model resulted in the following regression equation:

$$final\ diameter = -1.20343 + 1.29346 * inner + 0.023928 * thickness - 0.032722 * inner^2$$

In this context, “inner” refers to the nominal inner diameter defined in the CAD design, “thickness” to the nominal wall thickness of the hole, and “final diameter” to the effective diameter obtained after the annealing process. The model allows prediction of the final diameter for any combination of design parameters within the experimental range. Its strength lies in the possibility of inverting the regression equation to determine the nominal CAD diameter required to achieve a specific post-annealing size. This makes the model not only predictive but also directly applicable as a compensation rule during design, ensuring that the manufactured guides provide the correct fit for pins.

4.2.4. Discussion

The literature addressing design parameters or process tuning specifically for 3D printed surgical instruments remains limited. Since other authors have successfully applied Response Surface Methodology (RSM) to optimize the properties of FDM-printed parts and derive predictive models [162,163], the same methodological approach was adopted in this study. However, the focus was placed on a critical geometrical feature, the diameter of fixation pin holes, with the specific aim of developing a predictive compensation equation directly applicable during the design phase. It was hypothesized that, once a stable manufacturing process is defined, pin-hole geometry exhibits a systematic and measurable behaviour that can be characterized and exploited to achieve controlled and reliable final dimensions.

Similarly, Kwan et al. [164] investigated design parameters of in-house 3D-printed surgical jigs made of surgical-grade resin, assessing how thickness and saw-slot height affect cutting accuracy. While their work aimed to define design guidelines, it focused on purely geometrical features and did not account for dimensional changes introduced by printing or sterilization, as addressed in the present study. This makes their results broadly applicable across materials, but also limits their direct transferability to process-dependent workflows.

Wijnbergen et al. [165] evaluated annealing methods for FDM tough PLA prosthetic sockets, reporting that sand annealing produced the least deformation, while oven annealing of vertically placed rings led to the greatest dimensional changes but also the largest mechanical improvement. By measuring variations in inner diameter, thickness, and height of ring-like specimens, they also showed that part orientation during annealing can influence deformation, an aspect not considered in our work but relevant for future investigations. Consistent with our findings, thickness was less sensitive to dimensional changes ($p > 0.05$) than inner diameter ($p < 0.05$).

Our study aligns with the recommendation of Popescu et al. [161], who emphasized the importance of including adequate allowances in fit-critical areas during guide design. By focusing on pin-hole geometry, we developed an empirical regression model enabling CAD-based compensation rules, ensuring that post-annealing dimensions match surgical requirements. As also noted by Popescu et al., these considerations strongly depend on the material and process used.

4.2.5. Limitations

This study has some limitations that should be acknowledged when interpreting the results. First, the regression model obtained through RSM is valid only within the experimental range of inner diameter and thickness investigated. The approach cannot be directly extrapolated to substantially different values, such as very large holes or very thin walls, which were not part of the tested domain. The predictive equation should therefore be considered a local model, accurate within the tested domain but requiring new calibration if the design space changes.

Second, the specimens were deliberately simplified to cylindrical rings with constant height to isolate the effect of the two studied parameters. This controlled geometry facilitates a clear interpretation of the results but does not fully reflect the complexity of real surgical guides, which may include multiple adjacent holes, irregular curvatures, and other local features that could affect deformation. In such cases, dimensional changes may also be influenced by interactions between neighbouring elements or by structural constraints not reproduced in our setup.

Third, although specimen height was fixed at 5 mm, slight variations were still observed after annealing. Since height was not investigated as a factor, its potential influence on deformation remains unexplored. It cannot be excluded that taller or thinner components may show different shrinkage or expansion behaviour, suggesting that height should be systematically varied in future studies to assess its role as an additional parameter.

In addition, the measurement of final dimensions was performed manually using a digital calliper. While care was taken to minimize operator bias, this method inherently carries a small degree of uncertainty compared to automated or scanning-based measurements. Employing 3D scanning techniques or optical metrology could improve accuracy and enable a more detailed mapping of deformation across the entire geometry.

Finally, the model is strongly material- and process-dependent. The predictive equation developed here applies specifically to HTPLA processed with the selected printer, printing parameters, and annealing protocol. Any change in material, print settings, or thermal treatment would alter the deformation behaviour, requiring renewed tuning of the model. This highlights both a limitation and an opportunity: the methodology can be replicated and adapted, but calibration is necessary whenever process or material conditions differ.

5. CLINICAL OUTCOMES AND QUANTITATIVE ANALYSIS OF PSI IMPLEMENTATION

5.1. Introduction to Protocols and Cases Cohort

As previously mentioned, the collaboration between the Department of Industrial Engineering of the University of Bologna and the Paediatric Orthopedic and Traumatology Unit of the Rizzoli Orthopedic Institute has been ongoing since 2018, when the first joint research protocol was launched following approval by the Area Vasta Emilia Centro ethics committee, aimed at the development and clinical use of patient-specific bio models. In the initial years, the activity primarily focused on defining methodological frameworks and exploring the potential applications of virtual CAD-based planning and 3D printing technologies within the clinical workflow.

Since 2022, following the activation of a second research line building upon the previous work and approved by the same institutional ethics committee, the collaboration has entered its core phase. This phase is characterized by the formal implementation of the manufacturing of sterilizable PSIs produced via 3D printing, in accordance with the processes, materials, and technologies described above.

In this chapter, an assessment of the overall work carried out is presented. To provide methodological continuity, cases from activities conducted prior to 2022, the starting year of this doctoral research, are also included. Although these earlier cases were not developed within the formal framework of the PhD project, they document the progressive evolution of the workflow and offer essential context for understanding the subsequent structured implementation of PSIs planning and design.

The chapter first presents an overall analysis of the collected data, followed by a subcohort analysis stratified by anatomical region. It was hypothesized that procedures performed with PSIs and/or GSIs achieve improved outcomes mainly in terms of operative time, correction accuracy, and intraoperative fluoroscopy use.

5.2. General Overview of Cases

Over the years, a progressive implementation of the workflow has been observed (Figure 89). Initially, the activity was limited to segmentation, but as expertise was consolidated, the process was gradually optimized, first with an increasing number of cases undergoing VSP and subsequently with a growing proportion also including PSIs design and 3D printing, in line with the activation of a dedicated clinical trial authorized by the ethical committee. Today, PSI design has become the standard procedure, with only a few cases limited to segmentation or VSP alone. In the last two years (2024 and 2025), the observed reduction in case numbers reflects a shift from a high-throughput exploratory phase to a consolidation phase focused on workflow refinement and validation, resulting in lower case volume but increased process maturity.

Since 2018, 3D virtual reconstructions from CT and/or MRI scans have been performed for 141 paediatric and young adult patients, corresponding to 177 planned and performed procedures.

Each procedure corresponded to one correction. Accordingly, multiple corrections performed on different regions of the same bone during the same surgical session were considered distinct procedures. These cases underwent segmentation alone, segmentation with VSP, or segmentation and VSP combined with the design of customized PSIs and/or GSIs.

Among the 141 patients and 177 planned procedures, 170 were effectively carried out. Out of these, 26 were bilateral, requiring the correction and treatment of both limbs. Ten procedures were classified as multisegmental or multifocal, defined as the correction of more than one bone segment (regardless of side) or multiple regions of the same bone (e.g., proximal and distal femur). In four patients, the procedures were both multisegmental (e.g., involving correction of the femur and tibia within the same surgical session) and bilateral.

An initial visual analysis of the data shows that these technologies have been applied across different anatomical areas, with the lower limb representing the most frequently planned and treated region. Applications were mainly concentrated in non-diaphyseal areas, particularly the proximal and distal segments of the long bones, with a specific focus on the proximal femur. The subdivision of the cases addressed is presented in Figures 90 and 91, organized according to the anatomical area classification defined by the AO/OTA Fracture and Dislocation Classification Compendium [166].

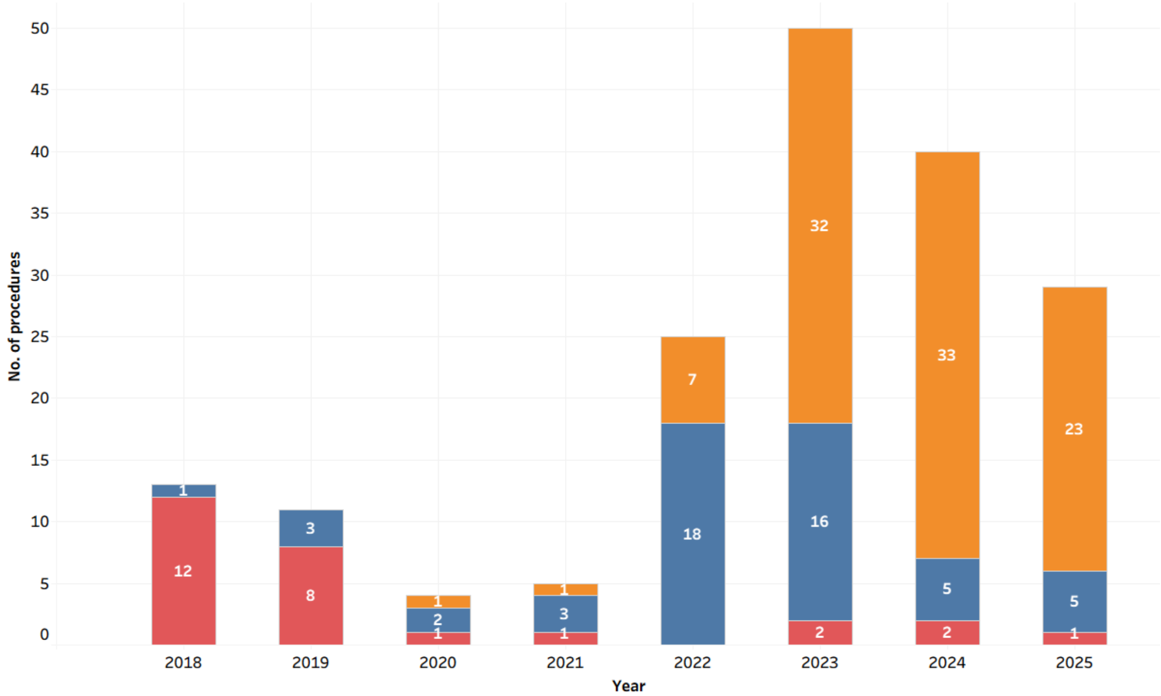

Figure 89. Distribution of procedures over time (2018–2025) according to workflow complexity. The x-axis represents the study protocol years (2018–2025), and the y-axis indicates the number of procedures. Procedures that underwent segmentation only (red bars), procedures that underwent VSP (which inherently includes segmentation) (blue bars), and procedures that additionally required PSIs design (representing a further step beyond VSP) (orange bars).

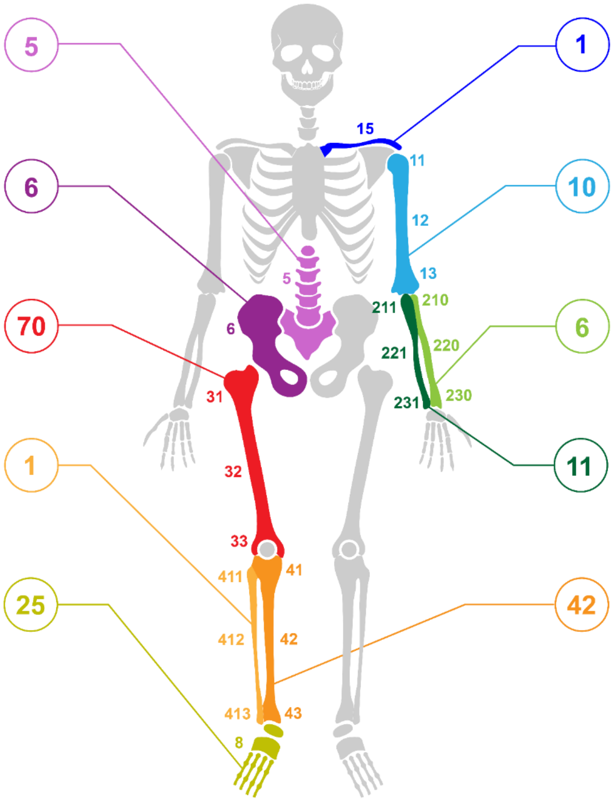

Figure 90. Distribution of procedures that underwent segmentation, VSP, and PSI design, grouped by bone segment. Regions are classified as proximal, diaphyseal, and distal using numerical labels according to the AO/OTA Fracture and Dislocation Classification Compendium [166]; circled numbers indicate totals per bone.

This patient group represents a heterogeneous cohort, as it includes a wide age range (paediatric patients typically range from birth to approximately 18 years, although in some contexts this definition may extend to include young adults), different pathologies such as bone tumours, hip dysplasia, Ollier's disease, and Blount's disease, as well as various types of treatment, including opening wedge osteotomies, shortening procedures, and fixation procedures. To make the cohort more homogeneous, oncologic patients (22 patients, corresponding to 22 procedures) could be analysed separately from non-oncologic patients, since bone tumours are managed with entirely different approaches, often involving massive resections and bone graft implantation. Moreover, the data relating to oncologic patients who underwent surgery almost always involved the design and application of PSIs and GSIs. Therefore, it is not possible to perform the same comparisons, since a control group treated with VSP or segmentation alone was not available.

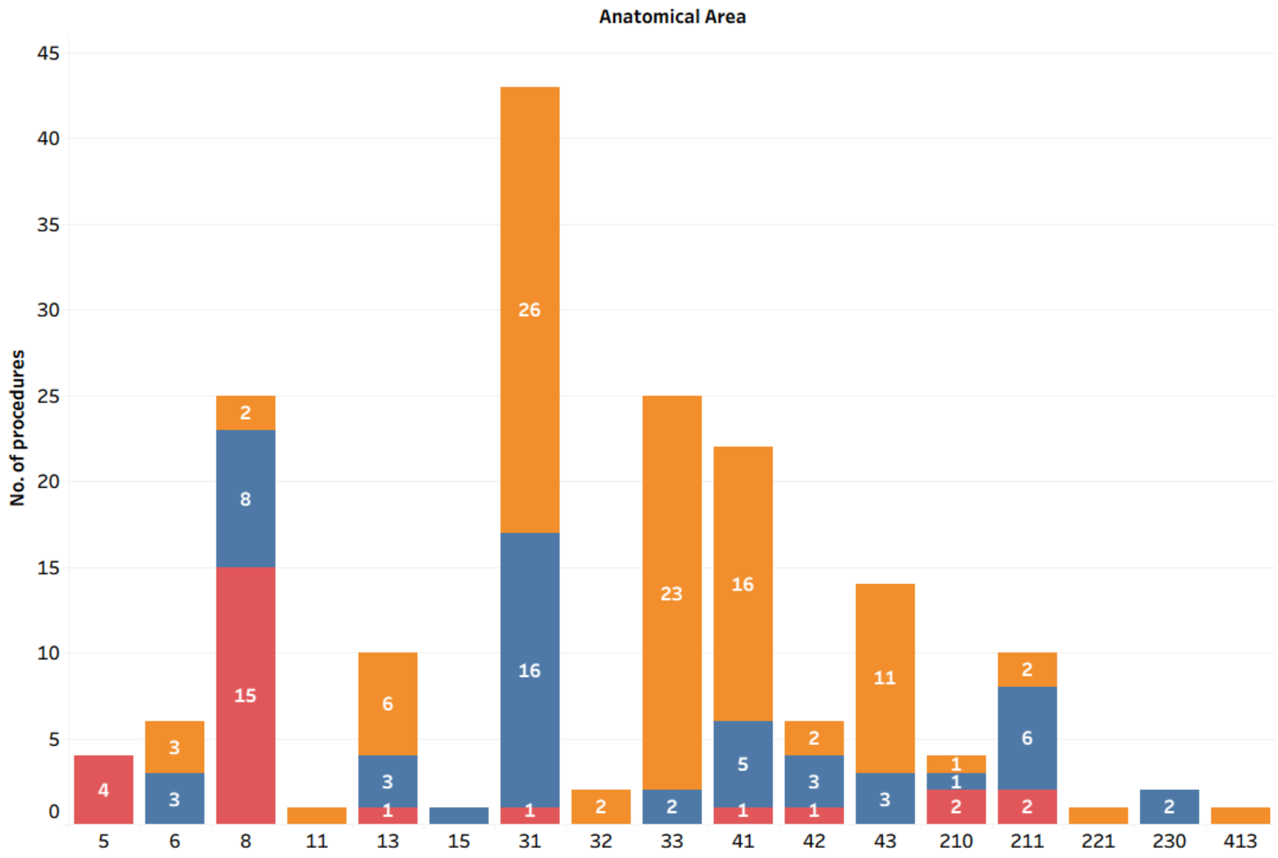

Figure 91. Distribution of procedures grouped by bone segment and workflow complexity. The y-axis indicates the number of procedures, while the x-axis reports bone segment classification codes identifying the involved bone and its anatomical region (proximal, diaphyseal, or distal), according to the AO/OTA Fracture and Dislocation Classification Compendium [166]. Bars represent procedures that underwent segmentation only (red), VSP (including segmentation) (blue), and procedures additionally requiring PSI design (orange).

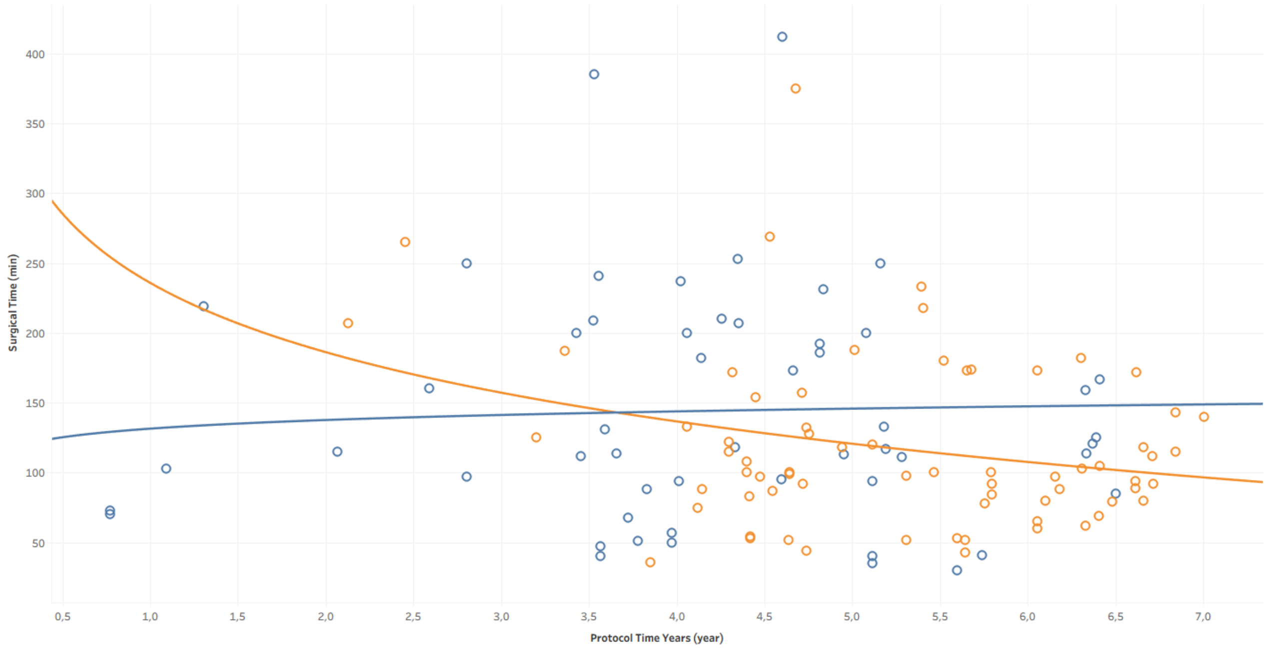

Figure 92. Representation of the correlation between surgical time and the number of segment corrections across the clinical trial timeline. The x-axis represents the protocol time years, defined as the number of years elapsed since the initiation of the first study protocol, while the y-axis reports surgical time. Procedures are distinguished between those performed with VSP only (blue) and those performed with VSP combined with PSIs (orange).

In the non-oncologic cohort, an overview of the remaining paediatric procedures which underwent surgery (122 procedure) and their surgical times indicates that, compared with cases planned using VSP alone, those in which both VSP and PSIs were employed progressively showed a reduction in operative time over the years (Figure 92).

In any case, the data remain highly heterogeneous. In the following paragraphs, different subgroups of the cohort are analysed to make the data as homogeneous as possible. Specifically, the analysis is focused on procedures involving the upper and lower limbs, cases requiring bone grafts, and oncologic patients undergoing massive resections followed by reconstruction with massive bone allografts. The comparisons consider procedures performed with VSP alone versus those supported by both VSP and the design of PSIs for intraoperative use. Cases involving segmentation only could not be included because, apart from image segmentation, surgical planning was performed using traditional methods and defined preoperatively by the surgeon without formal documentation, unlike procedures supported by VSP alone or by VSP combined with PSIs, for which complete digital planning reports and models were available.

For each patient, informed consent was obtained and demographic data, including age and underlying pathology, were collected. Preoperative CT scans, MRI, and radiographs were used to document relevant anatomical details and perform analyses. CT quality was recorded as suboptimal in the presence of artifacts, low image resolution, or partial acquisition. For each procedure, surgical time, procedure type (e.g., opening or closing wedge, shortening), duration of surgery, number of intraoperative fluoroscopy shots, and perioperative complications were recorded by the author, with clinical data collected in collaboration with the surgical staff. A set of corrections performed through a single surgical incision was counted as one segment correction. When multiple segments were corrected simultaneously, surgical time and fluoroscopy shots were divided by the number of segment corrections. VSP-only procedures and procedures combining VSP with the design and manufacturing of sterilizable PSIs for intraoperative use, corresponding to the blue and orange bars, respectively, in Figures 89 and 91.

For a necessary overall assessment of the outcomes of these procedures, only angular corrections were analysed, as these were the only parameters from postoperative radiographs (for example, assessing torsional corrections would require a postoperative CT scan, which is not part of standard clinical practice, especially when paediatric patients are involved). Planned correction (PC) angles were retrieved from the surgical planning reports routinely provided to the surgeon for process documentation and, when necessary, for illustrating the application of PSIs. Achieved correction (AC) angles were measured on postoperative radiographs. When radiographs obtained in the true plane of angulation were unavailable, the actual angulation was calculated using the Ilizarov triangle method [167]. This approach allows to measure the achieved angular correction on the true plane, independently of standard coronal and sagittal radiographic projections, using the angles measured on coronal (cor) and lateral (lat) radiographs through a simple trigonometric calculation.

$$AC\ (°) = \sqrt{\tan^2 cor + \tan^2 lat}$$

The difference between PC and AC was then calculated. To assess the accuracy of the angular correction, the error was quantified as the absolute difference between AC and PC, thus avoiding the cancellation of ipercorrections (+) and ipocorrections (–). The error was expressed both in degrees (°) and as a percentage (%), to provide a more comprehensive overview, given the presence of both small and large corrections that required normalization for comparison.

$$Angular\ correction\ difference\ (°) = AC - PC$$

$$Angular\ correction\ error\ (°) = |AC - PC|$$

$$Angular\ correction\ error\ (\%) = \frac{|AC - PC|}{PC} \times 100$$

The outcome measures considered were surgical time per procedure, number of intraoperative fluoroscopy images, incidence of complications, number of grafts, number of PSIs, number of GSIs, and angular correction error.

Data were collected using Excel (Microsoft Corporation, Redmond, WA, USA) and subsequently transferred to JASP (Version 0.95.2, University of Amsterdam, Amsterdam, The Netherlands) for statistical analysis. All measurement data are presented as standard deviation (SD), and corresponding range of values. Statistical analyses included independent t-tests for comparisons of continuous variables between groups, and contingency tables with Chi-square or Fisher's exact test for categorical variables. Descriptive statistics were complemented by box plots to illustrate the distribution and variability of continuous data. A p-value < 0.05 was considered statistically significant.

5.2.1. Upper limb subcohort

A total of 20 patients underwent 22 upper limb procedures. To maintain a homogeneous cohort focused on the arm, one patient who underwent a clavicle procedure was excluded from the analysis. The final cohort therefore included 19 patients who underwent 21 procedures, including 2 multisegmental corrections. The mean age at the time of surgery was 10.7 years (SD 3.3; range 6.5–16.2 years). The cohort comprised 9 females and 10 males.

Ten procedures were performed on the right arm and nine on the left. Regarding anatomical distribution, 9 procedures involved the distal humerus, 7 the proximal ulna, 1 the ulnar diaphysis, 2 the proximal radius, and 2 the distal radius.

In 9 out of 21 procedures, PSIs were employed to aid the surgical execution. A bone graft was required in 10 procedures, including 3 autologous and 7 homologous grafts. The 3 autologous grafts were all harvested locally and reinserted as flipping-wedge osteotomies, without the intraoperative support of GSIs, relying solely on the measurements defined during VSP. Among the 7 homologous grafts, 4 were delivered to the operating room in raw form and modelled according to VSP measurements, while 3 were pre-shaped by the BTM, also based exclusively on VSP indications.

The mean surgical time for procedures planned with VSP alone was 143 minutes (SD 56.4, range 70–209), compared to 136.1 minutes (SD 52.2, range 69–233) for procedures planned with both VSP and PSIs. Although the mean time was lower with PSIs, the difference was not statistically significant (p = 0.317).

The mean number of intraoperative fluoroscopy shots was 12.3 with VSP alone (SD 6.7, range 4–24) and 8.2 with the addition of PSIs (SD 3.11, range 4–12), with a p-value approaching significance ($p = 0.057$).

Nineteen procedures involved angular correction (10 planned with VSP only and 9 with VSP plus PSI), allowing measurement of the achieved correction on postoperative radiographs and comparison with the planned values. No improvement in accuracy was observed with the use of PSIs. The planned correction varied widely, with a mean of 23.9° (range 3–42°). The mean absolute deviation from the planned correction was 3.5° (SD 3.17; range 0–11; percentage deviation 0.15, SD 0.13; range 0–0.44) with VSP alone, and 7.0° (SD 6.86; range 0–22; percentage deviation 0.24, SD 0.22; range 0–0.63) with PSIs. The differences were not statistically significant (absolute deviation: $p = 0.92$; percentage deviation: $p = 0.86$). Boxplot are shown in Figure 93.

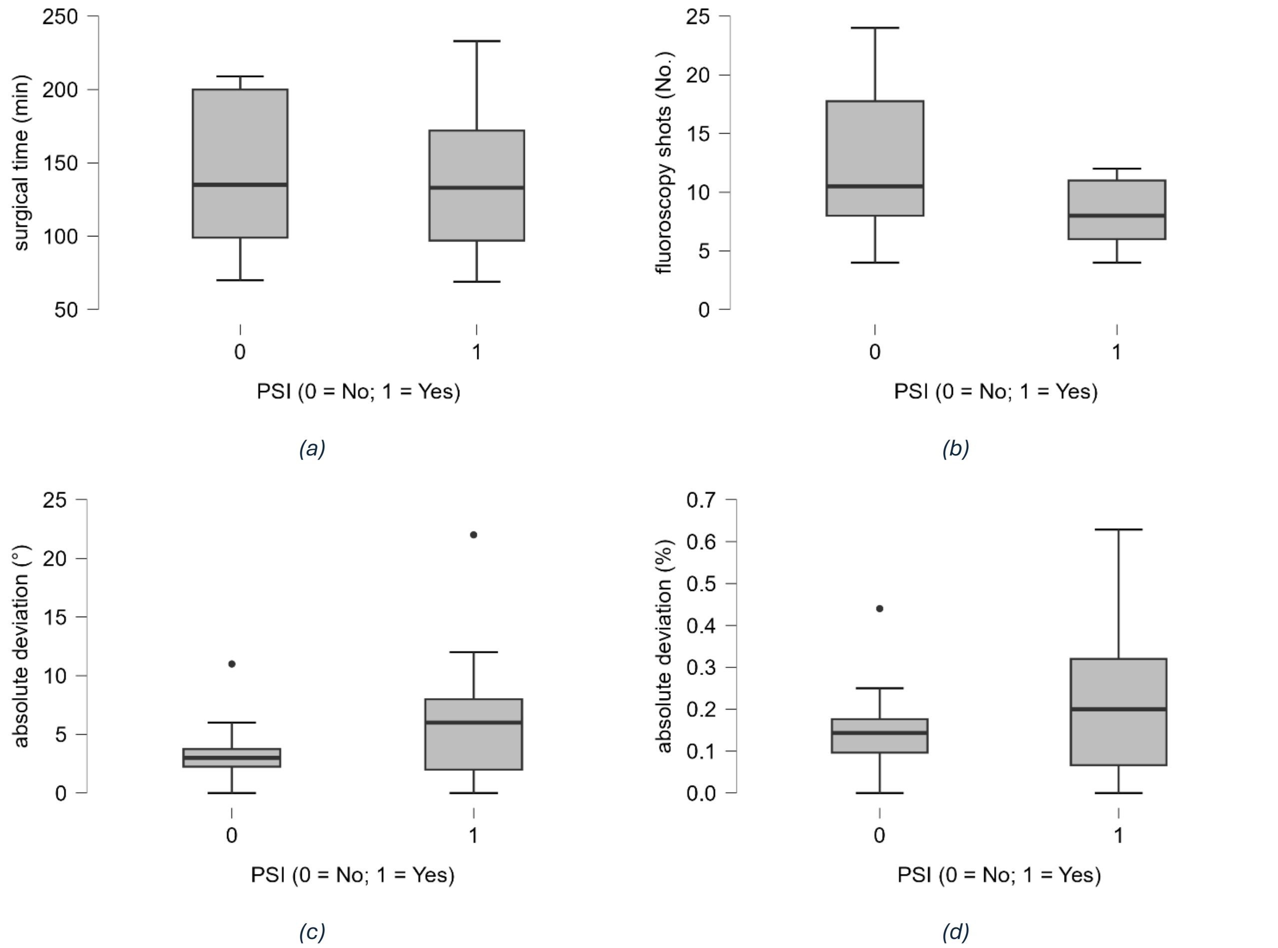

Figure 93. Boxplots of upper limb surgical time (a), number of intraoperative fluoroscopy shots (b), absolute deviation (°), and percentage absolute deviation of the achieved correction from the planned correction (c and d), comparing procedures performed with VSP alone and those supported by both VSP and PSIs.

The data were also analysed after further stratification by bone segment (distal humerus, proximal ulna, ulnar diaphysis, proximal radius, distal radius), but no statistically significant differences were found.

2 out of 12 procedures without PSIs and 3 out of 9 procedures with PSIs experienced complications. The difference was not statistically significant ($p=0.611$), indicating that the use

of PSIs carries a complication rate comparable to traditional surgery, with no evidence of additional risks. Overall, 17 PSIs were designed, 3D printed, sterilized, and used across 9 procedures. In only one case, difficulty was encountered with the cutting guide, as the PSI was slightly bulky relative to the surgical space.

5.2.2. Lower limb subcohort

A total of 100 lower limb procedures were performed on 72 patients. One patient was excluded from the analysis because the case involved post-traumatic reconstruction with a graft, representing a different surgical approach compared with the rest of the cohort. An effective total of 99 procedures on 71 patients (37 females, 34 males), with a mean age of 10.9 years (SD 5.0; range 1.8–19.2 years). Laterality was almost equally distributed, with 50 procedures performed on the right side and 49 on the left. Eighteen procedures involved multisegmental corrections, and ten were bilateral.

In terms of anatomical location, 4 procedures were performed on the pelvis and 8 on the foot. The remaining 87 procedures involved long bones of the lower limb and were distributed as follows: 40 on the proximal femur, 18 on the distal femur, 13 on the proximal tibia, 3 on the tibial diaphysis, 12 on the distal tibia, and 1 on the distal fibula.

Of the effective 99 procedures, 63 were performed using PSIs in the operating room, while 36 were carried out with VSP alone. A bone graft was used in 27 procedures, including 8 autologous and 19 homologous grafts. Among the 8 autologous grafts, 2 were harvested from a donor site different from the treated area (e.g., iliac crest or another bone segment). The remaining 6 consisted of local bone wedge removal and reinsertion after reorientation or reshaping (e.g., Flipping Wedge Osteotomy and Side-to-Side Flipping Wedge Osteotomy), one shaped with the use of GSIs. Among the 19 homologous grafts, 10 were brought into the operating room in raw form and 9 were pre-shaped by the BTM. Of the 11 raw grafts, 9 were manually shaped during surgery, while 1 was shaped with the aid of GSIs by the surgeon. Among the 9 pre-shaped grafts, 7 were modelled by the BTM in the clean room based solely on VSP measurement, while 2 were shaped with the aid of GSIs.

The mean surgical time for procedures planned with VSP alone was 138.3 minutes (SD 79.1; range 35–385), compared to 113.6 minutes (SD 53.2; range 36–269) for procedures planned with both VSP and PSIs. Although the mean time was lower with the use of PSIs, this difference was not statistically significant ($p = 0.09$). However, when focusing on the subcohort of 87 procedures performed on long bones of the lower limbs, thereby obtaining a more homogeneous group, the mean surgical time for VSP-only procedures was 161.3 minutes (SD 74.8; range 47–385), compared to 114.5 minutes (SD 53.9; range 36–269) with the use of PSIs. In this case, the difference was statistically significant ($p = 0.001$), corresponding to a mean time saving of 46.8 minutes. This result remained significant when further restricting the analysis to the 58 femoral procedures: the mean surgical time with VSP alone was 159.2 minutes (SD 65.9; range 47–250), compared to 111.1 minutes (SD 52.2; range 44–269) with PSIs ($p = 0.003$), with a mean reduction of 48.1 minutes. For the tibial subcohort of 29 procedures, a mean reduction of surgical time was observed with a mean of 165.4 minutes (SD 94.3; range 85-385) with VSP alone and a mean of 121 minutes (SD 57.9; range 36-218) with the use of PSIs, with a mean reduction of approximately 44 minutes, although this difference did not reach statistical significance.

Boxplots of surgical time for long bones of lower limbs and femoral procedures, with the use of VSP alone or with the use also of PSIs, are shown in Figure 94.

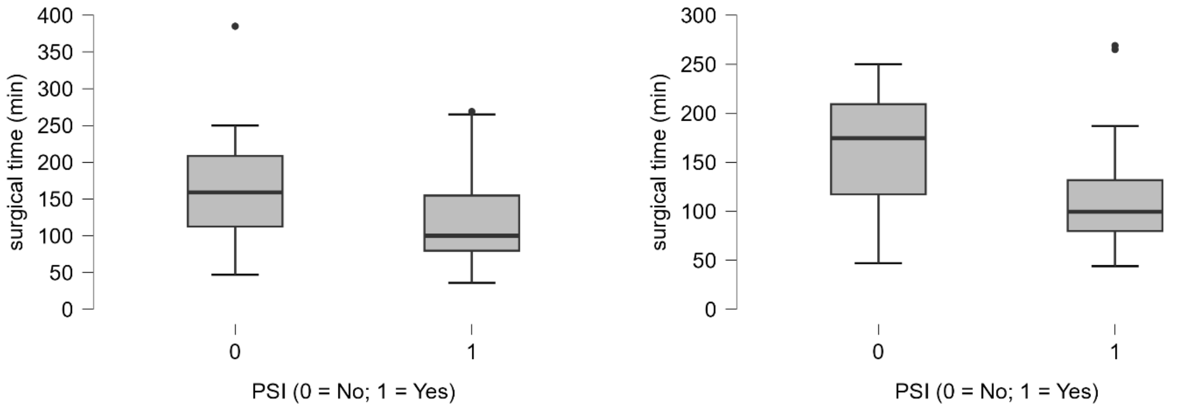

(a) *(b)*

Figure 94. Boxplots showing surgical times for long bones of lower limbs (a) and femoral (b) procedures performed with or without PSIs.

Considering the whole cohort of 99 procedures, the mean number of fluoroscopy shots with VSP alone was 25.1 (SD 24.1; range 1–101), compared to 15.7 (SD 12.6; range 3–80) when PSIs were used. This difference was statistically significant ($p = 0.046$), corresponding to a mean reduction of approximately 9 shots. When focusing on the 87 procedures involving long bones of the lower limbs, the difference became more pronounced. The mean number of fluoroscopy shots with VSP alone was 29.3 (SD 24.6; range 1–101), compared to 15.9 (SD 12.8; range 3–80) with PSIs ($p = 0.001$), corresponding to a mean reduction of about 13 shots. In the femoral subcohort, the mean number of shots with VSP alone was 28.6 (SD 22.6; range 1–96), compared to 18 (SD 14.3; range 3–80) with PSIs, resulting in a mean reduction of approximately 11 shots ($p = 0.026$). A stronger effect was observed in the tibial subcohort, with a mean of 30.6 shots for VSP alone (SD 29.4; range 8–101) and 11.6 for PSIs (SD 7.6; range 4–32), corresponding to a mean reduction of 19 shots, which was statistically significant ($p = 0.004$). Boxplots illustrating these differences are shown in Figure 95.

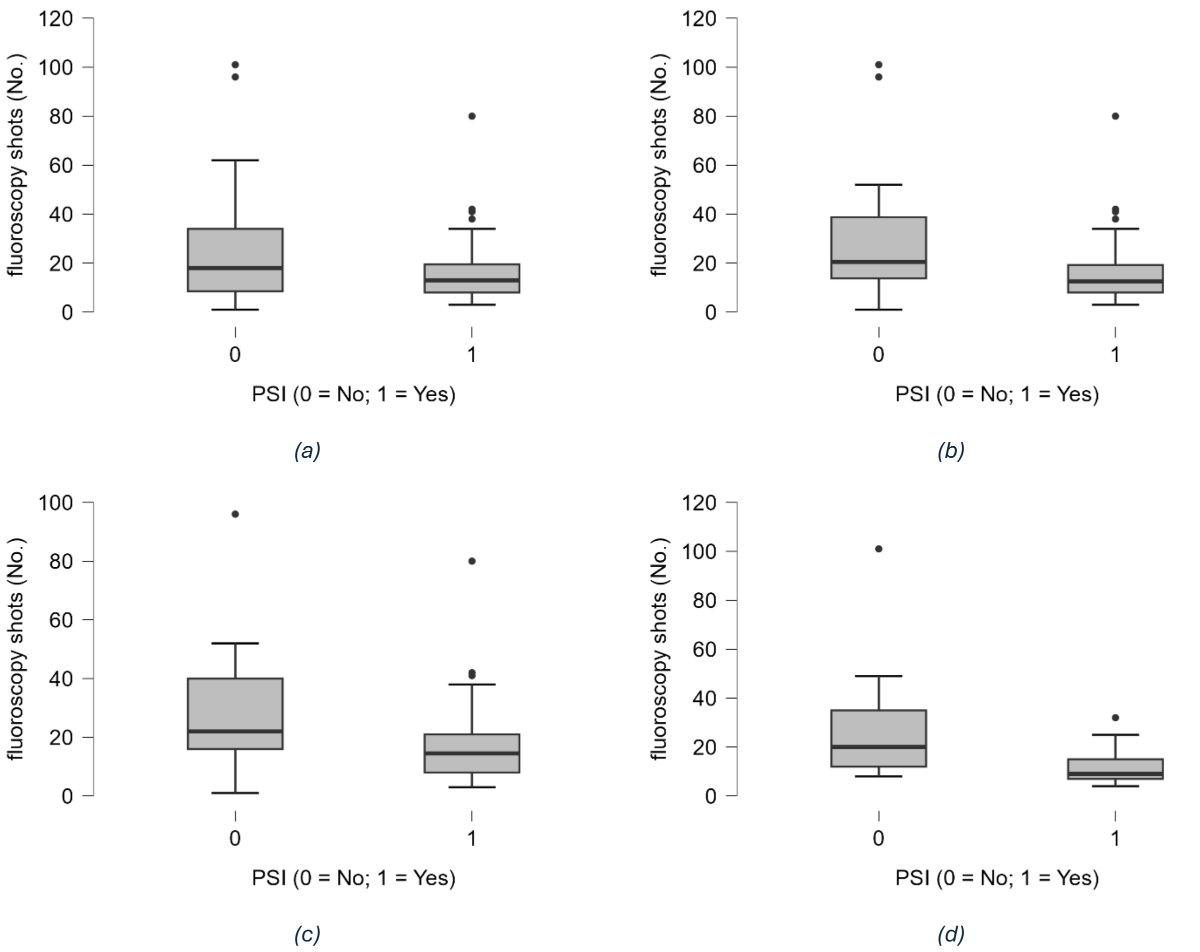

Figure 95. Boxplots showing the number of intraoperative fluoroscopy shots with VSP alone versus VSP combined with PSIs: (a) Entire cohort of 99 procedures; (b) long bone procedures of the lower limb; (c) femoral procedures; (d) tibial procedures.

A total of 71 procedures involved angular correction. However, foot procedures were excluded from the analysis due to the lack of a reliable and comparable postoperative radiographic evaluation. In foot deformities, the Ilizarov method used to quantify angular correction in long bones is not directly applicable, as postoperative assessment of the foot relies on dedicated weight-bearing radiographs acquired at specific angulations, which are not directly comparable with the imaging protocol used for the rest of the cohort. Moreover, corrections were highly complex, involving multiple procedures and multiple osteotomies per patient, often addressing several angular deformities simultaneously. This made it impossible to attribute a distinct postoperative angular outcome to each individual correction. Finally, the limited number of patients (3 patients, 4 procedures) further precluded meaningful analysis.

The remaining 67 cases (21 with VSP alone and 46 with VSP plus PSI) were assessed for achieved correction through postoperative radiographic measurements. No improvement in accuracy was observed with the use of PSIs. The planned correction varied widely, with a mean of 27.1° (range 7–151°). The mean absolute deviation from the planned correction was 6.4° (SD 5.5; range 0–19; percentage deviation 0.22, SD 0.16; range 0–0.56) with VSP alone, and 6.0° (SD 7.4; range 0–38; percentage deviation 0.28, SD 0.36; range 0–1.9) with PSIs. The difference was not statistically significant (absolute deviation: $p = 0.80$; percentage deviation: $p = 0.47$). Boxplots illustrating these results are shown in Figure 96.

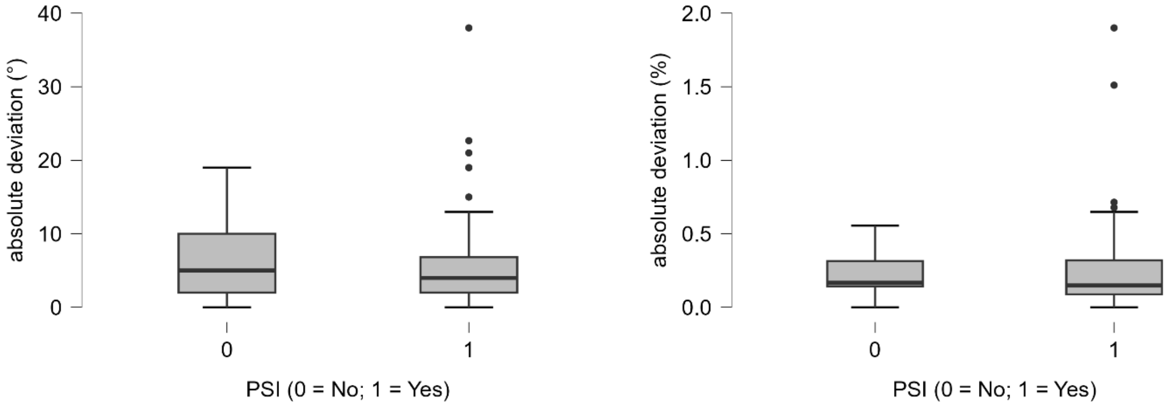

(a) *(b)*

Figure 96. Boxplots of angular correction accuracy in procedures planned with VSP alone versus VSP plus PSIs: (a) absolute deviation from the planned correction (°); (b) absolute percentage deviation from the planned correction.

The data were also analysed after further stratification by bone segment (femur only, distal femur, proximal femur, tibia only, proximal tibia, distal tibia), but no statistically significant differences were observed

Complications occurred in 13 of 63 procedures performed with PSIs and in 11 of 36 procedures performed with VSP alone. The difference was not statistically significant ($p = 0.27$), consistent with the findings from upper limb procedures and confirming that the use of PSIs is associated with a complication rate comparable to traditional surgery and can therefore be considered a safe approach.

In total, 137 PSIs were designed, 3D printed, sterilized, and used across 63 lower limb procedures. Technical issues related to PSIs were reported in a limited number of cases. One guide underwent slight deformation that made its use more challenging but still feasible. In another case, positioning was difficult because the guide did not sufficiently wrap around the bone. Eight cases involved segmentation of 3D models reconstructed from torsional CT axes, which are of poor quality and prevented PSIs optimal final fitting. One PSI fractured, likely due to excessive humidity during the manufacturing process, which may have impaired interlayer adhesion. In another case, the instruments were considered too bulky by the surgeon due to an inaccurate evaluation during the planning phase.

5.2.3. Bone graft subcohort

A total of 37 procedures were performed in 27 patients (mean age 11.4 years; SD 4.4; range 5.5–19.2; 17 females and 11 males) that involved the use of a bone graft, regardless of the anatomical site. Sixteen procedures were performed on the right side and 12 on the left. In one case, two procedures were carried out in a single surgical session, as the patient required bilateral grafting.

According to anatomical distribution, bone graft procedures included 2 involving the pelvis, 4 the foot, 1 the clavicle, 4 the distal femur, 11 the proximal tibia, 3 the tibial diaphysis, 3 the distal tibia, 1 the proximal radius, 2 the distal radius, 6 the proximal ulna, and 1 the ulnar diaphysis.

The graft size was highly variable, with a mean height of 13.4 mm (SD 8.35; range 2–44.4), which represents a rather wide distribution. A box plot of graft height stratified by anatomical area further illustrates this variability (Figure 97), highlighting the broad dispersion and the limited number of cases in some categories.

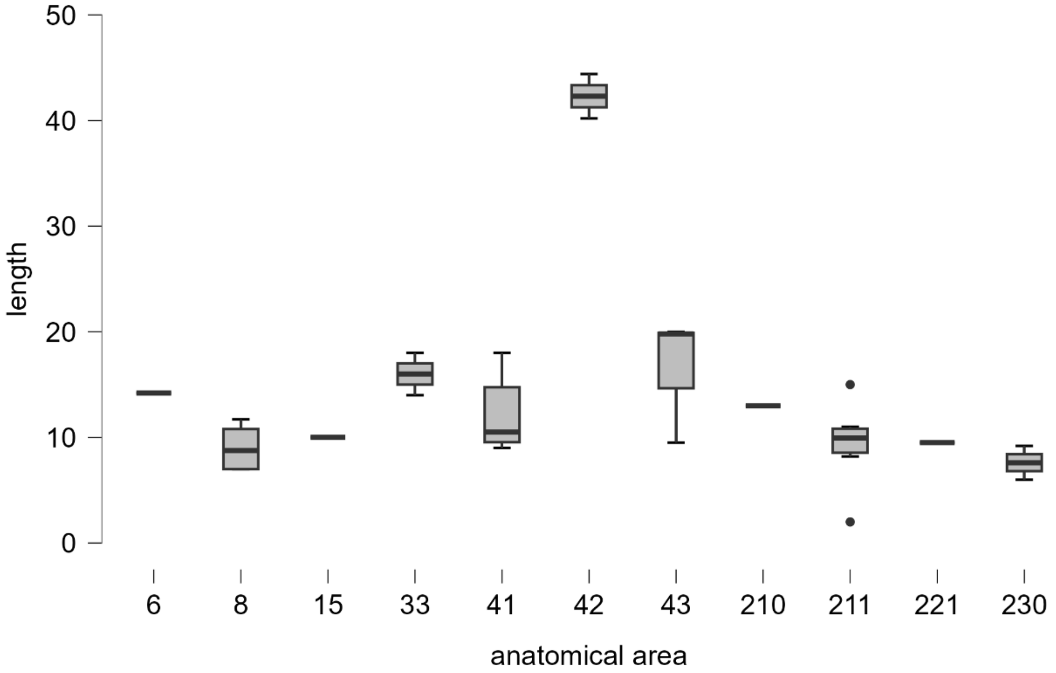

Figure 97. Boxplot of graft height (mm) stratified by anatomical area, according to the AO/OTA Fracture and Dislocation Classification Compendium [166].

Of the 37 planned bone grafts, 11 were autologous and 26 homologous. Among the 11 autologous grafts, 9 were local, obtained by reshaping and reorienting bone removed during the correction and reused at the same site, thereby avoiding additional incisions for harvesting from another anatomical area. One of these was modelled with the aid of GSIs. The remaining 2 autologous grafts were harvested from another site of the patient, most commonly the iliac crest. Among the 26 homologous grafts, 14 were delivered to the operating room in raw form: 1 was shaped intraoperatively using a GSI, while the others were modelled freehand according to the dimensions defined during VSP. The remaining 12 homologous grafts were pre-shaped by the BTM, 2 with the aid of GSIs and 10 following only VSP specifications. In total, 5 of the 38 procedures involved grafts shaped with the aid of GSIs, while the others were modelled freehand based solely on VSP measurements. Overall, 5 GSIs for bone graft modelling were designed, 3D printed, sterilized, and used. Among the 38 procedures, PSIs were employed in 17 cases.

The mean surgical time for procedures involving grafts shaped freehand based solely on VSP measurements was 147.9 minutes (SD 73.4; range 41–385), whereas for those shaped with the aid of GSIs it was 126.8 minutes (SD 24.0; range 100–157). Although the latter group showed a lower mean surgical time by an average of 21 minutes, the difference was not statistically significant ($p = 0.375$).

As for the use of intraoperative fluoroscopy, the mean number of shots was 17.0 (SD 17.8; range 3–101) when grafts were shaped freehand with VSP measurement guidance, and 12.3

(SD 8.1; range 3–20) when shaped with the aid of GSIs. Although the number was lower in the latter group, the difference was not statistically significant (p = 0.330).

Among the 37 procedures with grafts, 31 involved angular corrections. The planned correction varied widely, with a mean of 25.8° (range 10-60°). Accuracy did not appear to improve with the use of GSIs: the mean absolute deviation from the planned correction was 4.6° (SD 4.4; range 0–17; percentage deviation 0.19, SD 0.15; range 0–0.53) for grafts shaped freehand with VSP measurements, and 6.8° (SD 8.3; range 1–19; percentage deviation 0.29, SD 0.29; range 0.1–0.68) for grafts shaped with GSIs. The differences were not statistically significant (absolute deviation: p = 0.582; percentage deviation: p = 0.722).

The data were also analysed after further stratification by bone segment, but no statistically significant differences were observed, also because the cohort with the use of GSIs is really limited (for angular correction, 4 cases with GSIs and 27 with VSP alone).

Boxplots illustrating these results are shown in Figure 98.

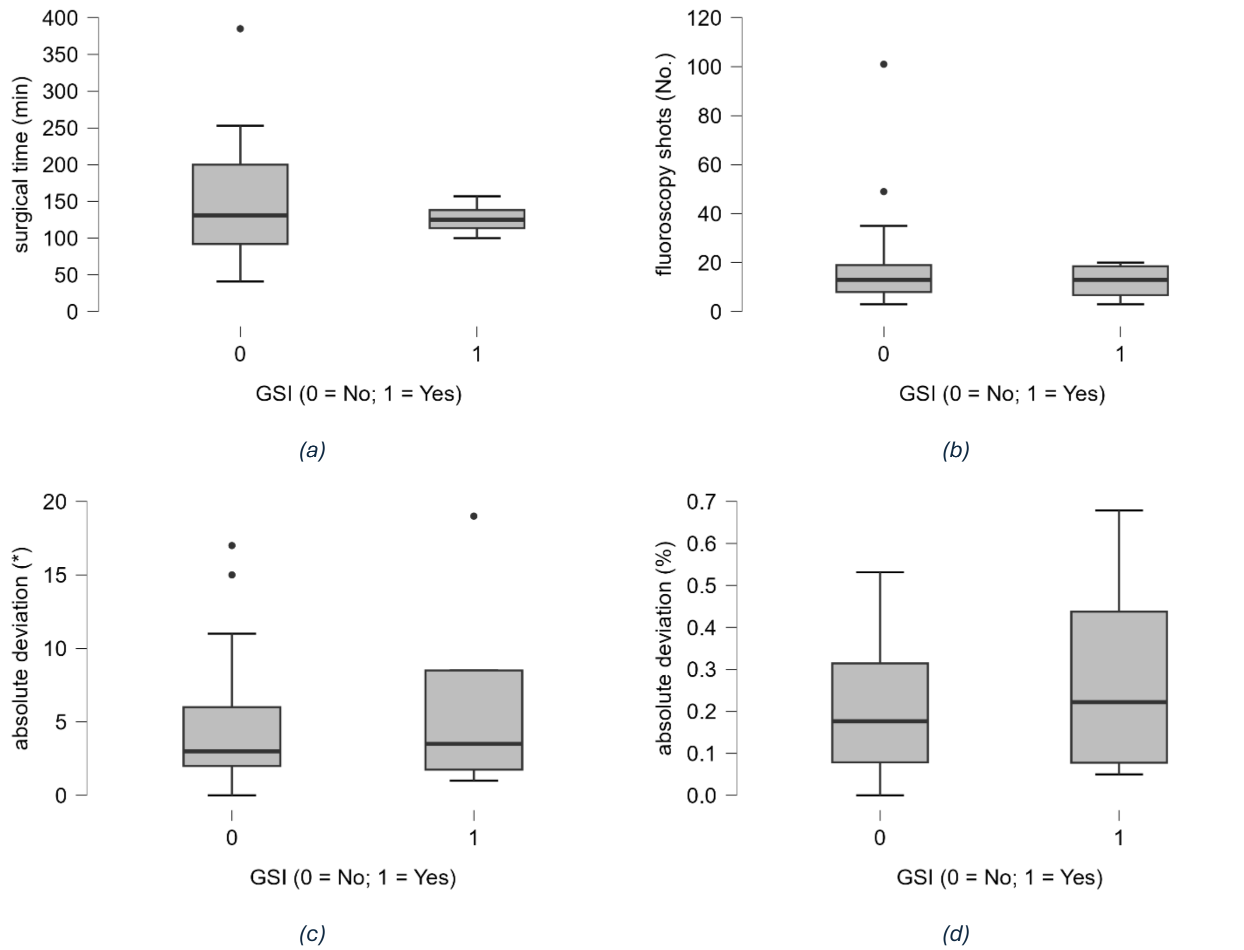

Figure 98. Boxplots illustrating outcomes of procedures involving bone grafts shaped freehand with VSP measurements versus with the aid of GSIs: (a) surgical time; (b) number of intraoperative fluoroscopy shots; (c) absolute deviation from planned angular correction; (d) percentage deviation from planned angular correction.

Complications occurred in 1 of 4 procedures performed with bone grafts shaped using GSIs and in 11 of 33 procedures performed with grafts shaped freehand following VSP alone. The difference was not statistically significant (p = 0.74), consistent with the findings from both upper and lower limb procedures with PSIs. Although the number of procedures performed with GSIs is currently limited, these devices share the same design and manufacturing process as PSIs, differing only in their application to the graft rather than directly to the patient. For this reason, it is reasonable to conclude that GSIs, like PSIs, can be considered a safe approach, with a complication rate comparable to traditional surgery. To date, no technical issues related to GSIs have been reported.

5.2.4. Oncologic subcohort

A total of 22 patients underwent 22 procedures for tumour resection, with a mean age of 16.2 years (SD 11.4; range 3.3-48.3). Although the cohort is primarily composed of paediatric patients, two adult cases were included. This decision reflects a protocol update aimed at extending the application of patient-specific technologies to young adult patients (up to 50 years of age) particularly in the oncological setting, where complex resections may benefit from customized preoperative planning and tools. The cohort included 10 female and 12 male patients, with an equal laterality distribution (11 right-sided and 11 left-sided resections).

The anatomical sites of tumour resection were: 1 pelvis, 1 foot, 1 proximal humerus, 2 proximal femur, 2 femoral diaphysis, 6 distal femur, 7 proximal tibia, 1 tibial diaphysis, and 1 distal tibia. This cohort is highly heterogeneous, and it is not possible to obtain robust statistical results. Nevertheless, descriptive and exploratory analyses were conducted to characterize the main surgical variables and evaluate the overall feasibility and accuracy of the proposed patient-specific workflow.

In 8 cases, the resection involved the joint surface. Of these, 3 patients underwent reconstruction with prostheses, while 5 received composite prosthetic reconstructions, in which the implant was anchored to structural allografts shaped to match the native anatomy. In the remaining case, an autograft harvested from the fibula was used to reconstruct the third metatarsal, including the distal joint surface. This was the only oncological case in which an autograft was employed, and no prosthetic components were implanted.

Among the 22 total procedures, excluding the 3 cases reconstructed with prostheses alone, the remaining 19 procedures involved bone grafts (18 homologous grafts from donors, provided by the BTM, and 1 autograft harvested from the patient). In only one case, the graft was pre-cut in a clean room by BTM using GSIs and delivered to the operating room already shaped. In the other 18 cases, including the autograft, the graft was shaped directly in the operating room: 16 with the use of GSIs and 2 using only measurements obtained during VSP, without the aid of cutting guides.

Across the entire cohort of 22 cases, only two procedures were performed without PSIs, relying solely on VSP. These two cases correspond to the same procedures in which GSIs were not used for graft shaping.

To improve clarity, the distribution of cases and the corresponding graft preparation methods are summarized in Figure 99.

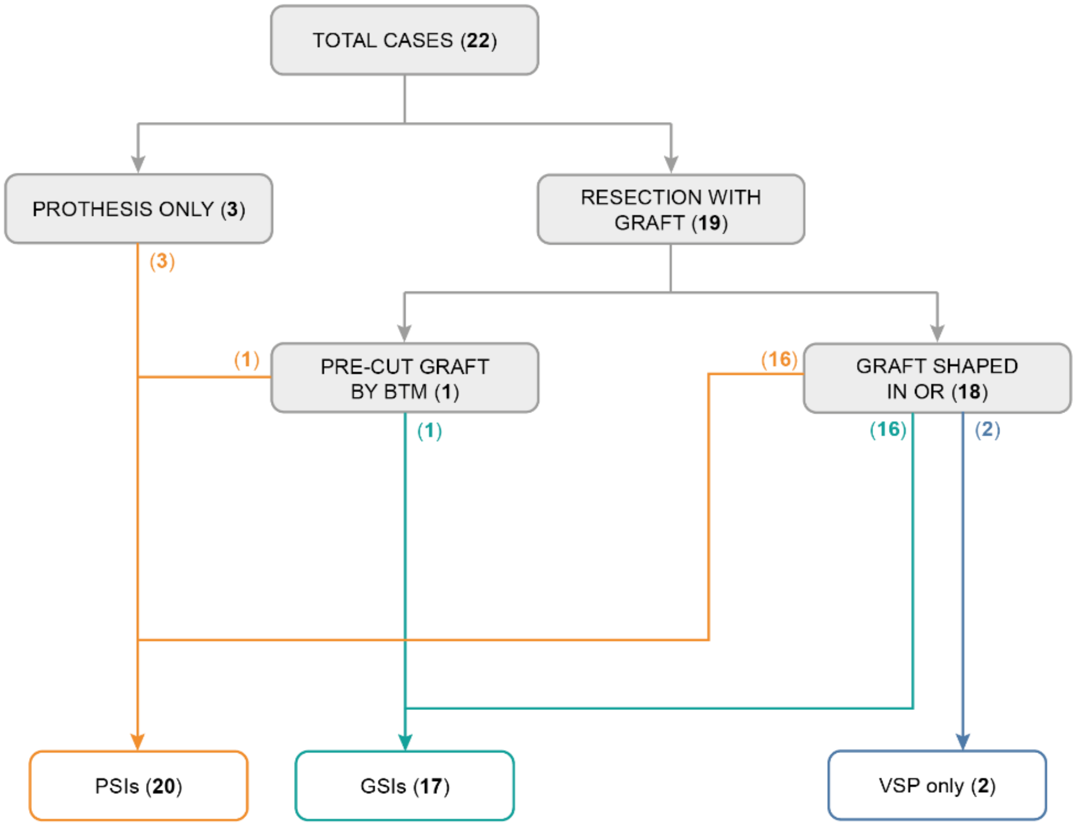

Figure 99. Flowchart illustrating the distribution of the 22 oncological resections according to the type of reconstruction and graft preparation.

Due to the limited number of procedures realised with VSP alone it was not possible to compare the two groups. However, an overview of the 17 procedures planned with both GSIs and PSIs can be provided. One case was excluded from the analysis because intraoperatively the tumour had grown beyond the planned margins, preventing the use of both PSIs and GSIs.

Among the remaining 16 procedures, the mean surgical time was 213.9 min (SD 55.2; range 108–323), and the mean fluoroscopy use was 11.7 shots (SD 8.6; range 0–24). The absolute error in graft length (absolute difference between planned and achieved values) averaged 6.2 mm (SD 5.9; range 0–23). Considering the signed values, 10 procedures (62.5%) resulted in over-resection, 4 (25.0%) in under-resection, and 2 (12.5%) showed exact correspondence between the planned and performed resection length. When expressed as a percentage of the planned resection length, the mean value was 0.98 (SD 0.07; range 0.78–1.11). Despite two outliers (–15 mm and +23 mm), most deviations remained within a few millimetres, and the relative error was consistently limited, ranging from –22% to +11% of the intended cut length (see Figure 100). Over-resections, although not desirable, usually result only in a slight loss of additional healthy bone or minor length discrepancies, whereas under-resections are more relevant to monitor, as they may reduce the safety margin required for oncological resections.

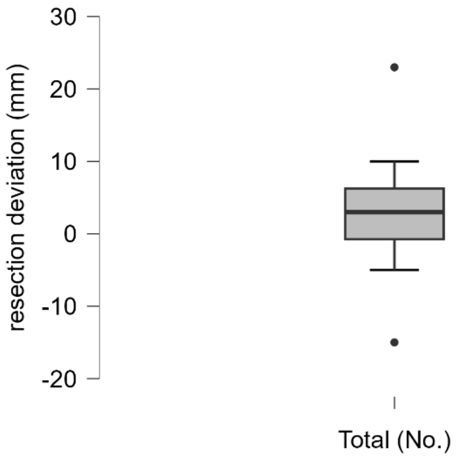

Figure 100. Boxplot of resection deviations in the 16 valid cases performed with both PSIs and GSIs.

5.2.5. Overall cohort

Overall, 170 procedures were performed in 137 patients. Of these, 144 (114 patients) underwent Virtual Surgical Planning (VSP) to define the optimal treatment. A total of 91 procedures involved angular correction. The planned correction varied considerably across the cohort, with a mean of 26.3° (range 3–151°).

Of the 144 procedures, 58 involved the use of bone grafts or massive bone allografts (13 autologous and 45 homologous), 22 of which were shaped using GSIs either intraoperatively or pre-modelled in the BTM cleanroom. Compared with grafts shaped only according to VSP measurements, cases using GSIs did not present unusual technical issues or complications. Complications occurred in 12 of 36 grafts shaped without GSIs and in 6 of 16 grafts shaped with GSIs ($p = 0.628$). Although the difference was not statistically significant, this result is consistent with complication rates observed in traditional surgery, confirming that the use of GSIs is at least as safe as standard practice.

In 93 cases, sterilizable PSIs were also designed and manufactured to replicate the VSP intraoperatively, with a total of 199 guides produced (per procedure: mean 2; SD 1; range 1–9). Similarly to what was just observed for GSIs and consistently with the results of the different sub-cohorts already analysed, the comparison of complications between procedures performed with VSP alone and those performed with the use of PSIs did not reveal a significant difference ($p = 0.721$), with 14/51 complications for VSP alone and 23/70 for PSIs. Once again, these rates are comparable to those of traditional surgery, confirming the safety of PSI use.

Interestingly, both surgical time and the number of fluoroscopic shots were significantly higher in patients who developed complications ($p < 0.001$ and $p = 0.007$, respectively). Correlation analysis revealed a moderate positive relationship between surgical time and fluoroscopy use ($r = 0.422$, $p < 0.001$), indicating that longer procedures typically required more intraoperative imaging. When entered separately into logistic regression models, both variables were significantly associated with complication risk (surgical time: OR 1.013, $p < 0.001$; fluoroscopy: OR 1.028, $p = 0.015$). However, when included together in the same model, only surgical time remained significant ($p < 0.001$), while fluoroscopy exposure lost significance ($p = 0.448$), suggesting that the relationship between fluoroscopy use and complications is largely explained by its correlation with operative duration. The odds ratio of 1.013 indicates that each additional minute of surgery increases the odds of developing a complication by approximately 1.3%. Although the effect per minute is modest, the cumulative impact is clinically relevant: for every 50 additional minutes of surgery, the odds of complications nearly double, and for every 100 minutes they triple.

Technical issues were reported for PSIs in 12 cases (6% of the total PSIs): 8 cases (4%) related to suboptimal fitting due to poor-quality torsional CT reconstructions, 1 (0.5%) guide fracture, 1 (0.5%) deformation, and 2 (1%) cases of excessive bulkiness.

Given the heterogeneity of the overall cohort, evaluating statistical significance for surgical time and fluoroscopy is of limited value, as the variability across procedures prevents meaningful comparisons. However, complication rates and technical issues can be reliably compared, as they are less dependent on the specific type of procedure, supporting the interpretation of safety outcomes.

5.3. Discussion

5.3.1. Upper limbs

The upper limb analysis included all procedures performed with VSP and VSP combined with PSIs over the years. This cohort, however, was small and heterogeneous, involving different anatomical segments and surgical indications. Therefore, statistical power was limited. Despite this, PSI use showed a trend toward shorter operative times and reduced intraoperative fluoroscopy, the latter approaching statistical significance, while no improvement was observed in angular correction accuracy.

Benayoun et al. [168] similarly reported, in children with complex forearm deformities, a significant reduction in surgical time with PSIs (129 ± 35.6 min vs. 171 ± 48.6 min; $p = 0.02$), lower intraoperative imaging requirements (38 ± 27 µGy vs. 125 ± 107 µGy; $p = 0.08$), comparable complication rates, and good recovery of prono–supination. In line with these findings, Hu et al. [169] demonstrated significantly shorter operating times in cubitus varus correction with 3D guides compared to conventional surgery ($p < 0.001$), without increased complications, and with significantly better symmetry between affected and contralateral sides ($p < 0.001$).

Overall, the literature supports the use of 3D printed PSIs in upper limb surgery, highlighting improved surgical precision and outcomes, with reductions in operative time and intraoperative radiation exposure [170–172]. Moreover, the costs of these technologies may be compensated by reductions in operative time and complication rates, ultimately suggesting a potential reduction in overall operative costs [169,173].

Our analysis of the upper limb cohort has several limitations. The heterogeneity and limited size of the cohort likely introduced bias and may explain the lack of statistical significance. Postoperative angular correction measurements were also challenging due to radiographic quality and projection variability, potentially introducing error. Nonetheless, no increase in complications, such as infections, was observed, confirming a safety profile comparable to traditional surgery. Functional outcomes were not assessed, as they were highly heterogeneous and are more appropriately addressed within the clinical domain.

5.3.2. Lower limbs

Given the numerosity of the cohort, our analysis focused primarily on the lower limb and the subgroups of femoral and tibial procedures. Zheng et al found an average decrease in surgical time from 47 minutes to 21 minutes, comparing proximal femur osteotomies performed with conventional technique and using cutting guides [174]. Sun et al. demonstrated that 3D printed osteotomy guide plates for developmental dysplasia of the hip significantly reduced surgical time (2.12 ± 0.13 h vs. 2.69 ± 0.10 h, $P < 0.001$), with a time saving of 57 minutes, comparable in magnitude to the 48 minutes observed in our series. They also reported a significant reduction in femoral procedure time (0.39 ± 0.08 hours vs. 0.70 ± 0.08 hours, $P < 0.001$), fluoroscopy use (2.56 ± 0.96 vs. 6.40 ± 0.99, $P < 0.001$) and intraoperative blood loss [175]. These results are consistent with the literature on developmental dysplasia of the hip, with Shi et al. also reporting increased precision in achieving the planned osteotomy angles [176].

The use of PSIs in the lower limb has generally been associated with comparable benefits across different applications. In the tibia, some studies reported their use as an aid in alignment during distraction osteogenesis with the Ilizarov technique, helping to preserve the planned angulation intraoperatively and to facilitate the installation of the ring fixator. Their application was shown to halve surgical time, reduce intraoperative fluoroscopy, and improve the accuracy of reduction [177]. Although no statistically significant difference in accuracy was observed when comparing procedures performed with or without PSIs, Belvedere et al. [178] reported a mean discrepancy of 1.2° ± 1.4° between the planned and achieved alignment when using a 3D-printed surgical guide and fixation plate for varus knee correction in high tibial osteotomy. Furthermore, they documented a reduction in surgical time of approximately 30%, which is consistent with our findings (mean operative time of 165 minutes with VSP alone vs. 121 minutes with PSI). Zaffagnini et al. [84] reported that a personalised 3D-printed surgical guide and fixation device for high tibial osteotomy resulted in a significant mean deviation of 2.1° ± 2.0° in the Hip-Knee-Ankle angle and 0.2° ± 0.4° in posterior tibial slope at six months.

Although we could not perform a specific evaluation for the foot, the literature reports several studies on the use of PSIs in foot surgery, showing improved precision, safety, and accuracy, along with shorter operative times, reduced radiation exposure, and decreased intraoperative blood loss [179,180].

Overall, these outcomes agree with the evidence available for femoral, tibial, and more generally for lower limb procedures, and are consistent with our analysis [181,182].

5.3.3. Bone grafts

Only a few studies in the literature have addressed the use of 3D printed instruments specifically designed for bone graft modelling and cutting. Lin et al. [183] applied this approach in Total Hip Arthroplasty (THA) for developmental dysplasia of the hip in adult female patients, in a small cohort without a control group. In their experience, 3D printed instruments were used both to guide bone cuts for THA and to prepare the autograft, with no postoperative complications observed, including implant loosening, stem sinking, graft loosening, or dislocation. Similarly, Huotilainen et al. [184] described a case in which a 3D printed patient-specific template was used to model a fresh osteochondral allograft, achieving a good fit at implantation.

However, no studies were found in the literature reporting the use of GSIs in larger cohorts, limiting direct comparison with our results.

5.3.4. Oncologic

The absence of a sufficiently large control group of surgeries performed without GSIs or PSIs did not allow for statistical comparisons. Nonetheless, the analysis showed that the absolute error, calculated by comparing the planned resection length with the pathologist's report, averaged 6.2 mm. Expressed as a percentage of the planned resection, most deviations were limited to a few millimetres, with relative errors ranging between –22% and +11%. Considering that the oncological resection margin is generally set at about 1 cm, these deviations remained within clinically acceptable limits. Over-resections, although not ideal, generally resulted in only minor loss of healthy bone, whereas under-resections are more critical as they may compromise oncological safety margins. In our cohort, however, under-resections were relatively infrequent (25% of cases), usually limited to –5 mm with only one outlier at –15 mm. Importantly, despite these deviations, the pathologist's report confirmed that all resection margins were oncologically safe.

Comparable findings have been reported in the literature. Evrard et al. [185] used PSIs for bone tumour resection and GSIs for shaping allografts, finding a mean difference between planned and obtained margins of 0.4 ± 1.8 mm (range –4.4 to +5 mm), close to our results. Müller et al. [186] analysed 11 resected surgical specimens with CT-based 3D modelling and reported a mean deviation of 3.6 ± 2.5 mm (range –6.4 to +7.7 mm), noting larger errors in complex curved osteotomies with multiple planes. Wang et al. [187] compared traditional osteotomies, conventional PSIs, and PSIs enhanced with fluoroscopic navigation (with K-wire reference holes for intraoperative alignment). The maximum deviation from the preoperative plan was 7.6 mm in the manual group, 7.2 mm in the conventional PSI group, and 3.4 mm in the fluoroscopically assisted PSI group, confirming improved accuracy compared with both freehand cutting and conventional PSIs.

A recent systematic review on bone tumour resections also concluded that PSIs and surgical navigation yield similar results in terms of negative margins, cut accuracy, local recurrence, and functional outcomes, with a planned margin of ≥5 mm considered oncologically safe for both long bones and pelvis [188]. PSIs were associated with shorter operative times, although limitations such as errors in long osteotomies and restricted working space were highlighted. These findings confirm that no 'perfect' technique exists. However, PSIs and, by extension, GSIs can be considered competitive and effective solutions in selected clinical scenarios.

Another potential advantage of PSIs and GSIs use is the reduction of intraoperative fluoroscopic dependency. Although our cohort cannot definitively prove a decrease in radiation exposure due to the absence of a control group, the mean number of fluoroscopic shots (11.7 ± 8.6) appears relatively modest. Similarly, Kamat et al. [87] reported a significant reduction in fluoroscopy exposure, with a mean exposure time of 4.09 minutes corresponding to 0.1–0.22 mSv. They also documented a mean resection margin of 1.2 mm and a reduction in operative time of 25 minutes compared to conventional techniques ($p = 0.049$), while blood loss did not differ significantly ($p = 0.24$). Overall, they concluded that 3D-assisted resections ensured adequate oncological clearance while minimizing resection length, surgical time, and radiation exposure.

Although our series lacks a conventional control group, our data support the feasibility, oncological safety, and acceptable precision of PSIs and GSIs use. Future comparative studies are warranted to further quantify their role in improving surgical accuracy, surgical times and reducing radiation exposure.

5.3.5. Overall

This study presents the experience of a single-centre institution with VSP primarily applied to deformity correction and tumour resection in growing-age patients, with particular focus on the role and impact of PSIs and eventually GSIs for bone graft. It aims to analyse one of the largest and most heterogeneous cohorts reported to date. Beyond the subgroup analyses, several relevant findings also emerged from the evaluation of the overall cohort.

The results confirm that in-hospital 3D printing of PSIs and GSIs to support VSP-assisted surgery is a safe and effective method for achieving precise corrections in paediatric orthopaedic procedures. Across all subgroups, this approach significantly reduced surgical time and the need for intraoperative fluoroscopy, without increasing complication rates. These findings are consistent with previous studies, which also reported reduced intraoperative blood loss, although this parameter was not considered in our evaluations [10].

Our study highlighted that both longer operative time and higher fluoroscopic exposure were initially associated with postoperative complications. However, multivariate analysis showed that only operative duration independently predicted complication risk, while fluoroscopy exposure lost significance once surgical time was accounted for. This finding suggests that the apparent effect of fluoroscopy is largely mediated by longer and more complex procedures, which inherently carry a higher risk of complications. The literature consistently indicates that prolonged operative time increases the likelihood of postoperative complications, with a 20% increase in surgical duration estimated to raise the odds of surgical site infection in orthopaedic procedures by 3.6 to 7.4 times [189]. Reducing operative time in such complex cases is therefore crucial, not only for a matter of costs but also to minimize complications and enhance surgical performance, but also to allow multiple corrections to be performed during the same session, thereby decreasing the need for repeated interventions.

Based on previous studies [4], the direct production cost of a single patient-specific cutting guide (including printer amortization, material costs, and operator time) has been estimated at approximately €485. However, this estimation does not account for the potential indirect cost savings associated with reduced operative time, decreased use of fluoroscopy and energy resources, and optimized utilization of operating room personnel. Although these factors are expected to contribute substantially to the overall cost–benefit balance, they have not yet been quantified in economic terms and will be addressed in future dedicated studies. In addition, potential downstream effects, such as a reduction in complication-related reoperations, shorter hospital stays, and lower overall resource utilization, may further influence the economic impact of these technologies. While these aspects were not assessed in the present work, their relationship with operative time and surgical complexity is well established in the literature and warrants investigation in future cost-effectiveness analyses [190,191].

Only about 6% of the guides experienced technical issues, indicating a generally robust design and manufacturing process. Most problems involved suboptimal fitting, bulkiness, or minor deformations, mainly related to input data quality and design accuracy. The eight cases of imperfect fitting (4%) were the most frequent and highlight how segmentation or anatomical reconstruction errors can affect guide conformity. Except for one fractured guide, all issues were manageable intraoperatively. Although the low rate of technical failures supports the clinical feasibility of PSIs, it also underscores the importance of quality control and preoperative validation, as similarly emphasized in previous reports describing occasional fitting problems or intraoperative adjustments required for 3D printed guides [89,90]. Beyond technical aspects, delays between imaging and surgery may allow anatomical changes to occur, representing a known limitation of template-based approaches and limiting their applicability in emergency or rapidly evolving conditions [192].

5.4. Limitations

This study presents several limitations that should be discussed. The main limitation lies in the heterogeneity of the cohort, which included patients of different ages, diagnoses, and anatomical districts, as well as various surgical procedures such as osteotomies, massive resections, and graft implantations. This variability reduces comparability across cases and may introduce selection bias. Moreover, the limited sample size of some subgroups decreases the statistical power and the ability to detect smaller effects. Future research should adopt a more rationalized approach, focusing on specific anatomical regions and homogeneous diagnostic or treatment categories to reduce heterogeneity and strengthen statistical analyses.

Another relevant limitation concerns the evaluation of correction accuracy. Postoperative angular corrections were not assessed by a radiologist but by the author, based solely on single-plane postoperative radiographs. Moreover, since VSP, PSIs and GSIs are specifically designed to enable three-dimensional, multifocal, or multisegmental corrections, enhancing precision and confidence, particularly in patients with small skeletal dimensions, a comprehensive postoperative evaluation including torsional assessment would be ideal. However, this would require postoperative CT scans, which are not routinely performed, especially in paediatric patients.

The variability in imaging quality also represents a limitation, as low-resolution torsional CT scans may have affected anatomical reconstruction accuracy and PSI fitting. In addition, the observed reduction in surgical time over the years for both VSP and PSI-assisted procedures suggests the presence of a learning curve effect, involving both the surgical team and the design engineers, with greater experience likely contributing to improved outcomes.

Some outcome measures, including operative time and fluoroscopy exposure, exhibit considerable variability due to intrinsic differences among cases, making data aggregation and statistical analysis non-trivial. Although complications and technical issues are generally considered more objective outcomes, they may still be affected by reporting bias, since the underlying cause of a complication cannot always be unequivocally attributed to the use of VSP, PSIs, or to patient- and procedure-related factors.

Another limitation is the lack of systematic follow-up, as the study focused mainly on intra- and perioperative actions and relevant complications. Long-term outcomes such as graft integration, remodelling, rejection, or functional recovery were not assessed and should be addressed in future studies. Furthermore, the absence of a control group of conventional surgeries limits the possibility of direct comparison. The included cases often involved severe and rare deformities, and retrospective comparisons with traditionally planned procedures are challenging, since conventional planning data are rarely documented. Future case control or prospective randomized studies comparing traditional surgery, VSP only, and VSP with PSIs/GSIs assisted approaches are therefore necessary to determine the true clinical efficacy of these technologies.

Finally, this was a single-centre study conducted within a specialized institution with consolidated workflows and expertise in 3D planning and printing. Therefore, the results may not be fully generalizable to other centres with different resources or levels of expertise. Future work should include external validation through multicentric studies or collaborations to confirm reproducibility and support the scalability of the approach.

5.5. Conclusion

This study presents one of the largest single-centre experiences with VSP, PSIs, and GSIs in paediatric orthopaedic surgery. The findings confirm the clinical feasibility and safety of in-hospital 3D printing workflows, showing reduced operative time and fluoroscopy use without increasing complication rates. These technologies enhance surgical efficiency and may allow multiple corrections within a single session, reducing hospitalization and overall surgical burden.

However, the heterogeneity of the cohort, the retrospective design, and the limited size of specific subgroups restrict the generalizability of the results. Imaging quality also proved critical, as low-resolution or distorted CT scans occasionally affected PSI fitting.

Future studies should be prospective and multicentric and should focus on more homogeneous cohorts. A shared protocol for virtual planning, PSI/GSI design, and postoperative evaluation would also enable meaningful comparison and validation across centres. Such collaborative efforts would strengthen the evidence supporting the proposed workflow and facilitate its scalability and broader integration into clinical practice, particularly for rare and complex paediatric musculoskeletal conditions.

6. ADVANCING PREOPERATIVE PLANNING – IMPROVED OUTCOMES THROUGH MUSCLE PROPERTY INTEGRATION

This chapter has been included to document the 4-months research period abroad carried out at Materialise (Leuven, Belgium) during the PhD program. Due to the highly theoretical and exploratory nature of the work, it must be considered as a research "spin-off" of the main doctoral project.

This chapter addresses a topic that is different yet closely related to the core research themes. Specifically, the literature review conducted at the company focused on the identification of muscle-related parameters (particularly of the shoulder region) that can be extracted from standard medical imaging modalities, with a primary focus on CT.

As for the doctoral project, CT is the main imaging modality used for anatomical model reconstruction, but it is employed exclusively for osseous structures. In contrast, this review examined the relevance of muscular anatomy and characteristics in VSP and outcome prediction, exploring the extractions of meaningful soft tissue data mainly from CT, but also from MRI and ultrasound.

Additionally, the potential application of these techniques to musculoskeletal disorders in pediatric patients was explored, outlining a possible future direction to enhance VSP through the integration of muscular parameters within the current bone-focused workflow.

6.1. Muscle Parameters Contribution to Postoperative Outcomes Prediction – Evidence from Shoulder Arthroplasty (PhD research abroad)

Preoperative planning is increasingly applied in surgical assessment, as it enables a better understanding of the patient's anatomy and provides a three-dimensional view of the morphology of the region of interest. It also supports the design of PSIs, which help achieve the objectives defined in the virtual surgical plan with greater precision [193]. This approach continues to evolve, allowing surgeons to virtually position implants to optimize correction, fixation, and, ideally, postoperative function, while minimizing complications. For instance, in shoulder arthroplasty, preoperative planning can facilitate accurate implant positioning and reduce the risk of bone erosion, such as scapular notching [194].

Shoulder arthroplasty is a well-established and increasingly adopted treatment for a wide range of pathologies, particularly when pain and loss of function (mobility and strength) can not be adequately managed through conservative methods. Its main goal is to restore mobility, reduce pain, and help patients maintain an active lifestyle [195]. In recent years, Reverse Shoulder Arthroplasty (RSA) has gained prominence, surpassing the use of traditional Total Shoulder Arthroplasty (TSA) [196,197]. RSA is primarily indicated for the treatment of end-stage shoulder arthropathy associated with significant rotator cuff deficiency [198] and for TSA revisions. The main indications for RSA are massive rotator cuff tears (MRCT) and the resulting cuff tear arthropathy (CTA). It is also increasingly used in cases of glenohumeral osteoarthritis (OA), particularly when associated with rotator cuff insufficiency. Advanced CTA often leads to pain and reduced range of motion (ROM), causing significant limitations in daily activities. Its design specifically compensates for a deficient or non-functioning rotator cuff by altering shoulder joint biomechanics: the normal ball-and-socket configuration is reversed, the centre of rotation is medialized, and the lever arm of the deltoid muscle is increased [199–201]. These biomechanical changes enable the deltoid to assume the role of the damaged rotator cuff, becoming the primary elevator of the arm and thereby restoring essential movements such as abduction and flexion and relieving pain [202,203].

An important aspect of shoulder arthroplasty planning is the evaluation of muscle properties, which plays a key role in assessing muscle diseases, age-related degeneration, and muscle decline. Muscle morphology and function can reflect underlying conditions, making their quantification essential. Treatment planning relies not only on joint and bone status but also on muscle quality. Identifying correlations between these parameters and clinical outcomes is crucial to improve planning, reduce the risk of failure and manage patient expectations. While implant positioning is critical, an accurate assessment of muscle quality, particularly of the deltoid and rotator cuff, is equally decisive in choosing between TSA and RSA and in predicting postoperative outcomes [204].

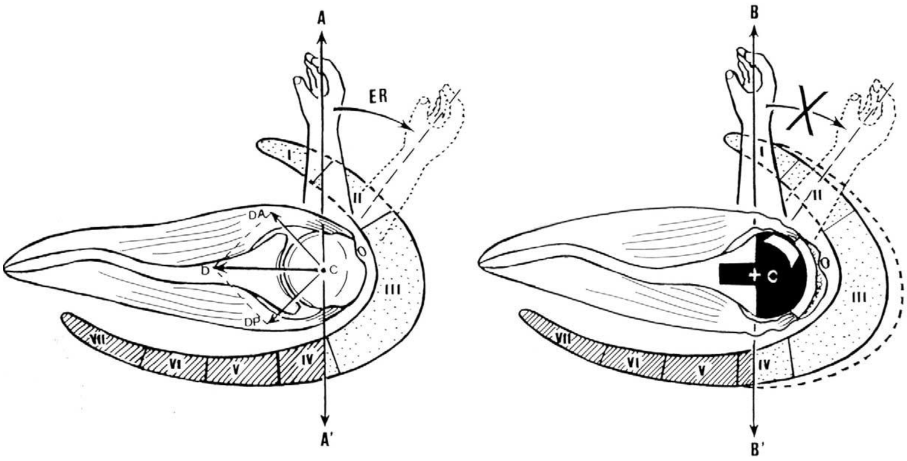

Figure 101. Shoulder external rotation before (left) and after (right) reverse shoulder arthroplasty, illustrating postoperative limitation due to humeral medialization, which reduces the posterior deltoid moment arm for external rotation (ER), with a possible contribution from slackening of the infraspinatus and teres minor. Taken from Boileau et al. [198].

Many studies have examined optimal implant positioning and how outcomes vary with placement modifications [205]. However, muscle status plays a crucial role and can significantly influence these strategies. For instance, while RSA consistently restores abduction and forward elevation - provided the deltoid is functional and in good condition - its effectiveness in improving movements such as external rotation remains uncertain, as it depends largely on muscle quality, particularly that of the rotator cuff [206,207]. In RSA, the anterior and posterior deltoid fibres are increasingly recruited for abduction and elevation, but this shift toward a more vertical force vector often reduces their rotational contribution[208]. Loss of anterior deltoid input to internal rotation can be compensated by intact internal rotators, whereas compromise of the posterior deltoid leaves external rotation reliant solely on the infraspinatus and teres minor [198,209,210]. A retrospective study by Kim et al. involving a cohort of 77 patients found that external rotation and internal rotation are particularly difficult to restore. This issue is significant because, while external rotation is often associated with overhead activities, internal rotation is critical for hygiene [195].

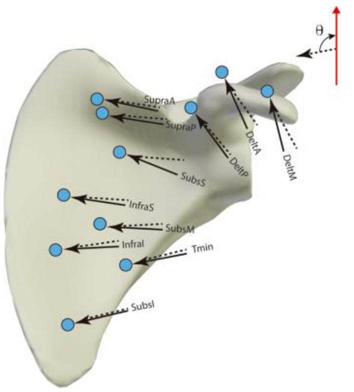

Figure 102. Muscle lines of action in the scapular plane for the anatomic and reverse shoulder at 0° of humeral abduction relative to a line parallel to the glenoid base (red arrow). Dashed arrows represent muscle lines for anatomical shoulder, while solid black arrows represent RSA. Blue circles represent the approximate centroid location of each muscle or sub-region origin. Taken from: Ackland et al. [208].

Some muscular characteristics are known to correlate with postoperative outcomes. The most significant are properties related to volume, fatty infiltration patterns, and muscle length (and, consequently, muscle tension). Both the size/shape and quality of a muscle are important factors that influence its force production capacity. A larger muscle has a greater cross-sectional area (CSA) and, therefore, a larger moment arm. As such, patients with greater muscle volume are likely to experience improved abduction/adduction and flexion/extension. These differences in joint loading may have important clinical implications for RSA complication rates, particularly regarding acromial and scapular stress fractures, instability, and aseptic loosening [211].

6.1.1. Imaging

Quantitative and qualitative muscle assessments, such as volume, density, composition, and adipose tissue distribution, are increasingly applied in conditions like sarcopenia, characterized by progressive loss of muscle mass, strength, and function [212]. Radiological evaluation of muscle properties is fundamental for assessing muscle diseases. As part of routine clinical practice, upright plain X-rays (XR) are performed in arthroplasty patients both pre- and postoperatively. Preoperatively, they can reveal advanced glenohumeral osteoarthritis and cranial migration of the humeral head, which is commonly associated with advanced rotator cuff tears. Postoperatively, XRs are used to assess prosthesis position and detect periprosthetic fractures [213]. Muscle and tendon status is sometimes inferred from an acromiohumeral interval (AHI) < 7 mm [214,215], although the reliability of XR for this purpose is limited [216]. For evaluating bony anatomy and planning surgery based on patient-specific anatomy, CT remains the most accurate preoperative imaging modality, superior to XR and MRI [217]. CT is particularly useful in preoperative planning, complementing radiography by demonstrating fractures, osteoarthritis, available bone for fixation, and morphological parameters such as humeral head retroversion or glenoid version [213]. Fatty degeneration of the rotator cuff muscles, commonly graded with the Goutallier system [218], is usually assessed with CT or MRI due to its superior soft tissue contrast. However, CT offers faster acquisition, wider availability, lower cost, and higher spatial resolution. Moreover, unlike MRI, CT can quantify muscle density (attenuation), which reflects fat content in Hounsfield units (Table 22). Muscle area (single slice) or volume (stack of slices) can be measured with both MRI and CT, though segmentation remains challenging due to low soft tissue contrast [106,219].

CT is increasingly used as a research tool to investigate skeletal muscle biology in vivo, allowing segmentation of individual tissues and direct measurement of CSA and volume. While Dual-energy X-ray Absorptiometry (DXA) and bioelectrical impedance can quantify lean and fat mass, only CT and MRI provide spatially resolved distribution of muscle and adipose tissue. By default, CT numbers are calibrated to water using the formula: CT number = $((\mu - \mu w)/\mu w) \times 1000$ [HU] [106,220].

Table 22. CT Hounsfield units to categorise muscle tissues.

CT values	Tissue
-190 to -30 [HU]	Adipose tissue
-29 to 150 [HU]	Muscle

MRI is mainly used preoperatively to assess rotator cuff tendons, muscle quality, and fatty infiltration, and remains superior for evaluating tear size, tendon retraction, and atrophy [213,221]. Ultrasound, increasingly studied and applied in this field, is portable, inexpensive, and effective for detecting hematomas, infections, and full-thickness cuff tears and does not expose patient to radiations, though its accuracy decreases for partial tears and depends on operator expertise [213,222]. While MRI offers comprehensive assessment and accuracy for re-tears, US provides higher spatial resolution and growing clinical relevance. Standardized imaging protocols are essential to maximize diagnostic accuracy and improve outcome prediction [223].

6.1.2. Muscle parameters

Several muscle parameters have been investigated in the literature, with some already well established and others only recently gaining attention. Classifications such as the Goutallier system [218] are routinely applied in clinical practice and have become traditional tools for clinicians. However, many of these approaches are subjective and qualitative, often relying on the assessment of a single two-dimensional image to describe a feature that is inherently three-dimensional, such as the tangent sign method [224]. As a result, the true three-dimensional characterization of muscle properties may differ from their conventional two-dimensional representation. To achieve an objective and reproducible assessment, it is important to adopt quantitative, operator-independent methodologies. Among the most important parameters investigated for guiding shoulder arthroplasty treatment, and for their potential predictive value in postoperative RSA outcomes, are the following.

1. Fatty infiltration

Fatty infiltrations (FI) are known to be one of the most impactful parameters affecting the outcomes of certain shoulder procedures, which are considered prognostic and are crucial for clinical decision-making as they seem to be non-reversible [225]. FI plays an important role in shoulder arthroplasty and can help guide patient expectations [204,226] and are among the factors that contribute to patient-reported and functional outcomes. For example, they appear to be negative predictor of patient-reported outcomes, and they negatively impacting force capacity and daily activities, especially those involving internal and external rotations in case of infraspinatus involvement [195,227]. The principal method for defining the stage of FI in muscles is a qualitative method described by Goutallier, which identifies five grades using CT

(Table 23) and considers fatty infiltration pathological from stage 2 onward. Additionally, Fuchs described a method for assessing FI on MRI [218,228].

Table 23. Grading of fatty infiltration of the Rotator Cuff Muscles with the system of Goutallier et al. and Fuchs et al.

Stage	Findings on CT and/or MRI scans
0	Completely normal muscle, without any fatty streak
1	The muscle contains some fatty streaks
2	The fatty infiltration is important, but there is still more muscle than fat
3	There is as much fat as muscle
4	More fat than muscle is present

These methods show poor interobserver reliability and are limited by assessing a 3D structure from a single 2D slice, as fat is unevenly distributed within muscles. Quantitative 3D methods provide more accurate evaluation of FI, better discrimination between Goutallier grades, and often reveal lower values than qualitative estimates [229,230]. Recent studies have also linked quantitative FI assessment with measures of muscle loss and atrophy [231,232].

Werthel et al. used CT-based 3D measurements of rotator cuff muscles to quantify fatty infiltration (3DFI), muscle mass (3DMM), and muscle loss (3DML), showing these methods to be reliable and more precise than 2D grading. Pathological shoulders had significantly higher 3DFI and 3DML than healthy ones, with CTA and MRCT showing the greatest changes, especially in the supraspinatus and infraspinatus. Moreover, 3D metrics correlated strongly with the traditional Goutallier score, particularly 3DML for the infraspinatus [233].

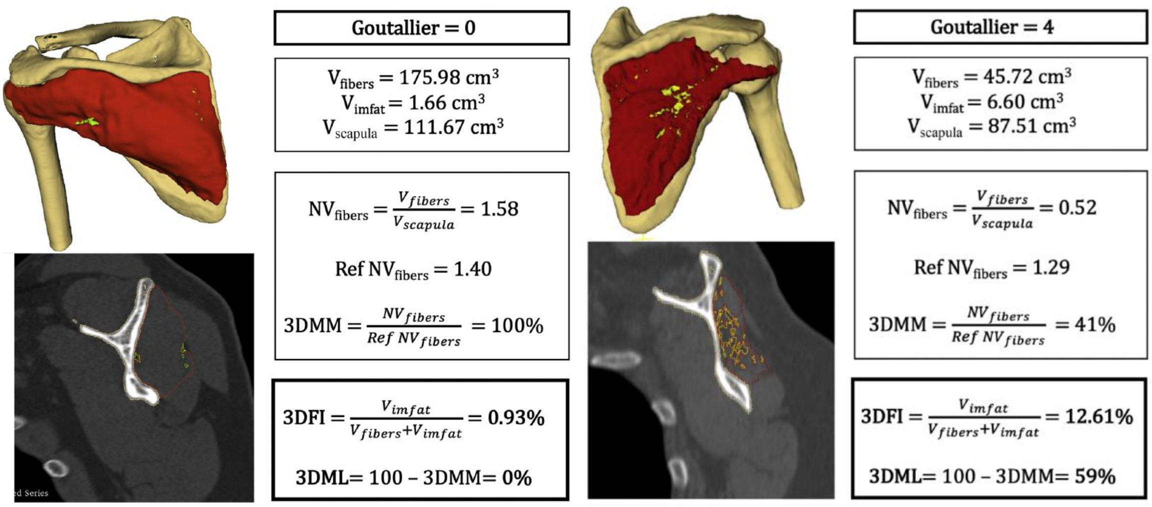

Figure 103. Two examples of three-dimensional reconstruction and sagittal view of the infraspinatus (red) and intramuscular fat (yellow). Vfibers, muscle fibre volume; Vimfat, intramuscular fat volume; Vscapula, scapular volume; NVfibers, normalized volume of muscle fibres; RefNVfibers, reference value for males (left image) and females (right image) for the infraspinatus; 3DMM, 3-dimensional muscle mass; 3DFI, 3-dimensional quantitative calculation of fatty infiltration; 3DML, 3-dimensional muscle loss. Taken from Werthel et al. [233].

Posterior cuff insufficiency limits external rotation after RSA. Wiater et al. [234] showed that infraspinatus fatty infiltration correlates with reduced external rotation, and when extended to the teres minor, it leads to poorer function. Subscapularis fatty infiltration may reduce internal rotation, though evidence is less clear [203,235]. Blakeney et al. confirmed with CT that 3D fatty infiltration of the rotator cuff progressively increases with disease severity, from OA to MRCT to CTA [236]. Other studies focusing on patients with Goutallier grade 3 and 4 rotator cuff muscles reported that, despite severe fatty degeneration, restoration of external and internal rotation was achievable with a more lateralized implant that increased cuff tension. These findings suggest that prosthetic design plays a significant role in postoperative active ROM (Figure 104), even in cases with a nonfunctional rotator cuff [237,238].

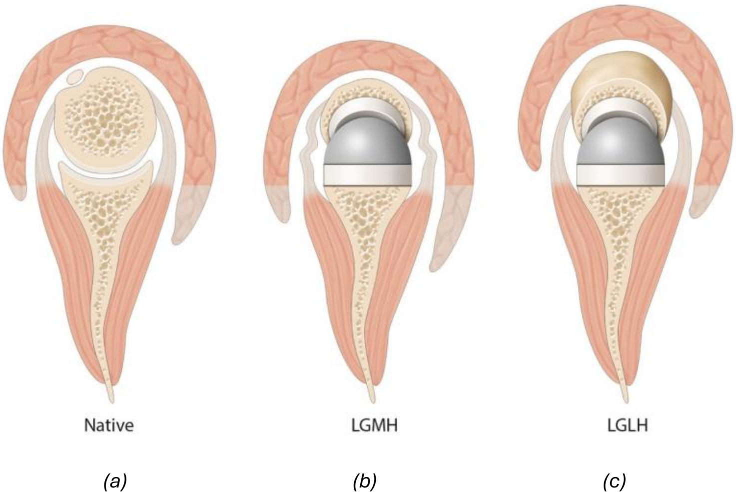

Figure 104. Factors influencing postoperative external rotation. (a) Native shoulder. The centre of rotation is in the humeral head, and the lever arm of the deltoid does not allow deltoid recruitment. (b) A combination of lateral glenoid/medial humerus (LGMH) RSA. As in native shoulders, the bony lateralization of the centre of rotation decreases recruitment of the deltoid for rotation. Additionally, due to the medialized centre of rotation compared to the native shoulder, the rotator cuff is slackened and thus less efficient in rotatory motion. (c) A combination of lateral glenoid/lateral humerus (LGLH) RSA. Additional lateralization on the humeral side allows important deltoid recruitment and a tenodesis effect and a retensioning of the remnant posterior cuff. Taken from: Nabergoj et al. [237].

Fatty infiltration grades have shown predictive value for postoperative outcomes. An infraspinatus FI grade >2 has been associated with a higher incidence of scapular notching, while a supraspinatus FI grade >1 often indicates a torn rotator cuff [239,240]. Moreover, patients with teres minor fatty infiltration of grade >2 tend to have significantly poorer clinical outcomes [235]. These findings highlight how the degree of muscle degeneration can directly influence both implant-related complications and functional recovery.

2. Trophicity

Trophicity refers to whether a muscle is atrophic, normal, or hypertrophic, reflecting its capacity to generate force and its potential association with patient-reported outcomes. However, the literature is controversial: while some studies suggest a possible link, other authors report that rotator cuff atrophy does not significantly affect clinical outcomes after RSA [204,241,242].

Werthel et al. analysed 102 CT scans (healthy, CTA, MRCT, and OA) and defined quantitative atrophy as the ratio between patient muscle volume and sex-specific healthy reference volumes. They found comparable atrophy across pathological groups for all rotator cuff muscles, except the supraspinatus, which was more atrophied in CTA and MRCT than in OA. Healthy reference volumes allowed standardized 3D assessment of atrophy, but since differences between pathological groups were minimal, the authors suggested that the role of muscle volume and atrophy (including fat) as independent outcome predictors may be overestimated. They concluded that atrophy should not be considered in isolation from intramuscular fat [232]. Similarly to fatty infiltration, teres minor atrophy plays a crucial role, being associated with poor postoperative recovery of external rotation after RSA [206,243]. Increasing attention has been given to the teres minor, as it becomes the only primary external rotator when the infraspinatus is compromised, making its condition a key prognostic factor for RSA outcomes. Teres minor hypertrophy may represent a compensatory adaptation to enhance external rotation strength, and patients with a hypertrophic teres minor have been reported to experience less preoperative pain and greater postoperative external rotation in absence of infraspinatus function [244–246].

3. Volume

Deltoid volume, closely linked to muscle force generation, was evaluated in a retrospective study by McClatchy et al. on 107 shoulders using CT and MRI. Patients with satisfactory postoperative forward elevation after reverse shoulder arthroplasty had significantly greater deltoid volume, an effect mainly observed in the rotator cuff-deficient group, where higher deltoid volume correlated with both better forward elevation and higher patient-reported outcomes, while no significant differences were found in the rotator cuff-intact group [247]. Normalized deltoid volume also appears predictive of patient-reported outcomes and overall shoulder function. In RSA patients, larger deltoid volume likely reflects greater abduction moment arms and efficiency, requiring less force to elevate the arm [211]. In patients with an intact rotator cuff, preservation of the supraspinatus muscle may further optimize active forward elevation and reduce the functional demand on the deltoid [248]. Conversely, a retrospective study by De Boer et al. on 59 shoulders suggested that, at longer follow-up, no correlation was found between preoperative deltoid volume and the Constant score or abduction strength [249]. Overall, a consensus indicates that muscle volume is significantly associated with better functional and patient-reported outcomes, though no specific thresholds or cut-off values for deltoid volume with predictive preoperative significance have yet been established.

Werthel et al., in a study on 102 CT scans including healthy shoulders, CTA, MRCT and OSA, found that rotator cuff muscle volumes were significantly greater in healthy shoulders compared to diseased cohorts, although no differences emerged among the pathological groups [232]. They also noted that normalization using scapular volume is feasible since, despite glenoid and/or acromial erosion in severe cases, scapular volume did not differ significantly between groups. As healthy muscle volume is a well-established surrogate marker of muscle force [250], they also defined the relative muscle volumes in healthy shoulder.

4. Length

Reverse shoulder arthroplasty relies on deltoid function, modifying its length, tension, and structural mechanics. Medialization of the centre of rotation increases fibre recruitment and enhances the lever arm, while distalisation restores tension, enabling elevation even in the absence of a functional cuff [205]. These changes, however, increase strain on the acromion and scapular spine, predisposing to fractures and neurologic injury. CT-based assessment of bone mineral density (BMD) through HU helps evaluate bone quality and risk of complications. Caldaria et al. found significant BMD changes at deltoid origins between pre- and postoperative states [251] (Table 24). Routine CT scans can thus identify patients at higher fracture risk.

Table 24. Bone mineral density values range to assess bone condition.

Condition	Bone HU
Osteoporosis	<100
Osteopenia	100-150
Normal	>150

Yoon et al. identified a distalisation threshold of ~35–38 mm, above which range of motion declined, while humeral lateralization improved external rotation [252] (Figure 105). Giles et al. reported that humeral lateralization reduces deltoid force and joint load, whereas glenosphere lateralization increases both despite reducing notching, suggesting humeral lateralization may balance adverse biomechanical effects [199].

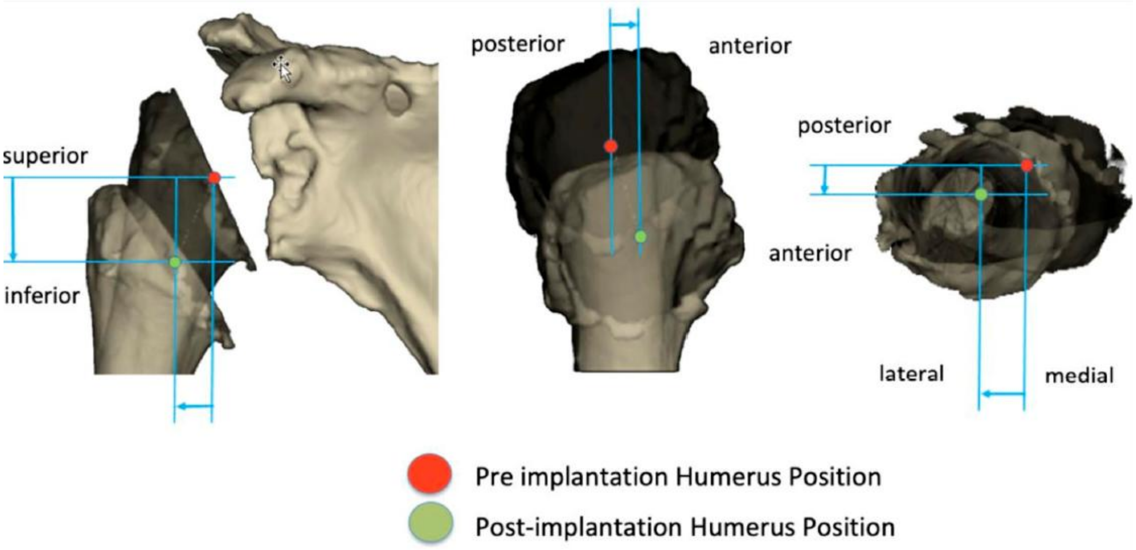

Figure 105. Illustration of how the arm change position (ACP) is measured in three dimensions. Taken from Yoon et al. [252].

Maxwell further showed that deltoid and rotator cuff muscle lengths varied with the preoperative diagnosis. All reverse shoulder arthroplasty designs produced relative deltoid lengthening and shortening of the subscapularis, infraspinatus, and teres minor, more pronounced in rotator cuff arthropathy. Prostheses with a lateralized centre of rotation preserved greater rotator cuff muscle length than medialized designs, despite similar deltoid lengthening [253].

A critical determinant of muscle force production is the force-length relationship (or Blix curve). Levin et al. found that all designs increase deltoid moment arms, with medial glenoid–lateral humerus giving the greatest gain. However, only the lateral glenoid–medial humerus preserved a favourable force–length relationship and supraspinatus moment arm, supporting its use when the tendon is intact [254]. Similarly, RSA medializes and lowers the greater tuberosity, reducing cuff rotational strength and limiting activities such as reaching the head. Medialized designs (e.g., Grammont) slacken the cuff and impair external rotation [198], leading to strategies like latissimus dorsi transfer or lateralization of the centre of rotation. Over the last decade, lateralized prostheses have been introduced. Herregodts et al. confirmed that humeral lateral offset has a greater effect on cuff elongation than glenoid offset, consistent with the Werthel classification [231]. Inferiorisation of the greater tuberosity shortens caudal cuff muscles and lengthens cranial ones, with humeral medialization correlating strongly with cuff shortening. A lower humeral position improves infraspinatus and subscapularis length, while humeral lateralization is more effective than glenoid lateralization for optimizing outcomes [255].

Despite increasing interest, the relationship between humeral lengthening and reverse shoulder arthroplasty outcomes remains unclear. An optimal range likely exists to achieve satisfactory forward elevation while minimizing complications such as acromial fractures [256].

5. Shape

In a study of 1057 patients, Rajabzadeh-Oghaz et al. found that deltoid flatness was associated with functional, clinical and patient-reported outcomes. Deltoids with low flatness appeared more planar, suggesting smaller moment arms, while higher flatness values indicated more curved shapes and potentially larger moment arms (Figure 106). Preoperatively, greater flatness correlated with better internal rotation and higher scores, especially in females. However, at ≥2 years after reverse shoulder arthroplasty, both males and females with higher flatness showed reduced strength, and men also had lower patient-reported scores [211].

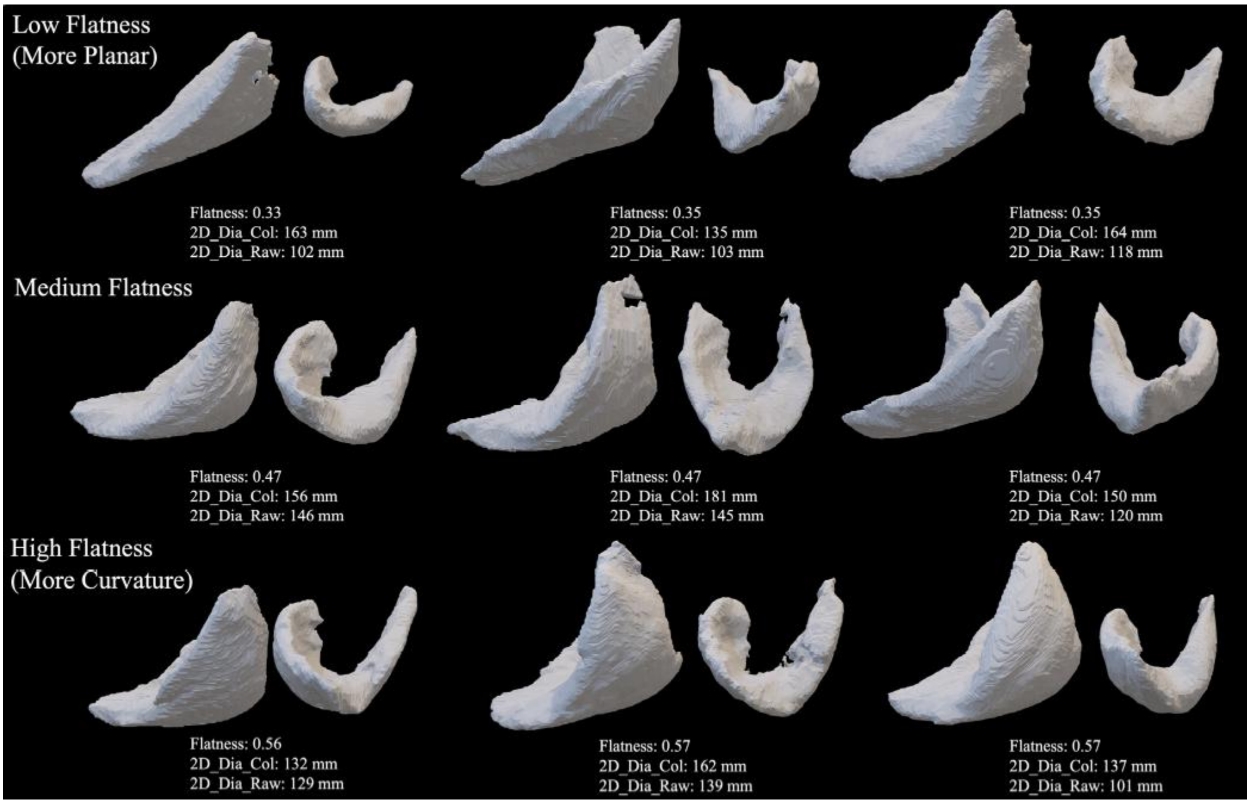

Figure 106. Representation of the Deltoid Muscle with Low (top row, more planar), Medium (middle row), and High (bottom row, more curvature) Values of Deltoid Shape Flatness for 3D Volumes Reconstructed from BONE Kernel CT Images. Taken from Rajabzadeh-Oghaz et al. [211].

6. Stiffness

Deltoid tension is critical for RSA outcomes, yet implant size, design, and optimal tension remain largely subjective. Implant choice determines humeral lateralization and distalisation, directly influencing tension: over-tensioning may cause pain, stiffness, and acromial fractures, whereas under-tensioning can lead to weakness, instability, and poor function [199–201].

Shear Wave Elastography (SWE) is an ultrasound-based technique that quantifies tissue stiffness in kPa by measuring shear wave velocity, which reflects tissue elasticity [257,258]. Mallet et al. reported increased middle deltoid stiffness immediately after RSA, which decreased after one year but correlated with acromion–tuberosity distance, range of motion, and function, with an average increase of 7 kPa [259]. Fenwick et al. similarly found higher deltoid stiffness post-RSA than in the contralateral side, especially in anterior and middle deltoid portions. Under isometric load, all regions adapted with greater elasticity after RSA, though no correlation with clinical outcomes was observed [260,261].

Hatta et al. validated a reliable protocol in 65 patients and found that active forward flexion correlated with gains in muscle strength elevation at 3–12 months postoperatively. Preoperative strength and patient-reported scores predicted improvements at 9–12 months, while radiological and clinical variables did not. Preoperative SWE values showed no association, but postoperative SWE partially correlated with strength gains, with thresholds of 50.0, 46.6, and 45.1 kPa at 3, 6, and 9 months predicting subsequent improvement [262,263]. Current literature indicates that SWE is a valuable tool for assessing postoperative deltoid tension and may help define recommendations and cut-off values to optimize deltoid forces in RSA [261].

6.2. Exploring Muscle Properties for Paediatric Orthopedic care

As previously mentioned, the investigation of muscle characteristics is clinically relevant in adult, but it is also highly relevant in paediatric population, as alterations in muscle mass, quality, and function are associated with low muscle strength, reduced muscle quantity/quality, and poor physical performance, and adverse health outcomes. A well-known example is sarcopenia, a muscle disease characterized by progressive decline in strength, mass, and quality, most frequently studied in aging adults but also reported in younger individuals with neuromuscular disorders or in combination with obesity [264–269]. Accurately quantifying both the quantity and quality of skeletal muscle in these conditions, may have a great impact on diagnosis and follow-up.

Different tools are available for this purpose. DXA is the most widely used method in both research and clinical practice due to its speed, low cost, and availability, though results may vary with hydration status and between vendors [264,270]. Ultrasound offers a radiation-free alternative and allows assessment of muscle thickness, CSA, echogenicity, fascicle length, and pennation angle, but is operator-skill dependent [271]. Bioelectrical Impedance Analysis (BIA) is portable and low-cost but indirect and hydration-dependent and less accurate than DXA or CT [272]. CT and MRI provide the most comprehensive assessment, quantifying both muscle mass and composition, including intramuscular fat infiltration, which is increasingly recognized as an indicator of muscle condition [273,274]. While CT is often accessible in patients already undergoing imaging, it carries higher radiation and cost compared to DXA. MRI avoids radiation and offers superior tissue characterization, typically through T1- and T2-

weighted sequences, though it is less widely available. Although literature on the assessment of muscle characteristics in children is more limited than in adults, although reference ranges for paediatric population exist for DXA, and BIA-derived parameters, studies confirm that advanced imaging methods such as CT and MRI can reveal clinically relevant alterations in children as well [266,275,276]. This emphasizes that the study of muscle characteristics is not only limited to aging but rather is present in children with a variety of pathologies, including paediatric-specific pathologies.

Unlike body weight and BMI, these newer tools for assessing muscle mass offer a more objective means of predicting functional outcomes and are becoming increasingly important for guiding therapeutic decisions [277].

Loss of muscle mass and function in young individuals can be associated with neuromuscular disorders, a group of conditions affecting the neuromuscular system, like cerebral palsy, muscular dystrophies and paralysis [267]. These disorders may impair muscle function either directly in specific muscles or indirectly through peripheral nervous system pathologies. Individually, these conditions are rare, with prevalence rates below 50 per 100,000 worldwide. Considered collectively, however, neuromuscular disorders reach prevalence rates comparable to Parkinson’s disease, ranging from 100 to 300 per 100,000 worldwide.

Low muscle mass is linked to reduced physical capacity, mobility disorders, higher risk of falls and fractures, and impaired daily functioning, all of which worsen with age. In paediatrics, where evidence is limited, exploring the relationship between muscle mass and health outcomes could support its use as an objective marker to guide interventions aimed at preserving function and reducing comorbidities [278].

Particularly in children with Cerebral Palsy (CP), several studies have shown that muscle mass is strongly and inversely correlated with Gross Motor Function Measure (GMFM) scores, a widely accepted classification of motor function, with greater muscle mass associated with higher GMFM score [279,280]. Compared to typically developing children (TDC), they show differences in overall body composition, and specific muscles play a key role: thoracic erector spinae thickness predicts gross motor function, while rectus abdominis and vastus lateralis thickness predict activities of daily living, including self-care activities and mobility [281].

Similarly, in children with congenital myotonic dystrophy and Duchenne muscular dystrophy (DMD), lean body mass is reduced compared to TDC and is closely associated with lower functional activity and muscle strength [282,283]. While the association between muscle mass and strength is strong in typically developing males, in boys with DMD the correlation between lean mass and thigh strength is much weaker, and no correlation is observed with arm strength. These findings suggest that weakness in DMD cannot be explained by lean tissue loss alone, as muscle quality also plays a role. Indeed, DMD muscle undergoes several pathological changes, including fibro-fatty replacement, inflammation, fibre splitting, regeneration, and atrophy, indicating that both reduced muscle mass (quantity) and impaired muscle function (quality) contribute to disease-related weakness [284].

Muscle mass is closely correlated with bone outcomes in both adults and children. Its assessment is relevant for parameters such as BMD, bone mineral content (BMC), bone mass, bone strength, and bone thickness. In TDC, higher muscle mass predicts higher BMC, supporting the theory that biomechanical muscle loading stimulates bone adaptation by signalling the need for greater strength [285]. This relationship varies by ethnicity, sex, and pubertal stage [286–288]. BMD is positively associated with lean body mass, and bone characteristics are also related to muscle power output and fitness. Thus, increasing lean body mass may represent an important therapeutic target to improve BMD and BMC. Based on this evidence, it is reasonable to conclude that conditions impairing muscle mass development in children will also lead to reduced bone content and density.

In general, muscle mass measures also impact overall health, being more predictive than weight or BMI for several indicators such as arterial function, insulin/glucose levels, and heart rate. Children with low muscle mass, including those with neuromuscular conditions, are therefore at increased cardiovascular and metabolic risk [289,290].

Muscle mass is a key predictor of functional, skeletal, and health outcomes, and its monitoring can guide interventions aimed at improving function, making it a promising clinical target that warrants further research in paediatric and underrepresented conditions [291].

6.2.1. Assessment of Muscle Parameters in Children with Neuromuscular Disorders

As previously mentioned, sarcopenia is a degenerative condition marked by loss of skeletal muscle strength, function, and mass, often age-related but also influenced by other aetiologies and can be noted even in young individuals. It is linked to falls, disability, and mortality, and can be assessed with DXA, MRI, CT, and ultrasonography. Among these, CT offers unique detail on specific muscles, adipose tissue, and organs not provided by DXA or BIA, and is of high practical value given its widespread clinical use, combining accessibility with precision in quantifying tissues and predicting whole-body composition [272].

Cerebral palsy is the most common motor disability in childhood. Population-based registries, mainly from Australia and Europe, report a prevalence of 1.5–2.5 per 1,000 live births [292]. Cerebral palsy is not a single disease but a group of conditions with variable severity and shared developmental features. It is defined as a group of permanent disorders of movement and posture, caused by non-progressive disturbances in the developing brain, often accompanied by sensory, cognitive, communicative, behavioural, epileptic, and musculoskeletal problems [293].

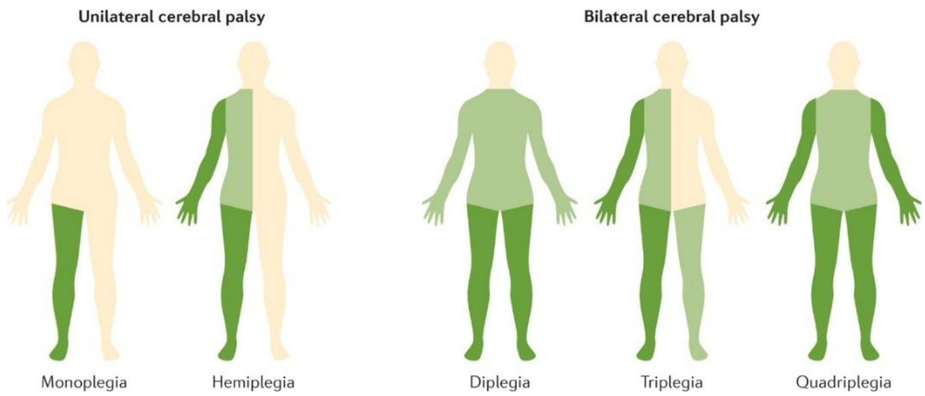

Figure 107. Topographical description in cerebral palsy: unilateral and bilateral cerebral palsy. Taken from Graham et al. [294].

The Gross Motor Function Classification System (GMFCS) is the gold standard for classifying motor function in children with cerebral palsy [295,296]. It is an age-specific, ordinal system proven to be valid, reliable, stable, and predictive of long-term outcomes. Motor impairment can be classified topographically (Figure 107): monoplegia (one limb, usually lower), hemiplegia (one side, upper limb more affected), diplegia (all limbs, predominantly lower), triplegia (one upper and both lower limbs, asymmetrically), and quadriplegia/tetraplegia (all four limbs and trunk) [294]. According to Surveillance of Cerebral Palsy Europe (SCPE) terminology, diplegia, triplegia, and quadriplegia are grouped under bilateral CP, while monoplegia and hemiplegia are unilateral forms [297].

Children with CP have significantly smaller muscles and atrophy than TDC, consistent with reduced motor function. Scoliosis is common in neurologic diseases and tends to be more severe than idiopathic forms, with sarcopenia contributing to ambulatory decline; in non-ambulatory patients, severe scoliosis is strongly associated with severe sarcopenia [290]. In CP, muscle loss and imbalance alter normal musculoskeletal growth, leading to gait deterioration and deformities [298].

Lower-limb muscles show a higher proportion of connective and fat tissue [299–304], reduced myofibre cross-sectional area, altered fibre type, and shorter, stiffer muscle cells with fewer sarcomeres [305–307], all of which limit force generation and mobility [308,309].

Early management focuses on reducing spasticity, slowing contracture development, and preserving walking ability through physiotherapy, casting, botulinum toxin, and surgery [310]. Surgery, typically performed after age 6, corrects deformities by precise muscle–tendon lengthening, improving gait while minimizing over- or under-correction [311–313]. A common example is equinus deformity, treated by gastrocnemius–soleus recession during single-event multilevel surgery [311,314]. Long bone torsion deformities are also frequent, caused by impaired muscle growth and leading to hip displacement and joint instability [315–317]. Although CT and MRI offer accurate torsion assessment, 3D ultrasound is emerging as a child-friendly alternative [318–321]. Rotational osteotomy, ideally between ages 6–12, corrects torsional deformities and improves gait when performed as part of single-event multilevel surgery [311,317,322].

In conclusion, the most consistent finding in spastic CP is reduced muscle size, reflected by lower volume, thickness, and physiological cross-sectional area, combined with increased fat infiltration compared with TDC. These changes impair muscle force and quality, contributing to weakness and functional limitation. Modern imaging now allows non-invasive assessment: MRI remains the gold standard for muscle volume and length, CT and MRI reveal tissue composition, and ultrasound offers a cost-effective evaluation of muscle architecture. Integrating structural and histological analyses is key to understanding how interventions affect both tissue and function, although quantitative muscle segmentation in paediatric CT or MRI studies is still limited [323].

MRI can be used not only for global muscle assessment but also for compositional analysis. Texture and radiomics approaches provide non-invasive insight into pathophysiology, can guide biopsies, and enable longitudinal follow-up. Combining quantitative fat fraction (Figure 108) with texture analysis helps predict muscle involvement in CP, offering a promising alternative to invasive biopsies. In the future, such models could be integrated into clinical decision-making and applied to other muscle diseases [324].

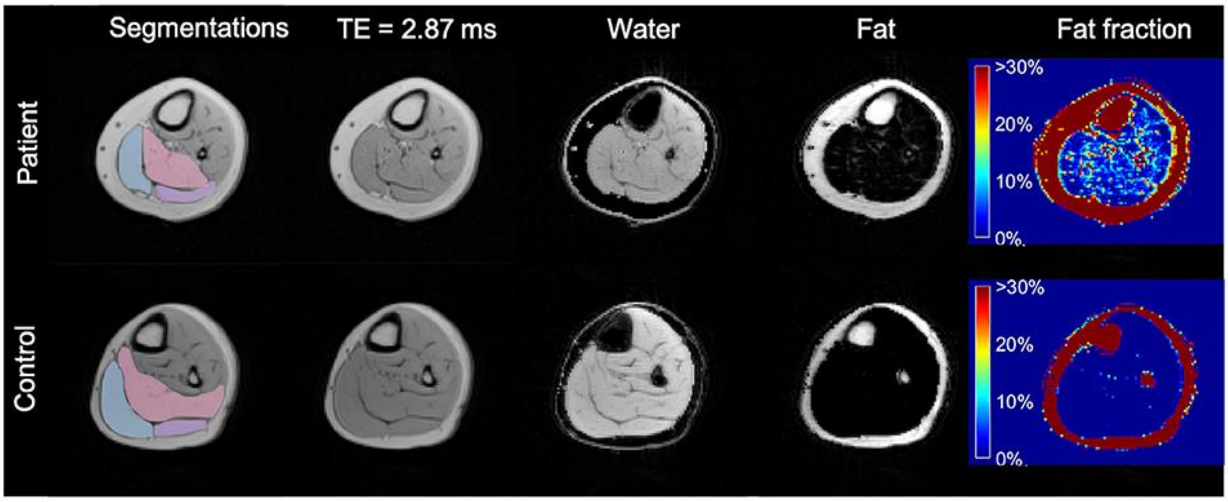

Figure 108. Axial MR images of the more affected calf of a patient (diparetic, boy, 11 years) and the dominant calf of healthy control (a typically developing 11 years boy with similar BMI). First column: segmented ROIs for soleus (pink), gastrocnemius medialis (light blue), and gastrocnemius lateralis (lilac); second column: 2nd echo image from the Dixon data set; third column: water-only image calculated from the Dixon dataset; fourth column: fat-only image calculated from the Dixon dataset; fifth column: fat fraction map ranging from 0 to 100% calculated from the Dixon dataset, showing a higher fat fraction in the CP patient. TE, Echo Time. Taken from Akinci D'Antonoli et al. [324].

Another important application of muscle analysis is in muscular dystrophies, a group of inherited diseases that cause the gradual loss of muscle structure and strength. The term dystrophy refers to fibrosis and fat infiltration, which become more evident as the disease progresses. The rate of progression, severity of symptoms, distribution of weakness, and inheritance pattern can vary widely between types. In paediatric neuromuscular disorders, one of the main goals is to identify the specific disease responsible for the weakness. Although genetic sequencing is now easier and more accessible, it remains costly. Because muscle changes follow characteristic patterns linked to certain genes rather than occurring randomly, imaging can help narrow the genetic search, enabling faster and more accurate diagnosis [274]. Several groups have proposed imaging protocols, contributing to the identification of many new genetic subtypes [325].

Among the most common muscular dystrophies are DMD and Becker muscular dystrophy (BMD). DMD usually appears in early childhood, causing progressive muscle weakness and loss of walking ability during adolescence [326], while BMD starts later and progresses more slowly.

Muscle imaging shows characteristic patterns. For example, in DMD, fat infiltration and muscle wasting begin in the adductor magnus and biceps femoris, later involving the quadriceps, while muscles such as the sartorius, gracilis, and long adductor are often preserved for a longer time (Figure 109). A fat fraction cutoff of 50% has been reported to predict loss of ambulation [327,328]. In BMD, the same muscles are affected, but changes occur later and are generally milder. These distribution patterns help distinguish between different types of dystrophies [329].

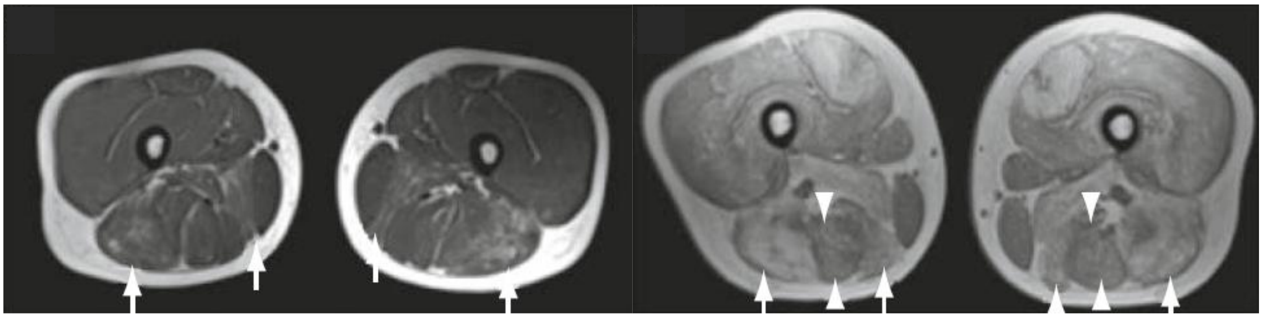

(a) *(b)*

Figure 109. (a) A 7-year-old patient with early involvement of Duchenne muscular dystrophy (DMD) and characteristic involvement of the adductor magnus and biceps femoris muscles (arrows); (b) A 10-year-old patient in intermediate stage of DMD with moderate involvement of the biceps and semimembranosus (arrows) but still relative sparing of the semitendinosus muscles (arrowheads). Taken from Fischer et al. [274].

In conclusion, integrating reliable muscle parameters represents a promising direction for paediatric orthopedics, making surgical planning more predictive and precise. MRI-based muscle assessment, often used to evaluate disease severity, may also have a prognostic role, enabling early stratification of patients from diagnosis and supporting more timely, targeted interventions. Advances in imaging analysis and dedicated software tools are also helping to recognize disease patterns more accurately, improving diagnosis and patient management.

7. CONCLUSIONS

7.1. Summary and Final Considerations

This doctoral project focused on the study, analysis, and optimization of surgical simulation and VSP processes, including the design and clinical application of PSIs and GSIs, to support surgical treatments for the correction of musculoskeletal disorders, with particular attention to paediatric conditions involving severe bone deformities and bone tumours. The work involved the application of CAD modelling and FDM 3D printing for the design and production of surgical tools (e.g. cutting/drilling guides), to support surgical treatment. These instruments are referred to as PSIs when designed for the patient, and GSIs when tailored to the donor bone.

The project was developed through an interdisciplinary collaboration between the Department of Industrial Engineering of the University of Bologna and the Paediatric Orthopedic and Traumatology Unit of the Rizzoli Orthopedic Institute, aimed at integrating these technologies directly into the hospital setting. The goal is to provide a personalized, in-house treatment planning and manufacturing service, commonly referred to as POC. By employing low- to medium-cost desktop technologies, this approach offers a scalable and sustainable model, significantly reducing both internal production costs and the need for outsourcing.

One of the most significant outcomes of this work was the definition and consolidation of a structured and rationalized workflow which is now routinely adopted in clinical practice. From the initial consultation with the surgeon to the identification of key planning parameters, all stages have been formalized, culminating in a standardized procedure for setting up virtual reference systems on 3D virtual anatomical models. A precise and reproducible deformity analysis protocol was developed and is systematically applied to patients undergoing complex surgical treatments, improving planning accuracy and facilitating communication with the clinical team. Traditional surgical approaches were revisited and restructured to align with this digital workflow, allowing for better integration within virtual simulation environments. Techniques such as the Flipping Wedge Osteotomy and the Side-to-Side Flipping Wedge Osteotomy approaches were refined and integrated into the planning workflow, enhancing the capability to address complex corrections.

In the manufacturing phase, new printing parameters were investigated and optimized to align with the updated planning strategies, complementing previous studies. This contributed to improved dimensional accuracy and supported the extension of this methodology into new clinical areas, particularly oncologic orthopaedics, where large resections and complex reconstructions require the design and production of larger and more robust surgical tools. Printing optimization demonstrated that low fan speed combined with a 45° infill pattern minimized 3D deformation, resulting in a standard deviation of 0.47 mm in 3D distance maps after thermal treatment. In addition, a regression-based compensation model was developed to adjust pin-hole diameters according to the selected manufacturing process, supporting a reliable transfer from digital planning to the final physical surgical guides.

The consolidated workflow was applied to a large clinical series including 144 procedures in 114 patients, with 22 oncological cases. Angular correction was achieved in 91 procedures (mean 26.3°, range 3–151°), while bone grafts or massive allografts were used in 58 procedures, 22 of which were shaped using GSIs. Sterilizable PSIs were employed in 93 procedures, with a total of 199 guides produced (mean 2 guides per procedure). Overall, complication rates were comparable to those reported for traditional surgery. Operative time was the only independent predictor of complications, while PSI-related technical issues were infrequent (6%) and mainly related to suboptimal imaging quality. No complications were attributed to the 3D printed instruments. Overall, the clinical evaluation confirmed the efficacy and safety of PSIs/GSIs in routine application. The workflow demonstrated clear advantages in terms of customization, surgical guidance, and procedural reliability, with the most consistent measurable benefits being reduced operative time and decreased intraoperative fluoroscopy use, supporting both surgical value and patient safety.

Finally, during the research period abroad, it was possible to explore new topics, mainly related to adult prosthetic orthopaedics and soft tissue interactions. Although these areas are beyond the main focus on paediatric bone correction, they opened interesting directions for future research. These insights could help expand simulation-based approaches to less explored areas of paediatric care, making it possible to include soft tissue considerations in future planning workflows.

7.2. Perspectives

This work explored several aspects of the overall process, with the aim of evaluating and improving different elements at each stage and providing a clearer and more rational overview of a complex workflow. However, this cannot yet be considered the final step of optimization. Several aspects can still be refined and improved, both in the process itself and in its evaluation.

First, the high heterogeneity of the available data is an inherent feature of paediatric clinical practice and represents a potential source of bias that can be mitigated only in large cohorts allowing the identification of homogeneous subgroups. In the perspective of further development, dedicated planning pathways tailored to specific treatments and anatomical regions will play an important role in supporting efficient and structured workflows. Targeted optimization studies will therefore be required to define specific sub-workflows, aiming to streamline design times while achieving more consistent and specialized results.

Although the technologies employed were intentionally selected for their low-cost accessibility, and the observed reduction in surgical time suggests potential cost savings per patient, a detailed cost analysis has not yet been performed. Such evaluation would be essential to quantify the actual economic impact of this in-house approach. Furthermore, regulatory aspects concerning the production and use of in-house 3D printed medical devices have not yet been thoroughly addressed, despite representing a crucial step toward the full implementation of a compliant and sustainable service. Nonetheless, this work can be considered a foundational step toward defining and controlling the overall process, from which future regulatory alignment can be developed.

Another important direction concerns external validation. Future multicentric studies, supported by shared protocols for virtual planning, PSIs and/or GSIs design, and postoperative evaluation, would enable more robust comparisons across centres and strengthen the generalizability and scalability of the workflow, particularly for rare and complex paediatric conditions.

Finally, until now, most of the focus has been placed exclusively on the bones. However, imaging-based approaches involving the analysis of muscle morphology and quality are gaining increasing attention and deserve further investigation. Integrating reliable muscle parameters represents a promising direction for paediatric orthopedics, making surgical planning more predictive and precise. MRI-based muscle assessment, often used to evaluate disease severity, may also have a prognostic role, enabling early stratification of patients from diagnosis and supporting more timely and targeted interventions.

In conclusion, this work provides a solid foundation for future research and clinical implementation. It has helped define a practical workflow that supports the use of 3D technologies in surgery, showing how low-cost, in-house solutions can make personalized surgery more accessible, efficient, accurate, and patient-centred.

REFERENCES

1. Osti, F.; Santi, G.M.; Neri, M.; Liverani, A.; Frizziero, L.; Stilli, S.; Maredi, E.; Zarantonello, P.; Gallone, G.; Stallone, S.; et al. CT Conversion Workflow for Intraoperative Usage of Bony Models: From DICOM Data to 3D Printed Models. *Applied Sciences (Switzerland)* **2019**, *9*, doi:10.3390/app9040708.

2. Frizziero, L.; Santi, G.M.; Liverani, A.; Napolitano, F.; Papaleo, P.; Maredi, E.; Di Gennaro, G.L.; Zarantonello, P.; Stallone, S.; Stilli, S.; et al. Computer-Aided Surgical Simulation for Correcting Complex Limb Deformities in Children. *Applied Sciences (Switzerland)* **2020**, *10*, doi:10.3390/app10155181.

3. Frizziero, L.; Santi, G.M.; Liverani, A.; Giuseppetti, V.; Trisolino, G.; Maredi, E.; Stilli, S. Paediatric Orthopaedic Surgery with 3D Printing: Improvements and Cost Reduction. *Symmetry (Basel).* **2019**, *11*, doi:10.3390/sym11101317.

4. Frizziero, L.; Santi, G.M.; Leon-Cardenas, C.; Donnici, G.; Liverani, A.; Napolitano, F.; Papaleo, P.; Pagliari, C.; Antonioli, D.; Stallone, S.; et al. An Innovative and Cost-Advantage Cad Solution for Cubitus Varus Surgical Planning in Children. *Applied Sciences (Switzerland)* **2021**, *11*, doi:10.3390/app11094057.

5. Frizziero, L.; Pagliari, C.; Donnici, G.; Liverani, A.; Santi, G.M.; Papaleo, P.; Napolitano, F.; Leon-Cardenas, C.; Trisolino, G.; Zarantonello, P.; et al. Effectiveness Assessment of CAD Simulation in Complex Orthopedic Surgery Practices. *Symmetry (Basel).* **2021**, *13*, doi:10.3390/sym13050850.

6. Frizziero, L.; Liverani, A.; Donnici, G.; Osti, F.; Neri, M.; Maredi, E.; Trisolino, G.; Stilli, S. New Methodology for Diagnosis of Orthopedic Diseases through Additive Manufacturing Models. *Symmetry 2019, Vol. 11, Page 542* **2019**, *11*, 542, doi:10.3390/SYM11040542.

7. Frizziero, L.; Santi, G.M.; Leon-Cardenas, C.; Donnici, G.; Liverani, A.; Papaleo, P.; Napolitano, F.; Pagliari, C.; Di Gennaro, G.L.; Stallone, S.; et al. In-House, Fast Fdm Prototyping of a Custom Cutting Guide for a Lower-Risk Pediatric Femoral Osteotomy. *Bioengineering* **2021**, *8*, doi:10.3390/bioengineering8060071.

8. Frizziero, L.; Santi, G.M.; Leon-Cardenas, C.; Ferretti, P.; Sali, M.; Gianese, F.; Crescentini, N.; Donnici, G.; Liverani, A.; Trisolino, G.; et al. Heat Sterilization Effects on Polymeric, FDM-Optimized Orthopedic Cutting Guide for Surgical Procedures. *J. Funct. Biomater.* **2021**, *12*, doi:10.3390/jfb12040063.

9. Menozzi, G.C.; Depaoli, A.; Ramella, M.; Alessandri, G.; Frizziero, L.; Rosa, A. De; Soncini, F.; Sassoli, V.; Rocca, G.; Trisolino, G. High-Temperature Polylactic Acid Proves Reliable and Safe for Manufacturing 3D-Printed Patient-Specific Instruments in Pediatric Orthopedics—Results from over 80 Personalized Devices Employed in 47 Surgeries. *Polymers 2024, Vol. 16, Page 1216* **2024**, *16*, 1216, doi:10.3390/POLYM16091216.

10. Alessandri, G.; Frizziero, L.; Santi, G.M.; Liverani, A.; Dallari, D.; Vivarelli, L.; Di Gennaro, G.L.; Antonioli, D.; Menozzi, G.C.; Depaoli, A.; et al. Virtual Surgical Planning, 3D-Printing and Customized Bone Allograft for Acute Correction of Severe Genu Varum in Children. *Journal of Personalized Medicine 2022, Vol. 12, Page 2051* **2022**, *12*, 2051, doi:10.3390/JPM12122051.

11. *Tachdjian’s Pediatric Orthopaedics From the Texas Scottish Rite Hospital for Children*;

12. Ağirdil, Y. The Growth Plate: A Physiologic Overview. *EFORT Open Rev.* **2020**, *5*, 498–507, doi:10.1302/2058-5241.5.190088.

13. Shim, K.S. Pubertal Growth and Epiphyseal Fusion. *Ann. Pediatr. Endocrinol. Metab.* **2015**, *20*, 8–12, doi:10.6065/APEM.2015.20.1.8.

14. Satoh, M.; Hasegawa, Y. Factors Affecting Prepubertal and Pubertal Bone Age Progression. *Front. Endocrinol. (Lausanne).* **2022**, *13*, 967711, doi:10.3389/FENDO.2022.967711/BIBTEX.

15. Paley, D. *PRINCIPLES OF DEFORMITY CORRECTION*; 2002;

16. Marsell, R.; Einhorn, T.A. The Biology of Fracture Healing. *Injury* **2011**, *42*, 551–555, doi:10.1016/J.INJURY.2011.03.031,.

17. Einhorn, T.A.; Gerstenfeld, L.C. Fracture Healing: Mechanisms and Interventions. *Nat. Rev. Rheumatol.* **2015**, *11*, 45–54, doi:10.1038/NRRHEUM.2014.164,.

18. Ilizarov, G.A. The Tension-Stress Effect on the Genesis and Growth of Tissues. Part I. The Influence of Stability of Fixation and Soft-Tissue Preservation. *Clin. Orthop. Relat. Res.* **1989**, *238*, 249–281, doi:10.1097/00003086-198901000-00038.

19. Nievelstein, R.A.J. Non-Traumatic Musculoskeletal Diseases in Children. **2021**, 283–292, doi:10.1007/978-3-030-71281-5_20.

20. Shapiro, F. Overview of Deformities. *Pediatric Orthopedic Deformities, Volume 1* **2016**, 159–254, doi:10.1007/978-3-319-20529-8_2.

21. Bone Deformity | International Center for Limb Lengthening Available online: https://www.limblength.org/conditions/bone-deformity/ (accessed on 9 July 2025).

22. Mirabello, L.; Troisi, R.J.; Savage, S.A. Osteosarcoma Incidence and Survival Rates from 1973 to 2004: Data from the Surveillance, Epidemiology, and End Results Program. *Cancer* **2009**, *115*, 1531–1543, doi:10.1002/CNCR.24121,.

23. Esiashvili, N.; Goodman, M.; Marcus, R.B. Changes in Incidence and Survival of Ewing Sarcoma Patients over the Past 3 Decades: Surveillance Epidemiology and End Results Data. *J. Pediatr. Hematol. Oncol.* **2008**, *30*, 425–430, doi:10.1097/MPH.0B013E31816E22F3,.

24. Arndt, C.A.S.; Rose, P.S.; Folpe, A.L.; Laack, N.N. Common Musculoskeletal Tumors of Childhood and Adolescence. *Mayo Clin. Proc.* **2012**, *87*, 475–487, doi:10.1016/J.MAYOCP.2012.01.015/ATTACHMENT/0A93B6C6-EC9A-47DD-804C-411C8A02C94F/MMC1.MP4.

25. Mankin, H.J.; Mankin, C.J.; Simon, M.A. The Hazards of the Biopsy, Revisited: For the Members of the Musculoskeletal Tumor Society. *Journal of Bone and Joint Surgery* **1996**, *78*, 656–663, doi:10.2106/00004623-199605000-00004,.

26. Ayerza, M.A.; Farfalli, G.L.; Aponte-Tinao, L.; Luis Muscolo, D. Does Increased Rate of Limb-Sparing Surgery Affect Survival in Osteosarcoma? *Clin. Orthop. Relat. Res.* **2010**, *468*, 2854–2859, doi:10.1007/S11999-010-1423-4,.

27. Neel, M.D.; Wilkins, R.M.; Rao, B.N.; Kelly, C.M. Early Multicenter Experience With a Noninvasive Expandable Prosthesis. *Clin. Orthop. Relat. Res.* **2003**, *415*, 72–81, doi:10.1097/01.BLO.0000093899.12372.25,.

28. Errani, C.; Tsukamoto, S.; Almunhaisen, N.; Mavrogenis, A.; Donati, D. Intercalary Reconstruction Following Resection of Diaphyseal Bone Tumors: A Systematic Review. *J. Clin. Orthop. Trauma* **2021**, *19*, 1, doi:10.1016/J.JCOT.2021.04.033.

29. Sdegno, A. Computer Aided Architecture: Origins and Development. *DISEGNARECON* **2016**, *9*, 4-1-4.6.

30. Sarkar, Jayanta. Computer Aided Design : A Conceptual Approach. **2015**, 713.

31. Vannier, M.W.; Marsh, J.L.; Warren, J.O. Three Dimensional CT Reconstruction Images for Craniofacial Surgical Planning and Evaluation. *Radiology* **1984**, *150*, 179–184, doi:10.1148/RADIOLOGY.150.1.6689758.

32. Pham, A.M.; Rafii, A.A.; Metzger, M.C.; Jamali, A.; Strong, E.B. Computer Modeling and Intraoperative Navigation in Maxillofacial Surgery. *Otolaryngol. Head. Neck Surg.* **2007**, *137*, 624–631, doi:10.1016/J.OTOHNS.2007.06.719.

33. Li, W.Z.; Zhang, M.C.; Li, S.P.; Zhang, L.T.; Huang, Y. Application of Computer-Aided Three-Dimensional Skull Model with Rapid Prototyping Technique in Repair of Zygomatico-Orbito-Maxillary Complex Fracture. *Int. J. Med. Robot.* **2009**, *5*, 158–163, doi:10.1002/RCS.242.

34. PALEY, D.; TETSWORTH, K. Mechanical Axis Deviation of the Lower Limbs. Preoperative Planning of Uniapical Angular Deformities of the Tibia or Femur. *Clin. Orthop. Relat. Res.* **1992**, *280*, 48???64, doi:10.1097/00003086-199207000-00008.

35. Paley, D.; Chaudray, M.; Pirone, A.M.; Lentz, P.; Kautz, D. Treatment of Malunions and Mal-Nonunions of the Femur and Tibia by Detailed Preoperative Planning and the Ilizarov Techniques. *Orthopedic Clinics of North America* **1990**, *21*, 667–691, doi:10.1016/S0030-5898(20)31511-X.

36. Wong, K.-C.; Kumta, S.M.; Chiu, K.-H.; Cheung, K.-W.; Leung, K.-S.; Unwin, P.; Wong, M.C.M. Computer Assisted Pelvic Tumor Resection and Reconstruction with a Custom-Made Prosthesis Using an Innovative Adaptation and Its Validation. *Computer Aided Surgery* **2007**, *12*, 225–232, doi:10.3109/10929080701536046.

37. Chapuis, J.; Schramm, A.; Pappas, I.; Hallermann, W.; Schwenzer-Zimmerer, K.; Langlotz, F.; Caversaccio, M. A New System for Computer-Aided Preoperative Planning and Intraoperative Navigation during Corrective Jaw Surgery. *IEEE Trans. Inf. Technol. Biomed.* **2007**, *11*, 274–287, doi:10.1109/TITB.2006.884372.

38. Wong, K.C.; Kumta, S.M.; Leung, K.S.; Ng, K.W.; Ng, E.W.K.; Lee, K.S. Integration of CAD/CAM Planning into Computer Assisted Orthopaedic Surgery. *Computer Aided Surgery* **2010**, *15*, 65–74, doi:10.3109/10929088.2010.514131.

39. Hull, C. On Stereolithography. *Virtual Phys. Prototyp.* **2012**, *7*, 177, doi:10.1080/17452759.2012.723409.

40. Kruth, J.P.; Leu, M.C.; Nakagawa, T. Progress in Additive Manufacturing and Rapid Prototyping. *CIRP Annals* **1998**, *47*, 525–540, doi:10.1016/S0007-8506(07)63240-5.

41. Karkun, M.S.; Dharmalingam, S. 3D Printing Technology in Aerospace Industry – A Review. *International Journal of Aviation, Aeronautics, and Aerospace* **2022**, 9, 4, doi:https://doi.org/10.15394/ijaaa.2022.1708.

42. Blakey-Milner, B.; Gradl, P.; Snedden, G.; Brooks, M.; Pitot, J.; Lopez, E.; Leary, M.; Berto, F.; du Plessis, A. Metal Additive Manufacturing in Aerospace: A Review. *Mater. Des.* **2021**, *209*, 110008, doi:10.1016/J.MATDES.2021.110008.

43. Mohanavel, V.; Ashraff Ali, K.S.; Ranganathan, K.; Allen Jeffrey, J.; Ravikumar, M.M.; Rajkumar, S. The Roles and Applications of Additive Manufacturing in the Aerospace and Automobile Sector. *Mater. Today Proc.* **2021**, *47*, 405–409, doi:10.1016/J.MATPR.2021.04.596.

44. Khajavi, S.H.; Mandolini, M. Additive Manufacturing in the Clothing Industry: Towards Sustainable New Business Models. *Applied Sciences 2021, Vol. 11, Page 8994* **2021**, *11*, 8994, doi:10.3390/APP11198994.

45. Javaid, Mohd.; Haleem, A. Additive Manufacturing Applications in Medical Cases: A Literature Based Review. *Alexandria Journal of Medicine* **2018**, *54*, 411–422, doi:10.1016/J.AJME.2017.09.003.

46. ISO/ASTM 52900:2021(En), Additive Manufacturing — General Principles — Fundamentals and Vocabulary Available online: https://www.iso.org/obp/ui/#iso:std:iso-astm:52900:ed-2:v1:en (accessed on 12 October 2025).

47. Thomas, D.S.; Gilbert, S.W. Costs and Cost Effectiveness of Additive Manufacturing. **2014**, doi:10.6028/NIST.SP.1176.

48. Cano-Vicent, A.; Tambuwala, M.M.; Hassan, S.S.; Barh, D.; Aljabali, A.A.A.; Birkett, M.; Arjunan, A.; Serrano-Aroca, Á. Fused Deposition Modelling: Current Status, Methodology, Applications and Future Prospects. *Addit. Manuf.* **2021**, *47*, 102378, doi:10.1016/J.ADDMA.2021.102378.

49. Shahrubudin, N.; Lee, T.C.; Ramlan, R. An Overview on 3D Printing Technology: Technological, Materials, and Applications. *Procedia Manuf.* **2019**, *35*, 1286–1296, doi:10.1016/J.PROMFG.2019.06.089.

50. Doshi, M.; Mahale, A.; Singh, S.K.; Deshmukh, S. Printing Parameters and Materials Affecting Mechanical Properties of FDM-3D Printed Parts: Perspective and Prospects. *Mater. Today Proc.* **2022**, *50*, 2269–2275, doi:10.1016/J.MATPR.2021.10.003.

51. Hashmi, A.W.; Mali, H.S.; Meena, A. The Surface Quality Improvement Methods for FDM Printed Parts: A Review. **2021**, 167–194, doi:10.1007/978-3-030-68024-4_9.

52. Bochmann, L.; Bayley, C.; Helu, M.; Transchel, R.; Wegener, K.; Dornfeld, D. Understanding Error Generation in Fused Deposition Modeling. *Surf. Topogr.* **2015**, *3*, 014002, doi:10.1088/2051-672X/3/1/014002.

53. Ledalla, S.R.K.; Tirupathi, B.; Sriram, V. Performance Evaluation of Various STL File Mesh Refining Algorithms Applied for FDM-RP Process. *Journal of The Institution of Engineers (India): Series C* **2018**, *99*, 339–346, doi:10.1007/S40032-016-0303-4/TABLES/4.

54. STL (STereoLithography) File Format Family Available online: https://www.loc.gov/preservation/digital/formats/fdd/fdd000504.shtml (accessed on 12 October 2025).

55. Elbashti, M.; Molinero-Mourelle, P.; Aswehlee, A.; Bornstein, M.M.; Abou-Ayash, S.; Schimmel, M.; Ella, B.; Naveau, A. Effect of Triangular Mesh Resolution on the Geometrical Trueness of Segmented CBCT Maxillofacial Data into STL Format. *J. Dent.* **2023**, *138*, 104722, doi:10.1016/J.JDENT.2023.104722.

56. Mankovich, N.J.; Cheeseman, A.M.; Stoker, N.G. The Display of Three-Dimensional Anatomy with Stereolithographic Models. *J. Digit. Imaging* **1990**, *3*, 200–203, doi:10.1007/BF03167610.

57. Choi, J.W.; Kim, N. Clinical Application of Three-Dimensional Printing Technology in Craniofacial Plastic Surgery. *Arch. Plast. Surg.* **2015**, *42*, 267, doi:10.5999/APS.2015.42.3.267.

58. Giannopoulos, A.A.; Steigner, M.L.; George, E.; Barile, M.; Hunsaker, A.R.; Rybicki, F.J.; Mitsouras, D. Cardiothoracic Applications of 3-Dimensional Printing. *J. Thorac. Imaging* **2016**, *31*, 253–272, doi:10.1097/RTI.0000000000000217.

59. Chae, M.P.; Rozen, W.M.; McMenamin, P.G.; Findlay, M.W.; Spychal, R.T.; Hunter-Smith, D.J. Emerging Applications of Bedside 3D Printing in Plastic Surgery. *Front. Surg.* **2015**, *2*, 25, doi:10.3389/FSURG.2015.00025.

60. Randazzo, M.; Pisapia, J.; Singh, N.; Thawani, J. 3D Printing in Neurosurgery: A Systematic Review. *Surg. Neurol. Int.* **2016**, *7*, S801, doi:10.4103/2152-7806.194059.

61. Wong, T.M.; Jin, J.; Lau, T.W.; Fang, C.; Yan, C.H.; Yeung, K.; To, M.; Leung, F. The Use of Three-Dimensional Printing Technology in Orthopaedic Surgery. *J. Orthop. Surg. (Hong Kong).* **2017**, *25*, doi:10.1177/2309499016684077.

62. Auricchio, F.; Marconi, S. 3D Printing: Clinical Applications in Orthopaedics and Traumatology. *EFORT Open Rev.* **2017**, *1*, 121–127, doi:10.1302/2058-5241.1.000012.

63. Jariwala, S.H.; Lewis, G.S.; Bushman, Z.J.; Adair, J.H.; Donahue, H.J. 3D Printing of Personalized Artificial Bone Scaffolds. *3D Print. Addit. Manuf.* **2015**, *2*, 56–64, doi:10.1089/3DP.2015.0001.

64. Hao, Y.; Luo, D.; Wu, J.; Wang, L.; Xie, K.; Yan, M.; Dai, K. A Novel Revision System for Complex Pelvic Defects Utilizing 3D-Printed Custom Prosthesis. *J. Orthop. Translat.* **2021**, *31*, 102–109, doi:10.1016/j.jot.2021.09.006.

65. Ambrose, J. Computerized Transverse Axial Scanning (Tomography): Part 2. Clinical Application. *British Journal of Radiology* **1973**, *46*, 1023–1047, doi:10.1259/0007-1285-46-552-1023.

66. Hounsfield, G.N. Computerized Transverse Axial Scanning (Tomography): Part 1. Description of System. *British Journal of Radiology* **1973**, *46*, 1016–1022, doi:10.1259/0007-1285-46-552-1016.

67. Tack, P.; Victor, J.; Gemmel, P.; Annemans, L. 3D-Printing Techniques in a Medical Setting: A Systematic Literature Review. *Biomed. Eng. Online* **2016**, *15*, doi:10.1186/S12938-016-0236-4.

68. Raza, M.; Murphy, D.; Gelfer, Y. The Effect of Three-Dimensional (3D) Printing on Quantitative and Qualitative Outcomes in Paediatric Orthopaedic Osteotomies: A Systematic Review. *EFORT Open Rev.* **2021**, *6*, 130, doi:10.1302/2058-5241.6.200092.

69. Yammine, K.; Karbala, J.; Maalouf, A.; Daher, J.; Assi, C. Clinical Outcomes of the Use of 3D Printing Models in Fracture Management: A Meta-Analysis of Randomized Studies. *Eur. J. Trauma Emerg. Surg.* **2022**, *48*, 3479–3491, doi:10.1007/S00068-021-01758-1.

70. Papotto, G.; Testa, G.; Mobilia, G.; Perez, S.; Dimartino, S.; Giardina, S.M.C.; Sessa, G.; Pavone, V. Use of 3D Printing and Pre-Contouring Plate in the Surgical Planning of Acetabular Fractures: A Systematic Review. *Orthop. Traumatol. Surg. Res.* **2022**, *108*, doi:10.1016/J.OTSR.2021.103111.

71. Aguado-Maestro, I.; Simón-Pérez, C.; García-Alonso, M.; Ailagas-De Las Heras, J.J.; Paredes-Herrero, E. Clinical Applications of “In-Hospital” 3D Printing in Hip Surgery: A Systematic Narrative Review. *Journal of Clinical Medicine 2024, Vol. 13, Page 599* **2024**, *13*, 599, doi:10.3390/JCM13020599.

72. Bos, D.; Guberina, N.; Zensen, S.; Opitz, M.; Forsting, M.; Wetter, A. Radiation Exposure in Computed Tomography. *Dtsch. Arztebl. Int.* **2023**, *120*, 135–141, doi:10.3238/ARZTEBL.M2022.0395.

73. Grover, V.P.B.; Tognarelli, J.M.; Crossey, M.M.E.; Cox, I.J.; Taylor-Robinson, S.D.; McPhail, M.J.W. Magnetic Resonance Imaging: Principles and Techniques: Lessons for Clinicians. *J. Clin. Exp. Hepatol.* **2015**, *5*, 246–255, doi:10.1016/j.jceh.2015.08.001.

74. Schmauss, D.; Haeberle, S.; Hagl, C.; Sodian, R. Three-Dimensional Printing in Cardiac Surgery and Interventional Cardiology: A Single-Centre Experience. *Eur. J. Cardiothorac. Surg.* **2015**, *47*, 1044–1052, doi:10.1093/EJCTS/EZU310.

75. Mitsouras, D.; Liacouras, P.; Imanzadeh, A.; Giannopoulos, A.A.; Cai, T.; Kumamaru, K.K.; George, E.; Wake, N.; Caterson, E.J.; Pomahac, B.; et al. Medical 3D Printing for the Radiologist. *Radiographics* **2015**, *35*, 1965–1988, doi:10.1148/RG.2015140320.

76. Greil, G.F.; Wolf, I.; Kuettner, A.; Fenchel, M.; Miller, S.; Martirosian, P.; Schick, F.; Oppitz, M.; Meinzer, H.P.; Sieverding, L. Stereolithographic Reproduction of Complex Cardiac Morphology Based on High Spatial Resolution Imaging. *Clin. Res. Cardiol.* **2007**, *96*, 176–185, doi:10.1007/S00392-007-0482-3.

77. Giannopoulos, A.A.; Pietila, T. Post-Processing of DICOM Images. *3D Printing in Medicine: A Practical Guide for Medical Professionals* **2017**, 23–34, doi:10.1007/978-3-319-61924-8_3.

78. Matsiushevich, K.; Belvedere, C.; Leardini, A.; Durante, S. Quantitative Comparison of Freeware Software for Bone Mesh from DICOM Files. *J. Biomech.* **2019**, *84*, 247–251, doi:10.1016/j.jbiomech.2018.12.031.

79. Belvedere, C.; Ortolani, M.; Marcelli, E.; Bortolani, B.; Matsiushevich, K.; Durante, S.; Cercenelli, L.; Leardini, A.; Belvedere, C.; Ortolani, M.; et al. Comparison of Bone Segmentation Software over Different Anatomical Parts. *Applied Sciences 2022, Vol. 12,* **2022**, *12*, doi:10.3390/APP12126097.

80. Taylor, R.H.; Mittelstadt, B.D.; Paul, H.A.; Hanson, W.; Kazanzides, P.; Zuhars, J.F.; Williamson, B.; Musits, B.L.; Glassman, E.; Bargar, W.L. An Image-Directed Robotic System for Precise Orthopaedic Surgery. *IEEE Transactions on Robotics and Automation* **1994**, *10*, 261–275, doi:10.1109/70.294202.

81. Depaoli, A.; Menozzi, G.C.; Di Gennaro, G.L.; Ramella, M.; Alessandri, G.; Frizziero, L.; Liverani, A.; Martinelli, D.; Rocca, G.; Trisolino, G. The Flipping-Wedge Osteotomy: How 3D Virtual Surgical Planning (VSP) Suggested a Simple and Promising Type of Osteotomy in Pediatric Post-Traumatic Forearm Deformity. *J. Pers. Med.* **2023**, *13*, 549, doi:10.3390/JPM13030549/S1.

82. Menozzi, G.C.; Depaoli, A.; Ramella, M.; Alessandri, G.; Frizziero, L.; Liverani, A.; Rocca, G.; Trisolino, G. Side-to-Side Flipping Wedge Osteotomy: Virtual Surgical Planning Suggested an Innovative One-Stage Procedure for Aligning Both Knees in “Windswept Deformity.” *Journal of Personalized Medicine 2023, Vol. 13, Page 1538* **2023**, *13*, 1538, doi:10.3390/JPM13111538.

83. Zhao, L.; Patel, P.K.; Cohen, M. Application of Virtual Surgical Planning with Computer Assisted Design and Manufacturing Technology to Cranio-Maxillofacial Surgery. *Arch. Plast. Surg.* **2012**, *39*, 309, doi:10.5999/APS.2012.39.4.309.

84. Zaffagnini, S.; Dal Fabbro, G.; Lucidi, G.A.; Agostinone, P.; Belvedere, C.; Leardini, A.; Grassi, A. Personalised Opening Wedge High Tibial Osteotomy with Patient-Specific Plates and Instrumentation Accurately Controls Coronal Correction and Posterior Slope: Results from a Prospective First Case Series. *Knee* **2023**, *44*, 89–99, doi:10.1016/j.knee.2023.07.011.

85. Zaffagnini, S.; Dal Fabbro, G.; Belvedere, C.; Leardini, A.; Caravelli, S.; Lucidi, G.A.; Agostinone, P.; Mosca, M.; Neri, M.P.; Grassi, A. Custom-Made Devices Represent a Promising Tool to Increase Correction Accuracy of High Tibial Osteotomy: A Systematic Review of the Literature and Presentation of Pilot Cases with a New 3D-Printed System. *J. Clin. Med.* **2022**, *11*, doi:10.3390/JCM11195717.

86. Ritacco, L.E.; Milano, F.E.; Farfalli, G.L.; Ayerza, M.A.; Muscolo, D.L.; Aponte-Tinao, L.A. Accuracy of 3-D Planning and Navigation in Bone Tumor Resection. *Orthopedics* **2013**, *36*, doi:10.3928/01477447-20130624-27.

87. Kamat, A.; Chinder, P.; Gopurathingal, A.; Hindiskere, S. 3D Printing in Orthopedic Oncology — Workflow and Outcomes of 59 Cases. *Indian J. Surg. Oncol.* **2025**, 1–13, doi:10.1007/S13193-025-02205-Y/TABLES/1.

88. Durastanti, G.; Belvedere, C.; Ruggeri, M.; Donati, D.M.; Spazzoli, B.; Leardini, A. A Pelvic Reconstruction Procedure for Custom-Made Prosthesis Design of Bone Tumor Surgical Treatments. *Applied Sciences 2022, Vol. 12, Page 1654* **2022**, *12*, 1654, doi:10.3390/APP12031654.

89. Meng, M.; Wang, J.; Sun, T.; Zhang, W.; Zhang, J.; Shu, L.; Li, Z. Clinical Applications and Prospects of 3D Printing Guide Templates in Orthopaedics. *J. Orthop. Translat.* **2022**, *34*, 22, doi:10.1016/J.JOT.2022.03.001.

90. Yilmaz, A.; Badria, A.F.; Huri, P.Y.; Huri, G. 3D-Printed Surgical Guides. *Ann. Jt.* **2019**, *4*, doi:10.21037/AOJ.2019.02.04.

91. George, M.; Aroom, K.R.; Hawes, H.G.; Gill, B.S.; Love, J. 3D Printed Surgical Instruments: The Design and Fabrication Process. *World J. Surg.* **2017**, *41*, 314–319, doi:10.1007/S00268-016-3814-5.

92. Ensini, A.; Timoncini, A.; Cenni, F.; Belvedere, C.; Fusai, F.; Leardini, A.; Giannini, S. Intra- and Post-Operative Accuracy Assessments of Two Different Patient-Specific Instrumentation Systems for Total Knee Replacement. *Knee Surg. Sports Traumatol. Arthrosc.* **2014**, *22*, 621–629, doi:10.1007/S00167-013-2667-9.

93. Crow, S. STERILIZATION PROCESSES: Meeting the Demands of Today's Health Care Technology. *Nursing Clinics of North America* **1993**, *28*, 687–695, doi:10.1016/S0029-6465(22)02895-X.

94. Qiu, Q.Q.; Sun, W.Q.; Connor, J. Sterilization of Biomaterials of Synthetic and Biological Origin. *Comprehensive Biomaterials* **2011**, *4*, 127–144, doi:10.1016/B978-0-08-055294-1.00248-8.

95. Tipnis, N.P.; Burgess, D.J. Sterilization of Implantable Polymer-Based Medical Devices: A Review. *Int. J. Pharm.* **2018**, *544*, 455–460, doi:10.1016/J.IJPHARM.2017.12.003.

96. Pérez Davila, S.; González Rodríguez, L.; Chiussi, S.; Serra, J.; González, P. How to Sterilize Polylactic Acid Based Medical Devices? *Polymers 2021, Vol. 13, Page 2115* **2021**, *13*, 2115, doi:10.3390/POLYM13132115.

97. Hamad, K.; Kaseem, M.; Yang, H.W.; Deri, F.; Ko, Y.G. Properties and Medical Applications of Polylactic Acid: A Review. *Express Polym. Lett.* **2015**, *9*, 435–455, doi:10.3144/EXPRESSPOLYMLETT.2015.42.

98. Gregor, A.; Filová, E.; Novák, M.; Kronek, J.; Chlup, H.; Buzgo, M.; Blahnová, V.; Lukášová, V.; Bartoš, M.; Nečas, A.; et al. Designing of PLA Scaffolds for Bone Tissue Replacement Fabricated by Ordinary Commercial 3D Printer. *J. Biol. Eng.* **2017**, *11*, doi:10.1186/S13036-017-0074-3.

99. Serra, T.; Planell, J.A.; Navarro, M. High-Resolution PLA-Based Composite Scaffolds via 3-D Printing Technology. *Acta Biomater.* **2013**, *9*, 5521–5530, doi:10.1016/j.actbio.2012.10.041.

100. Tyler, B.; Gullotti, D.; Mangraviti, A.; Utsuki, T.; Brem, H. Polylactic Acid (PLA) Controlled Delivery Carriers for Biomedical Applications. *Adv. Drug Deliv. Rev.* **2016**, *107*, 163–175, doi:10.1016/j.addr.2016.06.018.

101. Arce, K.; Morris, J.M.; Alexander, A.E.; Ettinger, K.S. Developing a Point-of-Care Manufacturing Program for Craniomaxillofacial Surgery. *Atlas Oral Maxillofac. Surg. Clin. North Am.* **2020**, *28*, 165–179, doi:10.1016/j.cxom.2020.06.002.

102. Meyer-Szary, J.; Luis, M.; Mikulski, S.; Patel, A.; Schulz, F.; Tretiakow, D.; Fercho, J.; Jaguszewska, K.; Frankiewicz, M.; Pawłowska, E.; et al. The Role of 3D Printing in Planning ComplexMedical Procedures and Training of Medical Professionals—Cross-Sectional Multispecialty Review. *Int. J. Environ. Res. Public Health* **2022**, *19*, 3331, doi:10.3390/IJERPH19063331/S1.

103. Beitler, B.G.; Abraham, P.F.; Glennon, A.R.; Tommasini, S.M.; Lattanza, L.L.; Morris, J.M.; Wiznia, D.H. Interpretation of Regulatory Factors for 3D Printing at Hospitals and Medical Centers, or at the Point of Care. *3D Print. Med.* **2022**, *8*, 1–7, doi:10.1186/S41205-022-00134-Y/TABLES/1.

104. EUR-Lex - 02017R0745-20260101 - IT - EUR-Lex Available online: https://eur-lex.europa.eu/legal-content/IT/TXT/?uri=CELEX%3A02017R0745-20260101 (accessed on 23 January 2026).

105. COMUNICATO STAMPA - LINEA GUIDA “LE TECNOLOGIE DI ADDITIVE MANIFACTURING IN SANITA’’" | AIIC” Available online: https://www.aiic.it/comunicato-stampa-linea-guida-le-tecnologie-di-additive-manifacturing-in-sanita/ (accessed on 23 January 2026).

106. Engelke, K.; Museyko, O.; Wang, L.; Laredo, J.D. Quantitative Analysis of Skeletal Muscle by Computed Tomography Imaging—State of the Art. *J. Orthop. Translat.* **2018**, *15*, 91–103, doi:10.1016/J.JOT.2018.10.004.

107. Harasen, G. Orthopedic Hardware and Equipment for the Beginner: Part 1. Pins and Wires. *The Canadian Veterinary Journal* **2011**, *52*, 1025.

108. Mostofi Zadeh Haghighi, D.L.; Xu, J.; Campbell, R.; Moopanar, T.R. Kirschner Wire vs Screw Osteosynthesis of Lateral Condyle Fractures in Paediatric Patients: A Systematic Review. *MUSCULOSKELETAL SURGERY 2024 109:1* **2024**, *109*, 9–15, doi:10.1007/S12306-024-00859-5.

109. Stein, B.E.; Ramji, A.F.; Hassanzadeh, H.; Wohlgemut, J.M.; Ain, M.C.; Sponseller, P.D. Cannulated Lag Screw Fixation of Displaced Lateral Humeral Condyle Fractures Is Associated with Lower Rates of Open Reduction and Infection than Pin Fixation. *Journal of Pediatric Orthopaedics* **2017**, *37*, 7–13, doi:10.1097/BPO.0000000000000579.

110. Tsunoda, E.; Fujioka-Kobayashi, M.; Koyanagi, M.; Arai, Y.; Inomata, T.; Inada, R.; Satomi, T. The Effect of Shavings from 3D-Printed Patient-Specific Cutting Guide Materials During Jaw Resection on Bone Healing. *Materials* **2025**, *18*, 5624, doi:10.3390/ma18245624.

111. Gielisch, M.W.; Thiem, D.G.E.; Ritz, U.; Bösing, C.; Al-Nawas, B.; Kämmerer, P.W. Assessing Cytotoxicity: A Comparative Analysis of Biodegradable and Conventional 3D-Printing Materials Post-Steam Sterilization for Surgical Guides. *Biomedical Materials* **2024**, *20*, 015001, doi:10.1088/1748-605X/ad8c8a.

112. Wurm, M.C.; Möst, T.; Bergauer, B.; Rietzel, D.; Neukam, F.W.; Cifuentes, S.C.; von Wilmowsky, C. In-Vitro Evaluation of Polylactic Acid (PLA) Manufactured by Fused Deposition Modeling. *Journal of Biological Engineering 2017 11:1* **2017**, *11*, 29-, doi:10.1186/s13036-017-0073-4.

113. Ferretti, P.; Leon-Cardenas, C.; Santi, G.M.; Sali, M.; Ciotti, E.; Frizziero, L.; Donnici, G.; Liverani, A. Relationship between FDM 3D Printing Parameters Study: Parameter Optimization for Lower Defects. *Polymers (Basel).* **2021**, *13*, doi:10.3390/POLYM13132190.

114. Ferretti, P.; Leon-Cardenas, C.; Sali, M.; Santi, G.M.; Gianese, F.; Donnici, G. Material Characterization Analysis of PLA & HTPLA FDM-Sourced Elements with Annealing Procedure and Optimized Printing Parameters. *Proceedings of the International Conference on Industrial Engineering and Operations Management* **2021**, 1410–1420.

115. Fawdington, R.A.; Johnson, B.; Kiely, N.T. Lower Limb Deformity Assessment and Correction. *Orthop. Trauma* **2014**, *28*, 33–40, doi:10.1016/j.mporth.2013.10.004.

116. Bonato, P.; Feipel, V.; Corniani, G.; Arin-Bal, G.; Leardini, A. Position Paper on How Technology for Human Motion Analysis and Relevant Clinical Applications Have Evolved over the Past Decades: Striking a Balance between Accuracy and Convenience. *Gait Posture* **2024**, *113*, 191–203, doi:10.1016/J.GAITPOST.2024.06.007.

117. Valente, G.; Grenno, G.; Benedetti, M.G.; Dal Fabbro, G.; Grassi, A.; Leardini, A.; Taddei, F.; Zaffagnini, S. Altered Motor Function during Daily Activities in Patients Eligible for High Tibial Osteotomy Is Primarily Driven by Knee Varus Deformity. *Bone Jt. Open* **2025**, *6*, 454–462, doi:10.1302/2633-1462.64.BJO-2024-0189.R1.

118. Caravaggi, P.; Sforza, C.; Leardini, A.; Portinaro, N.; Panou, A. Effect of Plano-Valgus Foot Posture on Midfoot Kinematics during Barefoot Walking in an Adolescent Population. *J. Foot Ankle Res.* **2018**, *11*, doi:10.1186/S13047-018-0297-7.

119. La Verde, M.; Belvedere, C.; Cammisa, E.; Alesi, D.; Fogacci, A.; Ortolani, M.; Sileoni, N.; Lullini, G.; Leardini, A.; Zaffagnini, S.; et al. Mechanically Aligned Second-Generation Medial Pivot Primary Total Knee Arthroplasty Does Not Reproduce Normal Knee Biomechanics: A Gait Analysis Study. *J. Clin. Med.* **2024**, *13*, doi:10.3390/JCM13185623.

120. Caravaggi, P.; Lullini, G.; Berti, L.; Giannini, S.; Leardini, A. Functional Evaluation of Bilateral Subtalar Arthroereisis for the Correction of Flexible Flatfoot in Children: 1-Year Follow-Up. *Gait Posture* **2018**, *64*, 152–158, doi:10.1016/j.gaitpost.2018.06.023.

121. Valente, G.; Grenno, G.; Dal Fabbro, G.; Grassi, A.; Leardini, A.; Berti, L.; Zaffagnini, S.; Taddei, F. High Tibial Osteotomy Effectively Restores Motor Function during Daily Activities in Patients with Knee Osteoarthritis and Varus Deformity. *J. Exp. Orthop.* **2025**, *12*, e70410, doi:10.1002/JEO2.70410;ISSUE:ISSUE:DOI.

122. Ruggeri, M.; Gill, H.S.; Leardini, A.; Zaffagnini, S.; MacLeod, A.; Ortolani, M.; Faccia, F.; Grassi, A.; Fabbro, G.D.; Durante, S.; et al. Superimposition of Ground Reaction Force on Tibial-Plateau Supporting Diagnostics and Post-Operative Evaluations in High-Tibial Osteotomy. A Novel Methodology. *Gait Posture* **2022**, *94*, 144–152, doi:10.1016/j.gaitpost.2022.02.028.

123. Belvedere, C.; Gill, H.S.; Ortolani, M.; Sileoni, N.; Zaffagnini, S.; Norvillo, F.; MacLeod, A.; Dal Fabbro, G.; Grassi, A.; Leardini, A. Instrumental Gait Analysis and Tibial Plateau Modelling to Support Pre- and Post-Operative Evaluations in Personalized High Tibial Osteotomy. *Applied Sciences 2023, Vol. 13,* **2023**, *13*, doi:10.3390/app132212425.

124. Frizziero, L.; Trisolino, G.; Santi, G.M.; Alessandri, G.; Agazzani, S.; Liverani, A.; Menozzi, G.C.; Di Gennaro, G.L.; Farella, G.M.G.; Abbruzzese, A.; et al. Computer-Aided Surgical Simulation through Digital Dynamic 3D Skeletal Segments for Correcting Torsional Deformities of the Lower Limbs in Children with Cerebral Palsy. *Applied Sciences 2022, Vol. 12, Page 7918* **2022**, *12*, 7918, doi:10.3390/APP12157918.

125. Leardini, A.; Durante, S.; Belvedere, C.; Caravaggi, P.; Carrara, C.; Berti, L.; Lullini, G.; Giacomozzi, C.; Durastanti, G.; Ortolani, M.; et al. Weight-Bearing CT Technology in Musculoskeletal Pathologies of the Lower Limbs: Techniques, Initial Applications, and Preliminary Combinations with Gait-Analysis Measurements at the Istituto Ortopedico Rizzoli. *Semin. Musculoskelet. Radiol.* **2019**, *23*, 643–655, doi:10.1055/S-0039-1697939.

126. Durastanti, G.; Belvedere, C.; Ruggeri, M.; Donati, D.M.; Spazzoli, B.; Leardini, A. A Pelvic Reconstruction Procedure for Custom-Made Prosthesis Design of Bone Tumor Surgical Treatments. *Applied Sciences 2022, Vol. 12,* **2022**, *12*, doi:10.3390/APP12031654.

127. Veerman, Q.W.T.; Tuijthof, G.J.M.; Verdonschot, N.; Brouwer, R.W.; Verdonk, P.; van Haver, A.; van der Veen, H.C.; Pijpker, P.A.J.; Heuvel, J. olde; Hoogeslag, R.A.G.; et al. A Structured Framework for Standardized 3D Leg Alignment Analysis: An International Delphi Consensus Study. *Knee Surgery, Sports Traumatology, Arthroscopy* **2025**, *33*, 2276–2292, doi:10.1002/KSA.12676.

128. Conte, P.; Anzillotti, G.; Pizza, N.; Chiappe, C.; Morales-Avalos, R.; Sanchis-Alfonso, V.; Monllau, J.C.; Perelli, S. Radiological Assessment of Lower Limb Torsional Deformities: A Narrative Review. *Ann. Jt.* **2025**, *10*, doi:10.21037/AOJ-24-42/COIF.

129. Dobbe, J.G.G.; Strackee, S.D.; Schreurs, A.W.; Jonges, R.; Carelsen, B.; Vroemen, J.C.; Grimbergen, C.A.; Streekstra, G.J. Computer-Assisted Planning and Navigation for Corrective Distal Radius Osteotomy, Based on Pre- and Intraoperative Imaging. *IEEE Trans. Biomed. Eng.* **2011**, *58*, 182–190, doi:10.1109/TBME.2010.2084576.

130. Butcher, C.C.; Atkins, R.M. (Ii) Principles of Deformity Correction. *Curr. Orthop.* **2003**, *17*, 418–435, doi:10.1016/j.cuor.2003.10.001.

131. Masquijo, J.J.; Artigas, C.; de Pablos, J. Growth Modulation with Tension-Band Plates for the Correction of Paediatric Lower Limb Angular Deformity: Current Concepts and Indications for a Rational Use. *EFORT Open Rev.* **2021**, *6*, 658–668, doi:10.1302/2058-5241.6.200098.

132. Nichols, L.R.B.; Tucker, N.J.; Fragomen, A.T.; Podeszwa, D.A.; Liu, R.W. Lower Limb Deformity Correction: Analysis and Preoperative Planning. *Instr. Course Lect.* **2022**, *71*, 251–270.

133. Meisterhans, M.; Flury, A.; Zindel, C.; Zimmermann, S.M.; Vlachopoulos, L.; Snedeker, J.G.; Fucentese, S.F. Finite Element Analysis of Medial Closing and Lateral Opening Wedge Osteotomies of the Distal Femur in Relation to Hinge Fractures. *J. Exp. Orthop.* **2023**, *10*, doi:10.1186/S40634-023-00597-W.

134. Barksfield, R.C.; Monsell, F.P. Predicting Translational Deformity Following Opening-Wedge Osteotomy for Lower Limb Realignment. *Strategies Trauma Limb Reconstr.* **2015**, *10*, 167–173, doi:10.1007/S11751-015-0232-4.

135. Launay, F. Techniques for Correcting Major Lower Limb Deformities. Corrections of Lower Limb Deformities. *Orthopaedics & Traumatology: Surgery & Research* **2025**, 104417, doi:10.1016/J.OTSR.2025.104417.

136. Reif, T.J.; Humphrey, T.J.; Fragomen, A.T. Osteotomies About the Knee: Managing Rotational Deformities. *Oper. Tech. Sports Med.* **2022**, *30*, 150938, doi:10.1016/J.OTSM.2022.150938.

137. Yun, Y.H.; Shin, S.J.; Moon, J.G. Reverse V Osteotomy of the Distal Humerus for the Correction of Cubitus Varus. *J. Bone Joint Surg. Br.* **2007**, *89*, 527–531, doi:10.1302/0301-620X.89B4.18509.

138. Hefti, F.; Morscher, E. The Femoral Neck Lengthening Osteotomy. *Orthopedics and Traumatology* **1993**, *2*, 144–151, doi:10.1007/BF02620521/METRICS.

139. Khosroabadi, A. Novel Techniques for Acute Lengthening of Metatarsal for Treatment of Brachymetatarsia with 2cm and More Shortening. *Foot Ankle Orthop.* **2022**, *7*, 2473011421S00722, doi:10.1177/2473011421S00722.

140. Brumat, P.; Mihalič, R.; Kovač, S.; Trebše, R. Acute Femoral Lengthening in Adults Using Step-Cut Osteotomy, Traction Table, and Proximal Femoral Locking Plate Fixation: Surgical Technique and Report of Three Cases. *Indian J. Orthop.* **2021**, *56*, 559–565, doi:10.1007/S43465-021-00547-7.

141. Hosny, G.A. Limb Lengthening History, Evolution, Complications and Current Concepts. *J. Orthop. Traumatol.* **2020**, *21*, doi:10.1186/S10195-019-0541-3.

142. Jansen, N.J.; Dockx, R.B.M.; Witlox, A.M.; Straetemans, S.; Staal, H.M. Windswept Deformity a Disease or a Symptom? A Systematic Review on the Aetiologies and Hypotheses of Simultaneous Genu Valgum and Varum in Children. *Children (Basel).* **2022**, *9*, doi:10.3390/CHILDREN9050703.

143. Montgomery, D.C.. Design and Analysis of Experiments. **2013**.

144. Jaisingh Sheoran, A.; Kumar, H. Fused Deposition Modeling Process Parameters Optimization and Effect on Mechanical Properties and Part Quality: Review and Reflection on Present Research. *Mater. Today Proc.* **2020**, *21*, 1659–1672, doi:10.1016/J.MATPR.2019.11.296.

145. Qamar Tanveer, M.; Mishra, G.; Mishra, S.; Sharma, R. Effect of Infill Pattern and Infill Density on Mechanical Behaviour of FDM 3D Printed Parts- a Current Review. *Mater. Today Proc.* **2022**, *62*, 100–108, doi:10.1016/J.MATPR.2022.02.310.

146. Agarwal, K.M.; Shubham, P.; Bhatia, D.; Sharma, P.; Vaid, H.; Vajpeyi, R. Analyzing the Impact of Print Parameters on Dimensional Variation of ABS Specimens Printed Using Fused

Deposition Modelling (FDM). *Sensors International* **2022**, *3*, 100149, doi:10.1016/J.SINTL.2021.100149.

147. Rodríguez-Panes, A.; Claver, J.; Camacho, A.M. The Influence of Manufacturing Parameters on the Mechanical Behaviour of PLA and ABS Pieces Manufactured by FDM: A Comparative Analysis. *Materials 2018, Vol. 11, Page 1333* **2018**, *11*, 1333, doi:10.3390/MA11081333.

148. Popescu, D.; Zapciu, A.; Amza, C.; Baciu, F.; Marinescu, R. FDM Process Parameters Influence over the Mechanical Properties of Polymer Specimens: A Review. *Polym. Test.* **2018**, *69*, 157–166, doi:10.1016/J.POLYMERTESTING.2018.05.020.

149. Vanaei, H.R.; Khelladi, S.; Deligant, M.; Shirinbayan, M.; Tcharkhtchi, A. Numerical Prediction for Temperature Profile of Parts Manufactured Using Fused Filament Fabrication. *J. Manuf. Process.* **2022**, *76*, 548–558, doi:10.1016/J.JMAPRO.2022.02.042.

150. Tao, Y.; Kong, F.; Li, Z.; Zhang, J.; Zhao, X.; Yin, Q.; Xing, D.; Li, P. A Review on Voids of 3D Printed Parts by Fused Filament Fabrication. *Journal of Materials Research and Technology* **2021**, *15*, 4860–4879, doi:10.1016/J.JMRT.2021.10.108.

151. Ravoori, D.; Salvi, S.; Prajapati, H.; Qasaimeh, M.; Adnan, A.; Jain, A. Void Reduction in Fused Filament Fabrication (FFF) through in Situ Nozzle-Integrated Compression Rolling of Deposited Filaments. *Virtual Phys. Prototyp.* **2021**, *16*, 146–159, doi:10.1080/17452759.2021.1890986.

152. Kim, H.-C.; Kim, D.-Y.; Lee, J.-E.; Park, K. Improvement of Mechanical Properties and Surface Finish of 3d-Printed Polylactic Acid Parts by Constrained Remelting. *Adv. Mater. Lett.* **2017**, *8*, 1199–1203, doi:10.5185/AMLETT.2017.1686.

153. Lee, S.K.; Kim, Y.R.; Kim, S.H.; Kim, J.H. Investigation of the Internal Stress Relaxation in FDM 3D Printing : Annealing Conditions. *Journal of the Korean Society of Manufacturing Process Engineers* **2018**, *17*, 130–136, doi:10.14775/KSMPE.2018.17.4.130.

154. Liao, Y.; Liu, C.; Coppola, B.; Barra, G.; Di Maio, L.; Incarnato, L.; Lafdi, K. Effect of Porosity and Crystallinity on 3D Printed PLA Properties. *Polymers 2019, Vol. 11, Page 1487* **2019**, *11*, 1487, doi:10.3390/POLYM11091487.

155. Wach, R.A.; Wolszczak, P.; Adamus-Wlodarczyk, A. Enhancement of Mechanical Properties of FDM-PLA Parts via Thermal Annealing. *Macromol. Mater. Eng.* **2018**, *303*, 1800169, doi:10.1002/MAME.201800169.

156. Singh, S.; Singh, M.; Prakash, C.; Gupta, M.K.; Mia, M.; Singh, R. Optimization and Reliability Analysis to Improve Surface Quality and Mechanical Characteristics of Heat-Treated Fused Filament Fabricated Parts. *International Journal of Advanced Manufacturing Technology* **2019**, *102*, 1521–1536, doi:10.1007/S00170-018-03276-8/METRICS.

157. Butt, J.; Bhaskar, R. Investigating the Effects of Annealing on the Mechanical Properties of FFF-Printed Thermoplastics. *Journal of Manufacturing and Materials Processing 2020, Vol. 4, Page 38* **2020**, *4*, 38, doi:10.3390/JMMP4020038.

158. Ferràs-Tarragó, J.; Sabalza-Baztán, O.; Sahuquillo-Arce, J.M.; Angulo-Sánchez, M.Á.; De-La-Calva Ceinos, C.; Amaya-Valero, J.V.; Baixauli-García, F. Autoclave Sterilization of an In-House 3D-Printed Polylactic Acid Piece: Biological Safety and Heat-Induced Deformation. *European Journal of Trauma and Emergency Surgery* **2022**, *48*, 3901–3910, doi:10.1007/S00068-021-01672-6/FIGURES/6.

159. Boursier, J.F.; Fournet, A.; Bassanino, J.; Manassero, M.; Bedu, A.S.; Leperlier, D. Reproducibility, Accuracy and Effect of Autoclave Sterilization on a Thermoplastic Three-Dimensional Model Printed by a Desktop Fused Deposition Modelling Three-Dimensional Printer. *Vet. Comp. Orthop. Traumatol.* **2018**, *31*, 422–430, doi:10.1055/S-0038-1668113.

160. Lluch-Cerezo, J.; Meseguer, M.D.; García-Manrique, J.A.; Benavente, R. Influence of Thermal Annealing Temperatures on Powder Mould Effectiveness to Avoid Deformations in ABS and PLA 3D-Printed Parts. *Polymers (Basel).* **2022**, *14*, doi:10.3390/POLYM14132607.

161. Popescu, D.; Iacob, M.C.; Marinescu, R. Dimensional Accuracy of 3D-Printed Surgical Cutting Guides after Hospital Sterilization: A Comparative Evaluation of Ten MEX Materials. *3D Print. Med.* **2025**, *11*, 1–18, doi:10.1186/S41205-025-00291-W/FIGURES/12.

162. Radhwan, H.; Shayfull, Z.; Farizuan, M.R.; Effendi, M.S.M.; Irfan, A.R. Optimization Parameter Effects on the Quality Surface Finish of the Three-Dimensional Printing (3D-Printing) Fused Deposition Modeling (FDM) Using RSM. *AIP Conf. Proc.* **2019**, *2129*, doi:10.1063/1.5118163.

163. Firtikiadis, L.; Tzotzis, A.; Kyratsis, P.; Efkolidis, N. Response Surface Methodology (RSM)-Based Evaluation of the 3D-Printed Recycled-PETG Tensile Strength. *Applied Mechanics 2024, Vol. 5, Pages 924-937* **2024**, *5*, 924–937, doi:10.3390/APPLMECH5040051.

164. Kwan, Y.H.; Owyang, D.; Ho, S.W.L.; Yam, M.G.J. 3D-Printed Patient Specific Surgical Guides: Balancing Accuracy with Practicality. *J. Clin. Orthop. Trauma* **2023**, *46*, 102293, doi:10.1016/J.JCOT.2023.102293.

165. Wijnbergen, D.C.; van der Stelt, M.; Verhamme, L.M. The Effect of Annealing on Deformation and Mechanical Strength of Tough PLA and Its Application in 3D Printed Prosthetic Sockets. *Rapid Prototyp. J.* **2021**, *27*, 81–89, doi:10.1108/RPJ-04-2021-0090/FULL/PDF.

166. Meinberg, E.G.; Agel, J.; Roberts, C.S.; Karam, M.D.; Kellam, J.F. Fracture and Dislocation Classification Compendium-2018. *J. Orthop. Trauma* **2018**, *32*, S1–S170, doi:10.1097/BOT.0000000000001063.

167. Ilizarov, G.A. Transosseous Osteosynthesis. *Transosseous Osteosynthesis* **1992**, doi:10.1007/978-3-642-84388-4.

168. Benayoun, M.; Langlais, T.; Laurent, R.; Le Hanneur, M.; Vialle, R.; Bachy, M.; Fitoussi, F. 3D Planning and Patient-Specific Surgical Guides in Forearm Osteotomy in Children: Radiographic Accuracy and Clinical Morbidity. *Orthopaedics & Traumatology: Surgery & Research* **2022**, *108*, 102925, doi:10.1016/J.OTSR.2021.102925.

169. Hu, X.; Zhong, M.; Lou, Y.; Xu, P.; Jiang, B.; Mao, F.; Chen, D.; Zheng, P. Clinical Application of Individualized 3D-Printed Navigation Template to Children with Cubitus Varus Deformity. *J. Orthop. Surg. Res.* **2020**, *15*, 1–9, doi:10.1186/S13018-020-01615-8/TABLES/1.

170. Oka, K.; Tanaka, H.; Okada, K.; Sahara, W.; Myoui, A.; Yamada, T.; Yamamoto, M.; Kurimoto, S.; Hirata, H.; Murase, T. Three-Dimensional Corrective Osteotomy for Malunited Fractures of the Upper Extremity Using Patient-Matched Instruments: A Prospective, Multicenter, Open-Label, Single-Arm Trial. *Journal of Bone and Joint Surgery - American Volume* **2019**, *101*, 710–721, doi:10.2106/JBJS.18.00765.

171. Byrne, A.M.; Impelmans, B.; Bertrand, V.; Van Haver, A.; Verstreken, F. Corrective Osteotomy for Malunited Diaphyseal Forearm Fractures Using Preoperative 3-Dimensional Planning and

Patient-Specific Surgical Guides and Implants. *Journal of Hand Surgery* **2017**, *42*, 836.e1-836.e12, doi:10.1016/j.jhsa.2017.06.003.

172. Bauer, A.S.; Storelli, D.A.R.; Sibbel, S.E.; Mccarroll, H.R.; Lattanza, L.L. Preoperative Computer Simulation and Patient-Specific Guides Are Safe and Effective to Correct Forearm Deformity in Children. *Journal of Pediatric Orthopaedics* **2017**, *37*, 504–510, doi:10.1097/BPO.0000000000000673.

173. Alonso, E.; Victoria, C.; Touati, N.; Vialle, R.; Fitoussi, F.; Bachy, M. Computer Aided Multiplanar Osteotomy Using Patient Specific Instrumentation to Treat Cubitus Varus in Children. *Orthopaedics & Traumatology: Surgery & Research* **2024**, *110*, 103808, doi:10.1016/J.OTSR.2023.103808.

174. Zheng, P.; Xu, P.; Yao, Q.; Tang, K.; Lou, Y. 3D-Printed Navigation Template in Proximal Femoral Osteotomy for Older Children with Developmental Dysplasia of the Hip. *Sci. Rep.* **2017**, *7*, doi:10.1038/SREP44993.

175. Sun, J.; Mu, Y.; Cui, Y.; Qu, J.; Lian, F. Application of 3D-Printed Osteotomy Guide Plates in Proximal Femoral Osteotomy for DDH in Children: A Retrospective Study. *J. Orthop. Surg. Res.* **2023**, *18*, 315, doi:10.1186/S13018-023-03801-W.

176. Shi, Q.; Sun, D. Efficacy and Safety of a Novel Personalized Navigation Template in Proximal Femoral Corrective Osteotomy for the Treatment of DDH. *J. Orthop. Surg. Res.* **2020**, *15*, 1–7, doi:10.1186/S13018-020-01843-Y/FIGURES/4.

177. Zheng, H.; Wang, L.; Jiang, W.; Qin, R.; Zhang, Z.; Jia, Z.; Zhang, J.; Liu, Y.; Gao, X. Application of 3D Printed Patient-Specific Instruments in the Treatment of Large Tibial Bone Defects by the Ilizarov Technique of Distraction Osteogenesis. *Front. Surg.* **2023**, *9*, 985110, doi:10.3389/FSURG.2022.985110/BIBTEX.

178. Belvedere, C.; Macleod, A.; Leardini, A.; Grassi, A.; Fabbro, G.D.; Zaffagnini, S.; Gill, H.S. 3D MEDICAL IMAGING ANALYSIS, PATIENT-SPECIFIC INSTRUMENTATION AND INDIVIDUALIZED IMPLANT DESIGN, WITH ADDITIVE MANUFACTURING CREATES A NEW PERSONALIZED HIGH TIBIAL OSTEOTOMY TREATMENT OPTION. *https://doi.org/10.1142/S0219519423400419* **2023**, *23*, doi:10.1142/S0219519423400419.

179. Liu, W.; Zhang, S.; Zhang, W.; Li, F.; Tueraili, A.; Qi, L.; Wang, C. Clinical Application of 3D Printing-Assisted Patient-Specific Instrument Osteotomy Guide in Stiff Clubfoot: Preliminary Findings. *J. Orthop. Surg. Res.* **2023**, *18*, 1–8, doi:10.1186/S13018-023-04341-Z/TABLES/3.

180. Zhang, Y.W.; You, M.R.; Zhang, X.X.; Yu, X.L.; Zhang, L.; Deng, L.; Wang, Z.; Dong, X.P. The Novel Application of Three-Dimensional Printing Assisted Patient-Specific Instrument Osteotomy Guide in the Precise Osteotomy of Adult Talipes Equinovarus. *Biomed Res. Int.* **2021**, *2021*, 1004849, doi:10.1155/2021/1004849.

181. Trisolino, G.; Depaoli, A.; Menozzi, G.C.; Lerma, L.; Di Gennaro, M.; Quinto, C.; Vivarelli, L.; Dallari, D.; Rocca, G. Virtual Surgical Planning and Patient-Specific Instruments for Correcting Lower Limb Deformities in Pediatric Patients: Preliminary Results from the In-Office 3D Printing Point of Care. *J. Pers. Med.* **2023**, *13*, doi:10.3390/JPM13121664.

182. Gómez-Palomo, J.M.; Meschian-Coretti, S.; Esteban-Castillo, J.L.; García-Vera, J.J.; Montañez-Heredia, E. Double Level Osteotomy Assisted by 3D Printing Technology in a Patient with Blount Disease: A Case Report. *JBJS Case Connect.* **2020**, *10*, E0477, doi:10.2106/JBJS.CC.19.00477.

183. Lin, C.R.; Chou, H.; Luo, C.A.; Chang, S.H. A Novel Technique for Autograft Preparation Using Patient-Specific Instrumentation (PSI) Assistance in Total Hip Arthroplasty in Developmental Dysplasia of Hip (DDH). *J. Pers. Med.* **2023**, *13*, 1331, doi:10.3390/JPM13091331.

184. Huotilainen, E.; Salmi, M.; Lindahl, J. Three-Dimensional Printed Surgical Templates for Fresh Cadaveric Osteochondral Allograft Surgery with Dimension Verification by Multivariate Computed Tomography Analysis. *Knee* **2019**, *26*, 923–932, doi:10.1016/J.KNEE.2019.05.007.

185. Evrard, R.; Schubert, T.; Paul, L.; Docquier, P.L. Quality of Resection Margin with Patient Specific Instrument for Bone Tumor Resection. *J. Bone Oncol.* **2022**, *34*, 100434, doi:10.1016/J.JBO.2022.100434.

186. Müller, D.A.; Stutz, Y.; Vlachopoulos, L.; Farshad, M.; Fürnstahl, P. The Accuracy of Three-Dimensional Planned Bone Tumor Resection Using Patient-Specific Instrument. *Cancer Manag. Res.* **2020**, *12*, 6533–6540, doi:10.2147/CMAR.S228038.

187. Wang, C.; Huang, S.; Yu, Y.; Liang, H.; Wang, R.; Tang, X.; Ji, T. Fluoroscopically Calibrated 3D-Printed Patient-Specific Instruments Improve the Accuracy of Osteotomy during Bone Tumor Resection Adjacent to Joints. *3D Print. Med.* **2024**, *10*, 1–10, doi:10.1186/S41205-024-00216-Z/TABLES/2.

188. Bruschi, A.; Donati, D.M.; Di Bella, C. What to Choose in Bone Tumour Resections? Patient Specific Instrumentation versus Surgical Navigation: A Systematic Review. *J. Bone Oncol.* **2023**, *42*, 100503, doi:10.1016/J.JBO.2023.100503.

189. Cheng, H.; Clymer, J.W.; Po-Han Chen, B.; Sadeghirad PhD, B.; Ferko, N.C.; Cameron, C.G.; Hinoul, P. Prolonged Operative Duration Is Associated with Complications: A Systematic Review and Meta-Analysis. *Journal of Surgical Research* **2018**, *229*, 134–144, doi:10.1016/J.JSS.2018.03.022.

190. Cordero-Ampuero, J.; De Dios, M. What Are the Risk Factors for Infection in Hemiarthroplasties and Total Hip Arthroplasties? *Clin. Orthop. Relat. Res.* **2010**, *468*, 3268–3277, doi:10.1007/S11999-010-1411-8.

191. Mounsef, P.J.; Aita, R.; Skaik, K.; Addab, S.; Hamdy, R.C. Three-Dimensional-Printing-Guided Preoperative Planning of Upper and Lower Extremity Pediatric Orthopedic Surgeries: A Systematic Review of Surgical Outcomes. *J. Child. Orthop.* **2024**, *18*, 360, doi:10.1177/18632521241264183.

192. Hess, S.; Husarek, J.; Müller, M.; Eberlein, S.C.; Klenke, F.M.; Hecker, A. Applications and Accuracy of 3D-printed Surgical Guides in Traumatology and Orthopaedic Surgery: A Systematic Review and Meta-analysis. *J. Exp. Orthop.* **2024**, *11*, e12096, doi:10.1002/JEO2.12096.

193. Erickson, B.J.; Chalmers, P.N.; Denard, P.; Lederman, E.; Horneff, G.; Werner, B.C.; Provencher, M.T.; Romeo, A.A. Does Commercially Available Shoulder Arthroplasty Preoperative Planning Software Agree with Surgeon Measurements of Version, Inclination, and Subluxation? *J. Shoulder Elbow Surg.* **2021**, *30*, 413–420, doi:10.1016/j.jse.2020.05.027.

194. Friedman, R.J.; Barcel, D.A.; Eichinger, J.K. Scapular Notching in Reverse Total Shoulder Arthroplasty. *Journal of the American Academy of Orthopaedic Surgeons* **2019**, *27*, 200–209, doi:10.5435/JAAOS-D-17-00026,.

195. Kim, M.S.; Jeong, H.Y.; Kim, J.D.; Ro, K.H.; Rhee, S.M.; Rhee, Y.G. Difficulty in Performing Activities of Daily Living Associated with Internal Rotation after Reverse Total Shoulder Arthroplasty. *J. Shoulder Elbow Surg.* **2020**, *29*, 86–94, doi:10.1016/J.JSE.2019.05.031,.

196. Halperin, S.J.; Dhodapkar, M.M.; Kim, L.; Modrak, M.; Medvecky, M.J.; Donohue, K.W.; Grauer, J.N. Anatomic vs. Reverse Total Shoulder Arthroplasty: Usage Trends and Perioperative Outcomes. *Seminars in Arthroplasty: JSES* **2024**, *34*, 91–96, doi:10.1053/J.SART.2023.08.014.

197. Rupani, N.; Combescure, C.; Silman, A.; Lübbeke, A.; Rees, J. International Trends in Shoulder Replacement: A Meta-Analysis from 11 Public Joint Registers. *Acta Orthop.* **2024**, *95*, 348, doi:10.2340/17453674.2024.40948.

198. Boileau, P.; Watkinson, D.J.; Hatzidakis, A.M.; Balg, F. Grammont Reverse Prosthesis: Design, Rationale, and Biomechanics. *J. Shoulder Elbow Surg.* **2005**, *14*, S147–S161, doi:10.1016/j.jse.2004.10.006.

199. Giles, J.W.; Langohr, G.D.G.; Johnson, J.A.; Athwal, G.S. Implant Design Variations in Reverse Total Shoulder Arthroplasty Influence the Required Deltoid Force and Resultant Joint Load. *Clin. Orthop. Relat. Res.* **2015**, *473*, 3615–3626, doi:10.1007/S11999-015-4526-0,.

200. Costantini, O.; Choi, D.S.; Kontaxis, A.; Gulotta, L. V. The Effects of Progressive Lateralization of the Joint Center of Rotation of Reverse Total Shoulder Implants. *J. Shoulder Elbow Surg.* **2015**, *24*, 1120–1128, doi:10.1016/j.jse.2014.11.040.

201. Hamilton, M.A.; Diep, P.; Roche, C.; Flurin, P.H.; Wright, T.W.; Zuckerman, J.D.; Routman, H. Effect of Reverse Shoulder Design Philosophy on Muscle Moment Arms. *Journal of Orthopaedic Research* **2015**, *33*, 605–613, doi:10.1002/JOR.22803.

202. Sirveaux, F.; Favard, L.; Oudet, D.; Huquet, D.; Walch, G.; Molé, D. Grammont Inverted Total Shoulder Arthroplasty in the Treatment of Glenohumeral Osteoarthritis with Massive Rupture of the Cuff. Results of a Multicentre Study of 80 Shoulders. *Journal of Bone and Joint Surgery - Series B* **2004**, *86*, 388–395, doi:10.1302/0301-620X.86B3.14024/LETTERTOEDITOR.

203. Boileau, P.; Watkinson, D.; Hatzidakis, A.M.; Hovorka, I. Neer Award 2005: The Grammont Reverse Shoulder Prosthesis: Results in Cuff Tear Arthritis, Fracture Sequelae, and Revision Arthroplasty. *J. Shoulder Elbow Surg.* **2006**, *15*, 527–540, doi:10.1016/j.jse.2006.01.003.

204. Gladstone, J.N.; Bishop, J.Y.; Lo, I.K.Y.; Flatow, E.L. Fatty Infiltration and Atrophy of the Rotator Cuff Do Not Improve after Rotator Cuff Repair and Correlate with Poor Functional Outcome. *American Journal of Sports Medicine* **2007**, *35*, 719–728, doi:10.1177/0363546506297539;WEBSITE:WEBSITE:SAGE;WGROUP:STRING:PUBLICATION.

205. Hoenecke, H.R.; Flores-Hernandez, C.; D'Lima, D.D. Reverse Total Shoulder Arthroplasty Component Center of Rotation Affects Muscle Function. *J. Shoulder Elbow Surg.* **2014**, *23*, 1128–1135, doi:10.1016/j.jse.2013.11.025.

206. Paclot, J.; Saab, M.; Szymanski, C.; Maynou, C.; Amouyel, T. A Low Teres Minor Index of Trophicity Negatively Impacts the Functional Outcomes of Reverse Shoulder Arthroplasty. *Orthopaedics and Traumatology: Surgery and Research* **2021**, *107*, doi:10.1016/j.otsr.2021.102902.

207. Nolan, B.M.; Ankerson, E.; Wiater, M.J. Reverse Total Shoulder Arthroplasty Improves Function in Cuff Tear Arthropathy. *Clin. Orthop. Relat. Res.* **2011**, *469*, 2476–2482, doi:10.1007/S11999-010-1683-Z,.

208. Ackland, D.C.; Wu, W.; Thomas, R.; Patel, M.; Page, R.; Sangeux, M.; Richardson, M. Muscle and Joint Function After Anatomic and Reverse Total Shoulder Arthroplasty Using a Modular Shoulder Prosthesis. *Journal of Orthopaedic Research* **2019**, *37*, 1988–2003, doi:10.1002/JOR.24335,.

209. Ackland, D.C.; Richardson, M.; Pandy, M.G. Axial Rotation Moment Arms of the Shoulder Musculature after Reverse Total Shoulder Arthroplasty. *Journal of Bone and Joint Surgery* **2012**, *94*, 1886–1895, doi:10.2106/JBJS.J.01861,.

210. Ackland, D.C.; Roshan-Zamir, S.; Richardson, M.; Pandy, M.G. Moment Arms of the Shoulder Musculature after Reverse Total Shoulder Arthroplasty. *Journal of Bone and Joint Surgery* **2010**, *92*, 1221–1230, doi:10.2106/JBJS.I.00001,.

211. Rajabzadeh-Oghaz, H.; Kumar, V.; Berry, D.B.; Singh, A.; Schoch, B.S.; Aibinder, W.R.; Gobbato, B.; Polakovic, S.; Elwell, J.; Roche, C.P. Impact of Deltoid Computer Tomography Image Data on the Accuracy of Machine Learning Predictions of Clinical Outcomes after Anatomic and Reverse Total Shoulder Arthroplasty. *Journal of Clinical Medicine 2024, Vol. 13, Page 1273* **2024**, *13*, 1273, doi:10.3390/JCM13051273.

212. Sabatino, A.; Sola, K.H.; Brismar, T.B.; Lindholm, B.; Stenvinkel, P.; Avesani, C.M. Making the Invisible Visible: Imaging Techniques for Assessing Muscle Mass and Muscle Quality in Chronic Kidney Disease. *Clin. Kidney J.* **2024**, *17*, doi:10.1093/CKJ/SFAE028.

213. Buck, F.M.; Jost, B.; Hodler, J. Shoulder Arthroplasty. *Eur. Radiol.* **2008**, *18*, 2937–2948, doi:10.1007/S00330-008-1093-8/TABLES/6.

214. Saupe, N.; Pfirrmann, C.W.A.; Schmid, M.R.; Jost, B.; Werner, C.M.L.; Zanetti, M. Association between Rotator Cuff Abnormalities and Reduced Acromiohumeral Distance. *American Journal of Roentgenology* **2006**, *187*, 376–382, doi:10.2214/AJR.05.0435/ASSET/IMAGES/05_0435_02E.JPEG.

215. Ellman, H.; Hanker, G.; Bayer, M. Repair of the Rotator Cuff. End-Result Study of Factors Influencing Reconstruction. *Journal of Bone and Joint Surgery. American volume* **1986**, *68*, 1136–1144, doi:10.2106/00004623-198668080-00002.

216. Deger, G.U.; Davulcu, C.D.; Karaismailoglu, B.; Palamar, D.; Guven, M.F. Are Acromiohumeral Distance Measurements on Conventional Radiographs Reliable? A Prospective Study of Inter-Method Agreement with Ultrasonography, and Assessment of Observer Variability. *Jt. Dis. Relat. Surg.* **2024**, *35*, 062–071, doi:10.52312/JDRS.2023.1288.

217. Rainey, J.; Hameed, D.; Sodhi, N.; Malkani, A.L.; Mont, M.A. Use of Computed Tomography for Shoulder Arthroplasty: A Systematic Review. *J. Orthop.* **2025**, *59*, 30–35, doi:10.1016/J.JOR.2024.05.007.

218. Goutallier, D.; Postel, J.-M.; Bernageau, J.; Lavau, L.; Voisin, M.-C. Fatty Muscle Degeneration in Cuff Ruptures. Pre- and Postoperative Evaluation by CT Scan. *Clin. Orthop. Relat. Res.* **1994**, *304*, 78???83, doi:10.1097/00003086-199407000-00014.

219. Chalmers, P.N.; Beck, L.; Stertz, I.; Aleem, A.; Keener, J.D.; Henninger, H.B.; Tashjian, R.Z. Do Magnetic Resonance Imaging and Computed Tomography Provide Equivalent Measures of Rotator Cuff Muscle Size in Glenohumeral Osteoarthritis? *J. Shoulder Elbow Surg.* **2018**, *27*, 1877–1883, doi:10.1016/j.jse.2018.03.015.

220. Aubrey, J.; Esfandiari, N.; Baracos, V.E.; Buteau, F.A.; Frenette, J.; Putman, C.T.; Mazurak, V.C. Measurement of Skeletal Muscle Radiation Attenuation and Basis of Its Biological Variation. *Acta Physiol. (Oxf).* **2014**, *210*, 489, doi:10.1111/APHA.12224.

221. Roy, J.-S.; Braën, C.; Leblond, J.; Desmeules, F.; Dionne, C.E.; Macdermid, J.C.; Bureau, N.J.; Frémont, P. Diagnostic Accuracy of Ultrasonography, MRI and MR Arthrography in the Characterisation of Rotator Cuff Disorders: A Systematic Review and Meta-Analysis., doi:10.1136/bjsports-2014-094148.

222. Okoroha, K.R.; Fidai, M.S.; Tramer, J.S.; Davis, K.D.; Kolowich, P.A. Diagnostic Accuracy of Ultrasound for Rotator Cuff Tears. *Ultrasonography* **2019**, *38*, doi:10.14366/usg.18058.

223. Nazarian, L.N.; Jacobson, J.A.; Benson, C.B.; Bancroft, L.W.; Bedi, A.; McShane, J.M.; Miller, T.T.; Parker, L.; Smith, J.; Steinbach, L.S.; et al. Imaging Algorithms for Evaluating Suspected Rotator Cuff Disease: Society of Radiologists in Ultrasound Consensus Conference Statement. *Radiology* **2013**, *267*, 589–595, doi:10.1148/RADIOL.13121947,.

224. Kissenberth, M.J.; Rulewicz, G.J.; Hamilton, S.C.; Bruch, H.E.; Hawkins, R.J. A Positive Tangent Sign Predicts the Repairability of Rotator Cuff Tears. *J. Shoulder Elbow Surg.* **2014**, *23*, 1023–1027, doi:10.1016/J.JSE.2014.02.014.

225. Siebert, M.J.; Chalian, M.; Sharifi, A.; Pezeshk, P.; Xi, Y.; Lawson, P.; Chhabra, A. Qualitative and Quantitative Analysis of Glenoid Bone Stock and Glenoid Version: Inter-Reader Analysis and Correlation with Rotator Cuff Tendinopathy and Atrophy in Patients with Shoulder Osteoarthritis. *Skeletal Radiol.* **2020**, *49*, 985–993, doi:10.1007/S00256-020-03377-0,.

226. Jensen, A.R.; Taylor, A.J.; Sanchez-Sotelo, J. Factors Influencing the Reparability and Healing Rates of Rotator Cuff Tears. *Curr. Rev. Musculoskelet. Med.* **2020**, *13*, 572–583, doi:10.1007/S12178-020-09660-W/TABLES/3.

227. Levy, O.; Walecka, J.; Arealis, G.; Tsvieli, O.; Della Rotonda, G.; Abraham, R.; Polyzois, I.; Jurkowski, Z.; Atoun, E. Bilateral Reverse Total Shoulder Arthroplasty—Functional Outcome and Activities of Daily Living. *J. Shoulder Elbow Surg.* **2017**, *26*, e85–e96, doi:10.1016/J.JSE.2016.09.010/ASSET/CEF47CB2-4DE2-436C-B7DB-4BA0C7378D87/MAIN.ASSETS/YMSE3672-FIG-0004.JPG.

228. Fuchs, B.; Weishaupt, D.; Zanetti, M.; Hodler, J.; Gerber, C. Fatty Degeneration of the Muscles of the Rotator Cuff: Assessment by Computed Tomography versus Magnetic Resonance Imaging. *J. Shoulder Elbow Surg.* **1999**, *8*, 599–605, doi:10.1016/S1058-2746(99)90097-6.

229. Vidt, M.E.; Santago, A.C.; Tuohy, C.J.; Poehling, G.G.; Freehill, M.T.; Kraft, R.A.; Marsh, A.P.; Hegedus, E.J.; Miller, M.E.; Saul, K.R. Assessments of Fatty Infiltration and Muscle Atrophy from a Single Magnetic Resonance Image Slice Are Not Predictive of 3-Dimensional Measurements. *Arthroscopy - Journal of Arthroscopic and Related Surgery* **2016**, *32*, 128–139, doi:10.1016/j.arthro.2015.06.035.

230. Williams, M.D.; Lädermann, A.; Melis, B.; Barthelemy, R.; Walch, G. Fatty Infiltration of the Supraspinatus: A Reliability Study. *J. Shoulder Elbow Surg.* **2009**, *18*, 581–587, doi:10.1016/j.jse.2008.12.014.

231. Werthel, J.D.; Walch, G.; Vegehan, E.; Deransart, P.; Sanchez-Sotelo, J.; Valenti, P. Lateralization in Reverse Shoulder Arthroplasty: A Descriptive Analysis of Different Implants in Current Practice. *Int. Orthop.* **2019**, *43*, 2349–2360, doi:10.1007/S00264-019-04365-3/FIGURES/4.

232. Werthel, J.D.; Boux de Casson, F.; Burdin, V.; Athwal, G.S.; Favard, L.; Chaoui, J.; Walch, G. CT-Based Volumetric Assessment of Rotator Cuff Muscle in Shoulder Arthroplasty Preoperative Planning. *Bone Jt. Open* **2021**, *2*, 552–561, doi:10.1302/2633-1462.27.BJO-2021-0081.R1/LETTERTOEDITOR.

233. Werthel, J.D.; Boux de Casson, F.; Walch, G.; Gaudin, P.; Moroder, P.; Sanchez-Sotelo, J.; Chaoui, J.; Burdin, V. Three-Dimensional Muscle Loss Assessment: A Novel Computed Tomography–Based Quantitative Method to Evaluate Rotator Cuff Muscle Fatty Infiltration. *J. Shoulder Elbow Surg.* **2022**, *31*, 165–174, doi:10.1016/j.jse.2021.07.029.

234. Wiater, B.P.; Koueiter, D.M.; Maerz, T.; Moravek, J.E.; Yonan, S.; Marcantonio, D.R.; Wiater, J.M. Preoperative Deltoid Size and Fatty Infiltration of the Deltoid and Rotator Cuff Correlate to Outcomes After Reverse Total Shoulder Arthroplasty. *Clin. Orthop. Relat. Res.* **2015**, *473*, 663–673, doi:10.1007/S11999-014-4047-2,.

235. Simovitch, R.W.; Helmy, N.; Zumstein, M.A.; Gerber, C. Impact of Fatty Infiltration of the Teres Minor Muscle on the Outcome of Reverse Total Shoulder Arthroplasty. *Journal of Bone and Joint Surgery* **2007**, *89*, 934–939, doi:10.2106/JBJS.F.01075,.

236. Blakeney, W.G.; Shao, W.; Werthel, J.-D.; Wang, A.; Bauer, S. Normalized Preoperative Muscle Volume Correlates with Shoulder Strength at Minimum 2 Years after Lateralized RTSA. *JSES Int.* **2025**, doi:10.1016/J.JSEINT.2025.04.037.

237. Nabergoj, M.; Onishi, S.; Lädermann, A.; Kalache, H.; Trebše, R.; Bothorel, H.; Collin, P. Can Lateralization of Reverse Shoulder Arthroplasty Improve Active External Rotation in Patients with Preoperative Fatty Infiltration of the Infraspinatus and Teres Minor? *J. Clin. Med.* **2021**, *10*, doi:10.3390/JCM10184130,.

238. Greiner, S.; Schmidt, C.; Herrmann, S.; Pauly, S.; Perka, C. Clinical Performance of Lateralized versus Non-Lateralized Reverse Shoulder Arthroplasty: A Prospective Randomized Study. *J. Shoulder Elbow Surg.* **2015**, *24*, 1397–1404, doi:10.1016/J.JSE.2015.05.041.

239. Lévigne, C.; Boileau, P.; Favard, L.; Garaud, P.; Molé, D.; Sirveaux, F.; Walch, G. Scapular Notching in Reverse Shoulder Arthroplasty. *J. Shoulder Elbow Surg.* **2008**, *17*, 925–935, doi:10.1016/J.JSE.2008.02.010.

240. White, A.E.; Dekhne, M.S.; Mazzucco, M.; Nathan, K.; Greditzer, H.G.; Kew, M.; Taylor, S.A. Preoperative Acromiohumeral Index and the Goutallier Classification Reliably Predict Rotator Cuff Integrity Using Computed Tomography and Magnetic Resonance Imaging as Confirmed Intraoperatively in Shoulder Arthroplasty Patients. *Seminars in Arthroplasty: JSES* **2025**, doi:10.1053/J.SART.2025.01.005.

241. Hung, L.W.; Wu, S.; Lee, A.; Zhang, A.L.; Feeley, B.T.; Xiao, W.; Ma, C.B.; Lansdown, D.A. Teres Minor Muscle Hypertrophy Is a Negative Predictor of Outcomes after Reverse Total Shoulder Arthroplasty: An Evaluation of Preoperative Magnetic Resonance Imaging and Postoperative Implant Position. *J. Shoulder Elbow Surg.* **2021**, *30*, e636–e645, doi:10.1016/J.JSE.2020.12.020,.

242. Puzzitiello, R.N.; Moverman, M.A.; Menendez, M.E.; Hart, P.A.; Kirsch, J.; Jawa, A. Rotator Cuff Fatty Infiltration and Muscle Atrophy Do Not Impact Clinical Outcomes after Reverse Total Shoulder Arthroplasty for Glenohumeral Osteoarthritis with Intact Rotator Cuff. *J. Shoulder Elbow Surg.* **2021**, *30*, 2506–2513, doi:10.1016/j.jse.2021.03.135.

243. Szymanski, C.; Boniface, O.; Demondion, X.; Deladerrière, J.Y.; Vervoort, T.; Cotten, A.; Maynou, C. Anatomic and CT Scan Assessment of Teres Minor: A New Index of Trophicity. *Orthopaedics and Traumatology: Surgery and Research* **2013**, *99*, 449–453, doi:10.1016/j.otsr.2012.10.019.

244. Gerber, C.; Blumenthal, S.; Curt, A.; Werner, C.M.L. Effect of Selective Experimental Suprascapular Nerve Block on Abduction and External Rotation Strength of the Shoulder. *J. Shoulder Elbow Surg.* **2007**, *16*, 815–820, doi:10.1016/j.jse.2007.02.120.

245. Ichinose, T.; Yamamoto, A.; Kobayashi, T.; Shitara, H.; Shimoyama, D.; Iizuka, H.; Koibuchi, N.; Takagishi, K. Compensatory Hypertrophy of the Teres Minor Muscle after Large Rotator Cuff Tear Model in Adult Male Rat. *J. Shoulder Elbow Surg.* **2016**, *25*, 316–321, doi:10.1016/j.jse.2015.07.023.

246. Jang, Y.H.; Kim, D.O.; Kim, S.H. Effect of Preoperative Teres Minor Hypertrophy on Reverse Total Shoulder Arthroplasty. *J. Shoulder Elbow Surg.* **2020**, *29*, 1136–1144, doi:10.1016/j.jse.2019.10.014.

247. McClatchy, S.G.; Heise, G.M.; Mihalko, W.M.; Azar, F.M.; Smith, R.A.; Witte, D.H.; Stanfill, J.G.; Throckmorton, T.W.; Brolin, T.J. Effect of Deltoid Volume on Range of Motion and Patient-Reported Outcomes Following Reverse Total Shoulder Arthroplasty in Rotator Cuff-Intact and Rotator Cuff-Deficient Conditions. *Shoulder Elbow* **2022**, *14*, 24–29, doi:10.1177/1758573220925046,.

248. Hill, J.R.; Velicki, K.; Chamberlain, A.M.; Aleem, A.W.; Keener, J.D.; Zmistowski, B.M. Rotator Cuff and Deltoid Muscle Changes Following Reverse Total Shoulder Arthroplasty. *Semin. Arthroplasty* **2023**, *33*, 304–314, doi:10.1053/J.SART.2022.12.004.

249. de Boer, F.A.; Pasma, J.H.; Huijgen, W.H.F.; Huijsmans, P.E.; Flikweert, P.E. Long-Term Relation between Deltoid Muscle Volume and Clinical Outcomes in a Reverse Shoulder Arthroplasty. *Seminars in Arthroplasty: JSES* **2022**, *32*, 664–670, doi:10.1053/J.SART.2022.07.010.

250. Akagi, R.; Takai, Y.; Ohta, M.; Kanehisa, H.; Kawakami, Y.; Fukunaga, T. Muscle Volume Compared to Cross-Sectional Area Is More Appropriate for Evaluating Muscle Strength in Young and Elderly Individuals. *Age Ageing* **2009**, *38*, 564–569, doi:10.1093/AGEING/AFP122,.

251. Caldaria, A.; Giovannetti de Sanctis, E.; Saccone, L.; Baldari, A.; Azzolina, D.; La Verde, L.; Palumbo, A.; Franceschi, F. Bone Density Changes at the Origin of the Deltoid Muscle Following Reverse Shoulder Arthroplasty. *Journal of Clinical Medicine 2024, Vol. 13, Page 3695* **2024**, *13*, 3695, doi:10.3390/JCM13133695.

252. Yoon, D.J.Y.; Odri, G.A.; Favard, L.; Samargandi, R.; Berhouet, J. Preoperative Planning for Reverse Shoulder Arthroplasty: Does the Clinical Range of Motion Match the Planned 3D Humeral Displacement? *J. Pers. Med.* **2023**, *13*, 771, doi:10.3390/JPM13050771.

253. Maxwell, M.J.; Glass, E.A.; Bowler, A.R.; Koechling, Z.; Lohre, R.; Diestel, D.R.; McDonald-Stahl, M.; Bartels, W.; Vancleef, S.; Murthi, A.; et al. The Effect of Reverse Shoulder Arthroplasty Design and Surgical Indications on Deltoid and Rotator Cuff Muscle Length. *J. Shoulder Elbow Surg.* **2025**, *34*, doi:10.1016/j.jse.2024.10.003.

254. Levin, J.M.; Pugliese, M.; Gobbi, F.; Pandy, M.G.; Di Giacomo, G.; Frankle, M.A. Impact of Reverse Shoulder Arthroplasty Design and Patient Shoulder Size on Moment Arms and Muscle Fiber Lengths in Shoulder Abductors. *J. Shoulder Elbow Surg.* **2023**, *32*, 2550–2560, doi:10.1016/j.jse.2023.05.035.

255. Herregodts, J.; Verhaeghe, M.; Poncet, D.; De Wilde, L.; Van Tongel, A.; Herregodts, S. A Functional Evaluation of the Rotator Cuff Length after Reverse Total Shoulder Arthroplasty. *JSES Int.* **2025**, *9*, 788–797, doi:10.1016/J.JSEINT.2024.12.012.

256. Haeffner, B.D.; Cueto, R.J.; Abdelmalik, B.M.; Hones, K.M.; Wright, J.O.; Srinivasan, R.C.; King, J.J.; Wright, T.W.; Werthel, J.D.; Schoch, B.S.; et al. The Association between Humeral Lengthening and Clinical Outcomes after Reverse Shoulder Arthroplasty: A Systematic Review and Meta-Analysis. *J. Shoulder Elbow Surg.* **2023**, *32*, e477–e494, doi:10.1016/j.jse.2023.05.024.

257. Chen, S.; Urban, M.W.; Pislaru, C.; Kinnick, R.; Zheng, Y.; Yao, A.; Greenleaf, J.F. Shearwave Dispersion Ultrasound Vibrometry (SDUV) for Measuring Tissue Elasticity and Viscosity. *IEEE Trans. Ultrason. Ferroelectr. Freq. Control* **2009**, *56*, 55–62, doi:10.1109/TUFFC.2009.1005,.

258. Sarvazyan, A.P.; Rudenko, O. V.; Swanson, S.D.; Fowlkes, J.B.; Emelianov, S.Y. Shear Wave Elasticity Imaging: A New Ultrasonic Technology of Medical Diagnostics. *Ultrasound Med. Biol.* **1998**, *24*, 1419–1435, doi:10.1016/S0301-5629(98)00110-0.

259. Mallett, K.; Nguyen, N.T. V.; Giambini, H.; Werthel, J.D.; Sanchez-Sotelo, J. Changes in Deltoid Muscle Tension after Reverse Shoulder Arthroplasty as Quantified by Shear Wave Elastography: Relationship with Radiographic Parameters and Functional Outcomes. *Seminars in Arthroplasty JSES* **2021**, *31*, 751–758, doi:10.1053/J.SART.2021.04.011.

260. Fenwick, A.; Reichel, T.; Eden, L.; Schmalzl, J.; Meffert, R.; Plumhoff, P.; Gilbert, F. Deltoid Muscle Tension Alterations Post Reverse Shoulder Arthroplasty: An Investigation Using Shear Wave Elastography. *J. Clin. Med.* **2023**, *12*, 6184, doi:10.3390/JCM12196184.

261. Schmalzl, J.; Fenwick, A.; Reichel, T.; Schmitz, B.; Jordan, M.; Meffert, R.; Plumhoff, P.; Boehm, D.; Gilbert, F. Anterior Deltoid Muscle Tension Quantified with Shear Wave Ultrasound Elastography Correlates with Pain Level after Reverse Shoulder Arthroplasty. *European Journal of Orthopaedic Surgery and Traumatology* **2022**, *32*, 333–339, doi:10.1007/S00590-021-02987-1,.

262. Hatta, T.; Mashiko, R. Quantified Deltoid Muscle Stiffness Can Predict Improved Muscle Strength for Elevation Following Reverse Shoulder Arthroplasty. *Journal of Clinical Medicine 2024, Vol. 13, Page 6038* **2024**, *13*, 6038, doi:10.3390/JCM13206038.

263. Hatta, T.; Giambini, H.; Sukegawa, K.; Yamanaka, Y.; Sperling, J.W.; Steinmann, S.P.; Itoi, E.; An, K.N. Quantified Mechanical Properties of the Deltoid Muscle Using the Shear Wave Elastography: Potential Implications for Reverse Shoulder Arthroplasty. *PLoS One* **2016**, *11*, e0155102, doi:10.1371/JOURNAL.PONE.0155102.

264. Cruz-Jentoft, A.J.; Bahat, G.; Bauer, J.; Boirie, Y.; Bruyère, O.; Cederholm, T.; Cooper, C.; Landi, F.; Rolland, Y.; Sayer, A.A.; et al. Sarcopenia: Revised European Consensus on Definition and Diagnosis. *Age Ageing* **2019**, *48*, 16–31, doi:10.1093/AGEING/AFY169.

265. Woo, J. Sarcopenia. *Clin. Geriatr. Med.* **2017**, *33*, 305–314, doi:10.1016/j.cger.2017.02.003.

266. McCarthy, H.D.; Samani-Radia, D.; Jebb, S.A.; Prentice, A.M. Skeletal Muscle Mass Reference Curves for Children and Adolescents. *Pediatr. Obes.* **2014**, *9*, 249–259, doi:10.1111/J.2047-6310.2013.00168.X,.

267. Bhatt, J.M. The Epidemiology of Neuromuscular Diseases. *Neurol. Clin.* **2016**, *34*, 999–1021, doi:10.1016/J.NCL.2016.06.017.

268. Prado, C.M.M.; Wells, J.C.K.; Smith, S.R.; Stephan, B.C.M.; Siervo, M. Sarcopenic Obesity: A Critical Appraisal of the Current Evidence. *Clinical Nutrition* **2012**, *31*, 583–601, doi:10.1016/j.clnu.2012.06.010.

269. Hales, C.M.; Carroll, M.D.; Fryar, C.D.; Ogden, C.L. Prevalence of Obesity Among Adults and Youth: United States, 2015-2016. *NCHS Data Brief* **2017**, 1–8.

270. Buckinx, F.; Landi, F.; Cesari, M.; Fielding, R.A.; Visser, M.; Engelke, K.; Maggi, S.; Dennison, E.; Al-Daghri, N.M.; Allepaerts, S.; et al. Pitfalls in the Measurement of Muscle Mass: A Need for a Reference Standard. *J. Cachexia Sarcopenia Muscle* **2018**, *9*, 269–278, doi:10.1002/JCSM.12268,.

271. Nijholt, W.; Scafoglieri, A.; Jager-Wittenaar, H.; Hobbelen, J.S.M.; van der Schans, C.P. The Reliability and Validity of Ultrasound to Quantify Muscles in Older Adults: A Systematic Review. *J. Cachexia Sarcopenia Muscle* **2017**, *8*, 702–712, doi:10.1002/JCSM.12210,.

272. Mourtzakis, M.; Prado, C.M.M.; Lieffers, J.R.; Reiman, T.; McCargar, L.J.; Baracos, V.E. A Practical and Precise Approach to Quantification of Body Composition in Cancer Patients Using Computed Tomography Images Acquired during Routine Care. *Applied Physiology, Nutrition and Metabolism* **2008**, *33*, 997–1006, doi:10.1139/H08-075,.

273. Lee, K.; Shin, Y.; Huh, J.; Sung, Y.S.; Lee, I.S.; Yoon, K.H.; Kim, K.W. Recent Issues on Body Composition Imaging for Sarcopenia Evaluation. *Korean J. Radiol.* **2019**, *20*, 205–217, doi:10.3348/KJR.2018.0479,.

274. Fischer, A.F.& D. Neuromuscular Imaging in Muscular Dystrophies and Other Muscle Diseases. *Imaging Med.* **2013**, *5*, 237â€“248-, doi:10.2217/IIM.13.26.

275. Lurz, E.; Patel, H.; Frimpong, R.G.; Ricciuto, A.; Kehar, M.; Wales, P.W.; Towbin, A.J.; Chavhan, G.B.; Kamath, B.M.; Ng, V.L. Sarcopenia in Children With End-Stage Liver Disease. *J. Pediatr. Gastroenterol. Nutr.* **2018**, *66*, 222–226, doi:10.1097/MPG.0000000000001792,.

276. Kawakubo, N.; Kinoshita, Y.; Souzaki, R.; Koga, Y.; Oba, U.; Ohga, S.; Taguchi, T. The Influence of Sarcopenia on High-Risk Neuroblastoma. *Journal of Surgical Research* **2019**, *236*, 101–105, doi:10.1016/j.jss.2018.10.048.

277. Kawakami, R.; Tanisawa, K.; Ito, T.; Usui, C.; Miyachi, M.; Torii, S.; Midorikawa, T.; Ishii, K.; Muraoka, I.; Suzuki, K.; et al. Fat-Free Mass Index as a Surrogate Marker of Appendicular Skeletal Muscle Mass Index for Low Muscle Mass Screening in Sarcopenia. *J. Am. Med. Dir. Assoc.* **2022**, *23*, 1955-1961.e3, doi:10.1016/J.JAMDA.2022.08.016.

278. Gilligan, L.A.; Towbin, A.J.; Dillman, J.R.; Somasundaram, E.; Trout, A.T. Quantification of Skeletal Muscle Mass: Sarcopenia as a Marker of Overall Health in Children and Adults. *Pediatr. Radiol.* **2020**, *50*, 455–464, doi:10.1007/S00247-019-04562-7/TABLES/1.

279. Więch, P.; Ćwirlej-Sozańska, A.; Wiśniowska-Szurlej, A.; Kilian, J.; Lenart-Domka, E.; Bejer, A.; Domka-Jopek, E.; Sozański, B.; Korczowski, B. The Relationship between Body Composition and Muscle Tone in Children with Cerebral Palsy: A Case-Control Study. *Nutrients* **2020**, *12*, doi:10.3390/NU12030864,.

280. Sung, K.H.; Chung, C.Y.; Lee, K.M.; Cho, B.C.; Moon, S.J.; Kim, J.; Park, M.S. Differences in Body Composition According to Gross Motor Function in Children With Cerebral Palsy. *Arch. Phys. Med. Rehabil.* **2017**, *98*, 2295–2300, doi:10.1016/j.apmr.2017.04.005.

281. Masaki, M.; Isobe, H.; Uchikawa, Y.; Okamoto, M.; Chiyoda, Y.; Katsuhara, Y.; Mino, K.; Aoyama, K.; Nishi, T.; Ando, Y. Association of Gross Motor Function and Activities of Daily Living with Muscle Mass of the Trunk and Lower Extremity Muscles, Range of Motion, and Spasticity in Children and Adults with Cerebral Palsy. *Dev. Neurorehabil.* **2023**, *26*, 115–122, doi:10.1080/17518423.2023.2171149.

282. Pucillo, E.M.; Dibella, D.L.; Hung, M.; Bounsanga, J.; Crockett, B.; Dixon, M.; Butterfield, R.J.; Campbell, C.; Johnson, N.E. Physical Function and Mobility in Children with Congenital Myotonic Dystrophy. *Muscle Nerve* **2017**, *56*, 224–229, doi:10.1002/MUS.25482.

283. Palmieri, G.M.A.; Bertorini, T.E.; Griffin, J.W.; Igarashi, M.; Karas, J.G. Assessment of Whole Body Composition with Dual Energy X-Ray Absorptiometry in Duchenne Muscular Dystrophy: Correlation of Lean Body Mass with Muscle Function. *Muscle Nerve* **1996**, *19*, 777–779, doi:10.1002/(SICI)1097-4598(199606)19:6<777::AID-MUS15>3.0.CO;2-I.

284. Skalsky, A.J.; Han, J.J.; Abresch, R.T.; Shin, C.S.; McDonald, C.M. Assessment of Regional Body Composition with Dual-Energy X-Ray Absorptiometry in Duchenne Muscular Dystrophy: Correlation of Regional Lean Mass and Quantitative Strength. *Muscle Nerve* **2009**, *39*, 647–651, doi:10.1002/MUS.21212.

285. Schoenau, E. From Mechanostat Theory to Development of the "Functional Muscle-Bone-Unit". *J. Musculoskelet. Neuronal Interact.* **2005**, *5*, 232–238.

286. Vicente-Rodríguez, G.; Urzanqui, A.; Mesana, M.I.; Ortega, F.B.; Ruiz, J.R.; Ezquerra, J.; Casajús, J.A.; Blay, G.; Blay, V.A.; Gonzalez-Gross, M.; et al. Physical Fitness Effect on Bone Mass Is Mediated by the Independent Association between Lean Mass and Bone Mass through Adolescence: A Cross-Sectional Study. *J. Bone Miner. Metab.* **2008**, *26*, 288–294, doi:10.1007/S00774-007-0818-0/METRICS.

287. Dorsey, K.B.; Thornton, J.C.; Heymsfield, S.B.; Gallagher, D. Greater Lean Tissue and Skeletal Muscle Mass Are Associated with Higher Bone Mineral Content in Children. *Nutr. Metab. (Lond).* **2010**, *7*, 1–10, doi:10.1186/1743-7075-7-41/TABLES/5.

288. Marwaha, R.K.; Garg, M.K.; Bhadra, K.; Mahalle, N.; Mithal, A.; Tandon, N. Lean Body Mass and Bone Health in Urban Adolescents from Northern India. *Indian Pediatr.* **2017**, *54*, 193–198, doi:10.1007/S13312-017-1029-Y/METRICS.

289. Kwarteng, E.A.; Shank, L.M.; Faulkner, L.M.; Loch, L.K.; Fatima, S.; Gupta, S.; Haynes, H.E.; Ballenger, K.L.; Parker, M.N.; Brady, S.M.; et al. Influence of Puberty on Relationships between Body Composition and Blood Pressure: A Cross-Sectional Study. *Pediatr. Res.* **2023**, *94*, 781–788, doi:10.1038/S41390-023-02503-7;KWRD=MEDICINE.

290. Kim, J.H.; Park, Y.S. Low Muscle Mass Is Associated with Metabolic Syndrome in Korean Adolescents: The Korea National Health and Nutrition Examination Survey 2009-2011. . **2016**, *36*, 1423–1428, doi:10.1016/J.NUTRES.2016.09.013.

291. Ferrara, I.R.; Sadowsky, C.L. Muscle Mass as a Biomarker for Health Status and Function in Pediatric Individuals with Neuromuscular Disabilities: A Systematic Review. *Children* **2024**, *11*, 815, doi:10.3390/CHILDREN11070815/S1.

292. Johnson, A. Prevalence and Characteristics of Children with Cerebral Palsy in Europe. *Dev. Med. Child Neurol.* **2002**, *44*, 633–640, doi:10.1111/J.1469-8749.2002.TB00848.X.

293. Rosenbaum, P.; Paneth, N.; Leviton, A.; Goldstein, M.; Bax, M. A Report: The Definition and Classification of Cerebral Palsy April 2006. *Dev. Med. Child Neurol.* **2007**, *49*, 8–14, doi:10.1111/J.1469-8749.2007.TB12610.X;CTYPE:STRING:JOURNAL.

294. Graham, H.K.; Rosenbaum, P.; Paneth, N.; Dan, B.; Lin, J.P.; Damiano, Di.L.; Becher, J.G.; Gaebler-Spira, D.; Colver, A.; Reddihough, Di.S.; et al. Cerebral Palsy. *Nat. Rev. Dis. Primers* **2016**, *2*, doi:10.1038/NRDP.2015.82,.

295. Palisano, R.J.; Rosenbaum, P.; Bartlett, D.; Livingston, M.H. Content Validity of the Expanded and Revised Gross Motor Function Classification System. *Dev. Med. Child Neurol.* **2008**, *50*, 744–750, doi:10.1111/J.1469-8749.2008.03089.X,.

296. Palisano, R.; Rosenbaum, P.; Walter, S.; Russell, D.; Wood, E.; Galuppi, B. Development and Reliability of a System to Classify Gross Motor Function in Children with Cerebral Palsy. *Dev. Med. Child Neurol.* **1997**, *39*, 214–223, doi:10.1111/J.1469-8749.1997.TB07414.X,.

297. Cans, C. Surveillance of Cerebral Palsy in Europe: A Collaboration of Cerebral Palsy Surveys and Registers. *Dev. Med. Child Neurol.* **2000**, *42*, 816–824, doi:10.1017/S0012162200001511,.

298. Alman, B. Overview and Comparison of Idiopathic, Neuromuscular, and Congenital Forms of Scoliosis. *The Genetics and Development of Scoliosis* **2010**, 73–79, doi:10.1007/978-1-4419-1406-4_4.

299. Obst, S.J.; Boyd, R.; Read, F.; Barber, L. Quantitative 3-D Ultrasound of the Medial Gastrocnemius Muscle in Children with Unilateral Spastic Cerebral Palsy. *Ultrasound Med. Biol.* **2017**, *43*, 2814–2823, doi:10.1016/j.ultrasmedbio.2017.08.929.

300. Pitcher, C.A.; Elliott, C.M.; Panizzolo, F.A.; Valentine, J.P.; Stannage, K.; Reid, S.L. Ultrasound Characterization of Medial Gastrocnemius Tissue Composition in Children with Spastic Cerebral Palsy. *Muscle Nerve* **2015**, *52*, 397–403, doi:10.1002/MUS.24549;JOURNAL:JOURNAL:10974598;REQUESTEDJOURNAL:JOURNAL:10974598;WGROUP:STRING:PUBLICATION.

301. Johnson, D.L.; Miller, F.; Subramanian, P.; Modlesky, C.M. Adipose Tissue Infiltration of Skeletal Muscle in Children with Cerebral Palsy. *Journal of Pediatrics* **2009**, *154*, doi:10.1016/j.jpeds.2008.10.046.

302. Noble, J.J.; Charles-Edwards, G.D.; Keevil, S.F.; Lewis, A.P.; Gough, M.; Shortland, A.P. Intramuscular Fat in Ambulant Young Adults with Bilateral Spastic Cerebral Palsy. *BMC Musculoskelet. Disord.* **2014**, *15*, doi:10.1186/1471-2474-15-236,.

303. Booth, C.M.; Cortina-Borja, M.J.F.; Theologis, T.N. Collagen Accumulation in Muscles of Children with Cerebral Palsy and Correlation with Severity of Spasticity. *Dev. Med. Child Neurol.* **2001**, *43*, 314, doi:10.1017/S0012162201000597,.

304. Rose, J.; Haskell, W.L.; Gamble, J.G.; Hamilton, R.L.; Brown, D.A.; Rinsky, L. Muscle Pathology and Clinical Measures of Disability in Children with Cerebral Palsy. *Journal of Orthopaedic Research* **1994**, *12*, 758–768, doi:10.1002/JOR.1100120603,.

305. Fridén, J.; Lieber, R.L. Spastic Muscle Cells Are Shorter and Stiffer than Normal Cells. *Muscle Nerve* **2003**, *27*, 157–164, doi:10.1002/MUS.10247,.

306. Smith, L.R.; Lee, K.S.; Ward, S.R.; Chambers, H.G.; Lieber, R.L. Hamstring Contractures in Children with Spastic Cerebral Palsy Result from a Stiffer Extracellular Matrix and Increased in

Vivo Sarcomere Length. *Journal of Physiology* **2011**, *589*, 2625–2639, doi:10.1113/JPHYSIOL.2010.203364,.

307. Barber, L.; Barrett, R.; Lichtwark, G. Medial Gastrocnemius Muscle Fascicle Active Torque-Length and Achilles Tendon Properties in Young Adults with Spastic Cerebral Palsy. *J. Biomech.* **2012**, *45*, 2526–2530, doi:10.1016/j.jbiomech.2012.07.018.

308. Malaiya, R.; McNee, A.E.; Fry, N.R.; Eve, L.C.; Gough, M.; Shortland, A.P. The Morphology of the Medial Gastrocnemius in Typically Developing Children and Children with Spastic Hemiplegic Cerebral Palsy. *Journal of Electromyography and Kinesiology* **2007**, *17*, 657–663, doi:10.1016/j.jelekin.2007.02.009.

309. Fry, N.R.; Gough, M.; McNee, A.E.; Shortland, A.P. Changes in the Volume and Length of the Medial Gastrocnemius after Surgical Recession in Children with Spastic Diplegic Cerebral Palsy. *Journal of Pediatric Orthopaedics* **2007**, *27*, 769–774, doi:10.1097/BPO.0B013E3181558943,.

310. Verschuren, O.; Smorenburg, A.R.P.; Luiking, Y.; Bell, K.; Barber, L.; Peterson, M.D. Determinants of Muscle Preservation in Individuals with Cerebral Palsy across the Lifespan: A Narrative Review of the Literature. *J. Cachexia Sarcopenia Muscle* **2018**, *9*, 453–464, doi:10.1002/JCSM.12287.

311. Thomason, P.; Baker, R.; Dodd, K.; Taylor, N.; Selber, P.; Wolfe, R.; Graham, H.K. Single-Event Multilevel Surgery in Children with Spastic Diplegia: A Pilot Randomized Controlled Trial. *Journal of Bone and Joint Surgery* **2011**, *93*, 451–460, doi:10.2106/JBJS.J.00410,.

312. Shore, B.J.; White, N.; Graham, H.K. Surgical Correction of Equinus Deformity in Children with Cerebral Palsy: A Systematic Review. *J. Child. Orthop.* **2010**, *4*, 277–290, doi:10.1007/S11832-010-0268-4/ASSET/3050C001-A3B5-4EAD-87F8-AD23C3C9202E/ASSETS/IMAGES/LARGE/10.1007_S11832-010-0268-4-FIG1.JPG.

313. McGinley, J.L.; Dobson, F.; Ganeshalingam, R.; Shore, B.J.; Rutz, E.; Graham, H.K. Single-Event Multilevel Surgery for Children with Cerebral Palsy: A Systematic Review. *Dev. Med. Child Neurol.* **2012**, *54*, 117–128, doi:10.1111/J.1469-8749.2011.04143.X;REQUESTEDJOURNAL:JOURNAL:14698749;PAGEGROUP:STRING:PUBLICATION.

314. Dreher, T.; Buccoliero, T.; Wolf, S.I.; Heitzmann, D.; Gantz, S.; Braatz, F.; Wenz, W. Long-Term Results after Gastrocnemius-Soleus Intramuscular Aponeurotic Recession as a Part of Multilevel Surgery in Spastic Diplegic Cerebral Palsy. *Journal of Bone and Joint Surgery* **2012**, *94*, 627–637, doi:10.2106/JBJS.K.00096,.

315. Stefko, R.; Swart, R. De; ... D.D.-J. of P.; 1998, undefined Kinematic and Kinetic Analysis of Distal Derotational Osteotomy of the Leg in Children with Cerebral Palsy. *journals.lww.comRM Stefko, RJ De Swart, DA Dodgin, MP Wyatt, KR Kaufman, DH Sutherland, HG ChambersJournal of Pediatric Orthopaedics, 1998•journals.lww.com*.

316. Rethlefsen, S.A.; Healy, B.S.; Wren, T.A.L.; Skaggs, D.L.; Kay, R.M. Causes of Intoeing Gait in Children with Cerebral Palsy. *Journal of Bone and Joint Surgery* **2006**, *88*, 2175–2180, doi:10.2106/JBJS.E.01280,.

317. Graham, H.K.; Selber, P. Musculoskeletal Aspects of Cerebral Palsy. *Journal of Bone and Joint Surgery - Series B* **2003**, *85*, 157–166, doi:10.1302/0301-620X.85B2.14066,.

318. Pons, C.; Rémy-Néris, O.; Médée, B.; Brochard, S. Validity and Reliability of Radiological Methods to Assess Proximal Hip Geometry in Children with Cerebral Palsy: A Systematic Review. *Dev. Med. Child Neurol.* **2013**, *55*, 1089–1102, doi:10.1111/DMCN.12169,.

319. Lee, S.H.; Chung, C.Y.; Park, M.S.; Choi, I.H.; Cho, T.J. Tibial Torsion in Cerebral Palsy: Validity and Reliability of Measurement. *Clin. Orthop. Relat. Res.* **2009**, *467*, 2098–2104, doi:10.1007/S11999-009-0705-1,.

320. Chung, C.Y.; Lee, K.M.; Park, M.S.; Lee, S.H.; Choi, I.H.; Cho, T.J. Validity and Reliability of Measuring Femoral Anteversion and Neck-Shaft Angle in Patients with Cerebral Palsy. *Journal of Bone and Joint Surgery* **2010**, *92*, 1195–1205, doi:10.2106/JBJS.I.00688,.

321. Terjesen, T.; Anda, S.; Rønningen, H. Ultrasound Examination for Measurement of Femoral Anteversion in Children. *Skeletal Radiol.* **1993**, *22*, 33–36, doi:10.1007/BF00191522,.

322. Rutz, E.; Donath, S.; Tirosh, O.; Graham, H.K.; Baker, R. Explaining the Variability Improvements in Gait Quality as a Result of Single Event Multi-Level Surgery in Cerebral Palsy. *Gait Posture* **2013**, *38*, 455–460, doi:10.1016/j.gaitpost.2013.01.014.

323. Barrett, R.S.; Lichtwark, G.A. Gross Muscle Morphology and Structure in Spastic Cerebral Palsy: A Systematic Review. *Dev. Med. Child Neurol.* **2010**, *52*, 794–804, doi:10.1111/J.1469-8749.2010.03686.X.

324. Akinci D'Antonoli, T.; Santini, F.; Deligianni, X.; Garcia Alzamora, M.; Rutz, E.; Bieri, O.; Brunner, R.; Weidensteiner, C. Combination of Quantitative MRI Fat Fraction and Texture Analysis to Evaluate Spastic Muscles of Children With Cerebral Palsy. *Front. Neurol.* **2021**, *12*, 633808, doi:10.3389/FNEUR.2021.633808/BIBTEX.

325. Quijano-Roy, S.; Avila-Smirnow, D.; Carlier, R.Y.; Allamand, V.; Barois, A.; Barnerias, C.; Yaou, R. Ben; Biancalana, V.; Bonne, G.; Carlier, P.; et al. Whole Body Muscle MRI Protocol: Pattern Recognition in Early Onset NM Disorders. *Neuromuscular Disorders* **2012**, *22*, doi:10.1016/j.nmd.2012.08.003.

326. Bushby, K.; Finkel, R.; Birnkrant, D.J.; Case, L.E.; Clemens, P.R.; Cripe, L.; Kaul, A.; Kinnett, K.; McDonald, C.; Pandya, S.; et al. Diagnosis and Management of Duchenne Muscular Dystrophy, Part 1: Diagnosis, and Pharmacological and Psychosocial Management. *Lancet Neurol.* **2010**, *9*, 77–93, doi:10.1016/S1474-4422(09)70271-6.

327. Fischmann, A.; Hafner, P.; Gloor, M.; Schmid, M.; Klein, A.; Pohlman, U.; Waltz, T.; Gonzalez, R.; Haas, T.; Bieri, O.; et al. Quantitative MRI and Loss of Free Ambulation in Duchenne Muscular Dystrophy. *J. Neurol.* **2013**, *260*, 969–974, doi:10.1007/S00415-012-6733-X/FIGURES/2.

328. Schwartz, M.S.; Swash, M.; Ryan, J. Why Is the Gracilis Muscle Relatively Uninvolved in Neuromuscular Disorders? *Neuromuscular Disorders* **1991**, *1*, 365–369, doi:10.1016/0960-8966(91)90123-A.

329. Tasca, G.; Iannaccone, E.; Monforte, M.; Masciullo, M.; Bianco, F.; Laschena, F.; Ottaviani, P.; Pelliccioni, M.; Pane, M.; Mercuri, E.; et al. Muscle MRI in Becker Muscular Dystrophy. *Neuromuscular Disorders* **2012**, *22*, doi:10.1016/j.nmd.2012.05.015.